N° d'ordre : 4665

THÈSE

PRÉSENTÉE A

L'UNIVERSITÉ BORDEAUX 1

ÉCOLE DOCTORALE DES SCIENCES CHIMIQUES

Par Srinivasa Rao POPURI

POUR OBTENIR LE GRADE DE

DOCTEUR

SPÉCIALITÉ: Physico-Chimie de la Matière Condensée

Etude expérimentale des relations structure-propriétés et des effets de dimensionnalité dans des oxydes de cobalt et de vanadium

Directeur de recherche : M. Antoine VILLESUZANNE, M. Michaël POLLET

Soutenance le 11 décembre 2012

Devant la commission d'examen formée de:

M. ALARIO-FRANCO Miguel	Professeur, Université Complutense de Madrid, Madrid	Président du Jury
M. PALSTRA Thomas	Professeur, Université de Groningen, Groningen	Rapporteur
Mme. HEBERT Sylvie	Directeur de Recherche, CRISMAT-CNRS, Caen	Rapporteur
M. MAGLIONE Mario	Directeur de Recherche, ICMCB-CNRS, Bordeaux	Examinateur
M. ETOURNEAU Jean	Professeur, Université de Bordeaux 1, Bordeaux	Examinateur
Mme. MICLAU Marinela	Chercheur, INCEMC, Timisoara	Examinateur
M. POLLET Michaël	Chargé de Recherche, ICMCB-CNRS, Bordeaux	Co-directeur de thèse
M. VILLESUZANNE Antoine	Chargé de Recherche, ICMCB-CNRS, Bordeaux	Directeur de thèse

Order No: 4665

THESIS

presented at

UNIVERSITY OF BORDEAUX 1

DOCTORAL SCHOOL OF CHEMICAL SCIENCES

by Srinivasa Rao POPURI

TO OBTAIN THE DEGREE OF

DOCTOR

SPECIALITY: Condensed Matter Physical Chemistry

Experimental investigation of structure-property relationships and dimensionality aspects in some cobalt and vanadium dioxides

Research directors: Dr. Antoine VILLESUZANNE, Dr. Michaël POLLET

Defended on: 11 December 2012

Before the review panel consists of:

Dr. Miguel ALARIO-FRANCO	Professor, Complutense University of Madrid, Madrid	Jury President
Dr. Thomas PALSTRA	Professor, University of Groningen, Groningen	Reviewer
Dr. Sylvie HEBERT	Director of Research, CRISMAT-CNRS, Caen	Reviewer
Dr. Mario MAGLIONE	Director of Research, ICMCB-CNRS, Bordeaux	Examiner
Dr. Jean ETOURNEAU	Professor, University of Bordeaux 1, Bordeaux	Examiner
Dr. Marinela MICLAU	Researcher, INCEMC, Timisoara	Examiner
Dr. Michaël POLLET	CNRS Researcher, ICMCB-CNRS, Bordeaux	Co-Advisor
Dr. Antoine VILLESUZANNE	CNRS Researcher, ICMCB-CNRS, Bordeaux	Advisor

Université Bordeaux 1
Les Sciences et les Technologies au service de l'Homme et de l'environnement

Dedicated to my family members

Table of contents

Acknowledgements

Grimaud, Romain Berthelot, Charlotte Mayer and **Philippe Bellanger** for their unconditional aide concerned with the technical problems, filling the administrative papers, fruitful scientific discussions and sharing pleasant working atmosphere.

In addition, there are number of people from ICMCB-CNRS as well as INCEMC to whom I owe a great deal of thanks for their enthusiastic support, help, and collaborations: ICMCB-CNRS - **Fabrice Mauvy** (scientific and non-scientific discussions), **Jean-Louis Bobet** (DSC & university administrative work), **Eric Lebraud** & **Stanislav Pechev** (XRD), **Laetitia Etienne** (ICP), **Annelise Brull** (SEM), **Michel Lahaye** (EPMA), **Dominique Michau** & **U-Chan Chung Seu** (SPS), **Rodolphe Decourt** (all transport measurements), **Olivier Nguyen** (MPMS), **Alla Artemenko** (ESR), **Christine Labrugere** (XPS-UPS), **Dominique Denux** (DSC/TGA), **François Weill** (TEM), **Sonia Gomez** (EELS); INCEMC - **Daniel Ursu** and **Kiran Kumar Bokinala** (Hydrothermal synthesis experiments), **Ina Bucur** (XRD), **Paula Sfarloaga** (SEM), **Alexandra Borza** (UV-Visible and TGA), **Radu Banica** (UV-Visible).

I am also very much grateful to **Stephane Toulin** (Library) for his quick response in providing required research articles and **Carole Malburet** (missions) for her generous help in money reimbursements for the internal and external travel.

I would like to thank both administration and infrastructure departments at ICMCB-CNRS and INCEMC for their constant support concerned with travel, administration and bureaucratic issues during my stay in Bordeaux and Timisoara.

I would like to thank all the SOPRANO members for their collaboration all along the past three years and for exchanging the scientific ideas, as well as spending good times in workshops and conferences. Additionally, I express here my sincere thanks to **Sylvie Hebert** (Co-ordinator - SOPRANO) for providing me the opportunity as a member of research network.

I am grateful to all of my friends in Bordeaux and Timisoara, who made my stay memorable one. The members of the group 1 at ICMCB-CNRS have contributed immensely to my personal and professional time in Bordeaux. The group members have been a source of friendships, lots of fun as well as good advices. I am especially grateful for the memorable time at Group 1 coffee breaks and apéroes. To **Madhu** (*Punctual*), **Manik** (*Emo*) and **Sourav** (*Chota Don*) as it has been a pleasure to having them as friends and sharing constant source

of joy and memorable week-end dinners. I would like to thank all the people whose names I did not include here, but who provided me with the necessary help and made it possible for me to complete this thesis.

I am really grateful to **my parents, sisters, brother-in-law and nephews** (**Sasi** and **Hari**), for their unconditional love, faith, support and waiting for my week-end phone calls. They have been a constant source of inspiration and this work is especially dedicated to them. To *Indu* for cheering me up whenever I felt low and being a great friend, the most supportive and caring.

Srinivasa Rao Popuri

Résumé

L'augmentation des besoins en énergie a décuplé l'intérêt pour des moyens plus efficaces ou alternatifs de production d'énergie. Dans ce contexte, les matériaux thermoélectriques, qui convertissent l'énergie thermique en énergie électrique, peuvent jouer un rôle essentiel à la fois dans la production d'énergie primaire et la conversion d'énergie. Les oxydes de métaux de transition sont une classe importante de matériaux qui présentent un large éventail de propriétés électroniques, et peuvent servir à cette fin. Les relations particulières qui existent entre structure et propriétés permettent souvent de moduler les propriétés et permettent de plus de mieux comprendre les mécanismes fondamentaux à l'origine des propriétés physiques macroscopiques. Le travail présenté dans cette thèse de doctorat porte sur la conception, la synthèse et la caractérisation physique des propriétés d'oxyde de cobalt ou de vanadium, avec à l'esprit leur application en thermoéletricité. La basse dimensionnalité a depuis longtemps été proposée comme un facteur pouvant être favorable à la thermoélectricité par: 1) l'amélioration du coefficient Seebeck en raison des effets de confinement dans les chaînes conductrices 1D ou les couches 2D; 2) la diminution de la conductivité thermique par diffusion des phonons à cause de la nature différente des liaisons chimiques entre les différentes chaînes ou couches, 3) la modification de la conductivité électrique par dopage du sous-réseau entre les chemins de conduction ou par limitation des pertes de mobilité des porteurs. Dans cette étude, nous nous sommes focalisés sur deux types de matériaux : des oxydes lamellaires de cobalt (2D) et des oxydes de vanadium mono- ou bi-dimmensionnels.

Les oxydes de cobalt lamellaires dérivent de la structure α-NaFeO$_2$. Il y a eu un vif intérêt pour ces oxydes de métaux de transition en couches pour les applications liées à l'énergie depuis la découverte d'un fort coefficient Seebeck associé à un comportement métallique dans Na$_x$CoO$_2$ ou encore de la supraconductivité dans le composé hydraté. Les delafossites sont une classe similaire d'oxydes de faible dimensionnalité ou des ions d^9 ou d^{10} occupent le feuillet du sodium. Dans ce cas, des valeurs élevées du coefficient de Seebeck ont déjà été observés, ce qui en fait des candidats intéressants pour des applications thermoélectriques. Ces composés sont aussi connus pour leurs propriétés de conducteurs transparents, des comportements magnétiques complexes dus à la frustration magnétique dans le réseau métallique triangulaire ou encore des effets multiferroïques. Profitant de basse dimensionnalité, nous avons fait varier la composition des Cobaltates P2-Na$_{0.7}$CoO$_2$ et D2-AgCoO$_2$, par des substitutions Mg et Mn en site cobalt pour moduler le rapport Co^{3+}/Co^{4+}. L'évolution des propriétés de transport a pu être expliquée sur la

base de changements structuraux et les caractéristiques thermoélectriques ont été discutées. Les propriétés électroniques sont effectivement très sensibles aux évolutions structurales et en particulier, l'expansion des paramètres de maille avec les substitutions augmente généralement la localisation des charges et introduit un fort désordre dans le système ce qui conduit à une réduction drastique de la conductivité.
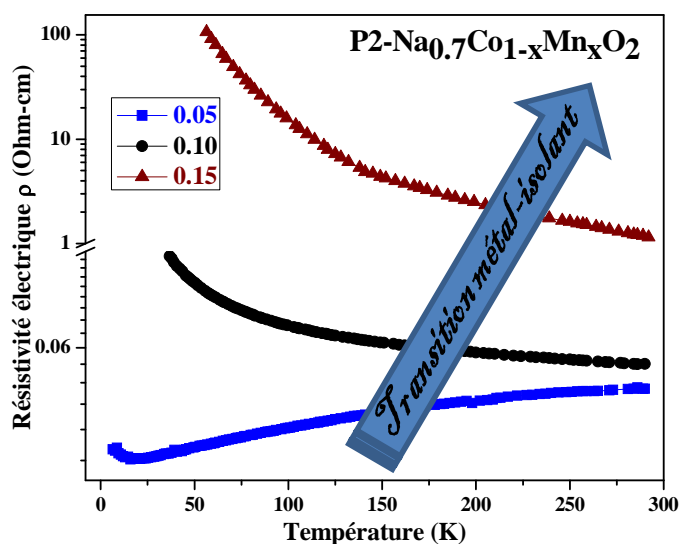
Fig. 1. Evolution thermique de la résistivité électrique mesurée pour les composés de la famille P2-$Na_{0.7}Co_{1-x}Mn_xO_2$.

En ce qui concerne les performances thermoélectriques, pour de faibles taux de substitution, cet effet est contrebalancé par une augmentation du coefficient Seebeck ce qui se traduit ponctuellement par un facteur de puissance plus élevé.
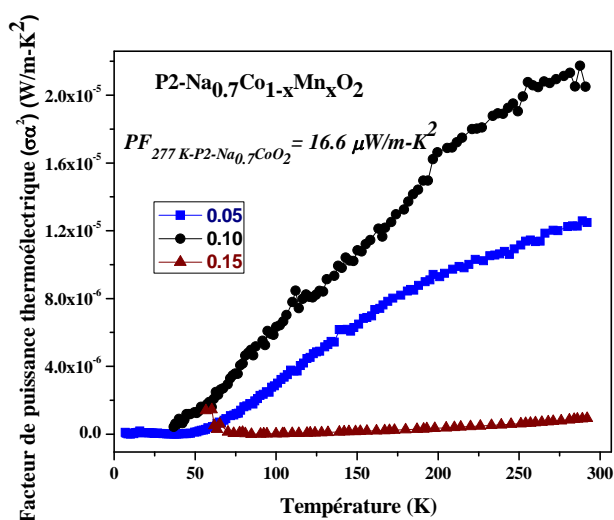
Fig. 2. Evolution thermique du facteur de puissance thermoélectrique mesurée pour les composés de la famille P2-$Na_{0.7}Co_{1-x}Mn_xO_2$.

Les oxydes de vanadium de structure quasi-1D ou 2D sont connus pour leurs nombreux polymorphes et pour leurs transitions métal-isolant (MIT) réversibles caractérisées par des variations brutales des propriétés électroniques. Parmi ces oxydes de vanadium VO_2 offre la température de transition la plus proche de la température ambiante avec $T_t = 340$ K. Bien que la nature de la transition elle-même ne soit pas totalement comprise, en raison des variations extrêmement brutales et intenses de ses propriétés à la transition VO_2 a été largement étudié en vue d'applications électroniques, optiques et applications connexes de l'énergie. Dans ce contexte, l'observation d'un régime métallique Curie-Weiss dans le système $V_{1-x}Mo_xO_2$, analogue à celui observé pour $Na_{0.7}CoO_2$, nous a incité à explorer ses propriétés thermoélectriques.
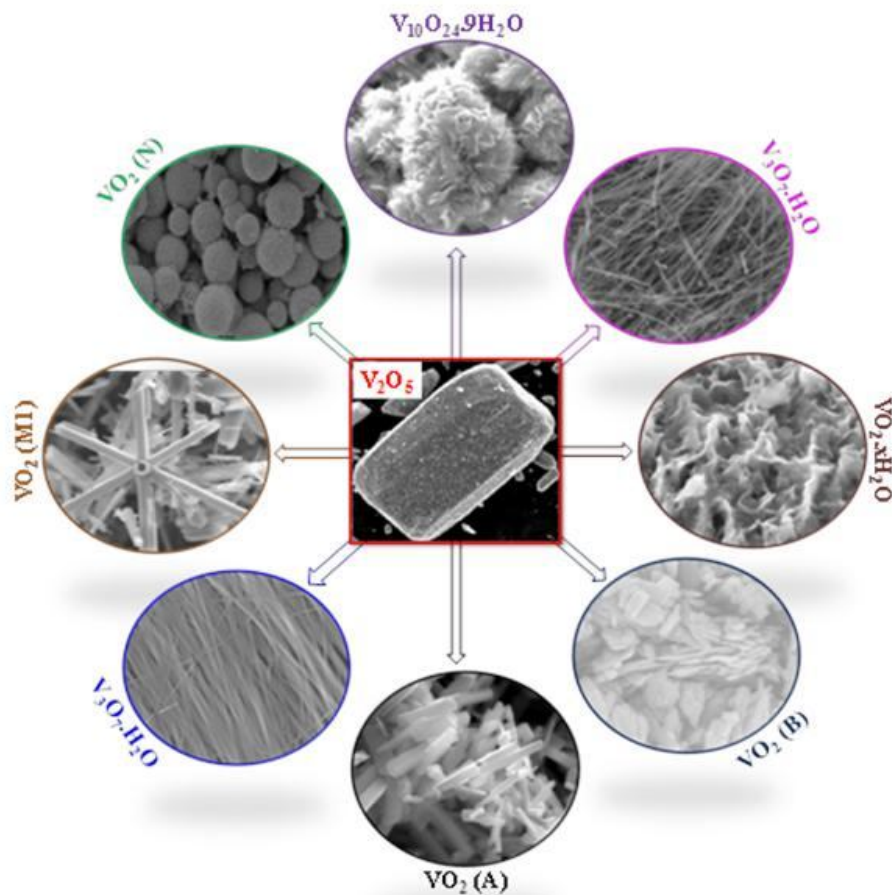
Fig. 3. Morphologies des composés finaux cristallins obtenus après la synthèse hydrothermale.

Par synthèse hydrothermale en une seule étape et par construction systématique des diagrammes de phases cinétiques, nous avons été en mesure de proposer des protocoles optimisés pour stabiliser divers polymorphes de VO_2 ainsi que certaines phases hydratées. Des expériences de substitution par voie hydrothermale nous ont aussi permis de stabiliser divers nouveaux composés mais aussi d'accéder à certains intermédiaires de réaction permettant ainsi d'élucider certains mécanismes réactionnels.

Nos études sur M1-VO_2 sont en accord avec l'hypothèse d'une transition de Mott renforcée par un état de Peierls prenant son origine dans l'ordre orbitalaire. Dans le cas particulier de M1-VO_2, les degrés de liberté de spin, orbitalaire et de réseau sont si fortement couplés que l'ordre orbitalaire et les états de Mott et Peierls se développent simultanément entrainant des changements brusques à la transition.
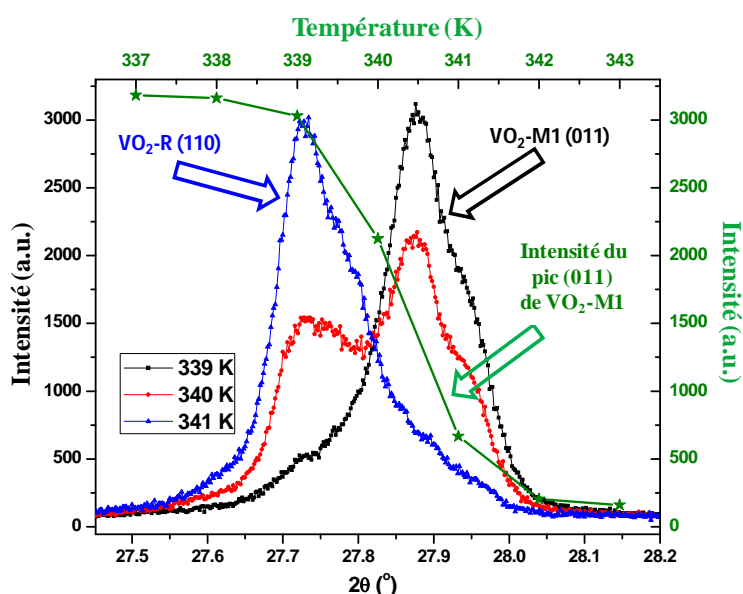
Fig. 4. Transition de phase structurale de VO2-M1 à R, par étude in situ de diffraction de poudre aux rayons X.

Nos travaux sur $V_{1-x}Mo_xO_2$ (M1/R) ont confirmé l'intérêt des systèmes fortement corrélés pour l'amélioration des propriétés thermoélectriques avec un maximum d'efficacité relevé pour une substitution de 7,5% dans le régime de Curie-Weiss métallique. Ce maximum est lié à un complexe équilibre des divers états de valences des différents cations présents et met en avant le rôle des transferts de charge sur l'intensité des corrélations et les propriétés électroniques

résultantes. La variation inattendue des moments magnétiques effectifs en fonction de la teneur en Mo écarte de plus le simple scénario de brisure de l'état Peierls par substitution.
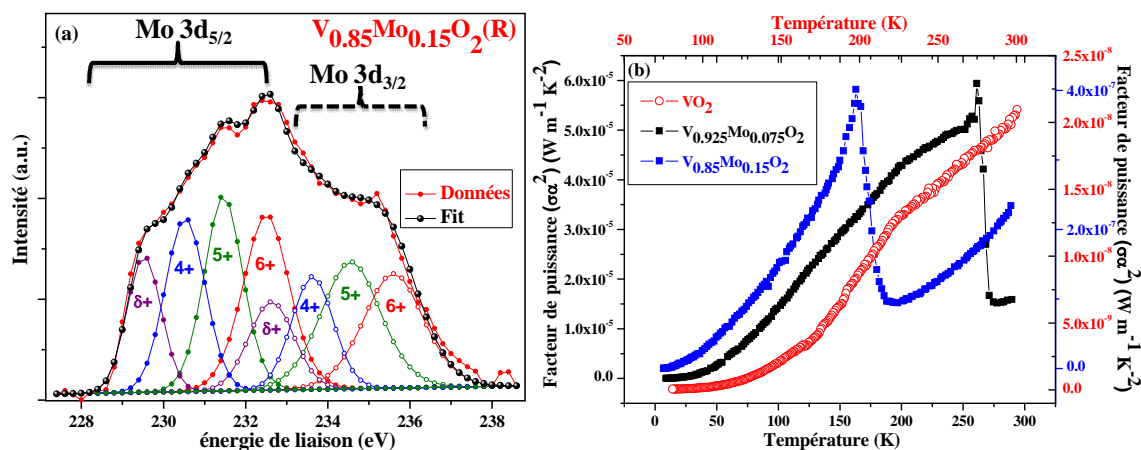
Fig. 5. (a) Spectre typique des niveaux de cœur XPS dans la région énergétique de Mo 3d pour $V_{0.85}Mo_{0.15}O_2$; (b) Evolution thermique du facteur de puissance thermoélectrique mesurée pour les composés de la famille $V_{1-x}Mo_xO_2$ (x=0; 0.075; 0.15).

Le frittage haute pression par Spark Plasma Sintering a été utilisé pour consolider les composés VO_2 (A) et VO_2 (B) et accéder aux propriétés intrinsèques électroniques de ces deux polymorphes. VO_2 (A) est caractérisé par une transition de phase structurale progressive et réversible accompagnée d'une transition semi-conducteur - semi-conducteur entre 150 K et 470 K. Dans ce cas, des interactions directes-indirectes entre les atomes de vanadium voisins conduient à un ordre orbitalaire à 530 K. Le découplage marqué entre ordre orbitalaire et états Mott/Peierls qui se développent à 437 K, conduit à de plus petits changements à la transition électronique. Contrairement aux composés A et M1, $VO2$ (B) ne présente aucun ordre à longue distance et aucun changement profond dans la structure cristalline. Ce résultat se traduit par une transition semi-conducteur - semi-conducteur « douce » centrée à environ 240 K ; la largeur de la transition est cependant très grande comparée à M1 et s'étale sur une centaine de degrés. Bien que la transition prenne son origine essentiellement dans des mécanismes similaires aux autres polymorphes, nous avons pu proposer sur la base de détails structuraux et magnétiques un scénario plus élaboré impliquant deux transitions avec un appariement à courte distance (paire V-V) à haute température suivi d'un ordre magnétique AFM à longue distance à basse température.

Structure-property relationships : Summary
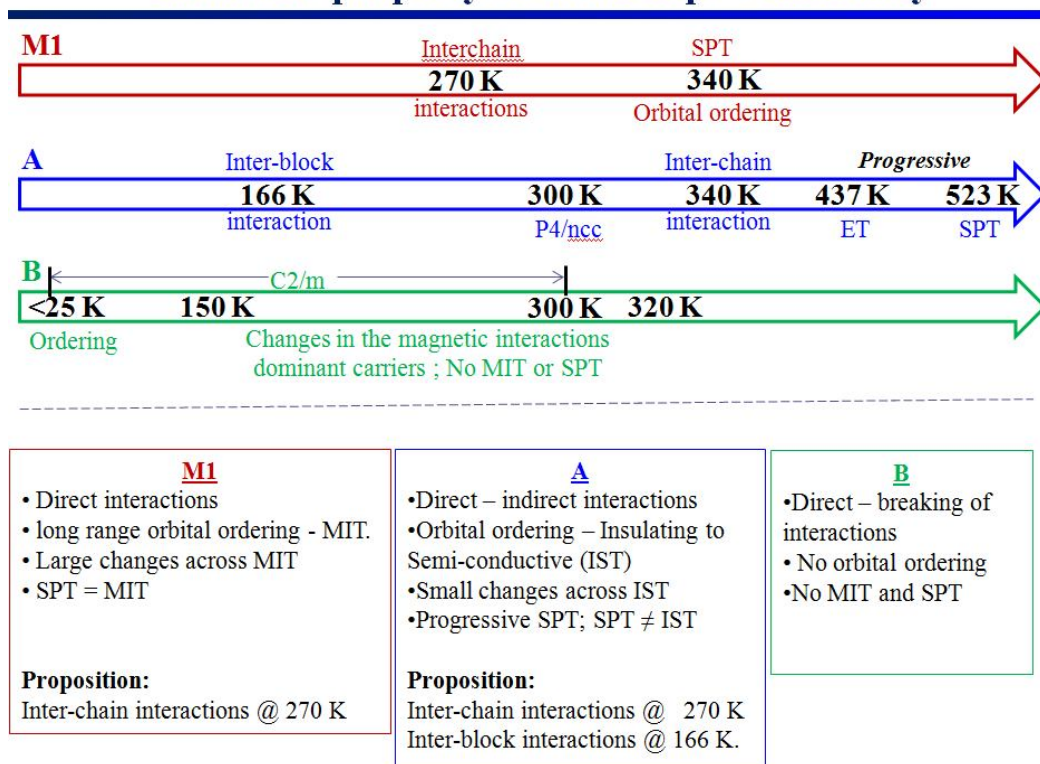
SPT: Structural phase transition; MIT: metal-insulator transition

Fig. 6. Résumé des observations expérimentales liées aux relations structure-propriétés dans le cas des polymorphes VO_2 A, B et M1.

The global need for energy alternatives has intensified interest in more effective means of power generation. In this contest, thermoelectric materials, which convert heat energy to electrical energy, can play a vital role in both primary power generation and energy conversion. Transition metal oxides are an important class of materials that exhibit a wide range of electronic properties, and can serve to this purpose. Their unique structure-property relationships often allow for property tuning and provide insight into the fundamentals of mechanisms behind the macroscopic physical properties. The ability to engineer the structure by solid state chemistry makes it possible to design new functional materials with specific and optimized properties. The present work in this doctoral thesis deals with the design, synthesis and physical properties characterization of cobalt and vanadium oxide materials, with thermoelectric applications in mind.

Low dimensionality is proposed to be favorable for thermoelectrics by: 1) an enhancement of the Seebeck coefficient due to the carrier confinement effects in the conducting 1D chains or 2D layers; 2) decreasing the thermal conductivity because of a phonon-scattering effect, due to the different chemical bonding between the chains or layers; 3) modifying the electrical conductivity by doping in the sub-lattice outside of the conducting paths to prevent the decrease in the carrier mobility [1].

Low dimensional lamellar cobalt oxides derive from the α-NaFeO$_2$ crystal structure type [2]. Since the discovery of large Seebeck coefficients with metallic behavior and superconductivity in non-hydrated and hydrated Na$_x$CoO$_2$, there has been intense interest in transition metal oxides with layered (quasi) two-dimensional (2D) crystal structures for energy related applications [3,4]. Similar class of low-dimensional materials that consist of 2D cobalt layers are the delafossite oxides. In this case, large values of the Seebeck coefficient have already been observed, making them interesting candidates for thermoelectric applications. These compounds with delafossite structure also exhibit transparent conductor properties, multiferroic behaviors and complex magnetic ordering from frustrated magnetic interactions in the metal triangular lattice [5]. Taking advantage of low dimensionality, we have varied the composition of P2-Na$_{0.7}$CoO$_2$ and D2-AgCoO$_2$ cobaltates, by Mg and Mn substitutions at Co site, to tune the Co^{3+}/Co^{4+} ratio. The modulated transport properties are understood on the basis of changes in the crystal structure and the thermoelectric characteristics are discussed.

Quasi 1D or 2D vanadium oxides are well known for their reversible metal-insulator transitions (MIT) followed by drastic changes in electronic properties and for their numerous polymorph structures [6]. Among vanadium oxides, the MIT temperature (T_t=340 K) of VO_2 is the closest to room temperature [7]. Owing to the outstanding changes across the MIT, VO_2 has been intensely investigated to be applied for electronic, optical and energy related applications, although the nature of the transition in still unclear [8]. In this context, the observation of Curie Weiss metallic region in the $V_{1-x}Mo_xO_2$ system, similarly to thermoelectric $Na_{0.7}Coo_2$ system, attracted us for probing its thermoelectric properties. In addition, we combined in-situ P-XRD studies and magnetic properties characterization to understand the mechanisms behind the structural phase transitions around the MIT. We further extended our studies to the transport properties of metastable polymorphs VO_2 (A) and VO_2 (B), and to their phase transition mechanisms.

Organization of the manuscript:

Chapter I: A review of the basic concepts in the context of the thermoelectricity, as well as some of the latest advances in cobalt based thermoelectric oxides, are presented.

Chapter II: The synthesis routes implemented for the preparation of pure and substituted layered cobalt double oxides are described.

Chapter III: The thermoelectric and magnetic properties of pristine, Mn substituted P2-$Na_{0.7}CoO_2$ and Mg, Mn substituted D2-$AgCoO_2$ materials are presented.

Chapter IV: A brief introduction to the existing phases in the vanadium / oxygen system, and on the nature of the metal-insulator and structural phase transitions in the context of VO_2 (M1) is given. In addition, we review the effects of the substituents that alter VO_2 (M1) phase transition temperatures. We summarize the hydrothermal synthesis and report properties of metastable VO_2 (A) and VO_2 (B) polymorphs.

Chapter V: The protocols used to prepare the pristine and substituted polymorphs of VO_2 using solid state synthesis and hydrothermal processes are presented. In addition, we describe optimized conditions for the preparation of several polymorphs of the V-O system by constructing systematic kinetic phase diagrams.

Chapter VI: We present results related to phase coexistence and correlations between structural phase transition and metal insulator transition in $V_{1-x}Mo_xO_2$ (M1). Furthermore, we studied the valence degree of V and Mo (using XPS measurements), magnetic and thermoelectric properties.

C*hapter VII:* We reinvestigated the crystal structure of VO_2 (A) and studied the phase transition mechanisms among LTP-, HTP-A and VO_2 (M1) phases. Finally, we present the physical properties of VO_2 (A).

Chapter VIII: We describe the structural and physical properties (electrical and magnetic properties) of VO_2 (B).

Chapter IX: Conclusion and perspectives to this work

References:

[1] L. D. Hicks and M. S. Dresselhaus, Phys. Rev. B 47, 12727 (1993); L. D. Hicks and M. S. Dresselhaus, Phys. Rev. B 47, 16631 (1993); R. Venkatasubramanian, E. Siivola, T. Colpitts, B.O. Quinn, Nature 413, 597 (2001); K. Koumoto, H. Koduka, W.S. Seo, J. Mater. Chem. 11, 251 (2001)

[2] R.D. Shannon, Acta Crystallogr. A 32, 751 (1976)

[3] K. Takada, Nature 422, 53 (2003)

[4] I. Terasaki, Y. Sasago, and K. Uchinokura, Phys. Rev. B 56, R12685 (1997)

[5] H. Kawazoe, M. Yasukawa, H. Hyodo, M. Kurita, H. Yanagi, H. Hosono, Nature 389, 939 (1997); E. Pachoud, K. Singh, Y. Breard, C. Martin, G. Andre, V. Hardy, Ch. Simon, and A. Maignan, Phys. Rev. B 86, 054437 (2012)

[6] F. J. Morin, Phys. Rev. Lett. 3, 34 (1959)

[7] J. P. Pouget, Phys. Rev. Lett. 35, 873 (1975)

[8] M. Soltani, M. Chaker, E. Haddad, and R. Kruzelesky, Meas. Sci. Technol. 17, 1052 (2006); M.J. Lee, Y. Park, D. S. Suh, E. H. Lee, S. Seo, D. C. Kim, R. Jung, B. S. Kang, J. S. Lim, and B. H. Park, Adv. Mater. 19, 3919 (2007); T. Driscoll, H. T. Kim, B. G. Chae, M. Di Ventra, D. N. Basov, Appl. Phys. Lett. 95, 043503 (2009)

Chapter I:
Introduction to layered cobalt double oxides

In this chapter, a background on the thermoelectricity and a simple model for the thermopower of a material are presented. The figure of merit is introduced, and furthermore a brief review of the current status of thermoelectric materials is given. Finally, possible applications of thermoelectric materials as heat pumps and generators of electrical power are discussed.
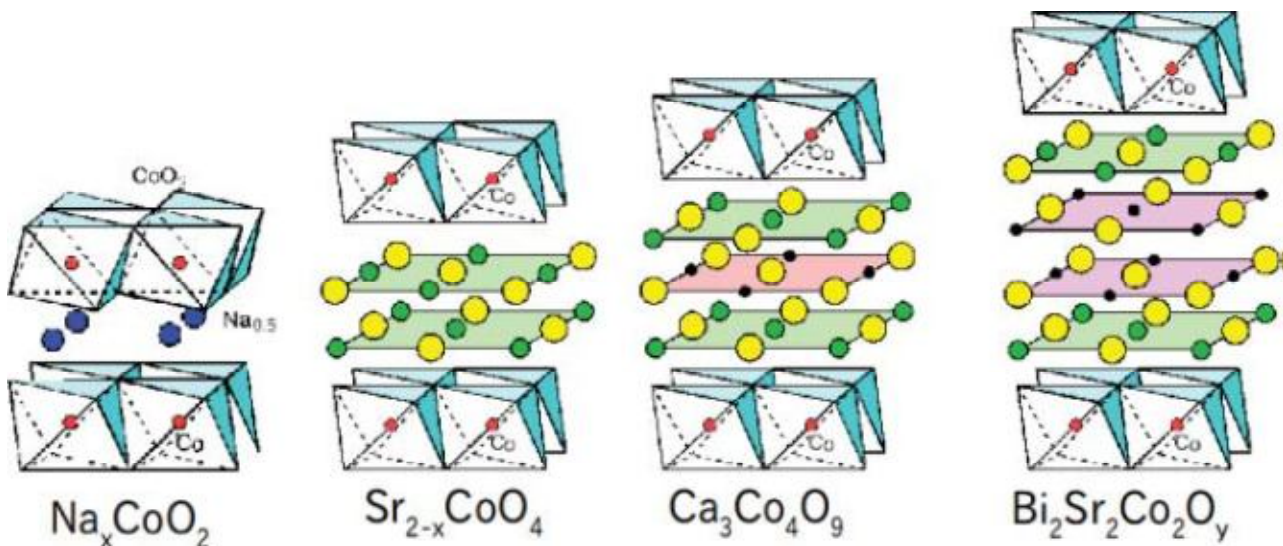
Contents

I.1. Introduction

Global energy demands are increasing continuously. To date, fossil fuels have served as a major energy source to meet these ever growing energy needs. It is generally accepted that while fossil fuel technology is well developed, it is not sustainable and its subsequent carbon footprint is a contributing factor to global warming. Alternative energy sources are thus necessary and they should be both renewable and environmentally clean. In addition to developing alternative energy sources to meet growing energy requirements, it is equally important to improve the efficiency of energy generation. Energy efficiency and alternative energy are said to be the "twin pillars" of sustainable energy policy. Approximately 90% of the world's electricity is generated by thermal energy, typically operating at only 30–40% efficiency, losing a major portion of the energy in the form of radiant heat to the environment.

Thermoelectric power generation technology is expected to help overcome global warming and climate change issues by recovering and converting waste heat into electricity, thus improving the total efficiency of energy utilization and suppressing the consumption of fossil fuels that are supposedly the major sources of CO_2 emission. The thermoelectric effect is a phenomenon in which a temperature gradient creates an electric potential. Efficient thermoelectric materials can thus partly convert some of the lost heat into useful electricity and increase the overall efficiency of the energy generation. Beyond the energy industry, segment applications are also explored like *e.g.* the capture of heat lost in the exhaust of automobiles to produce electricity for the on-board equipment. Because the working fluids are simply electrons and holes in solids, thermoelectric energy conversion technologies are environmentally friendly.

The nowdays immense interest in thermoelectric materials is highlighted in **Figure 1** [1] where the per-year number of publications on thermoelectric topics is plotted *vs* time. The first wave (labeled I) is related to the pionner work of Ioffe on doped-semiconductors while the second wave (labeled II) is related to recent progresses in materials shaping and design and strongly correlated materials understanding.
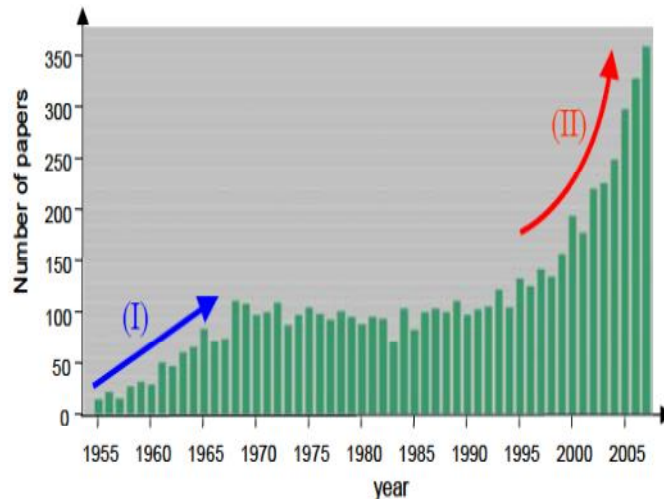
Figure 1. Number of papers on thermoelectric materials published as a function of year from 1955 to 2007.

I.2. Thermoelectricity

An electron in solid is an elementary particle that carries a negative charge (-e); applying a potential gradient results in the flow of these electric carriers and the creation of an electric current.

Similarly, since an enormous number of electrons are at thermal equilibrium in solids, they also carry heat and entropy; in the presence of a temperature gradient, they can flow from the hot side to the cold side, inducing a potential gradient.

Such coupling between thermal and electrical phenomena is called thermoelectric effects. In early 19th century, Thomas Seebeck and Jean Peltier, first discovered the phenomena that are the basis for today's thermoelectric technology. According to Seebeck effect, if we place a temperature gradient across the junctions of two dissimilar conductors, electrical current would flow. On the other hand, according to Peltier effect, when current passes through two dissimilar electrical conductors, either heat will be emitted or absorbed at the junction of the materials [2,3].

Using the Seebeck effect, thermal energy (heat) can be converted into electric energy, which is called thermoelectric power generation. **Figure 2a** shows the schematic picture of the thermoelectric power generation, in which a pair of n-type and p-type conductors is electrically connected in series. By imposing a temperature difference to the device, the electrical energy is produced. If a load is connected to the sample, the electric power is consumed at the load. Here the thermoelectric material acts as a kind of battery, where the thermoelectric power corresponds to the electro-motive force, and the resistivity corresponds to the internal resistance. Advantages of thermoelectric power generation are (i) electric power source without maintenance, (ii) energy recovery from waste heat, and (iii) long operating lifetime.
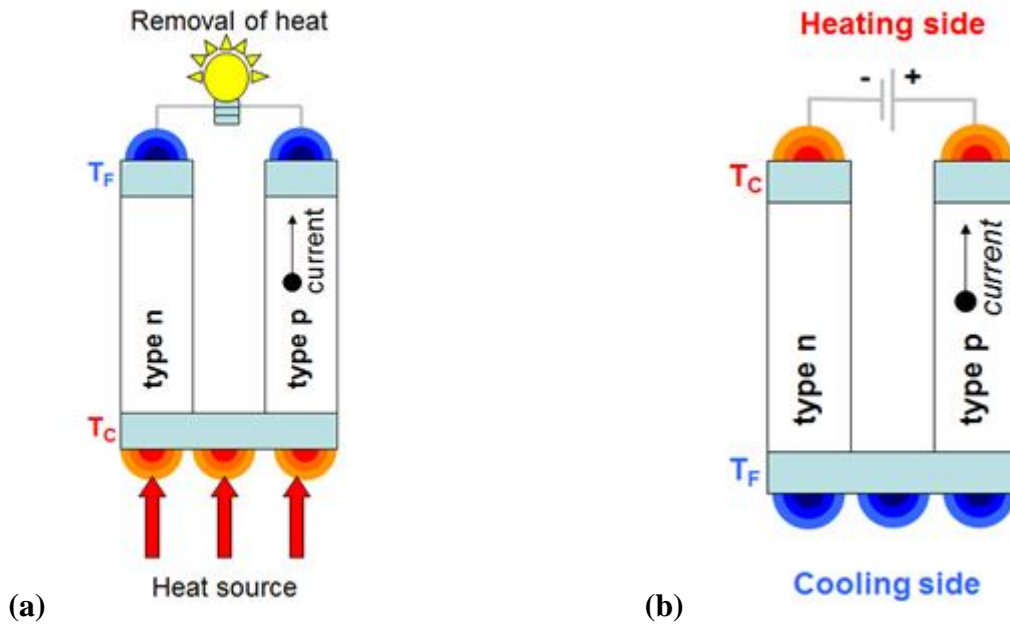
Figure 2. Schematic representation of the (a) thermoelectric power generation, based on Seebeck effect; (b) the thermoelectric cooler or heater, based on Peltier effect.

Using the Peltier effect, we can design thermoelectric (TE) coolers or heaters. **Figure 2b** shows the schematic picture of the thermoelectric (TE) cooler or heater. When DC voltage is applied to the module, the positive and negative charge carriers flow and transport in the same time some heat from one side to the opposite side. The surface where heat energy is absorbed becomes cold; the opposite surface where heat energy is released, becomes hot.

The choice of a cooling technology will depend heavily on the unique requirements of any given application, however, thermoelectric (TE) coolers offer several distinct advantages over other technologies: (i) TE coolers have no moving parts and, therefore, need substantially less maintenance (ii) lifetime of TE devices depends on lifetime of the operating materials (iii) TE coolers contain no chlorofluorocarbons or other materials, which may require periodic replenishment (iv) TE coolers can function in an environments that are too severe, too sensitive or too small for conventional refrigeration (v) The direction of heat pumping in a TE system is fully reversible. Changing the polarity of the DC power supply causes heat to be pumped in the opposite direction—a cooler can then become a heater.

The performance of a thermoelectric module is usually quantified using the figure of merit Z. Because Z is in units of inverse Kelvin, ZT is called the nondimensional figure of merit. It is customary to express the usefulness of a thermoelectric material for refrigeration or power generation applications in terms of this dimensionless quantity ZT where T is the temperature (in degrees Kelvin) and Z is the thermoelectric figure of merit [4,5]

$$ZT = \alpha^2 T / \rho \kappa$$

Where ρ is the electrical resistivity (electrical conductivity $\sigma = 1/\rho$), α is the Seebeck coefficient (or thermoelectric power) and κ is the thermal conductivity. Here $\alpha^2 \sigma$ is known as the (thermoeletric) power factor. For the development of a practical thermoelectric material, it is necessary to have large values of ZT. This requires in the same time high thermoelectric power, electrical conductivity and thermal resistivity. All these transport properties are interelated: in the classical picture, an increase in the thermoelectric power normally implies a decrease in the electrical conductivity and a decrease in the electronic contribution to thermal conductivity (Wiedemann-Franz law). A compromise on characteristics such as carrier concentration, effective mass, etc is thus needed to optimize the ZT. Additionally, ZT values are temperature dependent: they usually peak at a given temperature and drop-off elsewhere. Thus, refrigeration and power generation often require different materials, depending on the operational temperature range.

A thermoelectric power generator has a maximum efficiency given by

$$\eta = \frac{T_h - T_c}{T_h} \frac{\sqrt{1 + ZT_m} - 1}{\sqrt{1 + ZT_m} + T_c / T_h}$$

and a refrigerator has a maximum coefficient of performance (COP) given by

$$COP = \frac{T_c}{T_h - T_c} \frac{\sqrt{1 + ZT_m} - T_h / T_c}{\sqrt{1 + ZT_m} + 1}$$

Where T_h, T_c are the temperatures at the hot and cold sides, T_m is the mean temperature and Z is the thermoelectric figure of merit. These expressions show that high ZT thermoelectric devices approach the Carnot limit and highlight that the key to thermoelectric technology is finding materials with a large ZT. Because of the conflicting requirements on materials properties, high ZT materials are elusive. Compromise materials with reasonable ZT are usually heavily doped semiconductors and some semimetals. For making efficient devices, both n-type and p-type materials with comparable ZT are needed.

I.2.1. Factors affecting ZT

I.2.1.1. Seebeck coefficient

The Seebeck effect, caused by the heat gradient, induces an accumulation of the charge carriers on the cold side of each leg, thereby imposing a net voltage across the electrically coupled series. This voltage (ΔV) is proportional to the applied temperature gradient (ΔT), expressed as [6,7]

$$\Delta V = \alpha.\Delta T$$

where α is called the Seebeck coefficient (or thermoelectric power or thermopower). To ensure that the Seebeck coefficient is large, there should only be a single type of carrier. Mixed n-type and p-type conduction will lead to charge carriers moving both to the cold end, cancelling out the induced Seebeck voltages.

Consider a n type semiconductor subject to a temperature gradient, as shown in **Figure 3.** Suppose the temperature at one side is T1, and the temperature at the other side is T2 with T2>T1.
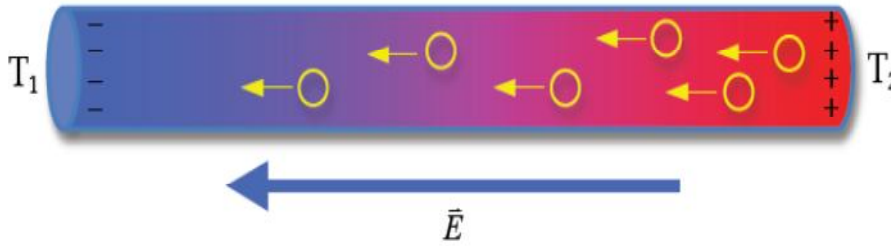
Figure 3. Representation of Charge Carrier Diffusion in Thermo-element.

Since the average electron velocity is larger at T2, electrons diffuse from the high temperature side (T2) to the low temperature side (T1). Because of charge neutrality, the side at T2 is positively charged, whereas the side at T1 is negatively charged. This implies that the system behaves like a capacitor in the temperature gradient, which is the origin of the thermoelectric voltage ΔV.

In a steady state,

$$\alpha = \Delta V/\Delta T$$

When T tends to infinite, the Seebeck coefficient (α) depends on the entropy S of the system and the number of charge carriers N.

$$\alpha_{T\to\infty} = -\frac{1}{e}\left(\frac{\partial S}{\partial N}\right)$$

The sign of the Seebeck coefficient depends on the type of carriers. If the dominant carriers are electrons then α will be negative and if the dominant carriers are holes then α will be positive. The thermal dependence of α is a function of the carrier concentration and carrier diffusion mechanisms, which leads to distinguish expressions of α for a metal and semiconductors.

The Mott equation describes the Seebeck coefficient behavior of metals as a function of temperature as

$$\alpha(T) = \frac{\pi^2 k_B^2}{3e} T \left[\frac{\partial \ln(\sigma(E))}{\partial E} \right]_{E=E_f}$$

In the case of semiconductor material, charged particle must be excited across an energy gap E_G, in this case the thermopower is approximated by

$$\alpha \approx \left(\frac{k_B}{e} \right) \frac{E_G}{k_B T}$$

where K_B is Boltzman constant, e is electron charge and σ is electrical conductivity.

I.2.1.2. Electronic conductivity

The electrical conductivity of a material is related to the number of charge carriers (n) and their mobility (μ), which is typically given by

$$\sigma = ne\mu.$$

Here the mobility can be estimated by

$$\mu = e\tau/m_e$$

Where m_e is the effective mass, e is electronic charge and τ is the mean scattering time between collisions for the carriers.

In general metals are characterized by a high value of electrical conductivity due to availability of large number of charge carriers and states. On the other hand for semiconductors, the charge carriers must be thermally excited across a gap for conduction to occur.

$$\sigma = \sigma_0 \exp(-E_g/kT)$$

The conductivity can occur through the contributions of both holes and electrons; the high conductivity in a semiconductor can be achieved, either by having a very small gap to excite across or by having very high mobility carriers.

I.2.1.3. Thermal conductivity

Additional materials design conflicts stem from the necessity for low thermal conductivity. Thermal conductivity in thermoelectrics comes from two sources: (1) electrons and holes transporting heat (κ_e) and (2) phonons travelling through the lattice (κ_L) [8,9].

Most of the electronic term (κ_e) is related to the electrical conductivity as expressed in the Wiedemann–Franz law:

$$\kappa_e = \sigma LT = ne\mu LT$$

where L is the Lorenz number (2.4×10^{-8} J^2 K^{-2}C^{-2} for free electrons).

The lattice thermal conductivity is due to the propagation of acoustic phonons in the solid. It can be described by the classical theory of transport in diffusive regimes:

$$\kappa_L = C_v V_s l_\phi$$

where C_v is the specific heat per volume unit, V_s is the sound velocity, and l_ϕ is the phonon mean free path.

I.2.2. The carrier concentration, a traditional key parameter

In a classical picture, to select a good thermoelectric material one should find the best compromise among large thermopower, high electrical conductivity and low thermal conductivity, to maximize the figure of merit [10].
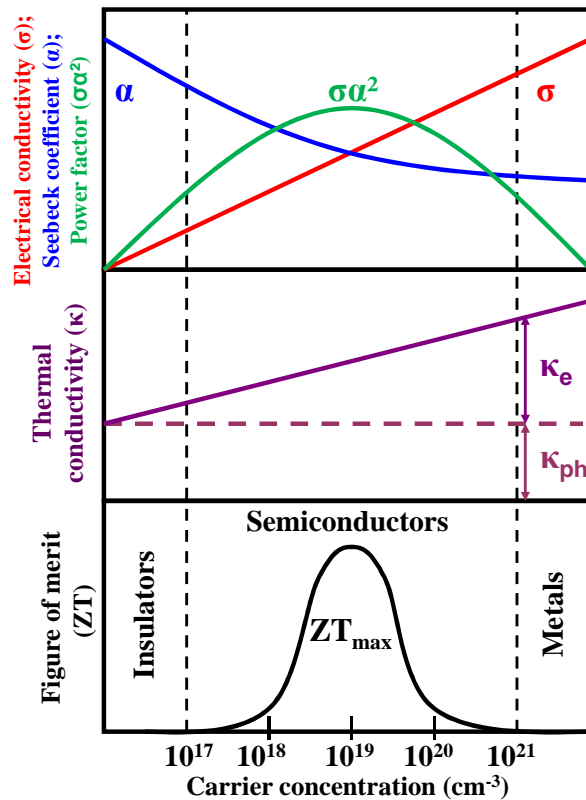
Figure 4. The conflicting constituents of the thermoelectric figure of merit (ZT). In this figure α is the Seebeck coefficient (blue), σ is the electrical conductivity (red), κ is the thermal conductivity (purple), $\alpha^2\sigma$ is the thermoeletric power factor (green), and ZT is the thermoelectric figure-of-merit (black).

Such compromise requirement lead to the concept of 'phonon-glass electron-crystal' (PGEC) [129]. The electron-crystal requirement stems from the fact that crystalline semiconductors have been the best at meeting the compromises required from the transport properties (Seebeck coefficient and

electrical conductivity). The phonon-glass requirement stems from the need for as low a lattice thermal conductivity. These two requirements typically occurs at carrier concentrations between 10^{18} and 10^{20} carriers per cm^3, shown in **Figure 4**, which falls in between common metals and semiconductors — that is, concentrations found in heavily doped semiconductors [130].

I.2.3. The dimensionality and size effects

In conventional three dimensional crystalline systems, α, σ and κ are inter-related and it is very difficult to control these variables independently to increase ZT. However, if the dimensionality of the material is decreased, a new variable –a length scale- becomes available. As the dimensionality is lowered a dramatic differences in the density of electronic states (**Figure 5**) appears and it is expected to allow for new opportunities to vary the quantities α, ρ and κ independently [131].
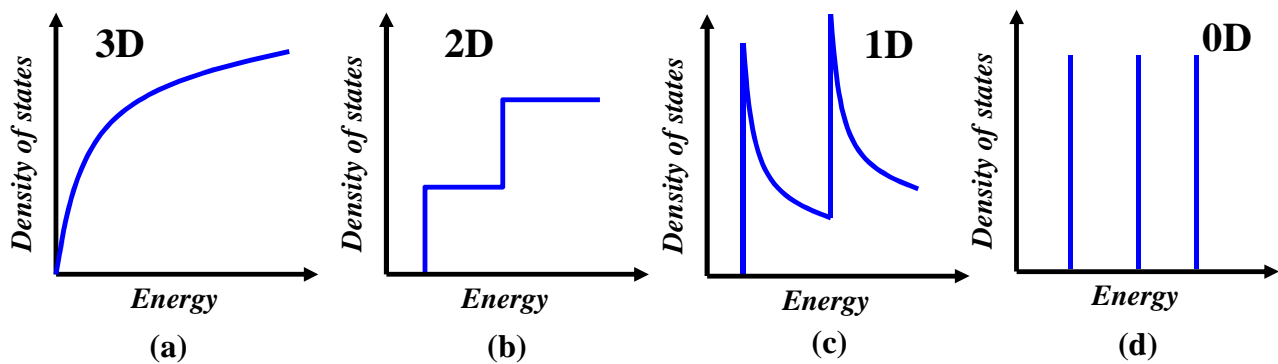
Figure 5. Schematic of electronic density-of-states of low-dimensional systems a) bulk 3D crystalline semiconductor, b) a 2D quantum well, c) a 1D nanowire or nanotube and d) a 0D quantum dot [132].

It was initially suggested that thermoelectric efficiency could be improved at the nanoscale because of two reasons. i) Low-dimensionality and quantum size effects could improve the Seebeck coefficient [11] and ii) Small feature sizes enhance phonon scattering on nanoscale interfaces and reduce thermal conductivity [12]. Indeed, large improvements of ZT in low-dimensional structures such as 0D quantum dots, 1D nanowires (NW), 2D superlattices and bulk nanocomposites have recently been achieved [13-24]. This was even achieved for common materials, and importantly in Silicon based systems such as Si, SiGe, and SiC [25-28]. Silicon, the most common semiconductor with the most advanced industrial processes, is a poor TE material with $ZT_{bulk} \sim 0.01$. Si NWs, on the other hand, have demonstrated ZT ~ 1, which is nearly a 100 fold increase [25-28], and they are now considered as emerging candidates for high efficiency and large scale production TE applications.

Higher ZT values of NWs originates from a dramatic reduction in the lattice thermal conductivity κ_L [29-33].

Until now, to increase the ZT for low dimensional systems, two main strategies are implemented; the first one is to reduce the thermal conductivity and the second one is to increase the power factor.

There are three general ways to reduce lattice thermal conductivity that have been successfully used. (1) To scatter phonons within the unit cell by creating rattling structures or point defects such as interstitials, vacancies or by alloying [40]. (2) To use complex crystal structures to separate the „electron-crystal" and the „phonon-glass" parts [129]. Here the goal is to achieve a phonon glass without disrupting the crystallinity of the electron-transport region. (3) To scatter phonons at interfaces, leading to the use of multiphase composites mixed on the nanometre scale [41]. These nanostructured materials can be formed as thin-film superlattices or as intimately mixed composite structures, by increasing the presence of interfaces which scatter phonons more effectively than electrons [42].

It has very recently become evident that benefits from κ_l reduction are reaching their limits, and further increases of ZT can only be achieved through improvements in the power factor $\alpha^2\sigma$ [34,35]. By nanostructuring, the electronic structure could be engineered to tune the Seebeck coefficient [36-38] and the electrical conductivity [39] independently, which could maximize $\alpha^2\sigma$. To increase the power factor several directions are explored like, (1) By enhancing the Seebeck coefficient by a sharp increase in the local density of states around the Fermi level [133] (2) Another strategy involves finding ways to increase the number of carrier pockets contributing to transport through imposing suitable perturbations to the electronic structure [42]. (3) Concept of energy filtering of carriers by the introduction of appropriate barriers which restrict the energy of carriers entering into a material at an interface, so that the mean energy of the carriers substantially exceeds those at the Fermi level E_F , thereby enhancing the thermopower which depends of the excess energy $(E - E_F)$ of carriers in the sample [43,44]. Using the energy filtering approach, barriers are introduced in such a way that the reduction in the electrical conductivity is more than compensated by the increase in the Seebeck coefficient S through the energy filtering process, thereby resulting in an increase in thermoelectric power factor.

Another size-dependent effect that can be exploited is the semimetal-semiconductor transition [45,46]: when the size of a semimetal nanowire decreases and few quantum states remain normal to the nanowire axis, the energy bands split into discrete levels that can be individually monitored. In this quantum regime, the lowest conduction subband energy level moves up in energy as the wire

diameter decreases while the highest valence subband energy level moves down. When the energy levels cross at the transition from semimetal (with overlapping energy states for the lowest conduction band and the highest valence band) to semiconductor (with a band gap between the valence and conduction bands), the material has one dominant carrier type (**Figure 6**). For example, alloying Bi with Sb changes the electronic structure of the bulk alloy [47]; calculations showed the dependence of the semimetal-semiconductor transition for a bismuth-antimony nanowire, on both wire diameter and antimony concentration [48]. These phenomena have also been confirmed experimentally [49] by changing both the wire diameter and Sb composition, thereby providing two variables for controlling and optimizing nanomaterials for enhanced thermoelectric performance.
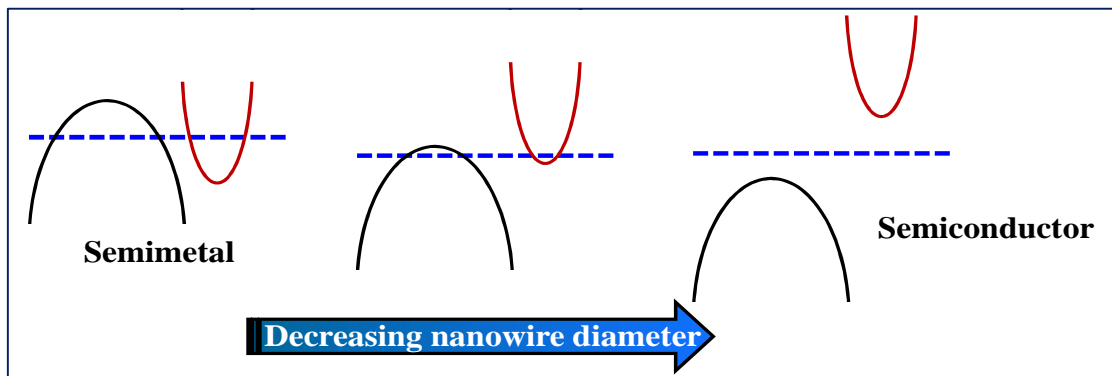
Figure 6. Schematic diagram of the bismuth nanowire semimetal - semiconductor electronic transition, by decreasing the nanowire diameter [49].

All of these concepts and strategies are currently being exploited in improving the performance of nanostructured materials for thermoelectric applications. Based on electron band-gap engineering and phonon engineering in nanostructures, significant progress have already been reported as highlighted in **Figure 7**.
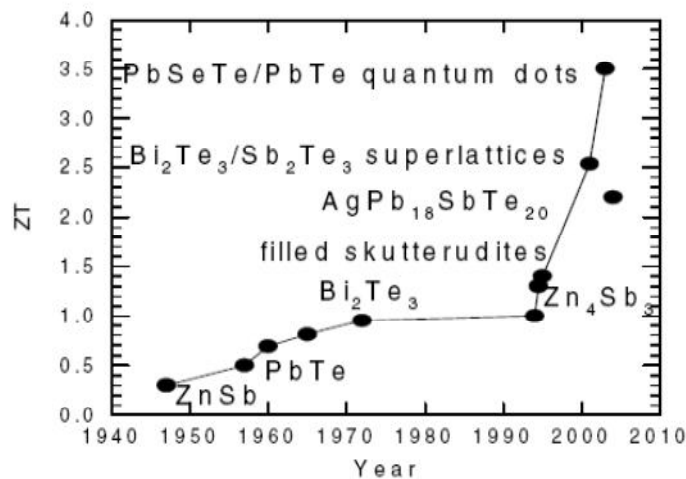
Figure 7. Evolution of ZT with time in case of non oxide based hetrostrctures [50].

I.3. Thermoelectric materials: non oxides versus oxides

Thermoelectric materials studied till now can be classified as non oxide based and oxide based materials. By far the most widely used thermoelectric materials are alloys of Bi-Te, Pb-Te and Sb-Te. For near-room-temperature applications, such as refrigeration and waste heat recovery up to 200 °C, Bi-Te alloys have been proved to possess the greatest figure of merit for both n- and p-type thermoelectric systems. For mid-temperature power generation, between 300 - 900°C, alloys of Co-Sb, Zn-Sb, Pb-Te and Si-Ge are typically used (**Figure 8)**. The main disadvantage of these materials are the toxicity and the scarcity of its constituent. Recently several silicon and oxide based thermoeletrics have been proposed to replace the above-mentioned classical thermoelectric materials due to their environmental friendly nature.
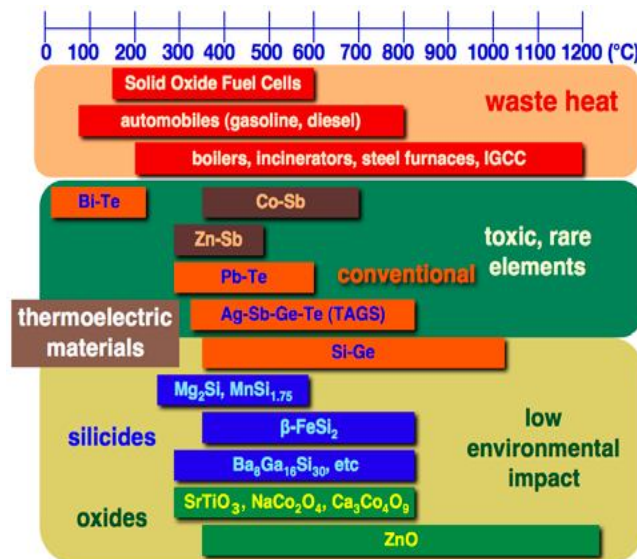
Figure 8. Typical waste heat and operating temperature ranges of various thermoelectric materials [51].

I.3.1. Non Oxide based thermoelectric materials

Some of the conventional thermoelectric materials developed until 1990s, includes chalcogenides, Zintl phases, clathrates, skutterudites, half-Heusler alloys, tellurides, silicides, intermetallic compounds and alloys like SiGe alloys, composites of tellurides and selenides, which have been selected on the basis of covalent bonding characters (for higher mobility), and consist of heavy elements (for lower κ_l) such as Bi, Te, Pb. **Figure 9** shows the figure of merit of some of the non oxide based thermoelectric materials.
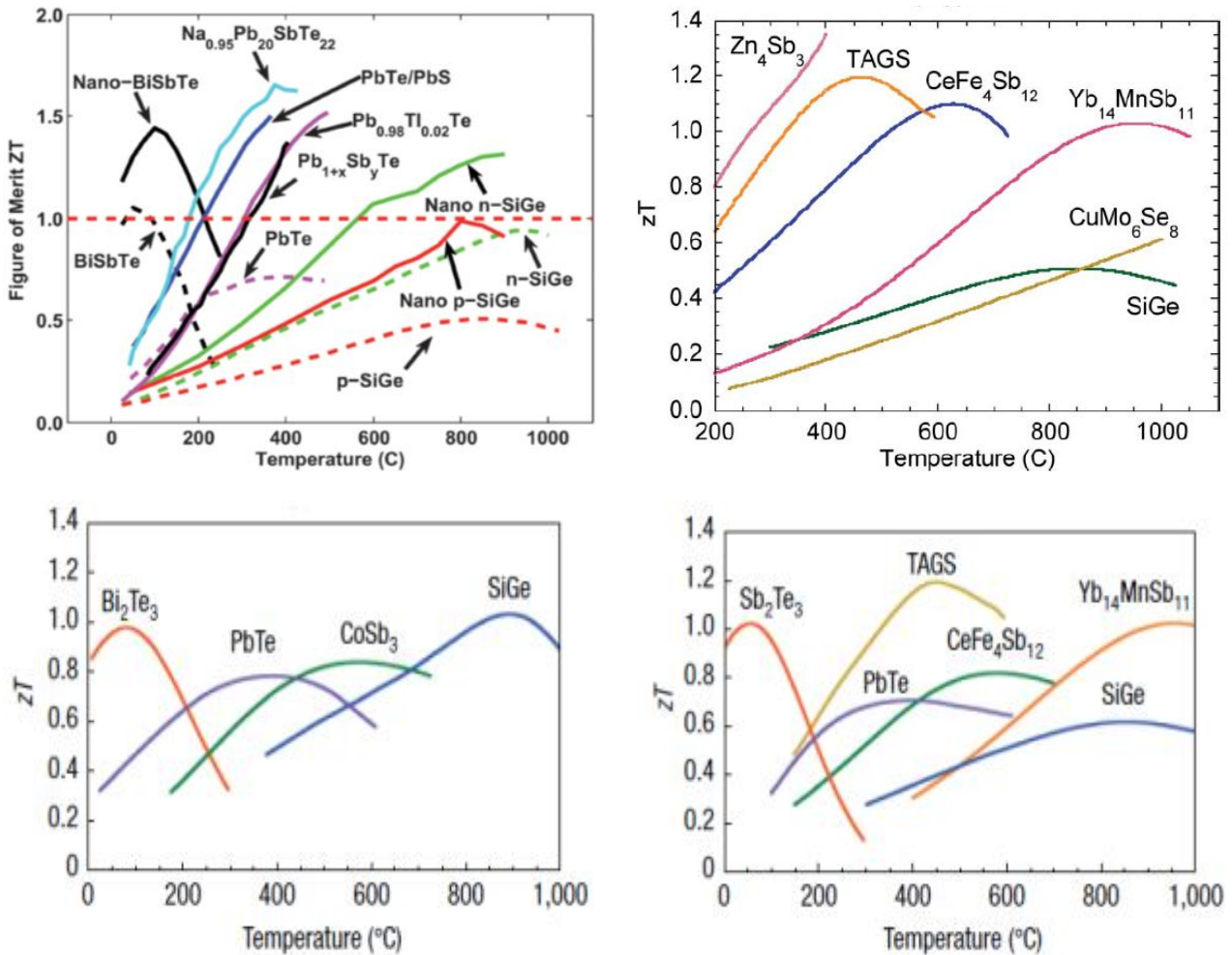
Figure 9. Figure-of-merit (ZT) of state-of-the-art non oxide based thermoelectric materials [52].

Even though some of these materials are interesting for practical device application due to ZT values higner than 1, a lot of shortcomings such as high toxicity, poor durability at high temperature in air, low abundance and thus high cost of the constituents make them incompatible with major energy conversion technologies and limit their use from wide commercialization.

I.3.2. Oxide based thermoelectric materials

Concerning thermoelectric materials, it is important not only to select materials having a large value of Z but also to examine carefully their thermal stability and impact on the environment. Boosted by the global environment issues and carbon dioxide mitigation problems, oxide based thermoelectric materials are considered as promising materials for future energy conversion applications due to their high durability at high temperature in air, non-toxicity, low cost and minimal environment impact. High potential oxide thermoelectrics are currently divided into three main groups: layered complex cobalt oxides, perovskite-type oxides and doped zinc oxide

derivatives. **Figure 10** illustrates the time line of discovery of several oxide based thermeoelectric materials, togther with their ZT values.
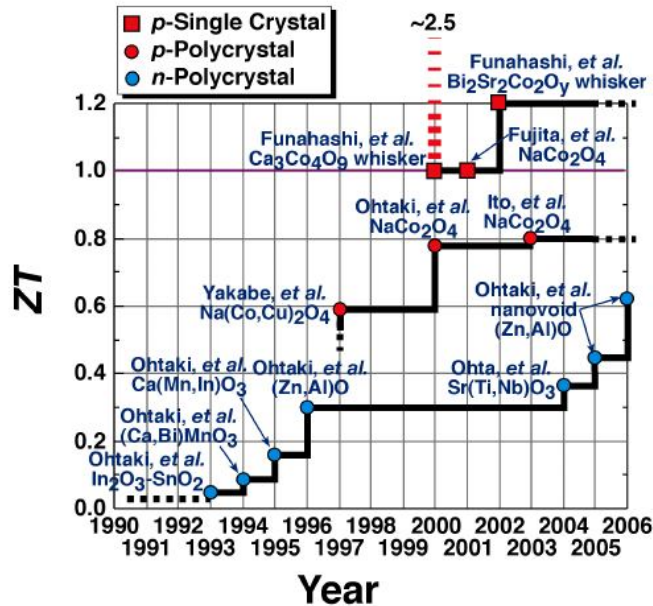
Figure 10. The timeline for the highest ZT of oxide thermoelectric materials [51].

I.3.2.1. Layered cobalt based oxides

Figure 11 shows the crystal structures of various layered cobalt oxides reported as good thermoelectric materials. All of these cobalt oxides have common CdI$_2$-type CoO$_2$ layer block, which is responsible for electric conduction. This CoO$_2$ layers alternately stacks with various block layers along the c axis. This structure is similar to high temperature superconducting copper oxides, except for the lattice misfit between the CoO$_2$ and block layer [53-55]. Its is believed that, this CoO$_2$ layer plays a important role for good thermoelectric properties.
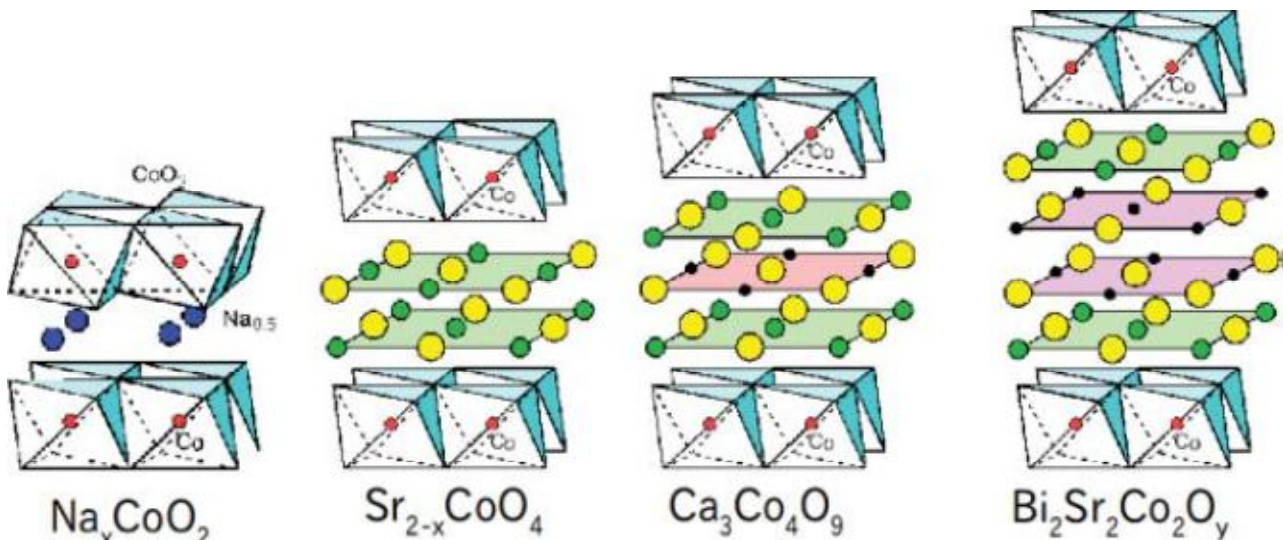
Figure 11. Crystal structures of the several layered cobalt oxides [53].

Some of these oxide materials have quite high ZT values that are comparable to the ones of semiconducting chalcogenides.

Figure 12 shows that the dimensionless figure of merit ZT of some of the oxide based thermoelectric materials [56]. For Na_xCoO_2 and $Bi_2Sr_2Co_2O_y$ single crystals, ZT approaches unity above 400^oC [57-59], and reaches 0.8 in ceramic samples [51, 60,61]. This is higher than in the case of p-type PbTe and Bi_2Te_3 and some layered cobalt oxides are already proposed for application in thermoelectric power generation.

Most of the cobalt oxide materials however have rather low ZT ~ 0.3 in their polycrystalline form [62,63] and a better understanding of the effects of the synthesis parameters on the microstructure, and modulation of the physical properties of these materials with appropriate composition variations, are expected to lead to the improvement on the thermoelectric properties.
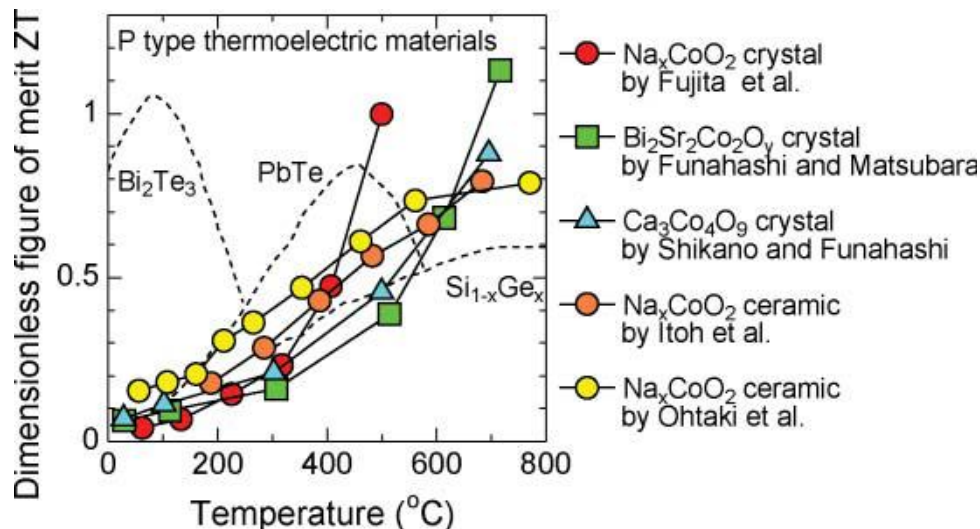
Figure 12. Dimensionless figure of merit ZT of the layered cobalt oxides, compared with conventional thermoelectric material (Dotted curves) [56].

I.3.2.2. Perovskite structure based oxides

Perovskite based compounds have the general formula ABO_3, in which the B site cations are centered in oxygen-corner-shared octahedra forming the 3D-lattice. The slightly bigger A site cation can be found inside the cub-octahedral cavity. Just like in previous case for cobalt ions the electron spin of the B transition metal element is an additional source of entropy that results in the large thermopower found in these systems. The amount of localised and mobile charge carriers can be tuned by suitable substitution reactions to adjust the electrical conductivity and thermoelectric coefficient. Some of these perovskite materials with small polaron hopping mechanism have been

shown to have relatively high thermoelectric performances although they have low carrier mobility values.

For example, $La_{1-x}Sr_xCrO_3$ is a highly conductive and high thermal durable perovskite-type oxide; it has been widely used in solid oxide fuel cells as interconnector. The conduction mechanism of this oxide was reported to be small polaron hopping with thermally activated carrier mobility and temperature independent thermopower [64]. The thermoelectric performance of $La_{0.85}Sr_{0.15}CrO_3$ was reported as ZT = 0.14 at 1600 K [65]. Interestingly, despite the hopping conduction with a constant carrier concentration, the positive α values linearly increases with increasing temperature.

Several studies also report on substituted $CaMnO_3$ which is basically showing a conduction mechanism similar to that of $La_{1-x}Sr_xCrO_3$ [66,67,68]. For example, substituting Bi for Ca, the conductivity of $Ca_{0.9}Bi_{0.1}MnO_3$ increases by more than 3 orders of magnitude at room temperature, $CaMn_{0.9}In_{0.1}O_3$ shows ZT = 0.16 at 900 °C [69] and simultaneous substitution at both Ca and Mn sites showed ZT = 0.21 [72]. A correlation between the hopping carrier mobility and the ionic radii of the substituent cations at B site was found. This correlation suggests that the larger is the ionic radii of the substituant, the shorter is the intersite distance and hence the higher is the hopping mobility. It is worth noting that the thermoelectric performance of such oxides with carrier mobility of as low as ~ 1 cm^2/V-s is higher than those of many high mobility oxides. Recently, $CaMnO_3$ based oxides with improved performance was employed as n-type leg in oxide thermoelectric modules [70,71].

I.3.2.3. Binary oxide based materials:

Zinc and Titanium based binary oxides:

The localized characters of the electronic carriers in oxides can be exploited when the carriers with large effective masses can be heavily doped, thereby realizing large α and high σ simultaneously; the layered cobalt oxides and Ti-based oxides can be classified into this category. Another approach, may be to reduce the ionicity of the metal–oxygen bonds in oxides in order to increase the carrier mobility. ZnO-based thermoelectric materials can be one of the examples of this strategy [73-77].

Zinc oxide is a well known wide band gap semiconductor with a direct band gap of 3.5 eV. Due to relatively large electro-negativity in Zn metal, Zn–O bond is less polarized compared to other metal–oxygen bonds in other metal oxides. In addition, even though the ratio of the ionic radii of Zn^{2+} and O^{2-} imposes a 6-fold coordination of O^{2-} around Zn^{2+}, Zn^{2+} practically prefers the 4-fold coordination, and hence ZnO crystallizes in the wurzite structure consisting of corner-shared ZnO_4 tetrahedra; such packing is much less dense than that of the closest packing [51]. This peculiar

coordination restricts the number of candidates for substitution as well as their solubility limit in ZnO. The orbitals of valence electrons of Zn in ZnO can be seen as sp^3 hybrid similar to that of C in organic compounds, suggesting a large covalency of the chemical bonds.

Non-doped bulk ZnO is an n-type semiconductor. A small amount of Al substitution increases its conductivity by more than 3 orders of magnitude at room temperature and changes the conduction behavior from semiconducting to metallic; the thermoelectric performances are maximum for x = 0.02 in $Zn_{1-x}Al_xO$ [78,79]: $Zn_{0.98}Al_{0.02}O$ ceramic has a large power factor of 10–18×10^{-4} W/m-K^2 over a wide temperature range. This value is comparable to that of Si-Ge alloys [80]. Co-doping with Al and Ga to ZnO successfully reduces the κ value leading to markedly improved thermoelectric performance with ZT = 0.47 at 1000 K and ZT = 0.65 at 1273 K for $Zn_{0.96}Al_{0.02}Ga_{0.02}O$ (**Figure 13a**). This is one of the highest ZT values so far reported for bulk n-type oxides [81].
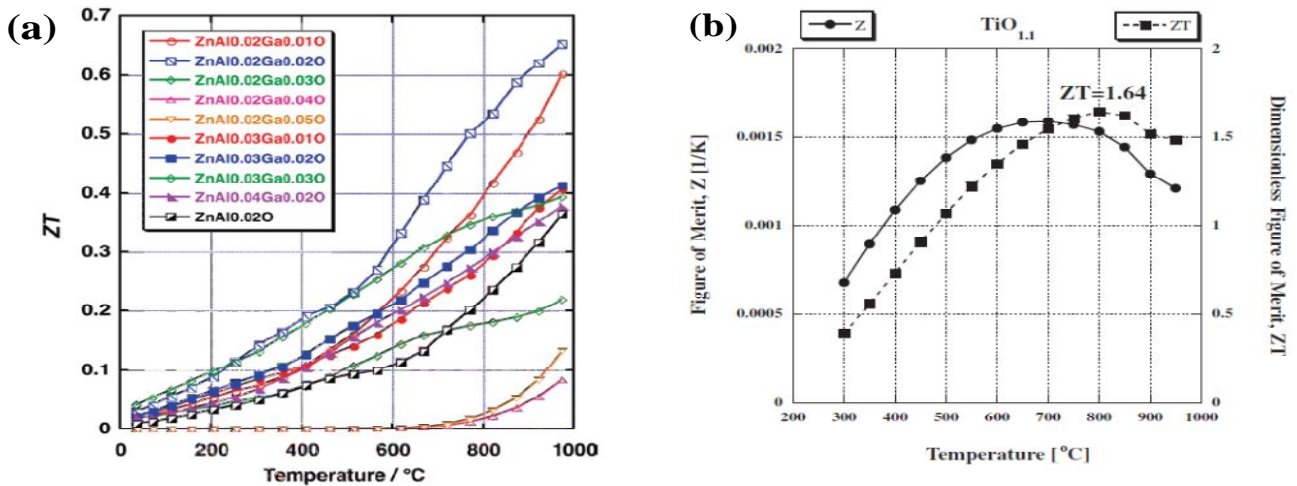
Figure 13. Thermoelectric figure of merit (ZT) of (a) Al and Ga substituted ZnO; (b) nonstoichiometric titanium oxide ($TiO_{1.1}$) [81].

Titanium monoxide is known as a conductive oxide. The thermoelectric properties of nonstoichiometric $TiO_{1.1}$ were investigated for high temperature thermoelectric conversion. Its dimensionless figure of merit ZT reaches 1.64 at 800 ^{o}C which is the largest value ever reported in this temperature region (**Figure 13b**). This study demonstrated the usefulness of nonstoichiometric oxides for high-temperature thermoelectric conversion and also highlights the interest for designing defect-controlled compounds for high-temperature thermoelectricity [82].

I.4. Layered Cobalt Oxide: $Na_{0.7}CoO_2$

As we mentioned earlier, in the last few decades, non oxide based materials have been developped as materials for high temperature thermoelectrics. However, the abovementioned materials are rarely used because of the expensive surface protection required to prevent oxidation or vaporization, or inherent temperature limitation due to phase transformation at high temperatures. With regard to the high operation temperature of thermoelectric modules, it is obvious that metal oxides are advantageous because of their excellent chemical stability *vs* temperature. Since the discovery of good thermoelectric properties in the layered cobalt oxide Na_xCoO_2, oxide thermoelectrics have been extensively investigated and a number of new oxides have been synthesized and examined as possible candidates for oxide thermoelectric materials [83].

Nomenclature:

The structure of lamellar oxides AMO_2 (A = alkaline element, M = transition element) derives from the structure type α-$NaFeO_2$ proposed by Goldsztaub [84] in 1933, which can be described from a NaCl network, chlorine being replaced by oxygen and the cationic sites being orderly occupied by sodium and iron along [111]. The difference in charge and size of the cations ($r_{Na+[VI]}$ = 1.02 Å and $r_{Fe3+[VI, LS]}$ = 0.645 Å) imposes an ordering of the cations along the [1 1 1] direction of the cubic lattice and causes a distortion of the rhombohedral network (**Figure 14**) [85].
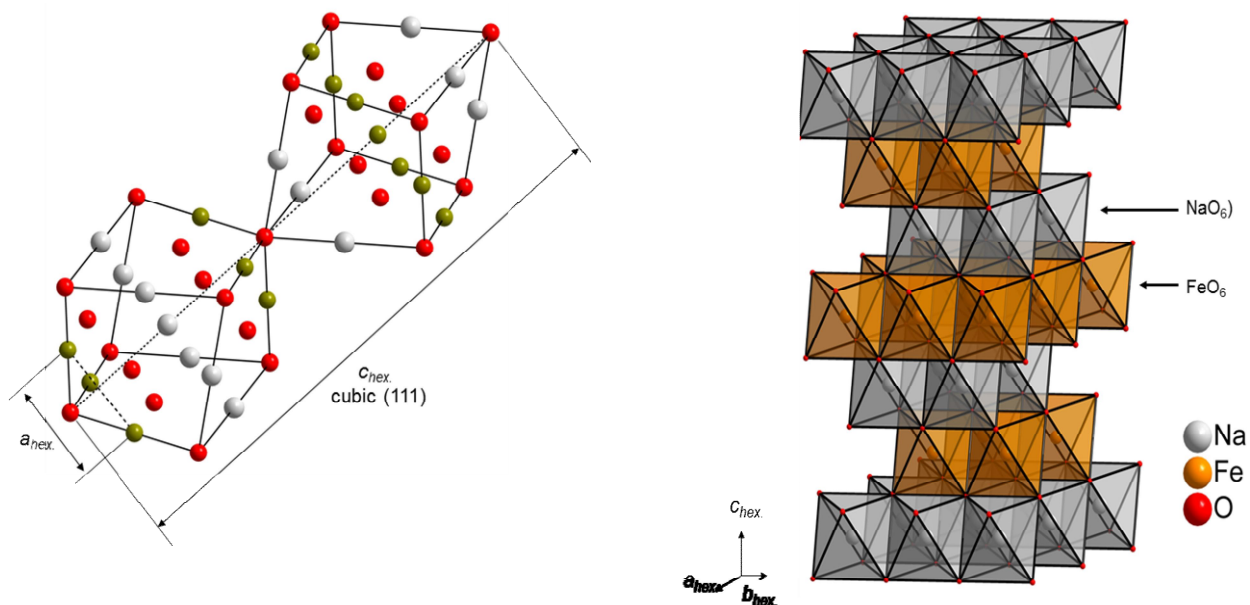
Figure 14. Schematic representation of crystal structure of α-$NaFeO_2$, after deformation of the cubic lattice due to ordering of the cations the Na and Fe.

The α-NaFeO$_2$ structure can be described as a stack of FeO$_6$ octahedra connected by the edges. These FeO$_6$ octahedra are seperated by the sodium ions being inserted in the interlayer space and occupying octahedral sites. The space group is monoclinic R-3m (No. 166), with a=b=c and β = 108.03°; sodium, iron and oxygen occupy respectively the crystallographic positions 3a (0, 0, 0), 3b (0, 0, 1/2) and 6c (0, 0, z) (**Figure 14**).

The other lamellar oxides (AMO$_2$) can be described by using simple elementary operations of translation and/or slips of rotation relative to the c$_{hex}$ axis of α-NaFeO$_2$. Such operations impose a change in the stacking sequence of oxygen but do not affect the overall lamellar character. To distinguish the different possible stacking sequences, Delmas et.al [86] proposed a simplified nomenclature. The α-NaFeO$_2$ structure for instance is designated as O3-NaFeO$_2$: the letter (here "O") describes the symmetry of the alkaline element (*i.e.* "O," "T," or "P" for an octahedral, tetrahedral, or prismatic site respectively) and the figure (here "3") represents the number of MO$_2$ layers per unit cell.

Four different phases have been reported in the Na$_x$CoO$_2$ system depending on the value of x: [87] (1) the α- phase or O3 phase for 0.9≤x≤1; (2) the α^l-phase for x=0.75, (3) the β-phase or P3 for 0.55≤x≤0.6 (4) γ-phase or P2 phase, for x ~ 0.7. There are two kinds of cobalt ions in the compounds depending on x: a fraction $(1 - x)$ is Co^{4+} with spin S = 1/2 and a fraction x is Co^{3+} ions with spin S = 0. The properties of Na$_x$CoO$_2$ thus strongly depend on the sodium content. For sodium content x > 0.5; Na$_x$CoO$_2$ behaves as a Curie-Weiss metal. For x < 0.5, it behaves as an usual paramagnetic metal. Unique properties appear at x = 0.5 as the compound becomes a charge–ordered insulator (**Figure 15**). Na$_{0.35}$CoO$_2$ becomes superconductive after further intercalation of water (Na$_{0.35}$CoO$_2$·1.3H$_2$O [88]).
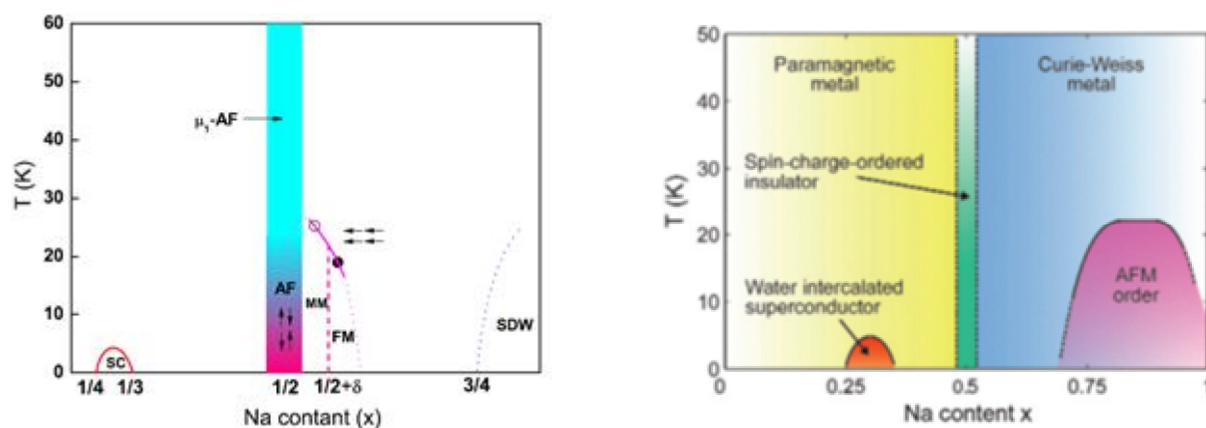
Figure 15. Phase diagram of Na$_x$CoO$_2$. (AF, antiferromagnetism; FM, ferromagnetism; MM, metamagnetism; SC, superconductivity; and SDW, spin density wave. The open and filled circles stand for the ferromagnetic transition point for Na$_{0.52}$CoO$_2$ and Na$_{0.55}$CoO$_2$, respectively.)

P2-$Na_{0.7}CoO_2$ consists of layers of edge-shared CoO_6 octahedra and Na layers alternately stacked along the c-axis. Two kinds of Na ion are present depending on whether the NaO_6 prism shares faces (Na_f) or edges (Na_e) with the surrounding CoO_6 octahedra (**Figure 16**). The Co layer is responsible for the electric conduction, whereas the Na layer act as a charge reservoir and donating electrons distributed among Co ions, is insulating and highly disordered. The electrons in CoO_2 layers are localized and confined due to the strong electron correlations, which is the likely source of low metallic like resistivity and enhanced thermopower. Thus significant reduction of the thermal conductivity is likely to occur because of the sandwicth structure made of the crystalline metallic layer and the incoherent distribution in the insulating layer.
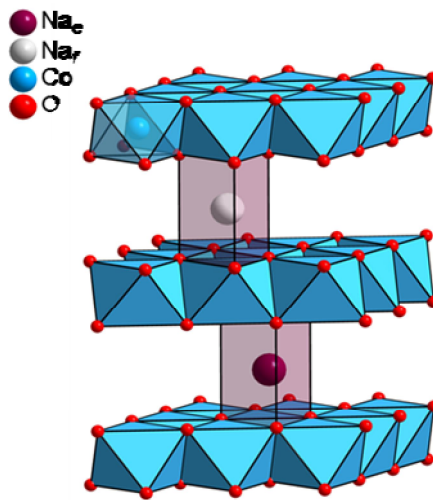
Figure 16. Crystal structure of P2-$Na_{0.7}CoO_2$.

I.4.1. Strong electron correlations and the source of enhanced thermopower

Among the several phases of Na_xCoO_2, x=0.7 phase was extensively investigated due to its coexistence of low resistivity and large in-plane thermoelectric power at room temperature. This material has high chemical stability and is nontoxic, making it as an interesting candidate for many thermoelectric applications. $Na_{0.7}CoO_2$ is a correlated electron system, where the electrons are localized at the atomic sites and lose their mobility due to the strong coulombic repulsion. Several evidences for strong electron correlations in this compound exist: 1) the calculated bandwidth W is much smaller than the Coulomb on-site repulsion U [89]; 2) the Sommerfeld coeficient γ ~ 48 mJ/mol-K^2 is much higher [90] than for standard metals, possibly due to the low dimensionality and frustrated spin structure of triangular CoO_2 sheet; 3) the continuous decrease of resistivity down to low temperature (4.2 K) [91].

Na$_{0.7}$CoO$_2$ is different from conventional semiconductors, because the carrier density is two to three orders of magnitude larger, and thereby the resistivity of Na$_{0.7}$CoO$_2$ remains low (200–500 μΩ-cm at room temperature). Thus, a central issue of this material is why and how such a large thermopower and a large electron density of 10^{21}–10^{22} cm^{-3} co-exist.

Two different approches have been proposed to understand this peculiar combination of properties; splitting of t$_{2g}$ orbitals under distorted ocahedral environment and spin/orbital degenaracy.

From an itinerant picture where band calculations are valid, Singh [89] pointed out that the electronic band structure of Na$_x$CoO$_2$ gives a thermopower of 110 mV K^{-1} at room temperature. In O$_h$ symmetry the crystal field stabilizes the triplet t$_{2g}$. The trigonal distortion in regular octahedron lifts the degeneracy of the t$_{2g}$ triplet by splitting into two e'$_g$ levels (doublet) and one a$_{1g}$ level (singlet) (**Figure 17**). Here e'$_g$, a broad band of charge carriers resposible for metallic behaviour and a$_{1g}$, a narrow band, is resposible for high Seebeck coefficient with localized carriers close to Fermi level. Some of the recent experimental results point out the consideration of lifting the orbital degeneracy, to account for the observed high temperature limit of the thermopower in some layered cobaltates [134].
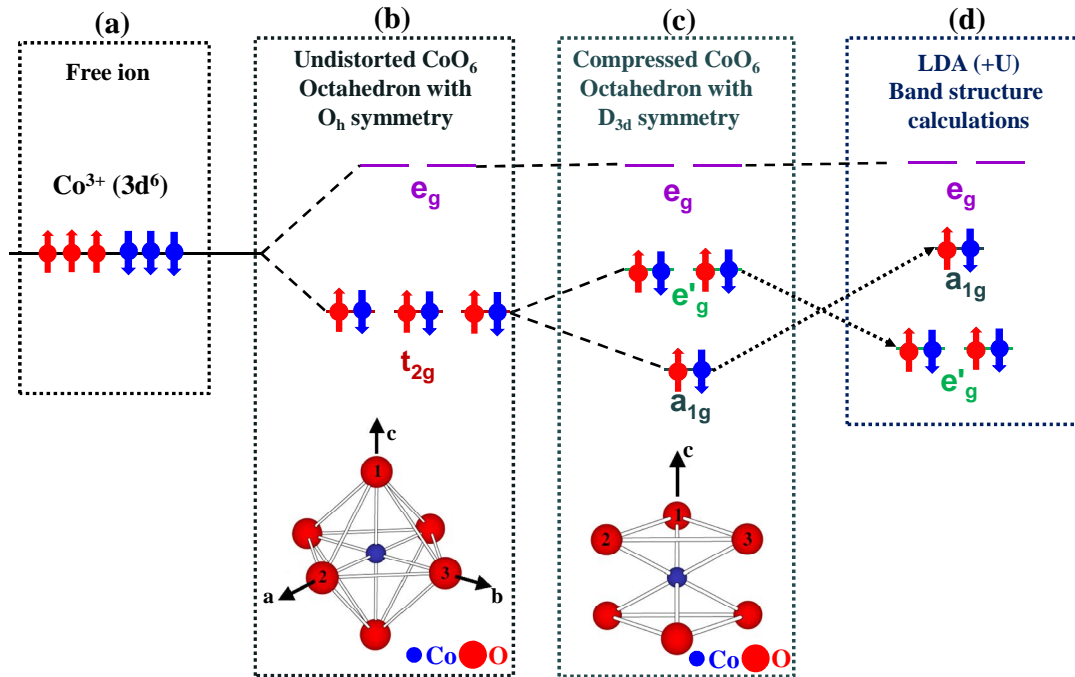
Figure 17. Crystal field of (a) Co^{3+} 3d states in free ion; Crystal- field splitting of Co 3d states in (b) undistorted CoO$_6$ and (c) distorted CoO$_6$ according to an ionic model and (d) relative energy positions of 3d bands obtained from LDA calculations. The e'$_g$ states spread over the ab plane, whereas the a$_{1g}$ state extends to the c-axis [135].

In contrast, using multi-electron picture involving electron correlations, Koshibae et al. [93] proposed that the degeneracy of the electron configurations of Co^{3+} and Co^{4+} ions is essential to the

thermopower at high temperatures. As no degenerate state exists in the Co^{3+} ion, it carries zero entropy (six electrons fully occupy the triply degenerate t_{2g} state). In contrast, the Co^{4+} ion is made by removing one electron from the Co^{3+} ion, which leads to a degeneracy of six (two from spin, three from orbital). As a result, the Co^{4+} ion includes a large entropy of k_B ln6. Then the transport entropy, entropy per charge, is estimated to be $k_B ln6/|e| = 150$ µV/K, which is roughly equal to the thermopower of the layered cobalt oxides at high temperatures. Wang et al.[95] found a suppression of the Seebeck coefficient in a longitudinal magnetic field at low temperature and argued that the spin entropy is the likely source for the observed large Seebeck coefficient.

Even though these models could quantitatively describe the high temperature features of Seebeck coefficient, understanding of the complexity of its temperature and composition dependences is not available so far.

I.4.2. Substitutions in $Na_{0.7}CoO_2$

In complex correlated transition metal oxides, such as $Na_{0.7}CoO_2$, the spin of electrons can become an additional source of entropy resulting in the large thermopower found in this system. Substitution has been often used to alter the ratio Co^{3+}/Co^{4+}, thereby changing the electronic transport properties and improving the thermoeletric characteristics. Particularly Na was substituted with Li, La, Ba, Ca, Ag, Cu, Ag, K, Ca, Sr, Y, Nd, Sm, Yb and Co with Ga, Mn, Ni, Ti, Cu, Pb, Al, to enhance the thermoelectric properties.

The thermoeletric properties of Li, La, Ba, Ca and Ag substituted $Na_{0.7}CoO_2$ compounds were investigated by Yakabe et.al. [96]. This group noticed that except for the Ag-substitution, the partial substitution with Li, La, Ba, Ca caused an increase in resistivity. Ying et al. studied the effect of K, Ca and Sr substituted $Na_{0.7}CoO_2$ compounds synthesized by the sol-gel method. Their results showed that the seebeck coefficient of $Na_{0.7}CoO_2$ is increased by substitution with Ca and Sr, whereas K substitution reduced the power factor [97]. In order to improve the thermoelectric properties of $Na_{0.7}CoO_2$, Nagira et.al [98] prepared polycrystalline samples of K, Sr, Y, Nd, Sm and Yb substituted $Na_{0.7}CoO_2$ compounds by a solid state reaction method. For Sr , the thermoelectric power and the electrical resistivity increased, and the electronic and lattice contribution to the thermal conductivity decreased compared to the non-substituted sample. These effects suggest that the carrier density was reduced by the substitution of Sr for Na. As a result, the figure of merit for Sr substituted $Na_{0.7}CoO_2$ sample was improved. On the other hand, for K, Y, Nd, Sm and Yb samples, in spite of the increase in the electrical resistivity, the thermoelectric power decreased. For all these compounds, except for the Y substituted one, the lattice contribution to the thermal conductivity decreased.

The effects of substitution with magnetic Mn ions or non magnetic Ga ions on the structural, electrical transport and magnetic properties of $Na_{0.7}CoO_2$ was investigated by Guo et.al. They noticed the increase in the electrical resistivity of $Na_{0.7}CoO_2$ with Ga doping, but the metallic conducting behaviour of the compound was not influenced. In contrast, 5% Mn doping leads to a metal–insulator transition at low temperatures in $Na_{0.7}Co_{1-x}Mn_xO_2$ [99]. Zhang et al. [100] observed low-temperature resistivity minimum in dilute Mn-doping $Na_{0.7}CoO_2$ system, which can be attributed to the scattering of conduction electrons by the spin frustration. A resistivity minimum is found with a characteristic of metal to semiconductor transition for all Mn compositions. Similar behaviour of the resistivity was observed by Gayathri et.al [101] and Zhang et.al [102] in Ni and Ti substituted samples as the temperature is lowered which suggests the occurrence of a metal–insulator transition (MIT). The temperature at which the transition occurs is increased with Ni content. The thermopower increases with Ni substitution from the pure pristine sample to 2 at.% Ni doped sample; beyond this value no perceptible change was observed. Pb doped $Na_{0.7}CoO_2$ samples showed enhanced thermoeletric properties because Pb increased the charge carrier concentration by reducing the $Co^{3+/4+}$ ratio [103].

I.5. Layered Delafossite Cobalt Oxide: AgCoO$_2$

The mineral Delafossite $CuFeO_2$, was discovered by Friedel in 1873 in the Yekaterinburg district [104]. The mineral was named after the French mineralogist and crystallographer Gabriel Delafosse whose work elucidated the interrelationships between crystal symmetry and physical properties. Delafossite structure of the general formula ABO_2 consists of alternating BO_6 edge-shared octahedral layers and two-dimensionally close-packed A layers in linear coordination with oxygen. Typical A elements are single charged transition metals with a d^9 configuration such as Ag or Cu and d^{10} configuration such as Pt, Pd. The M element in the trivalent oxidation state can be either a p-block metal, a transition metal or a rare earth elements [105]. Even though delafossite oxides are known for quite long time, many fundamental questions are still opened. From a basic point of view, whether the conduction occurs in the A layers or B layers remains an open question. One more interesting feature of the ABO_2 delafossites is that the A-A and B-B distances are very short, sometimes even shorter than those in pure A or B metals [106]. Despite such short metal-metal distances, the majority of the delafossite oxides are insulators or semiconductors, there are only a few number of metallic compounds such as $PdCoO_2$ [107-109], $PtCoO_2$ [110] and Ag_nNiO_2 (n = 1; 2) [111-115]. The difference in the several polytypes is in the oxygen stacking sequence along the c-axis

of the hexagonal cell. Most of the reports are mainly dealing with the so called D2 (H) and D3 (R) polytypes depending whether the oxygen atoms packing is AB-BA or AB-BC-CA, where the letters A to C label the usual three available triangular positions in a compact oxygen packing (**Figure 18**). Their respective space groups are P6$_3$/mmc and R-3m. Another D6 stacking was also reported, which actually combines D2 and D3 polytypes.
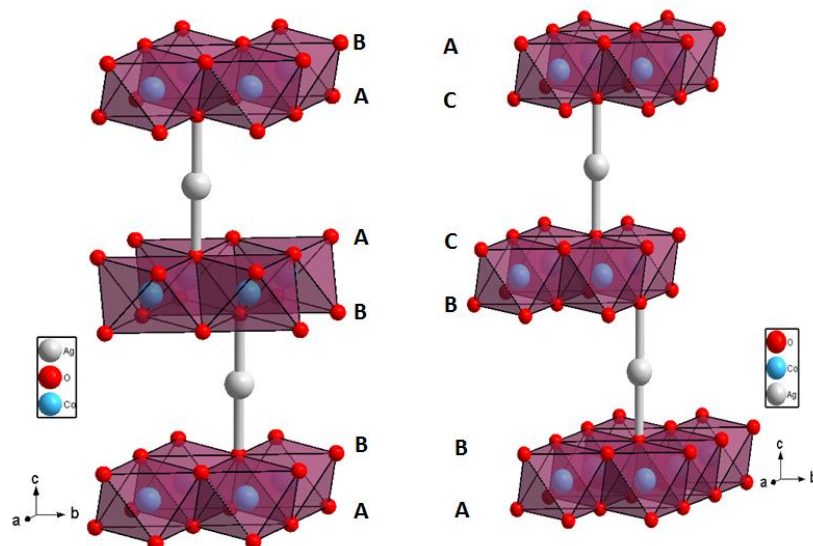
Figure 18. Delafossite crystal structure of AgCoO$_2$, (a) Hexagonal D2 polytype (b) Rhombohedral D3 polytype.

The main difference between the D2 and the D3 structures consists in the orientation of the successive MO$_2$ layers. In the D2 polytype, all the M cations are superimposed along the c-axis and each successive MO$_2$ slab are rotated by π/3 (**Figure 18a**). Therefore, the structure is described with two basic blocks: A-B and B-A. On the other hand in the D3 polytype, all the MO$_2$ slabs have the same orientation (**Figure 18b**), and the structure is described with three blocks: A-B, B-C and C-A. Due to this difference of packing a transformation from the D2 to D3 structure is not possible by topotactic process and requires to break Co-O bonds.

Most of the Delafossite compounds reported in the literature are based on monovalent Cu. The corresponding Ag based delafossite compounds are harder to produce, and generally require ion-exchange synthesis rather than a simple solid state reaction. Fabrication of pure silver delafossite compounds is of great difficulty. **Table 1 and Table 2** summarize the data related to structural, electrical and optical properties of some of the Ag based delafossite oxides.

Compound	a (Å)	c (Å)	Space group	Reference
$AgNiO_2$	2.937	12.237	P63/mmc	113
$AgCoO_2$	2.873	18.336	R-3m	106
$AgNiO_2$	2.939	18.370	R-3m	117
$AgCrO_2$	2.985	18.510	R-3m	118
$AgAlO_2$	2.8729	18.336	R-3m	106
$AgTlO_2$	3.568	18.818	R-3m	116
$AgScO_2$	3.2112	18.538	R-3m	116
$AgRhO_2$	3.0684	18.579	R-3m	106
$AgNiO_2$	2.936	18.35	R-3m	119
$AgInO_2$	3.2772	18.881	R-3m	106
$AgGaO_2$	2.9889	18.534	R-3m	106
$AgFeO_2$	3.0391	18.59	R-3m	106
$AgCo_{0.5}Ti_{0.5}O_2$	3.035	18.62	R-3m	111
$AgCo_{0.5}Sn_{0.5}O_2$	3.16	18.7	R-3m	111

Table 1. Structural parameters for some of the Ag based delafossite compounds.

Compound	Form	Sigma (S/cm)	Type/optical band gap (eV)	Reference
$AgAlO_2$	Powder	9×10^{-3}	3.6	120
$AgScO_2$	Powder	4×10^{-2}	3.8	120
$AgInO_2$	Crystal	1×10^{-4}	4.2	107
$AgInO_2$	Powder	10^{-7}		121
$AgInO_2$	Film	1×10^{-5}		122
$AgInO_2$	Powder	8×10^{-3}		120
$AgCoO_2$	Crystal	6.7×10^{-5}	P type/4.15	110
$AgCrO_2$	Bulk	1.4×10^{-6}		123
$AgFeO_2$	Crystal	3.3×10^{-8}		110
$AgGaO_2$	Crystal	2×10^{-8}	4.1	110
$AgGaO_2$	Bulk	2.5×10^{-7}		123
$AgInO_2$	Crystal	1×10^{-4}		110
$AgInO_2$	Film	1×10^{-5}		122
$AgNiO_2$	Bulk	100		124
$AgCoO_2$	Film	0.2	p	125

Table 2. Electrical and optical properties of some of the Ag based delafossite compounds.

I.5.1 Synthesis of Ag based delafossite oxides

Using traditional high temperature solid state synthesis processes, silver based delafossites can not be synthesized, due to low free energy of formation Ag_2O which decomposes before participating to any kind of reaction [110,120]. Therefore, it is neccesary to use alternative preparation methods, such as high-oxygen-pressure solid-state, ion –exchange reactions, oxidizing flux, and hydrothermal reactions to prepare silver based delafossites. Von Stählin and Ostwald first used hydrothermal synthesis for the preparation of the D3-$AgCoO_2$ polytype [126]. Later, in their extensive studies on the family of delafossite compounds Shannon, Rogers and Prewitt synthesized black hexagonal plate-like single crystal of $AgCoO_2$ [106,107]. However, they also proposed molten salts ionic exchange method to prepare the rhombohedral D3 polytype using lamellar O3-$LiCoO_2$ as precursor material. After this study, no other attempts are reported for the preparation of D3-

$AgCoO_2$. Later Shin et al. reported the hexagonal polytype (D2) synthesis using P2-Na$_{\sim0.7}$CoO2 as precursor with similar ionic exchange [111,112, 117]. Recently Muguerra et al. proposed a similar result with a slight change in the salts composition [127]. These results clearly show that the ionic exchange process occurs through a topotactic mechanism: the oxygen sequence of the initial alkali layered precursor directly impacts on the obtained $AgCoO_2$ polytype. This is nicely shown from the synthesis of D4 by Romain et al. [136].

These Ag based delafossite oxides are mostly insulating, but they can be turned into semiconductors by using appropriate substitutions. In this case large values of the Seebeck coefficient have already been observed making them interesting candidates for thermoelectric applications. Yagi et al. evidenced a significant increase in the conductivity in Ag-deficient Ag_xCoO_2 delafossite compounds prepared through ion exchange reactions [128]. However, their study was focused on the thermoelectric properties, and a full structural analysis of the Ag-deficient structure was not included. Among Ag based delafossites, Sn-doped $AgInO_2$ exhibits the highest conductivity. In the case of $AgCoO_2$, except $AgCo_{0.5}Ti_{0.5}O2$, $AgCo_{0.5}Sn_{0.5}O_2$ solid solutions, no attempts have been made to modify the electrical properties by using substitutions or by changing oxygen stoicheometry [111]. Even in case of pure $AgCoO_2$, reports of electrical properties are very seldom in literature, probably because of its preparation complexity. In pure form, $AgCoO_2$ is a p-type transparent semi-conductive oxide, with a room temperature conductivity of 0.02 S/cm. The Seebeck coefficient at 298 K is +250 µV/K evidencing the p-type nature of the carriers. The temperature-dependent resistivity shows a typical activated behavior, with an activation energy of 70 meV at high temperature. The optical band gap of $AgCoO_2$ is 4.15 eV. The optical transmission of a 150 nm $AgCoO_2$ film is 40–60% in the visible region [125].

I.6. References

[1]   http://www.isiwebofknowledge.com (Visited 17, April, 2012)

[2]   T.J. Seebeck. A.K. Akad. Wiss. Berlin, p. 289 (1821)

[3]   J.C. Peltier. Ann. Chem. Phys., 56, 371 (1834)

[4]   E. Altenkirch. Physicalische Zeitschrift, 10, 560 (1909)

[5]   E. Altenkirch. Physicalische Zeitschrift, 12, 920 (1911)

[6]   P. Chaikin, G. Beni. Phys. Rev. B, 13(2), 647 (1976)

[7]   J.P. Doumerc. J. Solid State Chem., 109(2), 419 (1994)

[8]   T. Tritt, editor. Thermal Conductivity: Theory, Properties, and Applications. Springer (2004)

[9]   R. Franz, G. Wiedemann. Annalen der Physik und Chemie, 165(8), 497 (1853)

[10] D.M. Rowe, editor. CRC Handbook of Thermoelectrics. CRC Press (1995)

[11] L.D. Hicks, and M. S. Dresselhaus, Phys. Rev. B, 47, 16631(1993)

[12] R. Venkatasubramanian, E. Siivola, T. Colpitts, and B. O' Quinn, Nature, 413, 597 (2001)

[13] R. Venkatasubramanian, E. Siivola, T. Colpitts, and B. O' Quinn, Nature, 413, 597 (2001)

[14] D.A. Broido and T. L. Reinecke, Phys. Rev. B, 51, 13797 (1994)

[15] T.C. Harman, P.J. Taylor, M.P. Walsh, B.E. LaForge, Science, 297, 2229 (2002)

[16] M. Dresselhaus, G. Chen, M.Y. Tang, R. Yang, H. Lee, D. Wang, Z. Ren, J.P. Fleurial, P. Gagna, Adv. Mater., 19, 1043 (2007)

[17] A. Shakouri, IEEE International Conference on thermoelectrics, 495–500 (2005)

[18] J.O. Sofo, G.D. Mahan, Appl. Phys. Lett., 65, 2690 (1994)

[19] W. Kim, S.L. Singer, A. Majumdar, D. Vashaee, Z. Bian, A. Shakouri, G. Zeng, J.E. Bowers, J.M.O. Zide, A.C. Gossard, Appl. Phys. Lett., 88, 242107 (2006)

[20] Y. Wu, R. Fan, P. Yang, Nano Lett., 2, 83 (2002)

[21] A.I. Boukai, Y. Bunimovich, J.T. Kheli, J.K. Yu, J. R. Heath, Nature, 451, 168 (2008)

[22] A.I. Hochbaum, R. Chen, R.D. Delgado, W. Liang, E.C. Garnett, M. Najarian, A. Majumdar, P. Yang, Nature, 451, 163 (2008)

[23] J. Tang, H.T. Wang, D.H. Lee, M. Fardy, Z. Huo, T.P. Russell, P. Yang, Nano Lett., 10, 4279 (2010)

[24] D. Li, Y. Wu, R. Fang, P. Yang, and A. Majumdar Appl. Phys. Lett., 83, 3186

[25] A.I. Boukai, Y. Bunimovich, J.T. Kheli, J.K. Yu, W.A.G. III, J. R. Heath, Nature, 451, 168 (2008)

[26] A.I. Hochbaum, R. Chen, R.D. Delgado, W. Liang, E.C. Garnett, M. Najarian, A. Majumdar, P. Yang, Nature, 451, 163 (2008)

27   J. Tang, H.T. Wang, D.H. Lee, M. Fardy, Z. Huo, T.P. Russell, P. Yang, Nano Lett., 10, 4279 (2010)

28   D. Li, Y. Wu, R. Fang, P. Yang, and A. Majumdar Appl. Phys. Lett., 83, 3186

29   D. Li, Y. Wu, R. Fang, P. Yang, and A. Majumdar Appl. Phys. Lett., 83, 3186

30   G. Chen, Semiconductors and Semimetals, 71, 203 (2001)

31   R. Chen, A.I. Hochbaum, P. Murphy, J. Moore, P. Yang, A. Majumdar, Phys. Rev. Lett., 101, 105501 (2008)

32   D. Li, S.T. Huxtable, A.R. Abramsin, A. Majumdar, Trans. of the ASME, 127, 108 (2005)

33   P. Martin, Z. Aksamija, E. Pop, and U. Ravaioli, Phys. Rev. Lett., 102, 125503 (2009)

34   K. Nielsch, J. Bachmann, J. Kimling, H. Böttner, Adv. Energy Mater., 1, 713(2011)

35   C.J. Vineis, A. Shakouri, A. Majumdar, M.C. Kanatzidis, Adv. Mater., 22, 3970 (2010)

36   L.D. Hicks, M. S. Dresselhaus, Phys. Rev. B, 47, 16631 (1993)

37   M. Dresselhaus, G. Chen, M.Y. Tang, R. Yang, H. Lee, D. Wang, Z. Ren, J.P. Fleurial, P. Gagna, Adv. Mater., 19, 1043 (2007)

38   C.M. Jaworski, V. Kulbachinskii, J.P. Heremans, Phys. Rev. B, 80, 125208 (2009)

39   N. Neophytou, H. Kosina, Phys. Rev. B, 83, 245305 (2011)

40   C.M. Bhandari, CRC Handbook of &ermoelectrics (editor. D.M. Rowe,), CRC, Boca Raton, 55–65 (1995)

41   M.S Dresselhaus, Adv. Mater. 19, 1043 (2007)

42   G. Chen, M.S. Dresselhaus, G. Dresselhaus, J.P. Fleurial, T. Caillat. In International Materials Review, 48, 45 (2003) (editor: M. J. Bevis), Institute of Materials Journals, 1 Carlton House Terrace, London

43   B.Y. Moizhes and V.A. Nemchinsky. In Proceedings for the 11th International Conference on Thermoelectrics. Institute of Electrical and Electronics Engineers, Inc., (1992)

44   Y.I. Ravich. In CRC Handbook of Thermoelectrics, edited by D. M. Rowe, pages 67-73, CRC Press, New York, (1995)

45   S. Takaoka and K. Murase, J. Phys. Soc. Jpn. 54, 2250 (1985)

46   J. Heremans, C.M. Thrush, Y.M. Lin, S. Cronin, Z. Zhang, M.S. Dresselhaus, and J.F. Mans, Phys. Rev. B 61, 2921 (2000)

47   A. L. Jain, Phys. Rev. 114, 1518 (1959)

48   O. Rabin. Bismuth Nanowire and Antidot Array Studies Motivated by Thermoelectricity. Ph. D. thesis, Massachusetts Institute of Technology, Department of Chemistry (June 2004)

49 Y.M. Lin. Thermoelectric Properties of $Bi_{1-x}Sb_x$ and superlattice nanowires. Ph. D. thesis, Massachusetts Institute of Technology, Department of Electrical Engineering and Computer Science (June 2003)

50 J. Yang, "Designing Advanced Thermoelectric Materials for Automotive Applications", DOE/EPRI High Efficiency Thermoelectric Workshop, San Diego, CA (February 19, 2004); F.R. Stabler, Mater. Res. Soc. Symp. Proc. 886, 0886 (2006)

51 M. Ohtaki, Micro Review

52 G.J. Snyder and E.S. Toberer, Nature, doi:10.1038/nmat2090

53 I. Terasaki, M. Iwakawa, T. Nakano, A. Tsukudaa and W. Kobayashi, Dalton Trans., 39, 1005 (2010)

54 A.C. Masset, C. Michel, A. Maignan, M. Hervieu, O. Toulemonde, F. Studer, B. Raveau and J. Hejtmanek, Phys. Rev. B: Condens. Matter Mater. Phys., 62, 166 (2000)

55 D. Pelloquin, A. Maignan, S. Hebert, C. Martin, M. Hervieu, C. Michel, L.B. Wang and B. Raveau, Chem. Mater., 14, 3100 (2002)

56 I. Terasaki, Proceedings of The 24th International Conference on Thermoelectrics (ICT2005), Clemson, 301–306 (2005)

57 K. Fujita, T. Mochida and K. Nakamura, Jpn. J. Appl. Phys., 40, 4644 (2001)

58 R. Funahashi and M. Shikano, Appl. Phys. Lett., 81, 1459 (2002)

59 M. Shikano and R. Funahashi, Appl. Phys. Lett., 82, 1851 (2003)

60 M. Ohtaki, Y. Nojiri and E. Maeda, Proceedings of The 19th International Conference on Thermoelectrics (ICT2000), Cardiff, pp. 190–195 (2000)

61 M. Ito, T. Nagira, D. Furumoto, S. Katsuyama and H. Nagai, Scr. Mater., 48, 403 (2003)

62 K. Kuroki and R. Arita, J. Phys. Soc. Jpn., 76, 083707 (2007)

63 W. Koshibae, K. Tsutsui and S. Maekawa, Phys. Rev. B: Condens.Matter Mater. Phys., 62, 6869 (2000)

64 D.P. Karim and A.T. Aldred, Phys. Rev. B, 20, 2255 (1979)

65 W.J. Weber, C.W. Griffin, and J.L. Bates, J. Am. Ceram. Soc., 70, 265 (1987)

66 M. Ohtaki, H. Koga, K. Eguchi, and H. Arai, Proc. 13th Int. Conf. Thermoelectrics, AIP Conference Proceedings No. 316, American Institute of Physics, p. 115 (1995)

67 M. Ohtaki, H. Koga, T. Tokunaga, K. Eguchi, and H. Arai, J. Solid State Chem., 120, 105 (1995)

68 M. Ohtaki, T. Tokunaga, K. Eguchi, and H. Arai, Proc. 16th Int. Conf. Thermoelectrics, IEEE Catalog Number 97TH8291, IEEE, Piscataway, p. 224 (1997)

[69] M. Ohtaki, T. Tokunaga, K. Eguchi, and H. Arai, Proc. 16th Int. Conf. Thermoelectrics, IEEE Catalog Number 97TH8291, IEEE, Piscataway, p. 224 (1997)

[70] D. Flahaut, T. Mihara, R. Funahashi, N. Nabeshima, K. Lee, H. Ohta, and K. Koumoto, J. Appl. Phys., 100, 084911 (2006)

[71] S. Urata, R. Funahashi, T. Mihara, A. Kusuge, S. Sodeoka, and T. Tanaka, Int. J. Appl. Ceram. Tech., 4, 535 (2007)

[72] X.Y. Huang, Y. Miyazaki, and T. Kajitani, Solid State Commun., 145, 132 (2008)

[73] M. Ohtaki, T. Tsubota, K. Eguchi, and H. Arai, J. Appl. Phys., 79, 1816 (1996)

[74] T. Tsubota, M. Ohtaki, K. Eguchi, and H. Arai, J. Mater. Chem., 7, 85 (1997)

[75] T. Tsubota, M. Ohtaki, K. Eguchi, and H. Arai, Proc. 16th Int. Conf. Thermoelectrics, IEEE, Piscataway, p. 240 (1997)

[76] T. Tsubota, M. Ohtaki, K. Eguchi, and H. Arai, J. Mater. Chem., 8, 409 (1998)

[77] M. Ohtaki, T. Tsubota, and K. Eguchi, Proc. 17th Int. Conf. Thermoelectrics, IEEE, Piscataway, p. 610 (1998)

[78] M. Ohtaki, T. Tsubota, K. Eguchi, and H. Arai, J. Appl. Phys., 79, 1816 (1996)

[79] T. Tsubota, M. Ohtaki, K. Eguchi, and H. Arai, J. Mater. Chem., 7, 85 (1997)

[80] M. Ohtaki, Materials Integration (in Japanese), 13, 27 (2000)

[81] M. Ohtaki, K. Araki, and K. Yamamoto, J Electron. Mater., 38, 1234 (2009)

[82] Noriyuki Okinaka and Tomohiro Akiyama, Japanese Journal of Applied Physics, 45, 7009 (2006)

[83] I. Terasaki, Y. Sasago and K. Uchinokura, Phys. Rev. B: Condens. Matter Mater. Phys., 56, R12685 (1997)

[84] S. Goldztaub. C.R. Acad. Sci. Paris, 196, 280 (1933)

[85] R.D. Shannon. Acta Crystallogr. Sect. A: Found. Crystallogr., 32(5), 751 (1976)

[86] C. Delmas, C. Fouassier, P. Hagenmuller, Physica B+C, 99, 81 (1980)

[87] C. Fouassier, G. Matejka, J.M. Reau, P.Hagenmuller, J. Solid State Chem. 6, 532 (1973)

[88] K. Takada, H. Sakurai, E. Takayama-Muromachi, F. Izumi, R. A. Dilanian and T. Sasaki. Nature, 422, 53 (2003)

[89] D. J. Singh. Phys. Rev. B, 61, 13397 (2000)

[90] Y. Ando, N. Miyamoto, K. Segawa, T. Kawata and I. Terasaki. Phys. Rev. B, 60, 10580 (1999)

[91] I. Terasaki. Proceedings of 18th ICT, Baltimore, p 569 (1999)

[92] K. Kuroki and R. Arita, J. Phys. Soc. Jpn., 76, 083707 (2007)

93   W. Koshibae, K. Tsutsui and S. Maekawa, Phys. Rev. B: Condens. Matter Mater. Phys., 62, 6869 (2000)

94   R. Ray, A. Ghoshray, K. Ghoshray and S. Nakamura, Phys. Rev. B: Condens. Matter Mater. Phys., 59, 9454 (1999)

95   Y. Wang, N.S. Rogado, R.J. Cava, N.P. Ong. Nature, 423, 425 (2003)

96   H. Yakabe, K. Fujita, K. Nakamura, and K. Kikuchi, 17th International Conference on Thermoeiectrics 551, (1998)

97   Li Ying et.al, The Chinese journal of nonferrous metals, 16, 142 (2006)

98   T. Nagira, M. Ito, S. Katsuyama, K. Majima, H. Nagai, Journal of Alloys and Compounds 348, 263 (2003)

99   Z.P. Guo, Y.G. Zhao, W.Y. Zhang, L. Cui, S.M. Guo and L.B. Luo, J. Phys.: Condens. Matter 18, 4381 (2006)

100 Z. Zhang, J. Zhang, Y. Xu, C. Jing, S. Cao, Y. Zhao, Phys. Rev. B 74, 045108 (2006)

101 N. Gayathri, A. Bharathi, V.S. Sastry, C.S. Sundar, Y. Hariharan, Solid State Communications 138, 489 (2006)

102 W.Y. Zhang, Y.G. Zhao, Z.P. Guo, P.T. Qiao, Solid State Communications 135, 480 (2005)

103 A. Mrotzek, E. Muller, J. Plewa, H. Altenburg, Proceedings ICT03- 22nd International Conference on Thermoelectrics IEEE.

104 C. Friedel, Compt. Rend. Acad. Sci. Paris 77, 211 (1873)

105 M.A. Marquardt, N.A. Ashmore, D.P. Cann. Thin Solid Films, 496(1), 146 (2006)

106 R.D. Shannon, D.B. Rogers, C.T. Prewitt, Inorg. Chem. 10, 713 (1971)

107 D. Rogers, R. Shannon, C. Prewitt, J. Gillson, Inorg. Chem., 10(4), 723 (1971)

108 M. Tanaka, M. Hasegawa, H. Takei. J. Phys. Soc. Jpn., 65(12), 3973 (1996)

109 M. Hasegawa, T. Higuchi, M. Tanaka, T. Tsukamoto, S. Shin, H. Takei. Mater. Trans., 42(6), 961 (2001)

110 D.B. Rogers, R. Shannon, C. Prewitt, J. Gillson, Inorg. Chem., 10(4), 723 (1971)

111 Y. Shin, J.P. Doumerc, M. Pouchard, P. Hagenmuller. Mater. Res. Bull., 28(2), 159 (1993)

112 Y.-J. Shin, J.-H. Kwak, S. Yoon. Bull. Korean Chem. Soc., 1997. 18(7), 775

113 T. Sörgel, M. Jansen. Z. Anorg. Allg. Chem., 631(15), 2970 (2005)

114 M. Schreyer, M. Jansen. Angew. Chem. Int. Ed., 41(4), 643 (2002)

115 H. Yoshida, Y. Muraoka, T. Sörgel, M. Jansen, Z. Hiroi. Phys. Rev. B, 73(2), 020408 (2006)

116 R.D. Shannon, C.T. Prewitt, Acta Crystallogr., B 25, 925 (1969)

[117] Y.J. Shin, J.P. Doumerc, P. Dordor, C. Delmas, M. Pouchard, P. Hagenmuller, J. Solid State Chem. 107, 303 (1993)

[118] E. Gehle, H. Sabrowsky, Z. Naturforsch. B 2, 1947 (1977)

[119] A. Wichainchai, P. Dordor, J.P. Doumerc, M. Marquestaut, M. Pouchard, P. Hagenmuller, A. Ammar, J. Solid State Chem. 74, 126 (1988)

[120] W.C. Sheets, E.S. Stampler, M.I. Bertoni, M. Sasaki,T.J. Marks, T.O. Mason, and K.R. Poeppelmeier, Inorganic Chemistry, 47, 2696 (2008)

[121] J.E. Clayton, D.P. Cann, N. Ashmore, Thin Solid Films, 411(1), 140 (2002)

[122] T. Otabe, K. Ueda, A. Kudoh, H. Hosono, H. Kawazoe, Appl. Phys. Lett. 72(9), 1036 (1998)

[123] R. Nagarajan, N. Duan, M.K. Jayaraj, J. Li, K.A. Vanaja, A. Yokochi, A. Draeseke, J. Tate, A.W. Sleight, Int. J. Inorg. Mater. 3, 265 (2001)

[124] Wichainchai, P. Dordor, J.-P. Doumerc, M. Marquestaut, M. Pouchard, P. Hagenmuller, A. Ammar, J. Solid State Chem. 74, 126 (1988)

[125] J. Tate, M.K. Jayaraj, A.D. Draeseke, T. Ulbrich, A.W. Sleight, K.A. Vanaja, R. Nagarajan, J.F. Wager, R.L. Hoffman, Thin Solid Films 411, 119 (2002)

[126] W.V.Stählin, H.R. Oswald. Z. Anorg. Allg. Chem., 367, 206 (1969)

[127] H. Muguerra, C. Colin, M. Anne, M.H. Julien, P. Strobel. J. Solid State Chem., 181(11), 2883 (2008)

[128] H. Yagi, W.S. Seo, K. Koumoto, Key Eng. Mater. 181, 63 (2000)

[129] G.A. Slack, CRC Handbook of Thermoelectrics (Ed.: D. M. Rowe), CRC, Boca Raton, FL, p. 407 (1995)

[130] H.J. Goldsmid, Applications of Thermoelectricity, Methuen, London (1960)

[131] L.D. Hicks and M.S. Dresselhaus, Phys. Rev. B 47, 12727 (1993); M.S. Dresselhaus, T. Koga, X. Sun, S.B. Cronin, K.L. Wang, and G. Chen. In Sixteenth International Conference on Thermoelectrics: Proceedings, ICT'97; Dresden, Germany, editor Armin Heinrich, 12-20, (1997)

[132] M.S. Dresselhaus, G. Chen, M.Y. Tang, R. Yang, H. Lee, D. Wang, Z. Ren, J.P. Fleurial, P. Gogna, Adv. Mater. 19, 1043 (2007)

[133] L.D. Hicks, T.C. Harman, X. Sun, M.S. Dresselhaus, Phys. Rev. B:Condens. Matter Mater. Phys. 53, R10493 (1996)

[134] M. Pollet, J.P. Doumerc, E. Guilmeau, D. Grebille, J.F. Fagnard, R. Cloots, J. Appl. Phys. 101, 083708 (2007); N. Kaurav, K.K. Wu, and Y.K. Kuo, G.J. Shu, F.C. Chou, Phys. Rev. B 79, 075105 (2009)

[135] M. Pollet, J.P. Doumerc, E. Guilmeau, D. Grebille, J.F. Fagnard, R. Cloots, J. Appl. Phys. 101, 083708 (2007); W.B. Wu, D.J. Huang, J. Okamoto, A. Tanaka, H.J. Lin, F.C. Chou, A. Fujimori, and C.T. Chen, Phys. Rev. Lett. 94, 146402 (2005)

[136] R. Berthelot, M. Pollet, J.P. Doumerc, and C. Delmas, Inorg. Chem., 50 (10), 4529 (2011)

Chapter II:
Synthesis of layered cobalt double oxides

The aim of this chapter is to present the synthesis procedures used for the preparation of pure and substituted layered cobalt double oxides. In the first part I will describe the synthesis protocol used for the preparation of precursor compounds P2- $Na_{0.7}CoO_2$, O3-$LiCoO_2$ followed by an introduction to ion exchange reactions to prepare D2-$AgCoO_2$ and D3-$AgCoO_2$. In the second part, I will present the direct hydrothermal synthesis of D3-$AgCoO_2$. In the last section I will outline the synthesis procedures for the preparation of Mg and Mn substituted layered cobalt double oxides.

Contents

II.1. Introduction

AgCoO$_2$ crystallizes with delafossite structure alternating edge-shared CoO$_6$ octahedra and Ag layers; it can accommodate both D2 and D3 stacking schemes and marginally even D6 stacking scheme. Like all silver-based delafossites, its synthesis requires non-conventional methods like ion-exchange or hydrothermal synthesis. **Table 1** summarizes the details of preparation conditions reported till now in the literature to obtain the different polytypes of AgCoO$_2$. In the following, we will present the optimized synthesis protocols for the preparation of D2 and D3 polytypes of AgCoO$_2$ starting from P2-Na$_{0.7}$CoO$_2$ and O3-LiCoO$_2$ using ion exchange processes; the synthesis conditions for ion exchange process were systematically optimized in order to prepare the several pure delafossite polytypes.

Precursors	Conditions	Method	Polytype	Lattice constants	Year	Shape	Ref.
Ag metal, CoOOH, NaOH	330°C and 300 atm	H	D3	a = 2.859 Å, c = 18.26 Å	1969	Powder	1
---			D6	a = 2.85 Å, c = 36.5 Å	1970	Small crystals	1
Ag$_2$O, Co$_3$O$_4$, NaOH	500°C/3000 atm/24 h/100 °C/hr cooling rate	H	D3	a=2.8729 Å c= 18.336 Å	1971	Platelets	2,3
P3-NaCoO$_2$, AgNO$_3$, KNO$_3$	300°C/10 days/AgNO$_3$ (50% excess)	I	D3	a=2.873 Å c=18.36 Å AgCoO$_{2-\delta}$	1997	Powder	
Na$_{0.7}$CoO$_{1.97}$	300°C/10 days/AgNO$_3$ (50% excess)	I	D2	a=2.872 Å c=12.24 Å Ag$_{0.95}$CoO$_{2-\delta}$	1997	Powder	4,5
Na$_{0.7}$CoO$_{1.97}$	300°C/10 days/ AgNO$_3$ (5% excess)	I	D2	a=2.872 Å c=12.25 Å Ag$_{0.75}$CoO$_{2-\delta}$	1997	Powder	
AgNO$_3$, Co$_3$O$_4$ and KOH	250°C/4 days	H	D6	--	2002	Powder	6
		S	c-axis oriented D6		2002	Film	6
Na$_{0.75}$CoO$_2$, NH$_4$NO$_3$, AgNO$_3$	10 days/AgNO$_3$ (5% excess)	I	D2	a = 2.871 Å, c = 12.222 Å AgCoO$_{2+\delta}$	2008	Powder	7

Table 1. Experimental details followed in the literature to prepare D2, D3 and D6 polytypes of AgCoO$_2$. (**H**: Hydrothermal; **I**: Ion exchange process; **S**: Sputtering)

I will also present the attempts to optimize the preparation conditions for the preparation of the D3 polytype using hydrothermal conditions.

II.2. Solid state synthesis: P2-Na$_{\sim 0.7}$CoO$_2$ and O3-LiCoO$_2$

We obtained P2-Na$_{0.7}$CoO$_2$ and O3-LiCoO$_2$ from solid-state reactions by using dry alkali carbonates of sodium and lithium and cobalt oxide Co$_3$O$_4$ as precursors. Stoichiometric ratio of precursors were intimately ground and the mixtures were respectively heated at 850 and 900°C for 24 h under oxygen flow with heating and cooling rates respectively set to 2 °C/min and 5 °C/min. For P2-Na$_{0.7}$CoO$_2$, an excess of 5 wt % of sodium carbonate was added for the preparation of P2-Na$_{0.7}$CoO$_2$ to balance to sodium loss at high temperature.

$$Na_2Co_3 + Co_3O_4 \xrightarrow[O_2]{850°C} Na_{0.7}CoO_2$$

$$Li_2Co_3 + Co_3O_4 \xrightarrow[O_2]{900°C} LiCoO_2$$

The 1:1 cation ratios in P2-Na$_{0.7}$CoO$_2$ and O3-LiCoO$_2$ were confirmed by Inductively Coupled Plasma Absorption Electron Spectroscopy analysis (ICP-AES) on a Varian 720-ES for which nearly 10 mg of powder samples of P2-Na$_{0.7}$CoO$_2$ and O3-LiCoO$_2$ were dissolved in HNO$_3$ solution and heated to 100°C. The powder X-ray diffraction (P-XRD) patterns of P2-Na$_{\sim 0.7}$CoO$_2$ and O3-LiCoO$_2$ are shown in **Figure 1** and **Figure 2** and the lattice parameters are respectively summarized in **Table 2** and **Table 3**.
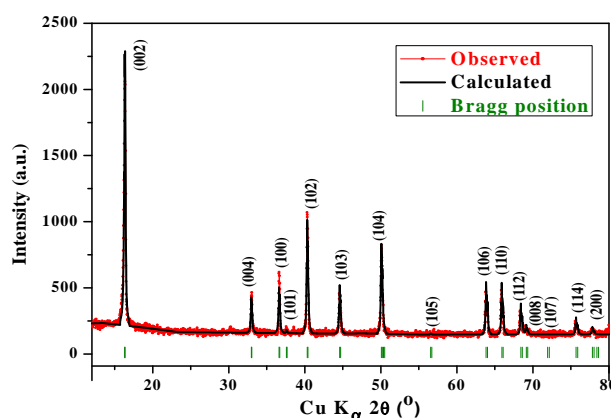
Figure 1. Profile matching refinement of P2-Na$_{0.7}$CoO$_2$ obtained by solid state reaction process. The observed (red points), calculated (black solid line) and the Bragg positions (green bars) are shown.

P2-Na$_{\sim 0.7}$CoO$_2$	
Space group: P6$_3$/m m c (194)	
Lattice parameters	a = 2.8361 (4) Å c = 10.873(2) Å
Profile parameters	Function: Pseudo-Voigt *Halfwidth parameters* U = 1.10 (8) V = -0.64 (5) W = 0.103(4)
***R*-factors**	R$_p$: 7.10 % ; R$_{wp}$: 9.52 %; R$_{exp}$: 6.99 % ; χ^2: 1.86

Table 2. Results of the profile matching refinement of the P2- Na$_{\sim 0.7}$CoO$_2$ phase.
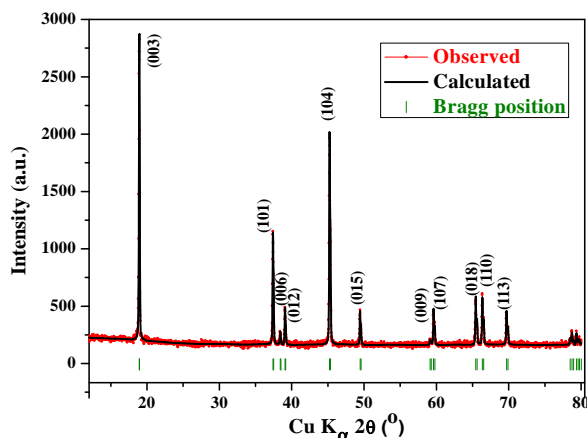
Figure 2. Profile matching refinement of O3-LiCoO$_2$ obtained by solid state reaction process. The observed (red points), calculated (black solid line) and the Bragg positions (green bars) are shown. Refined cell parameters are given in Table **2.**

O3-LiCoO$_2$	
Space group: R -3 m (166)	
Lattice parameters	$a = 2.8151$ (2) Å $c = 14.050$ (1) Å
Profile parameters	Function: Pseudo-Voigt *Halfwidth parameters* $U = 0.032$ (1) $V = -0.019$ (8) $W = 0.015$ (1)
***R*-factors**	R$_p$: 4.43 % R$_{wp}$: 5.78 % R$_{exp}$: 6.29 % χ^2: 0.843

Table 3. Results of the Profile matching refinement of the O3-LiCoO$_2$ phase.

II.3. Ion-Exchange Process: D2-AgCoO$_2$ and D3-AgCoO$_2$

Synthesis of D2 or D3 AgCoO$_2$ with the delafossite structure by solid state reaction is hindered by the low free energies of formation of Ag$_2$O which decomposes in air at 183°C much before the reaction can occur. Alternative methods to prepare D2 or D3 AgCoO$_2$ are based on ionic exchange in molten salts or hydrothermal process. Here we prepared D2 or D3 AgCoO$_2$ from P2-Na$_{0.7}$CoO$_2$ and O3-LiCoO$_2$ using ionic exchange process. We also tried to optimize the preparation conditions for the preparation of D3-AgCoO$_2$ using hydrothermal process.

II.3.1. D2-AgCoO$_2$

For the preparation of D2-AgCoO$_2$, we performed cation exchange reaction between P2-Na$_{\sim0.7}$CoO$_2$ and silver nitrate and potassium nitrate. The addition of potassium nitrate in the molar ratio AgNO$_3$/KNO$_3$ = 3/2 lowers the mixture melting point down to 130°C [8] and increases its volume what promotes the ionic exchange. Additionally, it has been shown that the addition of KNO$_3$ to the AgNO$_3$ suppresses the formation of Ag metal. We performed the ion exchange reactions at different temperatures: 180, 200, 300 and 400°C.
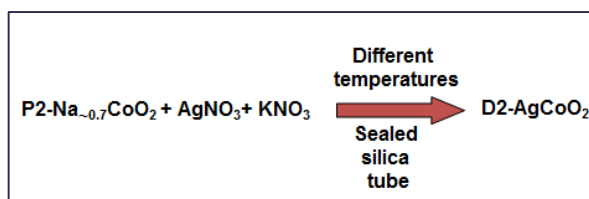
With all these temperatures the ion exchange was complete and we obtain D2-AgCoO$_2$. The final obtained powders were washed in water to remove the remaining nitrates and dried in oven. The P-XRD patterns of the final products synthesized at different temperatures are shown in **Figure 3** evidencing in all cases their purity within X-ray diffraction threshold.
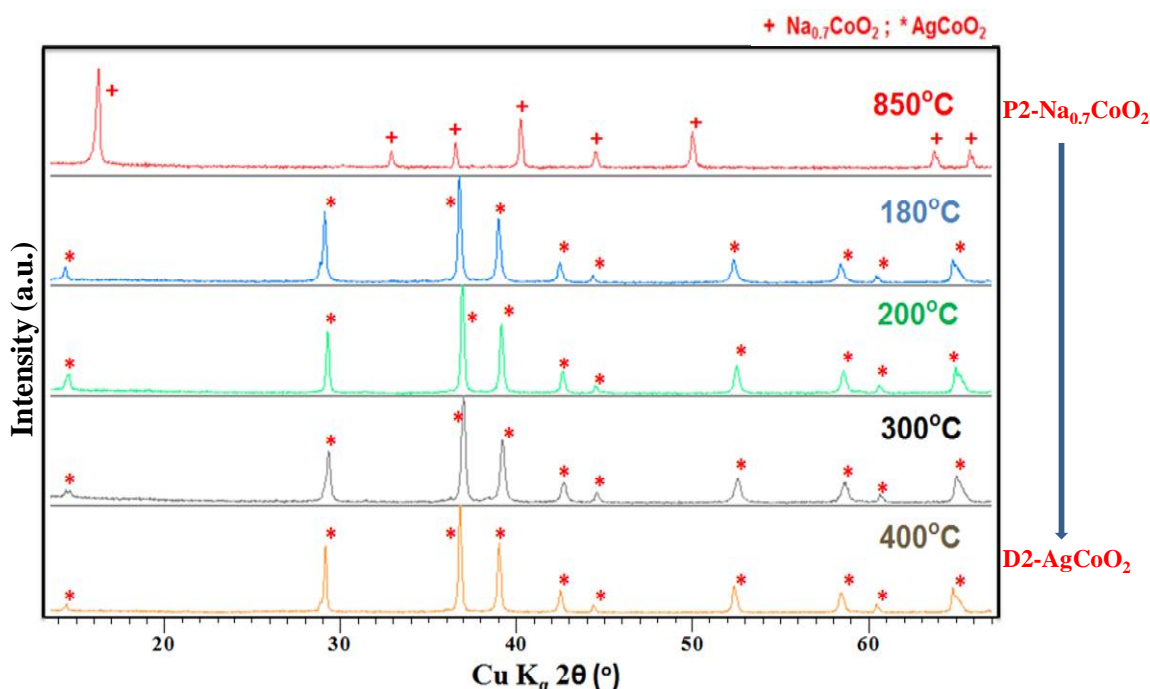
Figure 3. X-ray powder diffractions of final products after ion exchange between P2-Na$_{\sim0.7}$CoO$_2$ and AgNO$_3$/KNO$_3$ at different temperatures.

The profile matching refinement of D2-AgCoO$_2$ obtained by ion exchange process at 400°C is shown in **Figure 4**. All the reflections can be indexed in the hexagonal system using the P6$_3$/mmc space group, with cell parameters in good agreement with the literature; the refined cell parameters are given in **Table 4**.
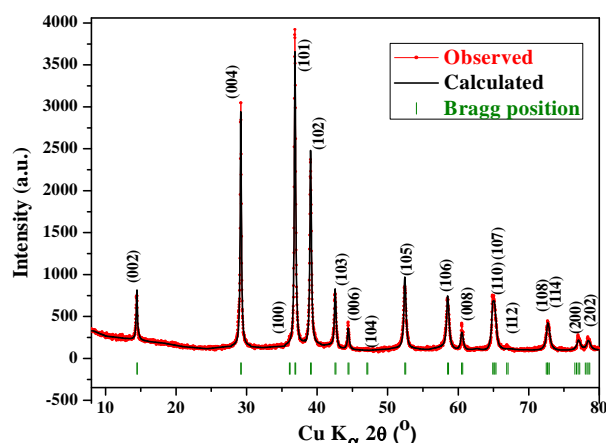
Figure 4. Profile matching refinement of D2-AgCoO$_2$ obtained by ion exchange process. The observed (red points), calculated (black solid line) and the Bragg positions (green bars) are shown.

D2-AgCoO$_2$	
Space group: P6$_3$/m m c (194)	
Lattice parameters	a = 2.8713 (2) Å c = 12.2236 (1) Å
Profile parameters	Function: Pseudo-Voigt *Halfwidth parameters* U = 0.70 (4) V = -0.36 (3) W = 0.07 (1)
R-factors	R$_p$: 7.16 % R$_{wp}$: 9.24 % R$_{exp}$: 6.48 % χ^2: 2.03

Table 4. Lattice parameters and reliability factors for D2-AgCoO$_2$ phase analysed with profile matching using FullProf suite.

The morphology of as-synthesized D2-AgCoO$_2$ product at 400°C observed by using scanning electron microscopy (not shown here) and consists of well-organized hexagonal shaped platelets. Such morphology is in agreement with both the two dimensional character and the hexagonal symmetry of D2-AgCoO$_2$. The crystallite size ranges from few hundred nm to a few microns. The 1:1 ratio between cations was confirmed with Energy-dispersive X-ray spectroscopy (EDX) and ICP analysis.

II.3.2. D3-AgCoO$_2$

In literature, the D3-AgCoO$_2$ polytype is usually obtained from an O3-LiCoO$_2$ precursor. However the ion-exchange is often incomplete and some residual precursor often remains in the final product. This is due to the fact that this exchange requires (i) a big change in the inter-slab thickness ($r_{VI}^{Li^+} < r_{VI}^{Na^+} < r_{VI}^{Ag^+}$) as well as (ii) a slab gliding to match symmetry requirements (from O$_h$ for Li$^+$ to D$_{\infty h}$ for Ag$^+$) [9]. To maximize the reaction yield, we systematically performed the ionic exchange reaction in molten salts between AgNO$_3$/KNO$_3$ (1:1) and O3-LiCoO$_2$ with a 1.5 times excess of silver nitrate as compared to the alkali nominal content. The duration of exchange reaction was fixed at 48 h and we tuned the temperature of the reaction from 150-600°C.
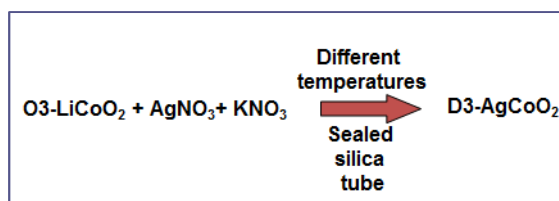
The final products were washed in water to remove the remaining nitrates and finally oven-dried overnight. The resulting P-XRD patterns are shown in **Figure 5**.
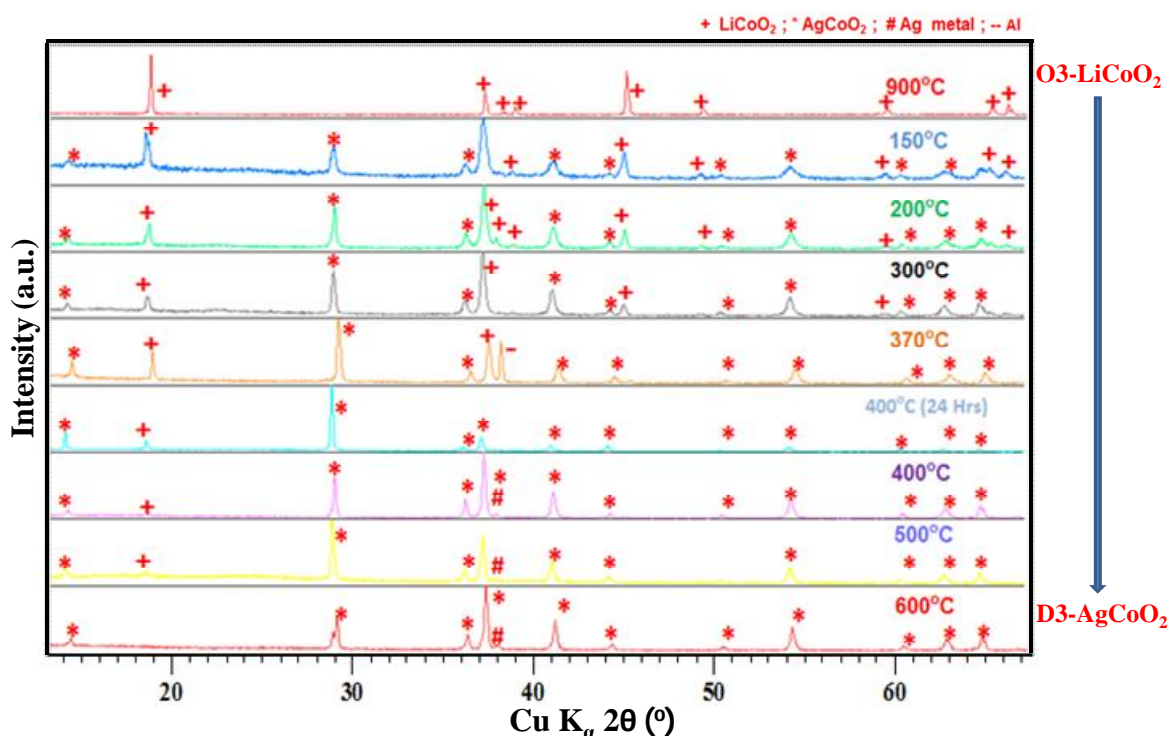
Figure 5. X-ray powder diffractions of final products after ion exchange between O3-LiCoO$_2$ and AgNO$_3$/KNO$_3$ at different temperatures. (*: AgCoO$_2$; +: O3-LiCoO$_2$; #: Ag; -: Al sample holder)

D3-AgCoO$_2$ begins to form at the lowest temperature (150 °C) and the reaction yield increases up to 400 °C when LiCoO$_2$ precursor fully disappears. However, at this temperature, metallic silver begins to form. In order to avoid its appearance, the reaction duration was shortened to 24 h. In this case however, some traces of the O3 precursor are visible. Further increasing the temperature in the same time only enhanced the formation of metallic silver (**Figure 5**). No further attempts were made to tune additional parameters and we kept the protocol [AgNO$_3$:KNO$_3$:O3-LiCoO$_2$=1.5:1.5:1, T=400 °C, t=48 h] as it gave to lowest secondary phase (Ag) amount.

Figure 6 shows as an example and for clarity the profile matching refinement of the P-XRD pattern of $D3\text{-}AgCoO_2$ obtained by ion exchange process at 600^oC, i.e. with a high Ag content. All the reflections can be indexed in the Rhombohedral $D3\text{-}AgCoO_2$ system using the $R\bar{3}m$ space group and in the cubic $Fm\bar{3}m$ Ag^0 system. The refined cell parameters given in **Table 5** for both compounds agree with the literature; the results are almost the same with other processing temperature.
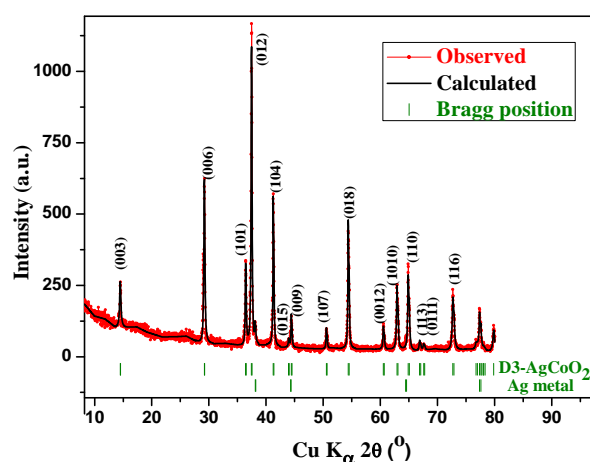
Figure 6. Profile matching refinement of D3-AgCoO$_2$ obtained by ion exchange process. The observed (red points), calculated (black solid line) and the Bragg positions (green bars) are shown.

D3-AgCoO$_2$	
Space group: R -3 m (166)	
Lattice parameters	$a = 2.8719\,(2)$ Å; $c = 18.340\,(2)$ Å
Profile parameters	Function: Pseudo-Voigt *Halfwidth parameters* $U = 0.88\,(7)$ $V = -0.74\,(6)$ $W = 0.17\,(1)$
Ag	
Space group: F m-3 m (225)	
Lattice parameters	$a = b = c = 4.0880\,(7)$ Å
Profile parameters	Function: Pseudo-Voigt *Halfwidth parameters* $U = 0.87\,(9)$ $V = -0.74\,(6)$ $W = 0.17\,(1)$
***R*-factors**	R$_p$: 12.9 % R$_{wp}$: 17.7 % R$_{exp}$: 11.55 % χ^2: 2.36

Table 5. Details of Lattice parameters and reliability factors for D3-AgCoO$_2$ phase analysed with profile matching by FullProf suite.

II.4. Hydrothermal Synthesis: D3-AgCoO$_2$

All chemical reagents used in this experimental procedure were of analytical grade. In a typical synthesis process, 0.0882 mmol of $AgNO_3$ and 0.0294 mmol of Co_3O_4 were added to 30 ml of deionized water with vigorous stirring. 1.5 M of KOH pellets was then added and the mixture was stirred for 30 min and further transferred to a Teflon-lined stainless-steel autoclave of 43 ml capacity. The hydrothermal reaction was carried out by placing the autoclave in a high temperature oven at 220^oC for 60 h. After reaction, the powder sample was filtered and washed several times with absolute alcohol and deionized water. The final product after cleaning process was dried in an oven at 80^oC for 6 h.
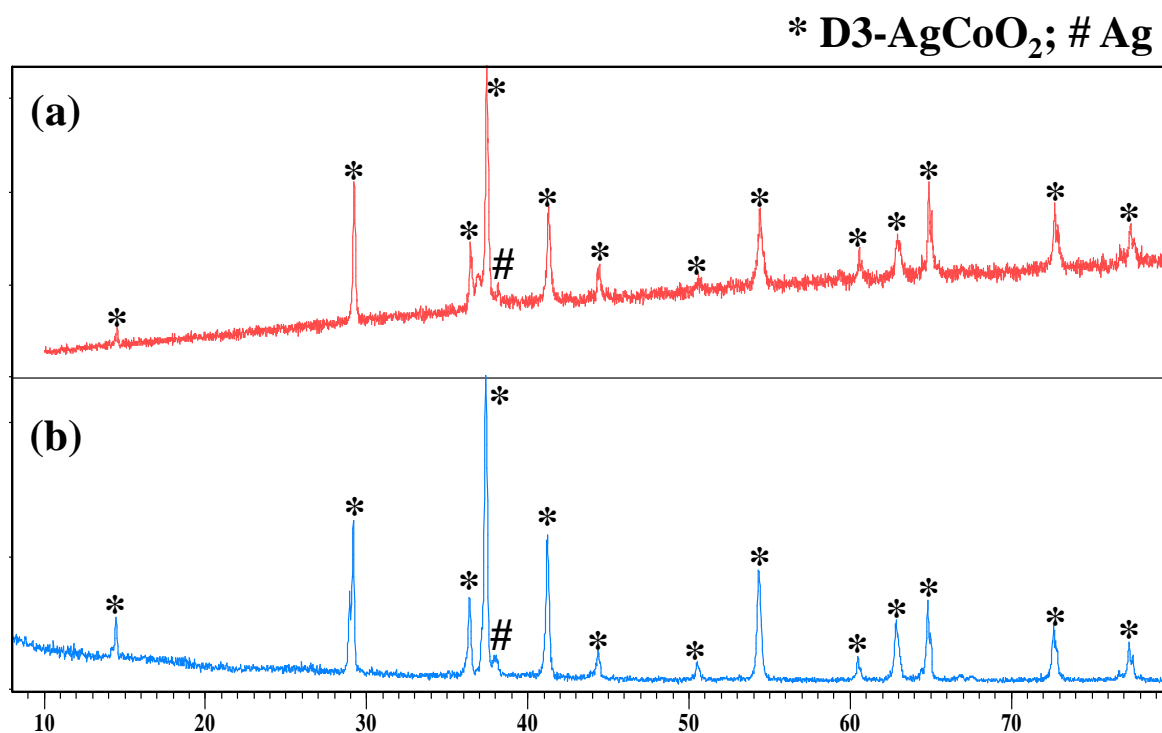
Figure 7. P-XRD patterns of D3-AgCoO$_2$ obtained by (a) Direct hydrothermal process and (b) Ion exchange process from O3-LiCoO$_2$ at 600°C. (*: D3-AgCoO$_2$; # Ag^0)

The P-XRD pattern of the product is shown in **Figure 7a** together, for comparison, with the P-XRD pattern for D3-AgCoO$_2$ prepared by ion exchange from O3-LiCoO$_2$ at 600 °C (**Figure 7b**). All the reflections can be assigned to the D3 polytype with space group R$\bar{3}$m with a tiny peak of Ag^0. The width of the peaks evidence the good crystallinity of the sample and the secondary phase appears less abundant than with ionic exchange. The morphology of D3-AgCoO$_2$ prepared by hydrothermal process is shown in **Figure 8a** nicely compares with the one obtained after ionic exchange and the 1:1 cation ratio is confirmed by EDX analysis (**Figure 8b**).
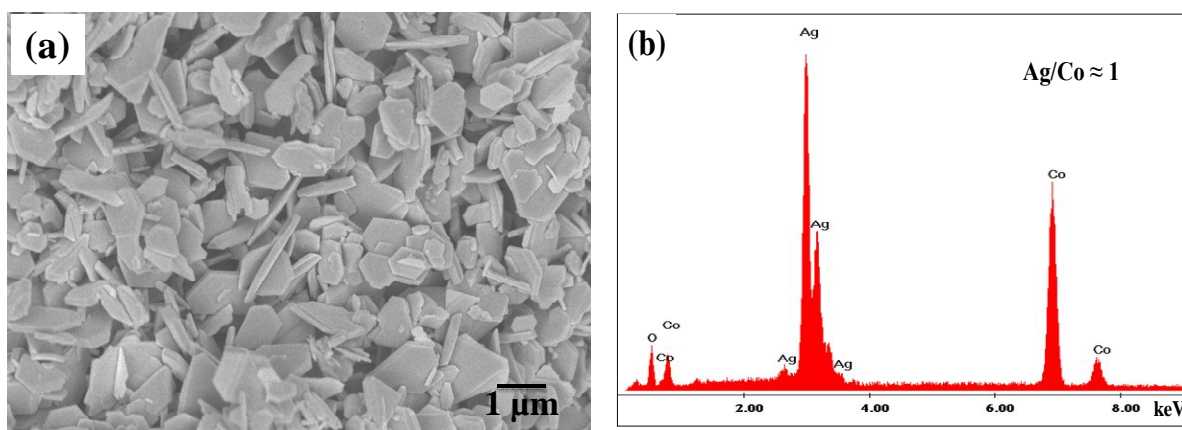
Figure 8. (a) Morphology of D3-AgCoO$_2$ obtained from direct hydrothermal process; **(b)** EDX profile of platelet like morphologies D3-AgCoO$_2$ phase, which shows nearly unit ratio between Ag and Co.

II.5. Synthesis of ACo$_{1-x}$Mg$_x$O$_2$ (A=Na$_{0.7}$; Ag)

II.5.1. P2-Na$_{0.7}$Co$_{1-x}$Mg$_x$O$_2$: Auto combustion process

Stoichiometric amounts of analytical grade Na$_2$CO$_3$ (5% excess), Co$_3$O$_4$ and Mg(OH)$_2$ powders were dissolved in a warm HNO$_3$ solution under continuous stirring. An appropriate amount of citric acid was added to this mixture and stirring was continued overnight. The auto-combustion process was promoted by increasing the temperature of the mixture. After the auto-combustion occurred, the as-obtained ash was calcinated at 850°C for 24 h under O$_2$ flow with +2/-5 °C/min heating/cooling rates.
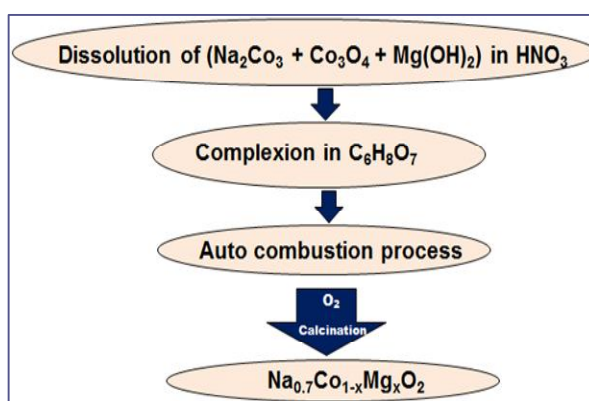
The P-XRD patterns were recorded using a PANalytical X'Pert Pro powder diffractometer in the Bragg-Brentano geometry using Cu K$_\alpha$ radiation as the X-ray source.

Figure 9 shows the x-ray diffraction patterns of $Na_{0.7}Co_{1-x}Mg_xO_2$ (x = 0, 0.02, 0.04, 0.08 and 0.10). Most of the diffraction peaks match with $P2-Na_{0.7}CoO_2$ but a minor peak owing to MgO is also present as indicated in the figures with a star (*). This secondary phase is however minority and it is unlikely that it will strongly influence the properties of the substituted samples.
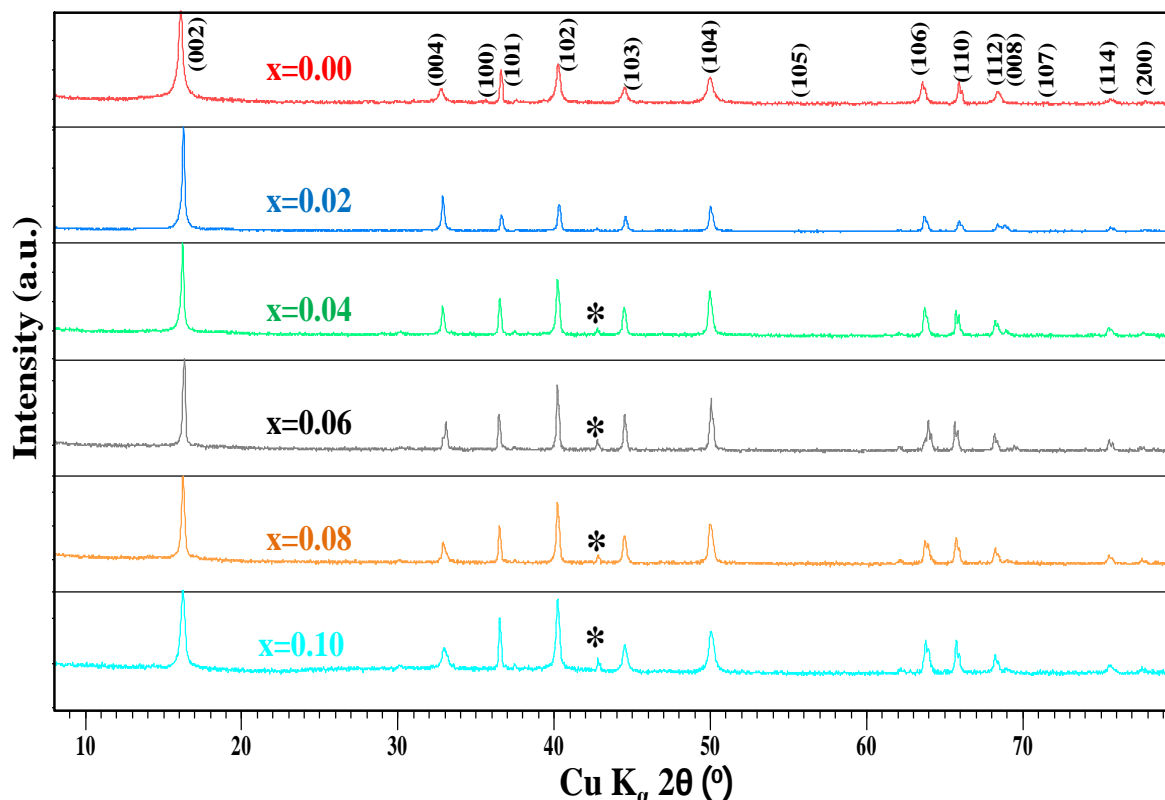
Figure 9. Powder XRD patterns of $P2-Na_{0.7}Co_{1-x}Mg_xO_2$ (0≤x≤0.10) samples obtained by auto combustion process. Peaks labelled * are diffraction peaks of MgO impurities. All the XRD reflections can be assigned to $P6_3/m\,m\,c$ space group and corresponding Bragg reflections are shown.

II.5.2. $D2-AgCo_{1-x}Mg_xO_2$: Ion exchange process

$D2-AgCo_{1-x}Mg_xO_2$ (0≤x≤0.10) samples were prepared by a cation exchange reaction between $P2-Na_{0.7}Co_{1-x}Mg_xO_2$ and $AgNO_3$.
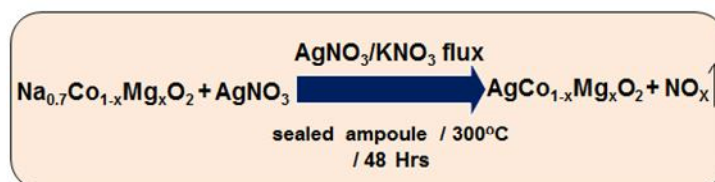
$Na_{0.7}Co_{1-x}Mg_xO_2$, $AgNO_3$ and KNO_3 were stoichiometrically weighed and mixed in a mortar for few minutes. The mixed powder was pressed into pellet and sealed in a silica tube under vacuum. The cation exchange reaction was performed by heating at these sealed tubes at $300^{o}C$ for 48 h. After the reaction, the sealed tubes were cooled down to room temperature; the samples were then washed in distilled water and dried at 100 °C in air for several hours. The P-XRD patterns (PANalytical X'Pert Pro powder diffractometer with Cu K_{α} radiation) for the resulting samples are shown in **Figure 10**.
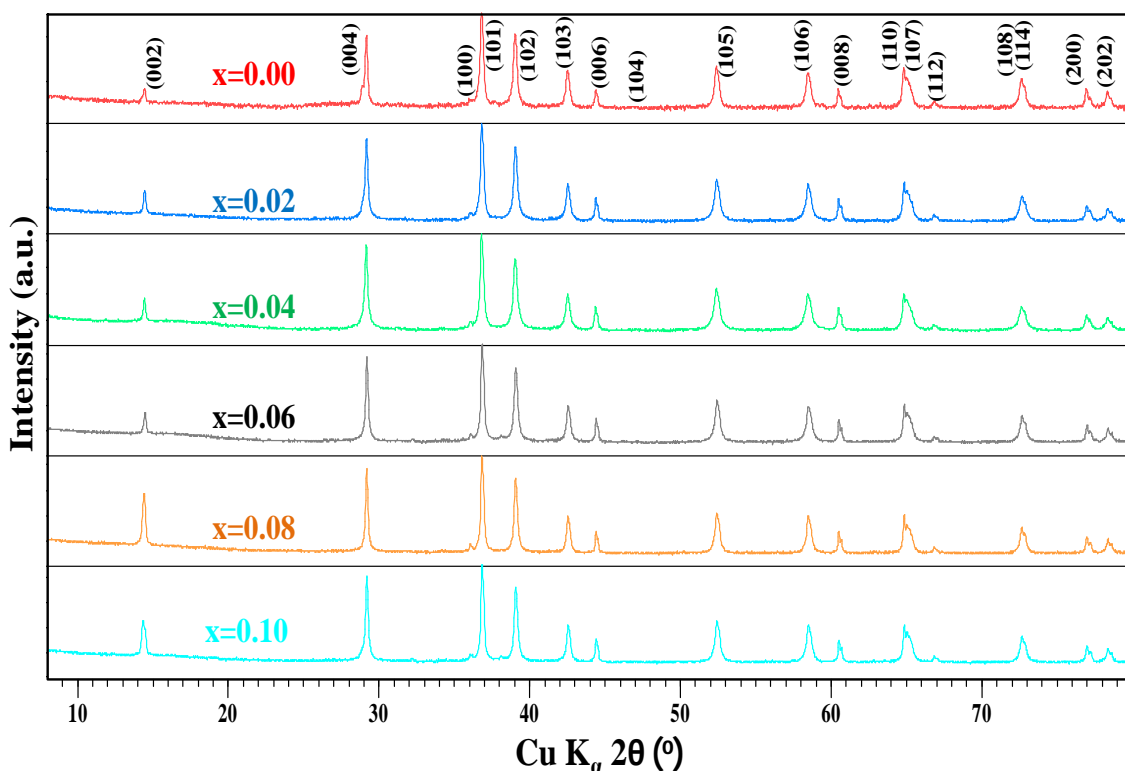
Figure 10. Powder XRD patterns of D2-$AgCo_{1-x}Mg_xO_2$ ($0 \leq x \leq 0.10$) samples obtained by ion exchange process from P2-$Na_{0.7}Co_{1-x}Mg_xO_2$ ($0 \leq x \leq 0.10$). All the XRD reflections can be assigned to $P6_3/mmc$ space group and corresponding Bragg reflections are shown.

II.6. Synthesis of $ACo_{1-x}Mn_xO_2$ ($A=Na_{0.7}$; Ag)

II.6.1. P2-$Na_{0.7}Co_{1-x}Mn_xO_2$: Solid state reaction process

Polycrystalline samples of Mn substituted P2-$Na_{0.7}CoO_2$ series P2-$Na_{0.7}Co_{1-x}Mn_xO_2$ (x =0, 0.05, 0.10, 0.15, 0.20, 0.25) were synthesized by a standard solid-state reaction method. A stoichiometric mixture of Na_2CO_3 (5% excess), Co_3O_4 and MnO_2 were ground and heated in O_2

flow at 850 °C for 24 h. As Na tends to evaporate during calcinations, we added 5% excess amount of Na_2CO_3 for all compositions. P-XRD patterns for resulting samples (X'Pert MRD diffractometer with Cu Kα radiation) are shown in **Figure 11**.
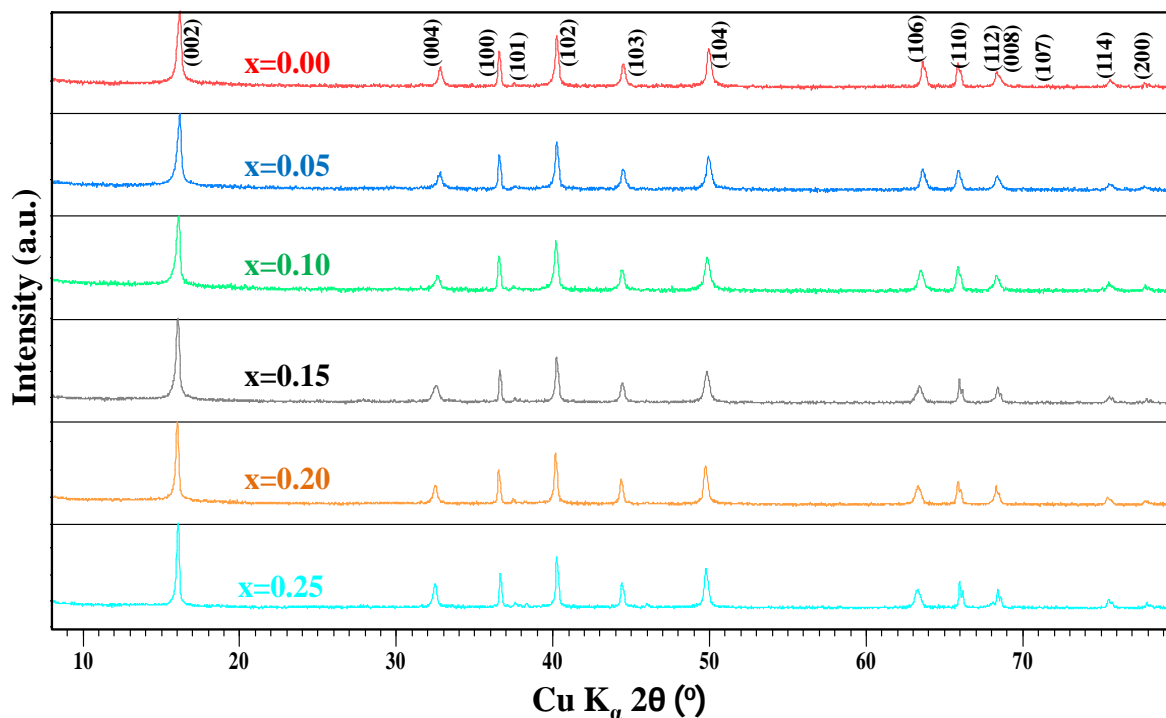
Figure 11. Powder XRD patterns of P2-$Na_{0.7}Co_{1-x}Mn_xO_2$ ($0 \leq x \leq 0.25$) samples obtained by solid state process. All the XRD reflections can be assigned to P6$_3$/mmc space group and corresponding Bragg reflections are shown.

All the samples are single phase what evidences that Mn completely substitutes for Co and all the peaks in the pattern can be indexed as P2-$Na_{0.7}CoO_2$ phase with P6$_3$/mmc space group.

II.6.2. D2-$AgCo_{1-x}Mn_xO_2$: Ion exchange process

The synthesis steps involved in the preparation of D2-$AgCo_{1-x}Mn_xO_2$ are similar to the ones used for D2-$AgCo_{1-x}Mg_xO_2$. P2-$Na_{0.7}Co_{1-x}Mn_xO_2$ compounds are thoroughly mixed and grounded with $AgNO_3$ and KNO_3 in a mortar. These mixed powders are pressed into disc shaped pellets by uniaxial press and placed in vacuum sealed silica tubes. The cation ion exchange reactions were performed by heating these sealed tubes at 300°C for 48 h. After the reaction the sealed tubes were cooled down to room temperature at 5°C per min and the samples were washed

in distilled water and further dried at 100°C in air for several hours. Phase identification process was performed by X-ray powder diffraction studies using XRD measurements with a PANalytical X'Pert Pro powder diffractometer by Cu K$_\alpha$ radiation.
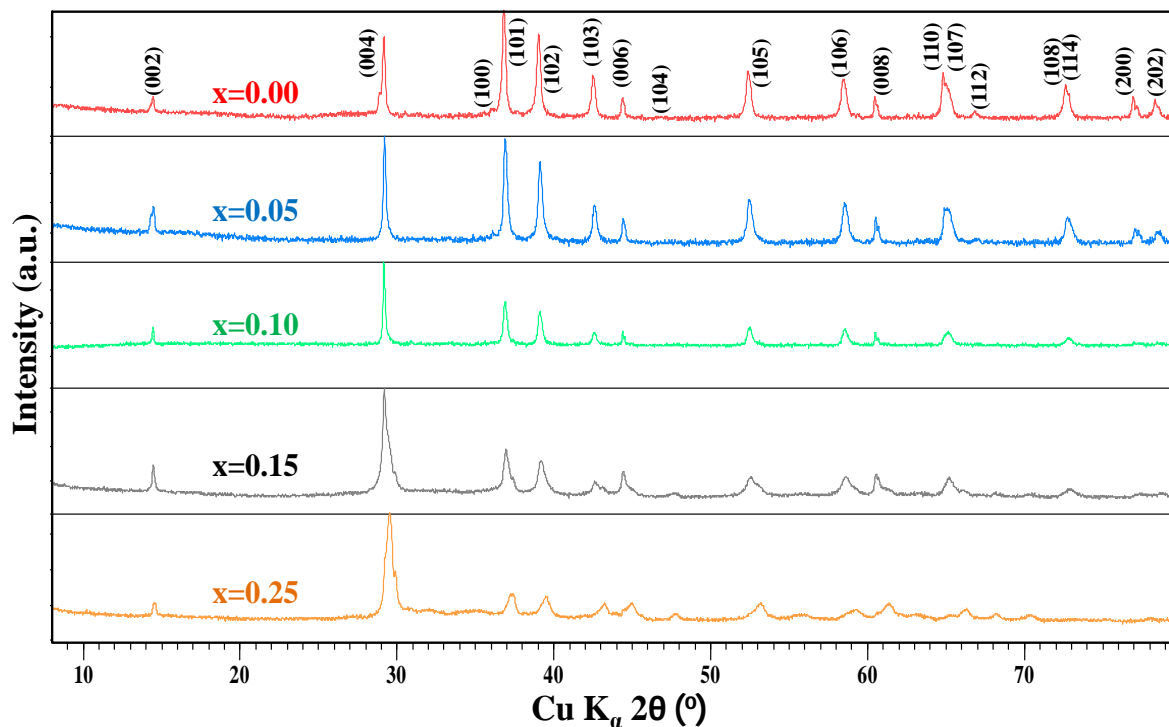
Figure 12. Powder XRD patterns of D2-AgCo$_{1-x}$Mn$_x$O$_2$ (0≤x≤0.25) samples obtained by ion exchange process from P2-Na$_{0.7}$Co$_{1-x}$Mn$_x$O$_2$ (0≤x≤0.25). All the XRD reflections can be assigned to P6$_3$/mmc space group and corresponding Bragg reflections are shown.

The P-XRD patterns in **Figure 12** all match with the one of D2-AgCoO$_2$. However, for higher level of Mn substitution, even though there is no visible secondary phase, we can clearly see the decrease in the intensity of certain reflections indicating the decrease in the crystallanity of the samples with increasing Mn concentration.

II.7. References

[1] W. Stählin, H.R. Oswald, Zeitschrift für anorganische und allgemeine Chemie 373, 69 (1970)

[2] R.D. Shannon, D.B. Rogers, C.T. Prewitt, Inorganic Chemistry 10, 713 (1971)

[3] D.B. Rogers, R.D. Shannon, C.T. Prewitt, J.L. Gillson, Inorganic Chemistry 10, 723 (1971)

[4] Y.J. Shin, J. H. Kwak, S.K. Yoon, Bull. Korean Chem. Soc. 18, 775 (1997)

[5] J.S. Kang, J.H. Kwak, Y.J. Shin, S.W. Han and K.H. Kim, B.I. Min, Phys. Rev. B 61, 10682(2000)

[6] J. Tate, M.K. Jayaraja, A.D. Draesekea, T. Ulbricha, A.W. Sleight, K.A. Vanaja, R. Nagarajan, J.F. Wager, R.L. Hoffman, Thin Solid Films 411, 119 (2002)

[7] H. Muguerra, C. Colin, M. Anne, M.H. Julien, P. Strobe, Journal of Solid State Chemistry 181, 2883 (2008)

[8] A. Ussow, Z. Anorg. Allg. Chem. 38, 419 (1904)

[9] R. Berthelot, M. Pollet, J.P Doumerc, C. Delmas, Inorg. Chem., 50, 4529 (2011)

Chapter III:
Thermoelectric properties of pristine and substituted P2-Na$_{0.7}$CoO$_2$ and D2-AgCoO$_2$

This section presents the thermoelectric and magnetic properties of pristine and Mg or Mn substituted P2-Na$_{0.7}$CoO$_2$ and D2-AgCoO$_2$ materials. The effects of substitution on electronic properties are presented in relationship with changes in the crystal structure.

Contents

III.1. Introduction

The cobalt based layered transition metal oxides have raised interest because of their promising thermoelectric properties. In particular there is a renewed interest for delafossite oxides because of their high Seebeck coefficient. The p-type conductivity of $AgCoO_2$ is low and it sounds interesting to try to improve it for practical applications. Element doping, as an effective way, has been often used to improve specific properties. To modulate the transport properties and possibly optimize the thermoelectric characteristics, we have varied the composition of P2-$Na_{0.7}CoO_2$ with Mn and D2-$AgCoO_2$ with Mg and Mn substitution at Co site.

III.2. Experimental details

The samples were synthesized by an auto combustion process followed by a solid-state reaction and ion exchange reaction. Details are summarized in *chapter II*. The powder samples were thoroughly ground and pressed into 10 mm in diameter disc shaped pellets under pressure of 10 MPa. The P2-$Na_{0.7}CoO_2$ pellets were heated at 850°C/12 h under an oxygen flow while the D2-$AgCoO_2$ pellets were heated at 300°C/12 h under vacuum; in both cases the heating and cooling rate were 2°C/min and 5°C/min respectively. The compactness of P2-$Na_{0.7}CoO_2$ and D2-$AgCoO_2$ series were close to 90 and 70% respectively.

Phase purity was confirmed by powder X-Ray Diffraction (P-XRD) with a PANanalytical X'pert diffractometer using Cu-K$_\alpha$ radiation and details about the structural parameters are given in *chapter II*. The electrical resistivity (ρ) was measured by the four-probe method and the thermoelectric power (α) was measured dc differential technique using homemade setups. Magnetic susceptibility was measured using a SQUID (Quantum Design MPMS) apparatus. Zero field cooled (ZFC) and field cooled (FC) experiments were carried out under 1000 Oe in the temperature range 5–300 K. Specific heat was measured in the temperature range 2-300 K using the Quantum Design Physical Property Measurement System (PPMS) cryostat.

III.3. Results and discussion

III.3.1. P2-Na$_{0.7}$CoO$_2$: Thermoelectric and magnetic properties

Figure 1 compiles the experimental results for the transport and magnetic properties as well as the heat capacity. All these results agree with the literature on pristine P2-Na$_{0.7}$CoO$_2$.
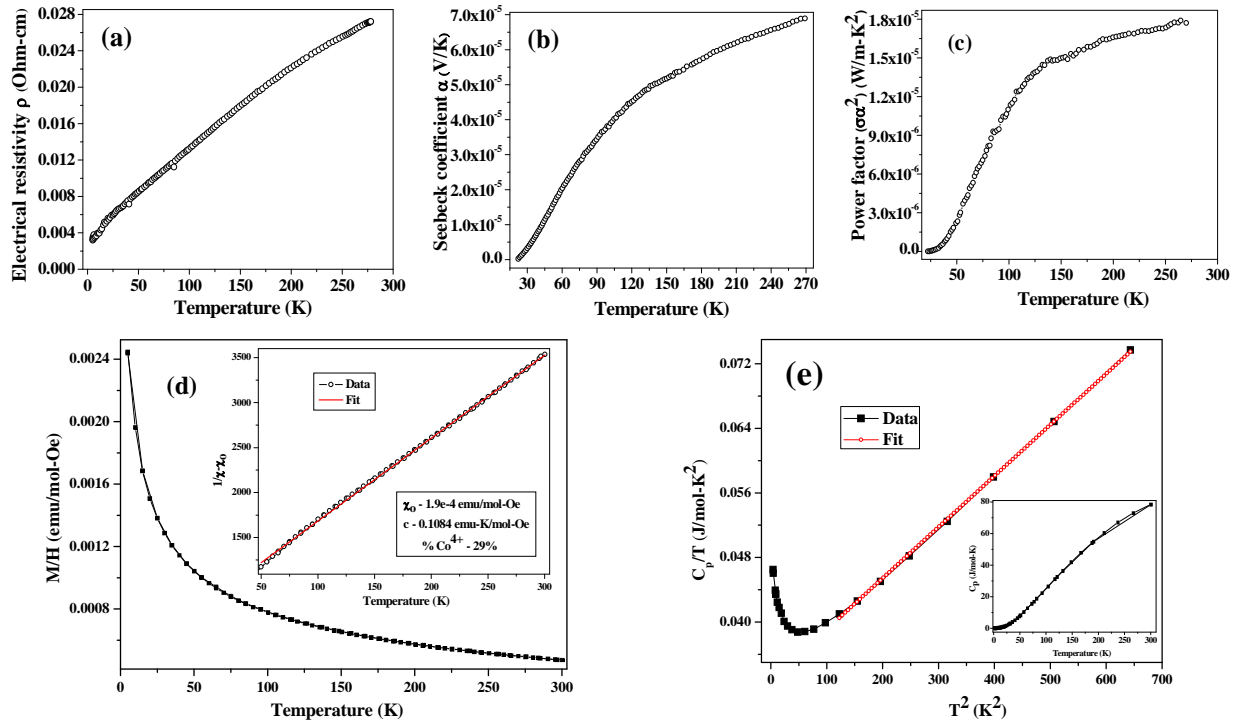
Figure 1. Temperature dependence of (a) the resistivity (b) the Seebeck coefficient and (c) the thermoelectric power factor for P2-Na$_{0.7}$CoO$_2$ (d) Temperature dependence of zero-field cooled (ZFC) dc magnetization susceptibility of polycrystalline P2-Na$_{0.7}$CoO$_2$ measured at 1000 Oe; the inset shows the temperature dependence of 1/χ-χ_o and the Curie Weiss fit. (e) C$_P$/T *vs* T^2; the specific heat *vs* temperature is given in the inset.

The resistivity increases with increasing temperature, exhibiting a metallic behavior (dρ/dT>0) in the explored temperature range similarly to the observation of in-plane single-crystal resistivity [1]; it indicates that in-plane conduction dominates in polycrystalline samples. The linear temperature was already reported and related to strong electron correlations. The sign of the Seebeck coefficient indicates p-type conduction with positive charges as major carriers; its enhancement as compared to normal metals is due to the spin contribution ($k_B/e \cdot ln2 \approx$

$60 \mu V/K$) thanks to the mixed valence (+3/+4) of cobalt ion. The power factor ($\sigma\alpha^2$) is high and reaches 0.166 µW/cm-K^2 which is close to the reported value for P2-Na$_{0.7}$CoO$_2$ polycrystalline samples (0.188 µW/cm-K^2 [2]). The FC and ZFC data do not display any significant difference and in particular there is no anomaly at 30-40 K discarding any presence of Co$_3$O$_4$ traces (AFM; T$_N$≈35K [3]). The Curie-Weiss fit with $\chi= \chi_o+C/(T+\theta)$ leads to a combined Pauli paramagnetism and core diamagnetism term χ_o as 1.9e10^{-4} emu/mol-Oe, $\theta \approx$ -68 K and C $\approx$ 0.1084. As Co^{3+} is in low spin state (S=0), the observed moments can broadly be understood in terms of low spin Co^{4+} (S = ½) leading to nearly 29% of Co^{4+} ions in agreement with the given composition for P2-Na$_{\sim0.7}$CoO$_2$. The heat capacity data do not exhibit any anomaly in particular around the Co$_3$O$_4$ antiferromagnetic transition temperature further supporting the absence of Co$_3$O$_4$ impurity. The linear fit of C$_p$/T *vs* T^2 between 11 and 25 K give a Sommerfeld coefficient γ=32.75 mJ/mol-K and Debye temperature θ_D=496 K in agreement with the values reported by Motohashi et al. and Sales et al. [4]. The significant deviation from linearity at low temperature suggests that magnetic fluctuations contribute significantly to the specific heat at very low temperatures [5].

III.3.2. P2-Na$_{0.7}$Co$_{1-x}$Mn$_x$O$_2$: Thermoelectric properties

All the studied samples have the parent compound hexagonal layered structure with space group P6$_3$/mmc. The absence of extra-peaks in the P-XRD patterns indicates the complete substitution of Mn for Co. The lattice parameters shown in **Figure 2** are in good agreement with previous reports of Fouassier et al. [6] and Zhang et al. [7]. With increasing Mn concentration, the lattice parameters a and c vary in opposite direction with *a* parameter decreasing exponentially and being almost constant from 10% Mn while *c* increases roughly linearly just like the unit cell volume does. The ionic radii of Co^{3+}, Co^{4+}, Mn^{3+} and Mn^{4+} are 0.545 Å, 0.477 Å [8], 0.58 Å, and 0.53Å, respectively [9]. The increase in the unit cell volume as the Mn concentration increases is compatible with the aliovalent substitution[❶] of Mn for Co as well as the preferential electron or hole localization on Mn ion[❷,❸] (oxydo-reduction) or their combination:

$$❶ \ Na_{0.7}(Co_{0.7}^{3+}Co_{0.3}^{4+})_{1-x}(Mn_{0.7}^{3+}Mn_{0.3}^{4+})_x O_2, \ Co^{4+}/Co^{3+} = 3/7$$

$$❷ Na_{0.7}Co_{0.7-x}^{3+}Co_{0.3}^{4+}Mn_x^{3+}O_2, \ Co^{4+}/Co^{3+} = 3/(7-10x)$$

$$❸ Na_{0.7}Co_{0.7}^{3+}Co_{0.3-x}^{4+}Mn_x^{4+}O_2, \quad Co^{4+}/Co^{3+} = (3 - 10x)/7$$
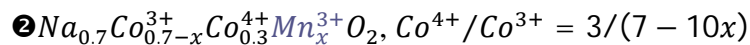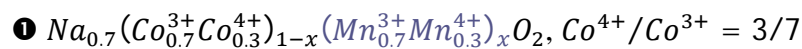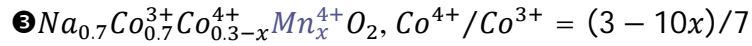
The small decrease in *a* parameter together with the increase in *c* parameter suggests a decrease in the trigonal distortion; some contribution of a Jahn–Teller effect on Mn^{3+} is not excluded.
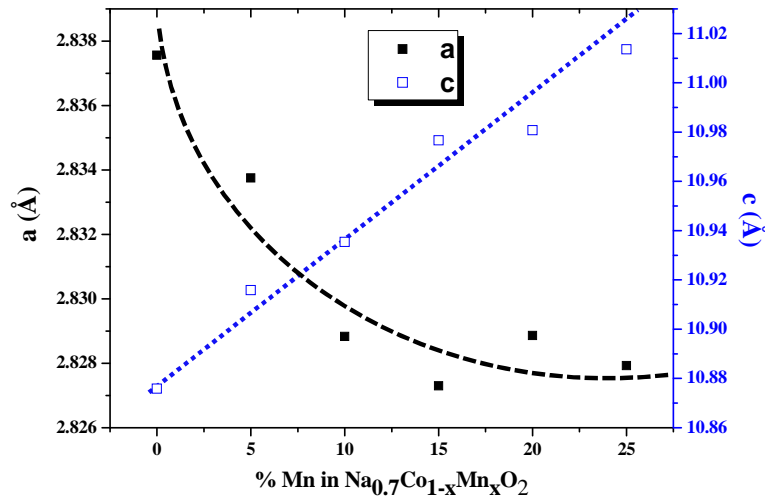
Figure 2. Variation of lattice parameters a and c in P2- Na$_{0.7}$Co$_{1-x}$Mn$_x$O$_2$.

Figure 3a shows the electrical resistivity as a function of temperature for P2-Na$_{0.7}$Co$_{1-x}$Mn$_x$O$_2$ with x=0.05, 0.10 and 0.15. For 5% Mn substitution, the curve is very similar to the pristine case and the variation is linear with temperature until 100 K marking the upholding of strong correlation for low Mn content. The main difference is in the small upturn at 20 K signing a metal to insulator transition, which is most likely due to the disorder introduced by the substitution for which low dimensional systems are usually very sensitive. With the substitution rate increase the resistivity is globally increasing and for the highest Mn content the resistivity continuously decreases with increasing temperature indicating a simple semiconductor behavior without any further trace of metal to insulator transition. For these samples, the Mott and Davis's small polaron hopping model reasonably account for the data as shown in **Figure 3b**. The thermopower data given in **Figure 3c** show a behavior similar to the pristine case for low Mn content while further substitution results in the increase of the Seebeck coefficient though the curve's shape remain the same. This confirms the existence of a substitution threshold after which the strong correlations and the spin entropy enhancement disappear leading to a conventional hoping system. It is interesting to note that after this threshold, the thermopower seems independent (within the studied limit) of the Mn content. Relating the "infinite"

temperature value of the thermopower to the Heikes approach, this independence on Mn content supports the aliovalent substitution scenario for which the mixed valence ratio is constant.
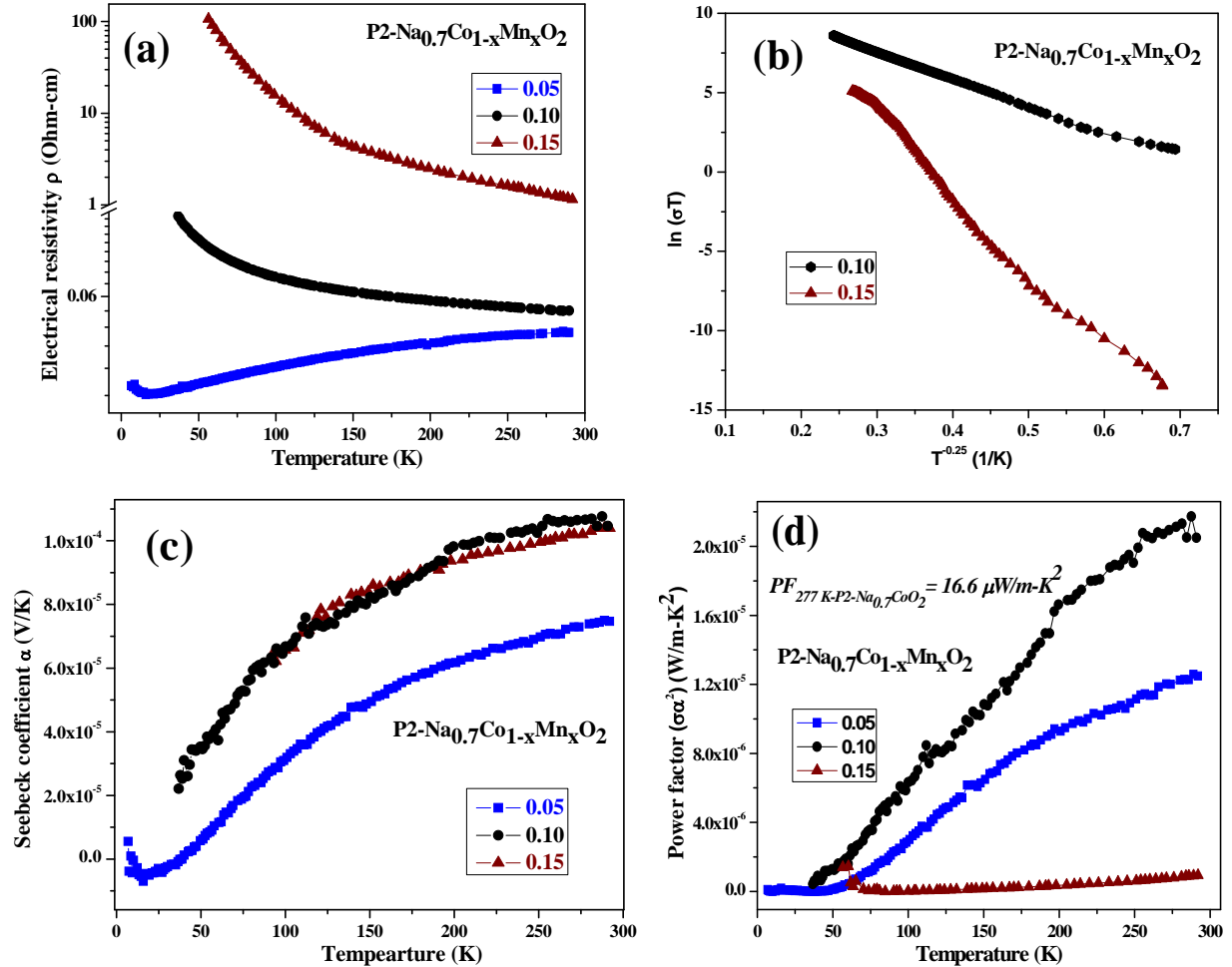
Figure 3. (a) Temperature dependence of electrical resistivity (ρ); (b) Plot of $\ln(\sigma T)$ versus $1/T^{-0.25}$ (c) Temperature dependence of Seebeck coefficient (α); (d) Temperature dependence of thermoelectric power factor for P2-$Na_{0.7}Co_{1-x}Mn_xO_2$.

The power factor for all three P2-$NaCo_{1-x}Mn_xO_2$ samples increases with increasing temperature (**Figure 3d**). It is here maximum with x = 0.10 probably because this value is close to the upper-mentioned threshold inducing both a reasonably low resistivity, close to the metallic one, and a jump in the Seebeck coefficient value, close to the one in the semi-conducing state.

III.3.3. D2-AgCoO$_2$: Thermoelectric and magnetic properties

The experimental results for the transport and magnetic properties of pristine D2-AgCoO$_2$ are shown in **Figure 4.** The conductivity is semiconducting-like with an increase with

temperature (**Figure 4a**). It is lower than the n-type semiconductors but very similar to copper based delafossite counter parts $CuAlO_2$, $CuGaO_2$, $CuInO_2$ series [10]. Delafossite are highly anisotropic [11]: the O-Ag-O dumbell is parallel to the c-axis while the layer of edge sharing CoO_6 octahedra layer is perpendicular to the c-axis and acts as an efficient conduction path for electrons *i.e.* the main conduction path is in the (ab) plane [12]. In our case the electrical resistivity of polycrystalline pellets, which are made from hexagonal plate-like crystals, is dominated by this in-plane component. The electrical-conduction mechanisms in delafossite compounds are generally reported to follow either small polaron like transport, band-conduction or variable-range hopping [13]. Our electrical conductivity data obey a Mott's law of the form $\sigma = A \cdot exp[(T_0/T)^{1/1+n}]$ with n adjusted to 3 (**Figure 4b**) suggesting a 3D variable range hopping mechanism [14,15]. Such mechanism is generally expected to be predominant at low temperature when the carriers are localized in Anderson states. This suggests the presence of a large number of localized states or that the low compacity of the pellet masks the intrinsic conductivity.

The thermopower is positive indicating p-type conduction; it is increasing roughly linearly (**Figure 4c**) with temperature suggesting a carrier diffusion through a hopping mechanism consistent with previous analysis. The power factor (PF = $\sigma\alpha^2$) increases as well with temperature (**Figure 4d**) and at 277 K it is nearly 200 times less than for P2-$Na_{0.7}CoO_2$. This decrease is mainly due to its poor electrical conductivity. The Curie-Weiss fit ($\chi=\chi_0+(C/(T-\theta))$) to the susceptibility data is shown in **Figure 4e**; the least-square-fit values are $\chi_0=7.55 \times 10^{-8}$ emu/mol-Oe, $\theta=-171$ K and C=2.437e-4; such low value of the Curie constant can be associated both with a small deviation from stoichiometry and the presence of very few secondary phases like Co_3O_4.
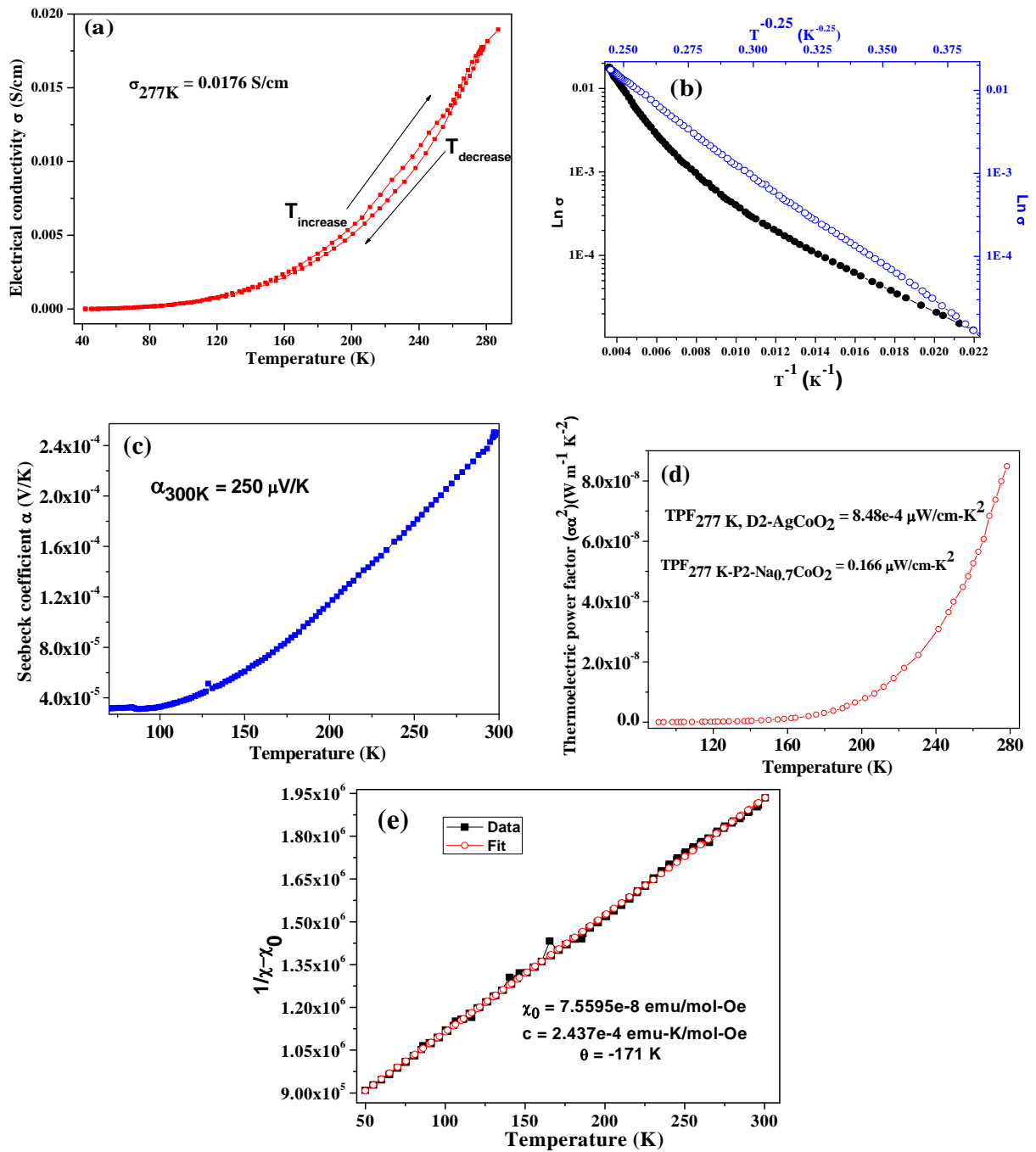
Figure 4. Electronic data for D2-AgCoO$_2$. (a) Electrical conductivity and (b) Mott's representation with n=0 and 3; (c) Seebeck coefficient and (d) power factor; (e) Curie-Weiss fit to the magnetic susceptibility.

III.3.4. D2-AgCo$_{1-x}$Mg$_x$O$_2$: Thermoelectric properties

The space group of the substituted samples is identical to the pristine one. The lattice parameters displayed in **Figure 5** offer the same trend with first a decrease down to *ca* 2% and

then a monotonous increase as x increases. The unit cell expansion can be simply understood on the basis of the bigger ion radius of Mg^{2+} (0.72 Å) as compared to cobalt ions. The initial decrease cannot be explained within such simple ionic picture.
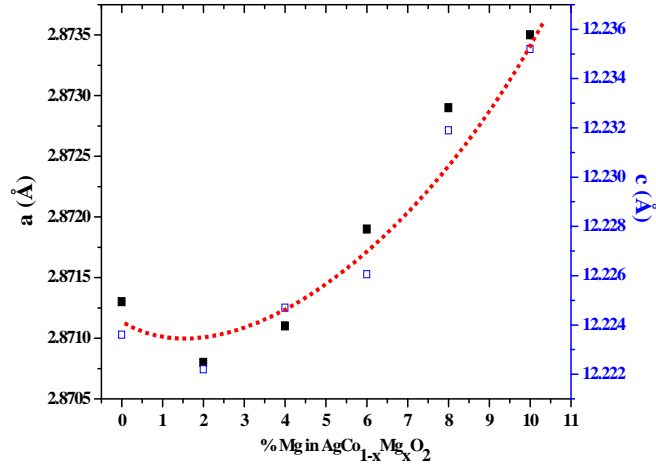
Figure 5. Variation of lattice parameter a and c as a function of Mg content in $D2-AgCo_{1-x}Mg_xO_2$. The dotted line is guide for the eye.

The 0th and 3rd order Mott's plot ($\sigma = A \cdot exp[(T_0/T)^{1/1+n}]$ with n=0 and 3) shown in **Figure 6** evidence a behavior similar to the pristine one with the appearance of two different regimes in the first case and a good correlation over the full range in the second case. The high temperature activation energies for n=0 estimated from the fits are given in **Table 1.**
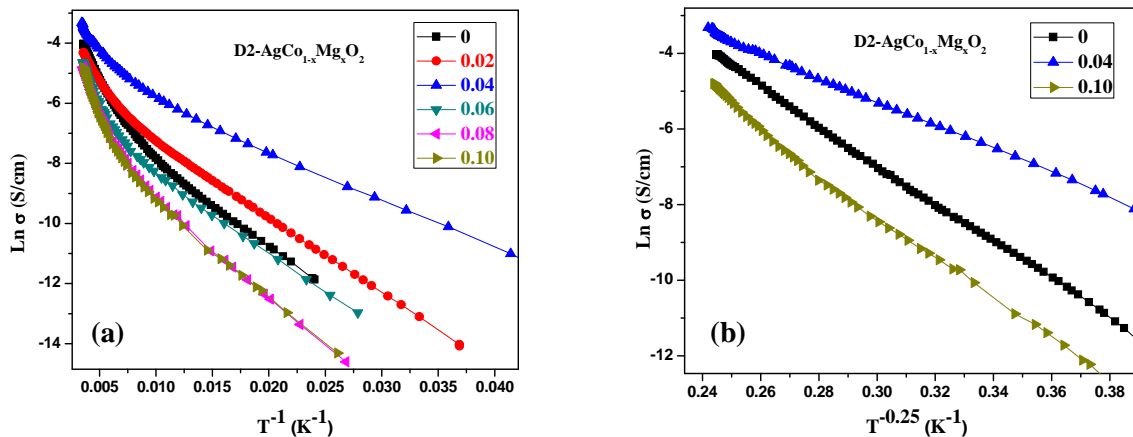
Figure 6. Temperature dependence of electrical conductivity fitted by (a) activated model (ln σ versus 1/T) and (b) three dimensional variable range hopping model (ln σ versus $1/T^{0.25}$).

They offer the same trend than the c/a ratio highlighting a minimum in the activation at *ca* 4%. Such common trend suggests that the high temperature regime could actually be

reasonably described with a standard Arrhenius law though the uncertainty on the actual values for the activation energy is here probably high due to the law compacity of the samples.

Mg content (%)	σ (S/cm)	α (μV/K)	E_a (meV)
0	0.0176	218	157. 2
2	0.013	187	113.3
4	0.03	228	87.2
6	0.0086	245	178.3
8	0.0078	241	197.3
10	0.0075	269	205.8

Table 1. Data of electrical conductivity (σ) and Seebeck coefficient (α) at 277 K and calculated activation energies (E_a) using Arrhenius plot for D2-AgCo$_{1-x}$Mg$_x$O$_2$ ($0 \leq x \leq 0.10$).

The thermopower data evidence a p-type conduction for all the samples (**Figure 7a**). The increase with temperature from zero also suggests a hopping mechanism for the transport. The 2% curve is the lowest one while the 4% curve display a specific behavior following first the trend of the other high substitution rate curves and then falling down on the pristine curve from *ca* 230 K. This specific behavior also manifests itself in the power factor which is maximum at 4% substitution (**Figure 7b**).
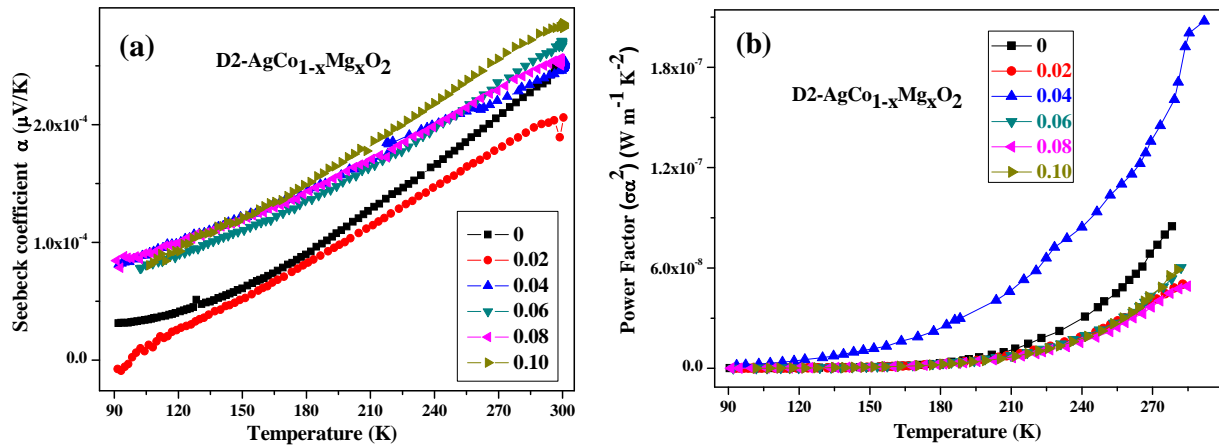
Figure 7. Temperature dependence of the thermoelectric power (a); and thermoelectric power factor (b) in the series D2-AgCo$_{1-x}$Mg$_x$O$_2$ ($0 \leq x \leq 0.10$).

The differences in the valence states and ionic radii of the dopants dominate the electrical conductivity, and hence affect the thermoelectric power factor. The conductivity of Mg-doped AgCoO$_2$ samples until 4% is higher than that of the un-doped sample and especially the increase in the conductivity is due to decrease of activation energy. Nevertheless, the conductivity

decreases when the doping concentration is further increased up to 10%, which might be ascribed to increase in the overlap of Co 3d and O 2p orbital which reflects from the increase of activation energy for Mg content higher than 4% and disorder introduced by the excess Mg atoms in the $AgCoO_2$ lattice. The overall increase in the thermoelectric power was compensated by decrease in the electrical conductivity.

III.3.5. D2-AgCo$_{1-x}$Mn$_x$O$_2$: Thermoelectric and magnetic properties

The structure is the same than in the pristine case and only the cell parameters slightly evolve as shown in **Figure 8** and **Table 2**.
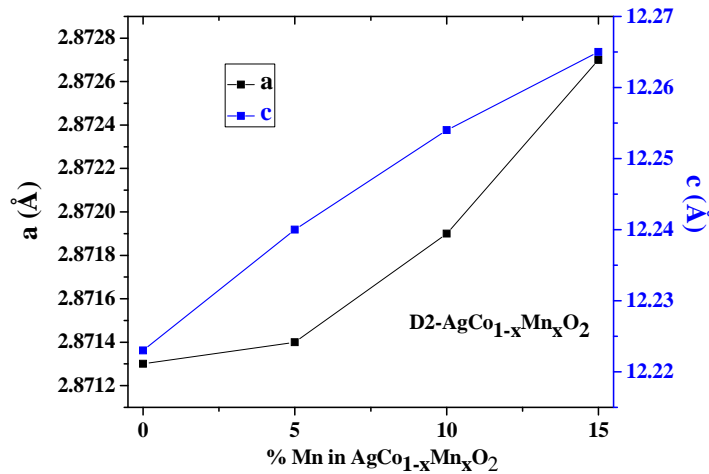
Figure 8. Variation of the lattice parameters of D2-AgCo$_{1-x}$Mn$_x$O$_2$ samples as a function of Mn content.

The electrical resistivity of all samples (**Figure 9a**) rapidly increases with temperature and Mn substitution. The low temperature data obey a third order Mott's law, *i.e.* a 3D variable-range-hopping mechanism, while at high temperature, in the 200-300 K range, the data can be modeled with a standard Arrhenius law. The activation energies are shown in **Figure 9b** together with the c/a ratio; the similar behavior suggests that the evolution of the conductivity with Mn substitution may not only be related to impurity scattering effects but also to the change in the structure. For each composition, the Co-O distance (d) and the angle θ between the 3-axis and the pseudo 4-axis calculated from the cells parameters ($a = 2d.sin(\theta).cos(30)$ and $c/2 = 2d.cos(\theta) + d_{O-Ag-O}$) assuming a constant interlayer thickness are given in Table 2. They show that while the Mn content increases, d nearly linearly increases, thus reducing the d-p

overlap and increasing localization; meanwhile, the trigonal distortion decreases (the ideal octahedral angle in O_h is $\theta_h = arccos(3^{-1/2}) \approx 54°7$). Surprisingly, the extrapolation to 100% substitution ("AgMnO$_2$") leads to d=1.974Å which in an ionic approach nearly perfectly matches with the Mn-O distance for $Mn_{LS}^{3+} - O^{2-}$ (=0.58+1.40); such result would contrast with the one of Mn-substituted Na$_x$CoO$_2$ where Mn^{3+} is reported in high spin state [16].
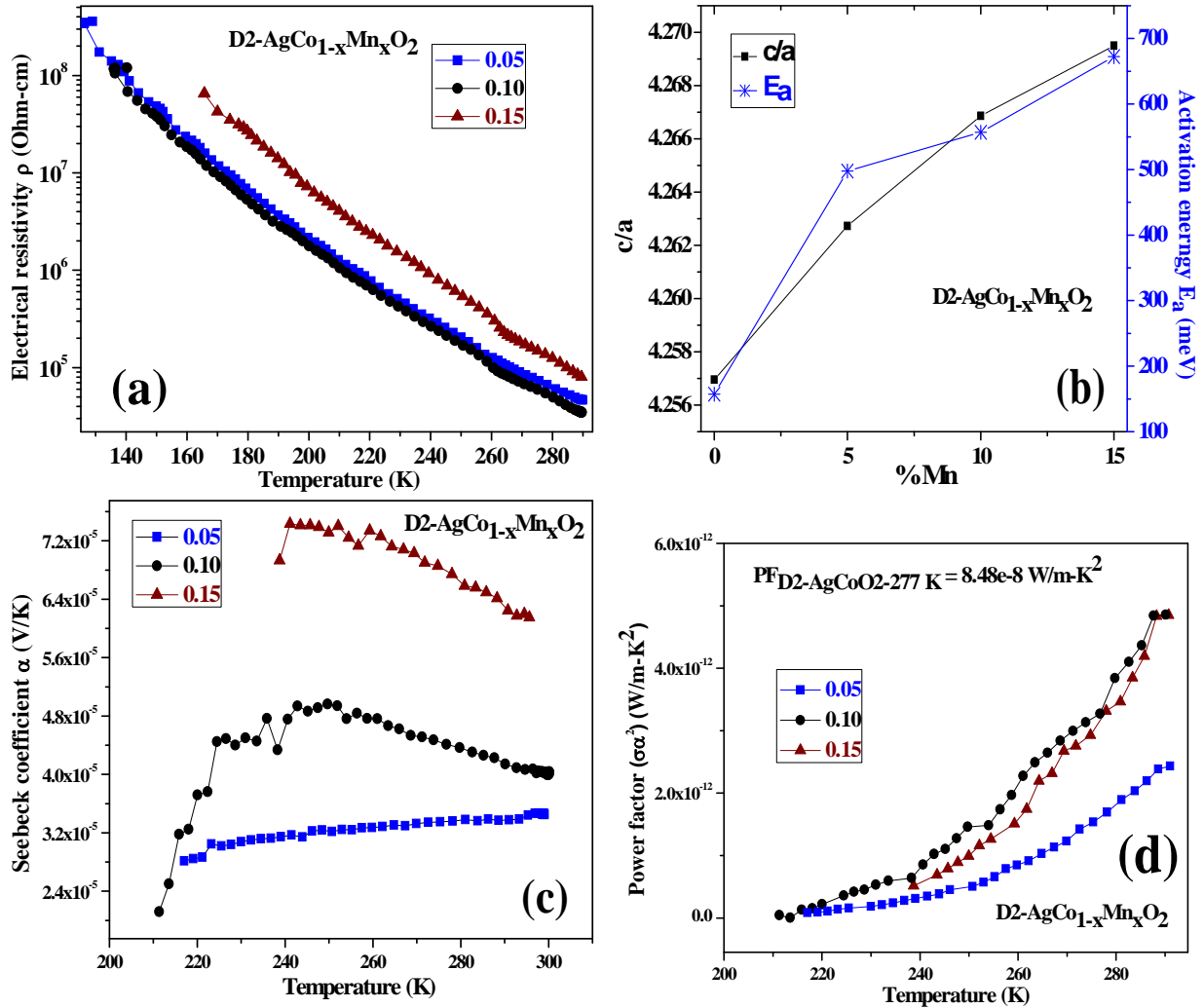
Figure 9. Temperature dependence of (a) electrical resistivity; (b) composition dependence of c/a ratio and E$_a$; (c) Temperature dependence of Seebeck coefficient (c) and thermoelectric power factor (d) for the D2-AgCo$_{1-x}$Mn$_x$O$_2$ (0≤x≤0.15) samples.

The Seebeck coefficient is positive for all D2-AgCo$_{1-x}$Mn$_x$O$_2$ (0≤x≤0.15) samples and initially decreases with Mn substitution and then increases as the Mn content increases (**Figure 9c**). As the resistivity offers a quite contrasted trend, the whole results can be understood on the basis of low mobility carriers: the presence of Mn substituent most probably enhances the hole

density as expected however these carrier might have a low mobility what results in a higher resistivity. An estimation of the carriers' activation energy for the 10% and 15 % substituted samples in the high temperature region actually gives 14 meV and 26 meV respectively that are indeed much lower than the activation energy, which includes the mobility component, obtained from the resistivity data. **Figure 9d** shows the variation of thermoelectric power factor for the D2-AgCo$_{1-x}$Mn$_x$O$_2$ (0≤x≤0.15) samples.

% Mn	a (Å)	c (Å)	E_a (meV)	d(Co-O) (Å)	θ	C	θ$_p$ (K)
0	2.8713	12.223	157. 2	1.933	59.03	0.0002	-171
5	2.8714	12.240	497.8	1.936	58.93	0.098	-5
10	2.8719	12.254	556.9	1.938	58.84	0.187	-3
15	2.8727	12.265	672.6	1.939	58.78	0.238	17

Table 2. Variation of lattice parameters (a and c) and activation energy (E_a) (between 200-300 K) for D2-AgCo$_{1-x}$Mn$_x$O$_2$ (0≤x≤0.15). The Co-O distance and the angle θ between the 3-axis and the pseudo 4-axis are calculated from the cells parameters and assuming a constant thickness of the interlayer (4.122 Å). The two last columns contain the values of the Curie constant and Weiss temperature.

The magnetic susceptibility as a function of temperature were measured on the D2-AgCo$_{1-x}$Mn$_x$O$_2$ samples with x = 0.05, 0.10 and 0.15 under a magnetic field of 1000 Oe. The linear plots of the inverse molar magnetic susceptibility 1/χ-χ$_0$ as a function of temperature are shown in **Figure 10** and the refined values for a Curie-Weiss model are given in Table 2. The Curie constant regularly increases with the Mn content. Setting for Mn^{3+} a low spin state (LS; S=1 for a t$_{2g}$ ground state or a regular e$_g$ ground state on trigonal compression; C=1) as suggested from the structural results is not sufficient to account for the observed value. Electron Spin Resonance (EPR) experiments (not shown) actually revealed the presence of extra paramagnetic centers centered at g=g$_e$ characteristic of LS d^{3,5} ions, *i.e.* as far as we are concerned Mn^{4+} or Co^{4+} ions. Their presence can be explained on the basis of non-stoichiometry; this was confirmed with ICP measurements that evidenced a depletion of the silver layer as the Mn content increases. In addition, for the highest substitution rate (15%), a clear anomaly is visible on the magnetic data; our EPR experiments actually suggest a charge transfer from Co^{4+} at low temperature to Mn^{4+} at high temperature. Finally, the evolution of the Weiss temperature can easily be interpreted on the basis of interaction weakening along c direction. Indeed, it is known

that the correlations are AFM in c direction while they are FM in (ab) plane [16]; as the c parameter increases, the AFM interactions decrease and only the FM ones survive (**Table 2**).
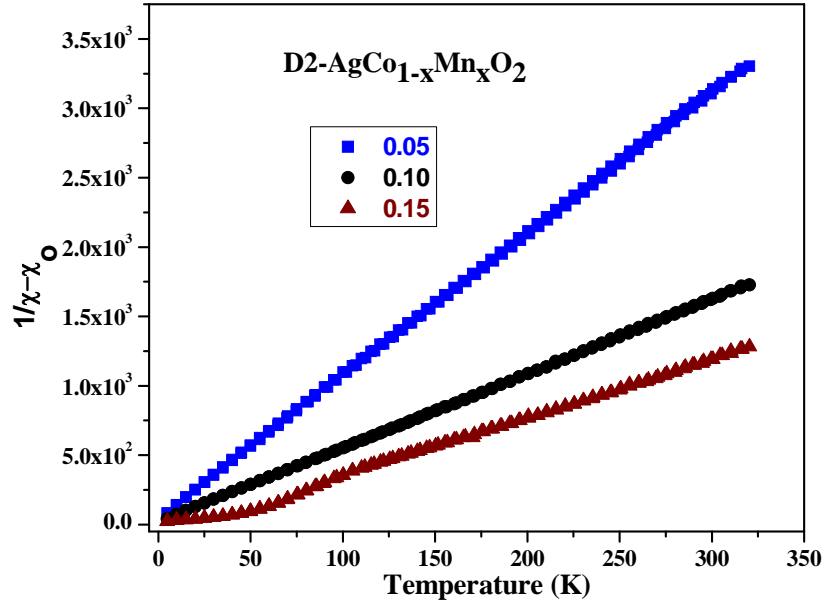
Figure 10. Temperature dependence of the inverse susceptibility of D2-AgCo$_{1-x}$Mn$_x$O$_2$ ($0 \leq x \leq 0.15$).

III.4. Conclusions

The structural, electronic transport and susceptibility studies show that thermoelectric properties at low temperatures are very sensitive to the structure details even though the changes can be very small depending on the substituent. The expansion in the lattice parameters with substitutions generally increases the charge localization and introduces strong disorder in the system. The p-type nature of the charge carriers is unaffected in the pure, Mg and Mn substituted cobalt double oxides. The thermoelectric performances can be slightly improved with substitution however the improvement remains small in the silver based compounds.

III.5. References

[1] I. Terasaki, Y. Sasago, K. Uchinokura, Phys. Rev. B 56, 12685 (1997)

[2] H. Kishan, V.P.S. Awana, M.A. Ansari, A. Gupta, R.B. Saxena, J. Appl. Phys. 97, 10A904 (2005)

[3] W.L. Roth, J. Phys. Chem. Solids 25, 1 (1964)

[4] B. C. Sales, R. Jin, K. A. Affholter, P. Khalifah, G. M. Veith, and D. Mandrus, Phys. Rev. B 70, 174419 (2004); T. Motohashi, R. Ueda, E. Naujalis, T. Tojo, I. Terasaki, T. Atake, M. Karppinen, and H. Yamauchi, Phys. Rev. B 67, 064406 (2003)

[5] J. T. Hertz, Q. Huang, T. McQueen, T. Klimczuk, J. W. G. Bos, L. Viciu, and R. J. Cava, Phys. Rev. B 77, 075119 (2008)

[6] C. Fouassier, G. Matejka, J.M. Reau and P. Hagenmuller, J. Solid State Chem. 6 532 (1973)

[7] W.Y. Zhang, H.C. Yu, Y.G. Zhao, X.P. Zhang, Y.G. Shi, Z.H. Cheng, J.Q. Li, J. Phys.: Condens. Matter 16 , 4935 (2004)

[8] M. Pollet, J.P. Doumerc, E. Guilmeau, J.F. Fagnard, R. Cloots, J. App. Phys. 101, 083708 (2007)

[9] R. D. Shannon, Acta Crystallogr. A 32, 751 (1976)

[10] J. Tate, M.K, Jayaraj, A.D. Draeseke, T. Ulbrich, A.W. Sleight, K.A. Vanaja, R. Nagarajan, J.F. Wager, R.L. Hoffman, Thin Solid Films 411, 119 (2002)

[11] D. B. Rogers, R. D. Shannon, C. T. Prewitt, J. L. Gillson, Inorganic Chemistry, 10, 1971 723

[12] A. Buljan, P. Alemany, E. Ruiz, J. Phys. Chem. B 103, 8060 (1999)

[13] J. Tate, H.L. Ju, J.C. Moon, A. Zakutayev, A.P. Richard, J. Russell, and D.H. McIntyre, Phys. Rev. 80, 165206 (2009)

[14] N.F. Mott, E.A. Davis, Electronic process in non-crystalline materials; Clarendon Press: Oxford (1979)

[15] P. Cox, Transition metal oxides: an introduction to their electronic structure and properties; Clarendon Press: Oxford (1995)

[16] L.B. Luo, Y.G. Zhao, G. M. Zhang, S. M. Guo, L. Cui, J.L. Luo, Phys. Rev. B 73, 245113 (2006)

Chapter IV:
Introduction to Vanadium oxides

This chapter first presents a brief introduction to the existing phases in the vanadium/oxygen system based upon reported solid state phase diagrams. Then I will give a more detailed introduction to vanadium dioxide (VO_2) and its phase transition, including some of the latest reports about the nature of the several transitions - metal-insulator transition and structural phase transitions - in which whether electron-electron correlations or structural instabilities dominates during the transitions. I will give some brief review about the effect of the substituents used till now to alter VO_2 phase transition temperature. In the last part, I will summarize the hydrothermal synthesis and reported properties of metastable VO_2 (A) and VO_2 (B) polymorphs.

Contents

IV.1. Introduction

Investigation of strongly correlated electron systems, compounds whose properties are dominated by strong electron-electron correlations is one of the most challenging branches in solid state physics. This kind of correlations arises when the on-site electron-electron repulsion (U) is much higher than the energies associated with the overlap of atomic orbitals belonging to different atoms. In a solid, these energies are characterized by the width (W) of the energy band under consideration. A large U/W ratio is expected in systems involving well-localized electrons like the 3d, 4f and 5f electrons of transition metals, rare earths and actinides respectively [1]. The best example to understand the importance of electron-electron correlations in influencing the basic properties of a compound is CoO. In the independent-electron approximation, CoO is expected to be metallic with an odd number of electrons per unit cell and a partially filled d band. But in reality, as a consequence of strong correlations which are suppressing charge fluctuations CoO is a rather good insulator at all temperatures with an optical gap of about 6 eV [2]. More in general, strong electron-electron correlations can give rise to a large variety of interesting physical phenomena, like the most famous high-temperature superconductivity, heavy-fermion and Kondo-insulating behaviours, spin-Peierls phase transition, spin-gap phenomena, colossal magnetoresistance, metal insulator transitions etc.

Vanadium oxides comprise compounds with several formal vanadium valence states from two in VO, three in V_2O_3, four in VO_2 to five in V_2O_5. In addition to these, the vanadium-oxygen system is complex due to existence of wide range of ordered and disordered defect structures. Amongst the latter are the so-called Magneli phases and Wadsley phases, defined by the general stoichiometric formula V_nO_{2n-1} and $V_{2n}O_{5n-2}$ respectively. Magneli kind of homologous series has been reported for the first time by A. Magneli in the case of the molybdenum oxides [3]. Today Magneli series are known for the vanadium, titanium, niobium, and tungsten oxides. The synthesis of stoichiometric VO_2 is hampered by the existence of these several stable vanadium oxide phases; one needs to work out an elaborate synthesis protocol to ensure the formation of pure VO_2 and to avoid other undesirable vanadium oxide phases. **Figure 1** shows the phase diagram of VO_x system.

Figure 1. VO_x phase diagram [4].

Vanadium oxides have largely attracted scientific attention due to their structural phase transitions and metal to insulator transitions. Some of the potential applications includes cathode material in lithium batteries [5,6,7], intelligent window coatings [8], Mott field-effect transistors [9,10], electrical-optical switching devices [11], chemical sensors or actuators [12,13,14], bolometers [15], memristors [16], tunable frequency metamaterials [17], data storage [18], low-frequency two- and three-terminal electrical switches [19,20,21], RF-microwave switches, tunable filters [22,23,24,25], power limiters [26], THz and nano resonators [27] and optical components [28,29] etc. Out of the several V-O phases, VO_2 exists in multiform polymorphic stable and metastable forms. It is reported that VO_2 has at least seven polymorphs (other than hydrate phases): rutile VO_2 (R), monoclinic VO_2 (M1) [30] and triclinic VO_2 (T) [31] are close in structure, and there are four other VO_2 phases designated as tetragonal VO_2 (A) [32], monoclinic VO_2 (B) [33], paramontroseite VO_2 [34], and VO_2 with a new body-centred cubic structure [35]. Here we will only focus on M1, A and B polymorphs.

IV.2. VO_2 (M1)

Vanadium dioxide (VO_2 (M1)) holds the attention of researchers for half a century since 1959 when F.J. Morin first observed its remarkable first order metal-to-insulator transition (MIT) at T_t= 340 K [30]. At or near T_t, VO_2 also undergoes a structural transformation of the crystal lattice, from a tetragonal/rutile (R) metallic phase at high-temperature to a monoclinic (M1) insulator phase at low-temperature. The MIT is accompanied by substantial change (nearly 5 orders of magnitude) in electrical conductivity and optical transmittance, which can span at proximity to room temperature (**Figure 2**).

Figure 2. Variation of (a) electrical resistivity and (b) optical reflection in VO_2 [36].

This metal to insulator transition can be triggered as a function of temperature [30], strain [37], electric field [38], particle size [39], stoichiometry [40], doping [40] or optical excitation [41]. The metal-insulator transition in VO_2 attained special recognition in the field of condensed matter physics as one of the best examples of the orbital - lattice couplings and instabilities mediated by strong electronic correlations. There are several reasons for the overwhelming interest in this seemingly simple binary oxide. There are some structural and compositionally more complex transition metal oxide compounds such as cuprates and manganites, which also exhibit analogous aspects of electron-correlation, structural inhomogeneity with composition variation similar to vanadium dioxide [42]. Consequently, VO_2 can serves as somewhat model system to understand and separate the distinctive roles of electron-phonon and electron-electron interactions, which in turn manifests electronic and magnetic transport properties in high-T_c superconductors, colossal magnetoresistance materials etc.

IV.2.1. Crystal structure and band diagram

Figure 3 shows the structures of VO_2 in both metallic (rutile) and insulator states (monoclinic) [43].
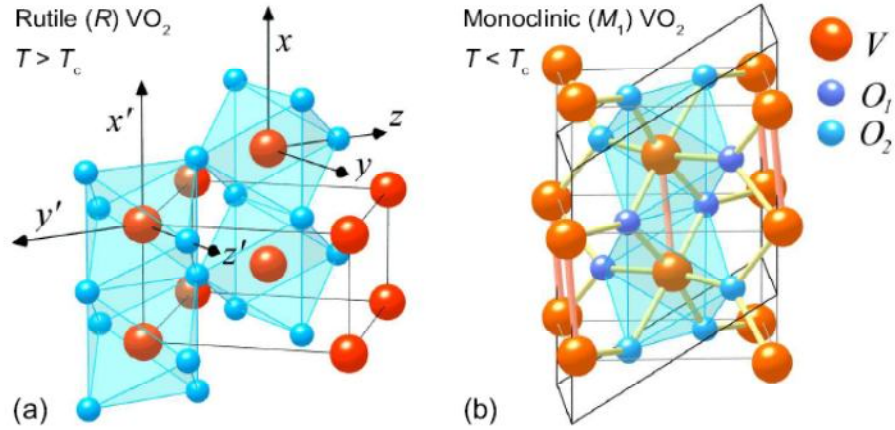
Figure 3. (a) Rutile VO_2 lattice structure above the structural phase transition temperature (b) Monoclinic VO2-M1 lattice structure of the low temperature insulating phase. (Large red and orange circles represent V ions, small blue circles represent O ions).

The rutile structure is based on a simple tetragonal lattice with space group $P4_2/mnm$ where vanadium cations form a body-centered-tetragonal array with two vanadium atoms per unit cell; each is surrounded by a distorted octahedron of oxygen atoms. These octahedra share an edge along the c-direction and share corners in the perpendicular direction. The closest V-V distance is 2.85 Å in chains along the c-direction.

The insulating monoclinic phase ($P2_1/c$) is characterized by the pairing of vanadium ions along the c-axis and the alternation of short and long metal-metal distances resulting in the doubling of the unit-cell size; at the same time, each vanadium ″pair″ is tilted with respect to the c-axis and the vanadium atoms are no longer at the centre of the distorted octahedron. The two different V-V distances occur along the monoclinic a-axis: 2.619 Å and 3.164 Å. Goodenough presented a schematic energy band diagram for both the metallic and the insulating phases [44]. Using electrostatic considerations for the effective ionic charges, he placed the oxygen 2p levels well below the vanadium 3d states.

In the metallic phase, the fivefold degenerated 'd' levels of the V^{4+} ion ($3d^1$) are subject to octahedral crystal field splitting into doubly degenerate e_g levels and triply degenerate t_{2g} levels. The e_g orbitals are strongly hybridized with the O 2p orbitals and have a large bandwidth. The $3d_{3z^2-r^2}$ and $3d_{x^2-y^2}$ orbitals point towards the ligands and form bonding σ and anti-bonding σ^* bands with the O 2p orbitals. The t_{2g} levels are further split into a d_{xy} singlet and a d_{xz}, d_{yz} doublet by the tetragonal perturbation. Here the singlet gives rise to a band d_{ll}, whereas the doublet mixes with the O 2p orbital forming a wider π^* band. Since the π^* orbitals are more hybridized with the O 2p than the d_{ll} orbitals, the π^* bands have higher energies and a wider bandwidth. Thus the d_{ll} and π^* bands are situated right near the Fermi

level. Here d_{ll} orbitals are aligned along the rutile c-axis and are consequently of almost 1D character. On the other hand, the d_{ll} orbitals are rather nonbonding. Thus the d_{ll} and π^* bands overlap at the Fermi level as shown in the schematic diagram in **Figure 4**.
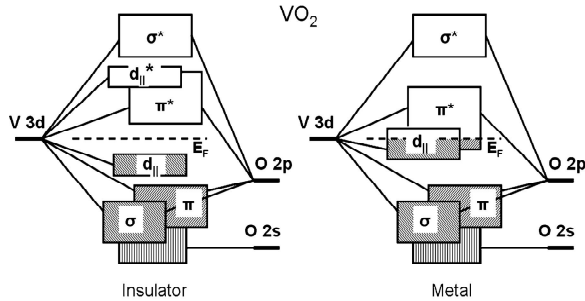
Figure 4. Band level diagram for VO$_2$(M1) [45].
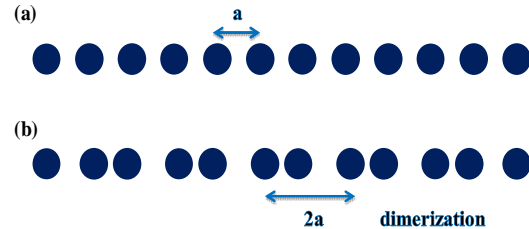
Figure 5. Representation of a 1D system (a) before and (b) after the Peierls transition.

In the insulating low temperature monoclinic phase, the dimerization of the V atoms, *i.e.* their pairing and tilting with respect to the 'c'-axis as a part of the monoclinic distortion, causes the splitting of the d_{ll} band into bonding d_{ll} and anti-bonding d_{ll}. Because of the change in the V-O hybridization, the energy of the more hybridized π^* band rises above the Fermi level and becomes empty. As a result, a band gap opens between the top of d_{ll} and the bottom of π^*.

IV.2.2. Nature of phase transition: Peierls or Mott, to Mott assisted Peierls transition

In fact, it is the intricate interplay between electronic and structural degrees of freedom between carrier localization due to electron-electron repulsion (Mott-Hubbard correlation) and unit-cell doubling due to lattice instability (Peierls distortion) that has been at the heart of an enduring debate about the precise cause-and-effect link in the mechanism of the VO$_2$ transition. Till now, research was mainly focused on understanding the mechanism responsible for the structural phase transition between the monoclinic insulating phase and the tetragonal metal phase and its effect on the MIT [46].

IV.2.2.1 Peierls Insulators

In a 1D chain of electrons, a Peierls transition can cause the system to become insulating, due to distortion in the crystal lattice. This kind of transition takes place in a system of equally spaced atoms with one unpaired spin each. As two ions come closer they

dimerize. The energy cost to shift the atoms from their original positions is overcome by an energy gain associated with pairing the electrons. This distortion produces the energy gap and the resulting insulating behaviour (**Figure 5**). It is worth noting that speculations also exist on the possibility of dimerization in s=1/2 chains.

IV.2.2.2. Mott Insulators

In this kind of insulators the electron's mobility is limited by the Coulomb repulsion that would ensue from the hop of one electron to an already occupied neighbouring site and thus the band gap is created. Indeed, if an electron hops to an orbital that already holds one electron, a considerable energy $E_g = U - 2zt$ is needed to overcome the resulting coulomb repulsion (U) where E_g stands for the energy gap between the bands, z is the number of nearest neighbours and t is the transfer integral or the energy of the hopping electron. Such correlations result in localizing the electrons, leading to a Mott insulator.

IV.2.2.3. Theoretical perspective

In VO_2 (M1), vanadium ion is in d^1 configuration what allows the single electron to be shared by the $3d_{ll}$ and $3d_{\pi}$ bands. Because of their different widths and anisotropies ($3d_{ll}$ is highly anisotropic while $3d_{\pi}$ is more spherical), these two bands are expected to respond in a different way to electron-electron interactions (significant only for the narrow $3d_{ll}$ band) or to a lattice distortion. As discussed earlier, based on relatively simple crystal field theory considerations, Goodenough proposed a more rigorous molecular picture of this transition process [44]. According to Goodenough's phenomenological model, the lattice distortion (tilting) in the VO_2 (M1) phase raises the antibonding $3d_{ll}$ band above the Fermi level and leaves the $3d_{ll}$ band half filled. The controversial point here is that, whether the phase transition in VO_2 is due to the splitting of the $3d_{ll}$ band, which originates from V-V pairing along the rutile c-axis and unit-cell doubling (Peierls mechanism) [44,47], or from the opening of a correlation gap due to the presence of strong electron-electron correlations especially in the $3d_{ll}$ band (Mott mechanism) [48].

The Peierls-like influence of the lattice degrees of freedom on the VO_2 transition was supported by electronic structure calculations based on density functional theory within the local density approximation. Wentzcovitch et al. [49] used a variable cell-shape approach to allow for simultaneous relaxation of the atomic positions and the primitive translations. As a result, starting from different intermediate structures, they obtained the monoclinic M1 structure as the most stable one. The calculated lattice parameters for both cells were in good agreement with the experimental data. However, the calculations failed to yield the opening

of the M1-phase band gap. This result was attributed to the typical failure of the local density approximation to correctly reproduce measured optical band gaps.

Latter, from first principles electronic structure calculations, Eyert [43] also found semimetallic behaviour, with a band overlap of 0.1 eV rather than the observed optical bandgap. Since both types of 3d bands were found to be coupled by charge conservation rather than hybridization, the M1 phase was interpreted as arising from a Peierls-like instability of the $3d_{ll}$ bands but in an embedding reservoir of $3d_{ll}$ electrons.

Further, another band model was proposed by Paquet and Leroux-Hugon et al. They incorporated directly both the electron-electron interactions and the electron-lattice interactions on an equal basis [50]. Using experimentally derived parameters they concluded that, the metal-insulator transition is primarily driven by electron-electron correlations. However, these correlations would be strongly renormalized by the lattice distortion and the electrostatic interaction between the d_{ll} and the π^* electrons. Biermann et al. [51] calculated the electronic structures of tetragonal metallic phase and monoclinic semiconducting phase. They used a cluster extension of dynamical mean-field theory (C-DMFT) in combination with density functional theory within the local density approximation (DFT-LDA). They considered structural as well as correlation aspects at the same time by choosing the V-V dimers as the fundamental block of the calculation. In this case, they succeeded in correctly predicting the insulating nature of the M1 phase, with a band gap of 0.6 eV, in good agreement with experimental observations. They concluded that non local correlations effectively assist the Peierls-like transition.

IV.2.2.4. Experimental perspective

Several experimental techniques like optical spectroscopy and micro X-ray diffractions are used to probe the behaviour of the structural and electrical transition. Cavalleri et al. [52] showed the evidence of structurally driven metal to insulator transition in VO_2 (M1) using ultrafast pump-probe spectroscopy. They measured the transition time for changes in the optical reflectivity and transmission of VO_2 thin film in the range 15 fs -1.5 ps. Their observation indicates that an atomic rearrangement of the unit cell is necessary for the formation of the metallic phase of VO_2, which suggests a significant band-like (Peierls-like) character for the semiconducting phase. These observations do not rule out however the possibility of electronic correlations.

In 2005, Haverkort et al. [53] measured polarization-dependent X-ray absorption spectra (XAS) in the metal and insulating phases of single-crystal at the V L_2 and L_3 edges.
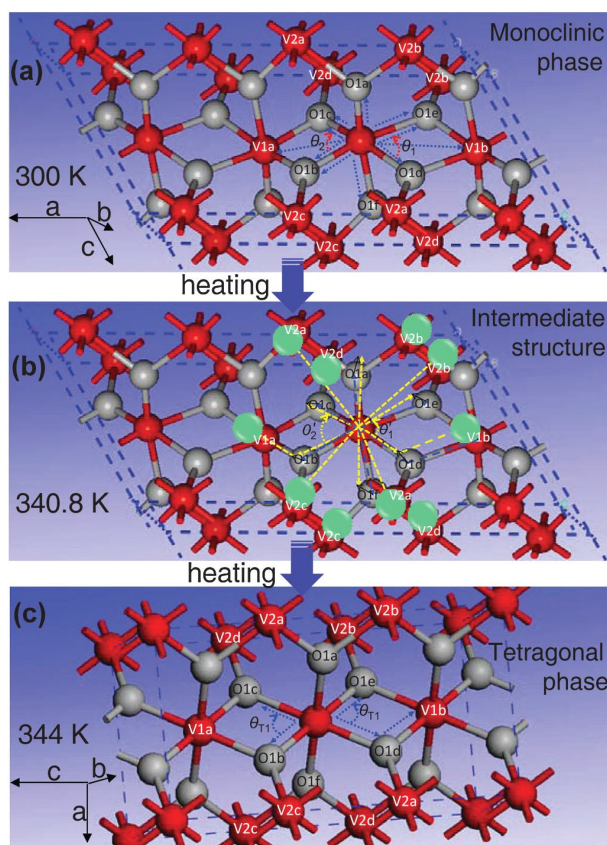
Figure 6. (a) The initial monoclinic phase, (b) the intermediate structure during the heating process, and (c) the final tetragonal phase. θ_{T1} in the tetragonal phase evolve to θ_1 and θ_2 angles in the monoclinic phase [54].

They noticed dramatic switching of the orbital occupation across the metal insulator transition, from isotropic $3d_{ll}$ in metallic phase to almost completely $3d_{ll}$ polarized in insulating phase. This evidences the key role of orbital and lattice in correlated motion of the electrons. According to this study, the phase transition is an orbital-assisted Mott-Peierls transition. Based on the temperature-dependent in situ X-ray absorption fine structure measurements and density-functional theory calculations, Tao Yao et al. [54] have revealed that the monoclinic-to-tetragonal phase transition of VO_2 (M1) near the critical temperature is characterized by a sharp decrease in the twisting angle of the nearest V–V coordination (**Figure 6**). They suggest that the metallic tetragonal VO_2 phase occurs through an intermediate monoclinic like structure with a large twist of V–V pairs and they conclude that the structural rearrangement is a key factor to narrow the insulating band gap.

Qazilbash et al. [55] measured the electromagnetic response of a VO_2 thin film using scattering scanning near-field infrared microscopy (s-SNIM) and far-field infrared spectroscopy, on a spatial scale of 20 nm. With temperature variation around insulator-to-metal transition they noticed the appearance of nanoscale metallic puddles in a narrow

temperature range. These nanoscale metallic puddles have completely different characteristics from the tetragonal metallic phase of VO_2 with an optical pseudogap in the electronic density of states, an enhancement of the low-frequency effective optical mass at T = 342 K compared to the tetragonal phase value at T = 360 K and a divergent temperature-dependence of the low-frequency effective optical mass in the vicinity of the insulator-to-metal transition.
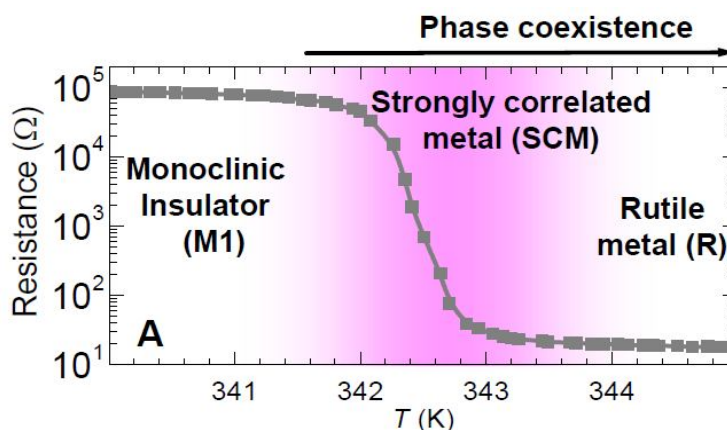
Figure 7. Resistance *vs* temperature for VO_2 showing the insulator-to-metal transition [55]. (The pink shaded area highlights the region of the phase diagram in which strong correlations with divergent quasiparticle mass and optical pseudogap exist)

From these observations, they concluded that the M1 phase should be classified as a Mott insulator with charge ordering. The temperature induced insulator-to-metal transition in VO_2 occurs from the monoclinic insulator to strongly correlated metal in the form of nanoscale puddles in the tetragonal metal phase (**Figure 7**). The precise lattice structure of the strongly correlated metal phase still remains unclear.

Using femto-second pump-probe and measuring the temperature dependence of both the resistance and X-ray diffraction, Kim et al. [56] proposed an entirely different picture of the phase transition. They argued that, the metal-insulator transition and structural transformation from rutile to monoclinic lattice occur separately at different temperatures. In this picture, there exists an intermediate metallic monoclinic phase between the MIT and the structural phase transition. The fact that there is no lattice transformation to rutile phase at the MIT excludes the Peierls model and the driving mechanism of the MIT is considered to be the Mott transition. The origin of the metallic monoclinic phase was explained with hole-driven MIT theory [57].

The physical mechanisms underlying metal insulator transition in VO_2 are not fully elucidated and it is still unclear whether the transition is driven by the crystalline phase transition (from monoclinic to the tetragonal phase) or by electron–electron correlations (pure

electronic Mott transition). Recent advances in theoretical calculations [51,58], optical spectroscopies [53,59], and nanoscale imaging techniques [55] are now providing an unprecedented level of detail with superb spatial and temporal resolution for piecing together the electronic and structural aspects of nature of this transition. Although recent reports apparently favour the combination of both mechanisms simultaneously, at the same time appearance of several new phases during the structural phase transition makes the situation more critical to give definite conclusions about the nature of the transition.

IV.2.3. Substitutions in VO$_2$:

IV.2.3.1. Mono-substitutions

One well-established way to modify the phase stabilities is to introduce substituents that either induce or hinder phase transformations by selective stabilization of one region of the phase diagram. In the case of vanadium dioxide, substitutions of the vanadium sublattice with other transition metals can strongly modify the phase-transition temperature and hysteresis. This was commonly used to shift the phase transition from higher temperature to room temperature. The central issue remains to understand the role of the substituting ion in the modification of the transition temperature through the several new freedom degrees it introduces: ionic radii, electronic structure. In addition to the ion nature, one also needs to care for the nature of the predominant electronic defects (electrons or holes) and donor-like defects caused by the oxygen deficiency. These factors essentially influence on the behaviour of VO$_2$ in its transition temperature, crystallographic distortions, conductivity jump [60].

Before detailing the known effects of individual substituents, some general remarks based upon pioneer works can be made. The effect of ionic radii and electronic structure of the substituting ion was first systematically studied by J.B. MacChesney et al. from Bell labs [61]. Series of vanadium dioxide single crystals containing low concentration impurity ions were prepared by thermal decomposition technique and the impurity ions were chosen in such a way that they will have different electronic structure as compared to V^{4+}. It was expected that these ions would produce a systematic change in the MIT. Contrary to expectations, no correlation with the electronic configuration of the substituent ions was identified. The conclusion of this study was, regardless of the origin of the phase transition, the effects of incorporation of impurity ions on the transition temperature are not readily explained by invoking changes in the band structure. Rather it appears that if the transition is of electronic origin, then the band structure giving rise to these transitions must be sensitive

to changes in the lattice produced by incorporation of impurity ions into VO_2 (M1) crystals. Three qualitative conclusions were anyway drawn from their observations relating the effect of impurities to the transition in conductivity: (1) The transition temperature is unaffected by the carrier concentration (2) significant changes in the transition temperature are produced only by high doping levels (3) ionic radii of those ions which cause an increase in transition temperature, are smaller than that of V^{4+} while all the ions that cause a decrease in the transition temperature are larger than V^{4+}, *i.e.* the direction of the change in transition temperature is simply correlated with the relative size of the substituting ion. Pierce and Goodenough [62] suggested however that the reason for increasing or decreasing the transition temperature of VO_2 (M1) by substitution is caused by the change in carrier densities. Later, Pordan et al. [63] studied the effect of Mo substitution on VO_2 (M1) phase transition and they also concluded that the electronic configuration of the doped ions does not affect the transition temperature but it has an influence on the magnitude of the transition. These early results illustrate the complexity of the debate.

Several substituents like W, Mo Nb, Al, Cr, Cu, Ti, Mn, Fe, Au, Eu, Mg, Ge, Co, Ni, Ta, Sn, Mg were used in vanadium sublattice as well as fluorine in the oxigen sublattice to modify the transition temperature and to study their impact on the structural and electronic phase diagrams [64]. Out of these doping elements W, Mo, Nb, Fe, Co, Ni, Au, Mg and Ta all decrease the transition temperature on increasing the substitution rate [65]. On the other hand, Cr, Ti, Ge and Sn are increasing the transition temperature on increasing the substitution rate [66]. In the case of Al substitution, contradictory results are reported [61,67]. In the case of Cu substitution, a non-linear variation of the transition temperature was reported [68]. It was found that, at first, the transition temperature of Cu^{2+} ion doped VO_2 (M1) decreased with the increase of Cu^{2+} concentration and T_t reached its lowest point in $V_{0.98}Cu_{0.02}O_2$ composition but with further increase in Cu^{2+} content T_t increased. In addition, and as compared to other substitutions, Al, Fe, Cr and Ti substitution leads to several new phases like VO_2 (T) (triclinic), VO_2 (M2) (monoclinic) and VO_2 (M3) (monoclinic) at room temperature. **Figure 8** represents some of the structural phase diagrams reported in literature concerning Al, Fe, Cr and Ti substitutions [69].
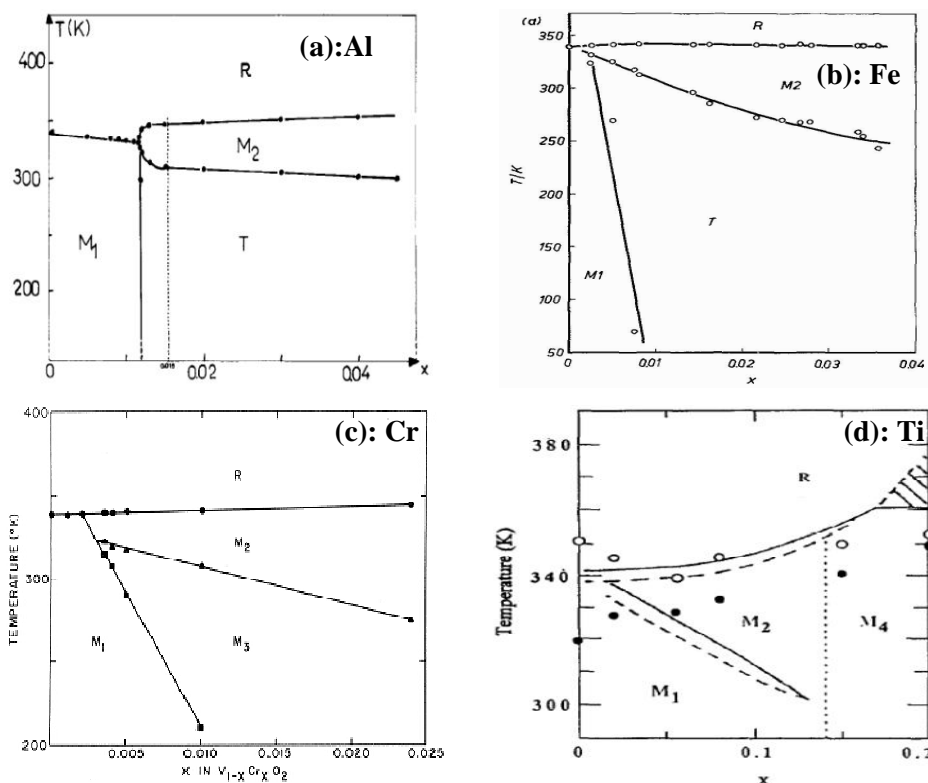
Figure 8. Phase diagrams of (a) $V_{1-x}Al_xO_2$; (b) $V_{1-x}Fe_xO_2$; (c) $V_{1-x}Cr_xO_2$ and (d) $V_{1-x}Ti_xO_2$ [69].

Nb^{4+} (d^1) and Mo^{4+} (d^2) ions are very similar in size, however their solid solutions with VO_2 show dramatic difference in behaviour [70] what could reflect an effect of electron doping. Such assumption is suggested by the different variation of the lattice parameters in the solid solutions $V_{1-x}Nb_xO_2$ and $V_{1-x}Mo_xO_2$ and the composition dependence of the c/a ratios for $V_{1-x}Mo_xO_2$ and $V_{1-x}Nb_xO_2$ as shown in **Figure 9**. In both cases, the a parameter grows the same but the behaviour along the c-axis is different: in Nb series, there are two linear regimes with first an increase of c up to *ca* 6% for 50% substitution and then a decrease of about 2% for the full Nb compound; in the Mo series, up to 50% substitution only, two near linear regimes were also observed but the inversion is at *ca* 20% substitution and the maximum change is less than 3.5 %. Although the ionic radii of the substituent in both series are similar, their influence on structural properties is different and it can reasonably be assumed that this can originate from the electron doping in the Mo series.
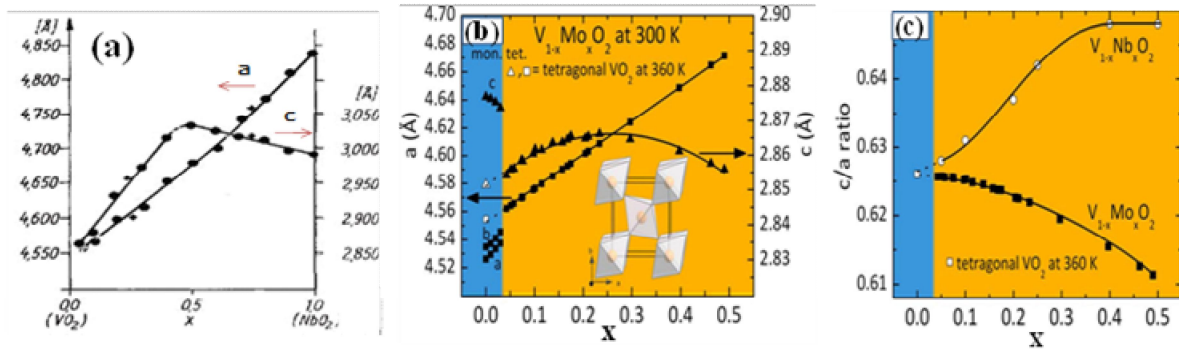
Figure 9. Variation of lattice parameters in (a) $V_{1-x}Nb_xO_2$ (b) $V_{1-x}Mo_xO_2$ and (c) composition dependence of the c/a ratios for $V_{1-x}Mo_xO_2$ and $V_{1-x}Nb_xO_2$ [70].

IV.2.3.2. Co-substitutions

It is possible for substituents with high oxidation degree to reduce T_t from 340 K to room temperature [71]. W and Mo are the most efficient substituting ions with lowering rate as high as 27 K/at% for W and 15 K/at% for Mo [72]. As the dependence of the phase transition temperature on a single substituent is linear [73], it is simply necessary to use the proper amount of substituent to decrease T_t to the temperature desired for applications. Unwisely, this generally requires a high level doping and the phase transition characteristics are adversely affected by the increase of doping concentration [74]. For example, the optical transition in visible and infrared range in semiconductor state strongly decreases, and the optical and electrical switching performances between phase transition largely declines what is attributed to the increase of the carrier density in the semiconductor state induced by the substituting ions [75]. In some other cases, with higher substitution rates, deterioration due to larger disorder is observed in the electrical and optical properties such as a decrease of optical transmittance. In such case, the problem was proposed to be solved using a double substitution in which one substitution ion would decrease the transition temperature while another one would enhance the optical transmittance. Several attempts were made in this direction by using several substituents' combinations like W-Ti, W-Ta, W-Si, W-F, W-Mo and Mn-F [76]. It is worth noting however that very few studies were done to understand the behaviour of the phase transition properties of VO_2 codetermined by two different substituents. Counterexamples are in the works of (i) Burkhardt et al. [77] who investigated the thermochromic properties of W/F co-substituted VO_2 and found that the two substituents affect the transition temperature almost independently and (ii) Soltani et al. [78] and Takahashi et al. [79] who studied the thermochromic performance of W/Ti co-doped VO_2 and observed an interaction between the substituents with the enhancement of the transition temperature lowering rate and the almost quenching of the hysteresis.

The existence of contradictory reports, of additional intermediates depending on the substituent, of impacts beyond the size effects, of interacting defects, etc highlights the complexity of the problem. In addition several other effects are still there and till now they are fully ignored like, the effect of non-stoichiometry or simply eluded like the accurate determination of the valence of the substituting ion.

IV.3. Synthetic techniques: Focus on hydrothermal process

Numerous synthetic procedures exist to prepare the pristine and substituted VO_2 polymorphs in bulk, film and nanostructure form. Some of these includes solid state reaction, vapour transport [80], sol-gel [81], chemical vapor deposition [82], pulsed laser ablation [83], magnetron sputtering [84], template-assisted synthesis [85], thermolysis [86], solution-based synthesis [87], controlled oxidation and sputtering [88], ion implantation [89], hydrothermal synthesis [90] etc.

Among these, solution-based hydrothermal synthesis is of low cost and suitable for large-scale synthesis in which some rigid experimental conditions such as high temperature and special equipments are not necessary. In general, the main strategy to prepare VO_2 under hydrothermal conditions is to reduce stable high oxidation degree of vanadium oxides using reductants. Hydrothermal process received much attention due to its selective nature and the number of variable parameters during reaction process.
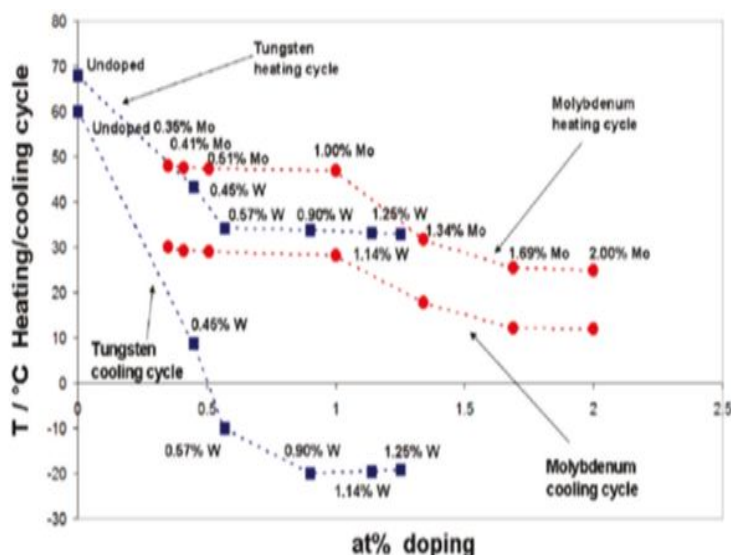
Figure 10. Transition temperature evolution in $V_{1-x}M_xO_2$ nanobelts [91].

This method not only offers an advantage for synthesising a selected compound, but also to control the morphologies of the products. For example, by using different reductants like formic acid, oxalic acid, ethylene glycol, borohydride, butanol and surfactants, one can modify the morphology as well as the produced phases [92]. The substantial control over added substituents, particle dimensions and morphology makes hydrothermal process the most popular synthetic methodology for the preparation of vanadium dioxides. The new objects such grown often offer distinctive features. For example, the M-I transition temperature of 340 K in bulk VO_2 decreases linearly with W and Mo substitution while for lower dimension objects grown with hydrothermal method, the behaviour notably changes as illustrated in **Figure 10**: the abrupt initial decrease of the transition temperature below 1% concentrations is replaced with a nearly constant behaviour for higher substitution rate [91].

IV.4. VO$_2$ (A)
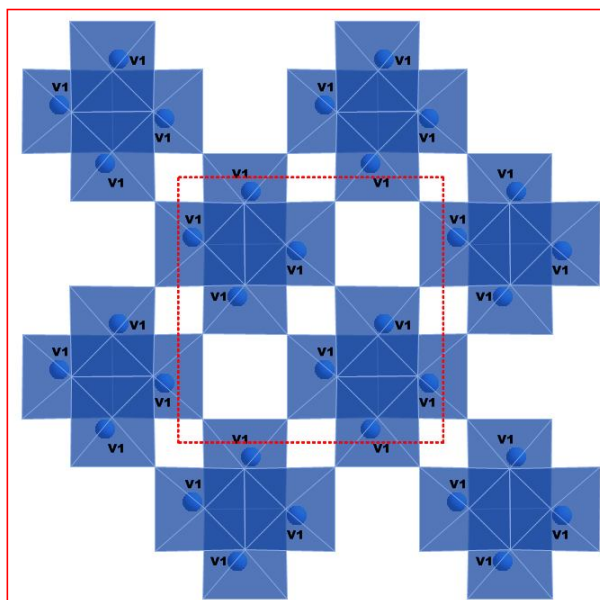
Figure 11. Structure of VO_2 (A) viewed along [001].

In 1977, VO_2 (A) was first reported by Théobald [93] in his extensive hydrothermal studies on VO_2–$VO_{2.5}$–H_2O system. This phase appeared as an intermediate in the transformation of VO_2 (B) to VO_2 (R). VO_2 (A) was obtained at reaction temperatures between 220 and 330 °C from a suspension of V_2O_3 and V_2O_5. The crystal structure of VO_2 (A) was not clarified until 1998 which set a new starting point for the research on this compound. In particular, Oka et al. [94], Yao et al. [95] prepared VO_2 (A) by hydrothermal method using $VO(OH)_2$ and $VOCl_2$ as the precursors and they found that VO_2 (A) undergoes a phase transition at 435 K (from P4/ncc to I4/m) [96]. Its structure consists in a three-

dimensional framework of VO_6 edge-shared dimmers that stack perpendicularly along the c-direction to form characteristic crosses (**Figure 11**). The resulting cross-shaped chains are linked together by the octahedra corners. At high temperature, the through edge V-V distances are uniform but on decreasing the temperature two sets of distances appear, either short or long as shown in **Figure 12.**
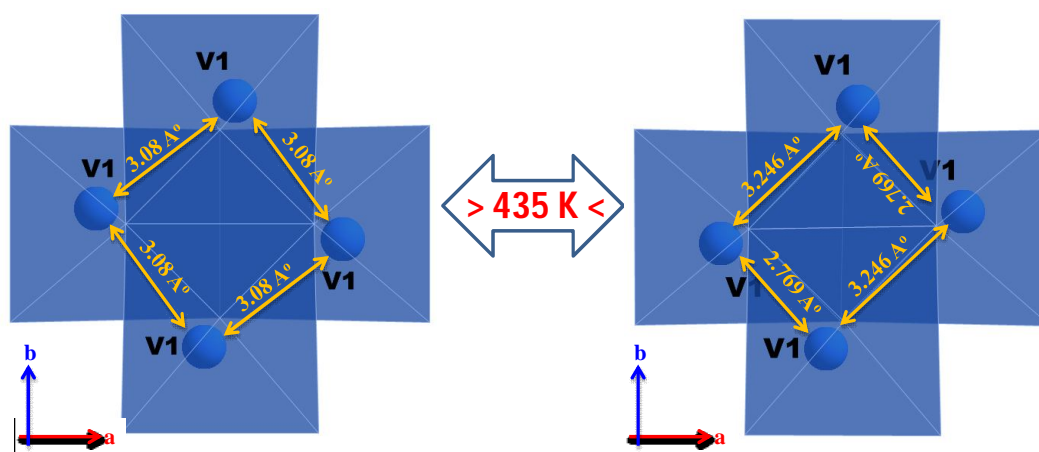
Figure 12. Schematic diagram of the transition mechanism in VO_2 (A).

Only some basic physical properties of VO_2 (A), such as resistivity and thermal stability, have been studied on pressed powders. Its relationship to the other VO_2 phases still lacks a systematic and in-depth study. The influence of substitution on the stability and the phase transition was only studied W-substituted VO_2 (A) nanorods synthesized with hydrothermal method from the reduction of V_2O_5 with oxalic acid. The substitution limit is about 0.5-0.75 at%. The phase transition temperature decreases with W rate and an inhomogeneous distribution of tungsten was reported [97].

IV.5. VO$_2$ (B)

VO_2 (B) is one of the vanadium dioxide polymorphs reported by Théobald [93]. This metastable polymorph is known to form upon soft-chemical synthesis. This compound undergoes a structural transition near room temperature that is accompanied by an anomaly in the magnetic susceptibility. The structures of the high (300 K) and low (50 K) temperature forms of VO_2 (B) were determined by Oka et al. [98]. They established that the structural transition arises as a result of a V^{4+}–V^{4+} dimerization, although the dimerization pattern is distinct from that observed in VO_2 (M1). There is no change in the monoclinic space group across the phase transition. **Figure 13** shows the structure of monoclinic VO_2 (B) along [010]. VO_6 octahedra are distorted due to the off-centering of the V ions and there are two

available sites for V ions. In (110) plane, edge-shared VO_6 zig-zags form chains along the b-axis between the two non-equivalent V1 and V2 ions and V1 ions; these chains are linked through VO_6 edges either by V1 ions with long distance or V2 ions with short distance; the resulting 2D sets stack along the c-axis with links through the corners of VO_6 octahedra and with a shift of (1/2, 1/2, 0).
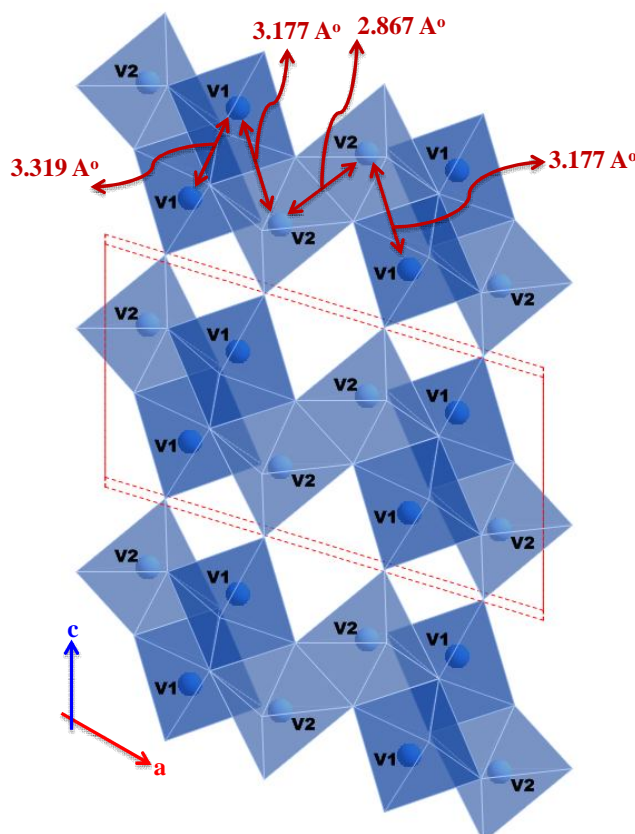
Figure 13. Crystal structure of VO_2 (B).

The transition from high to low temperature is marked by the contraction of the c-axis together with the expansion of the a- and b-axes and the increase of the monoclinic angle [98]. These changes were attributed to the pairing of half of the V ions due to the shortening of V(2)-V(2) distance in the ac plane. **Figure 14** reproduced from Ref. 98 shows that the volume fraction of the low temperature phase saturates at about 70 % below 150 K; Corr et al. however report that the transformation from the high temperature phase to the low temperature phase extends until 423 K [99].
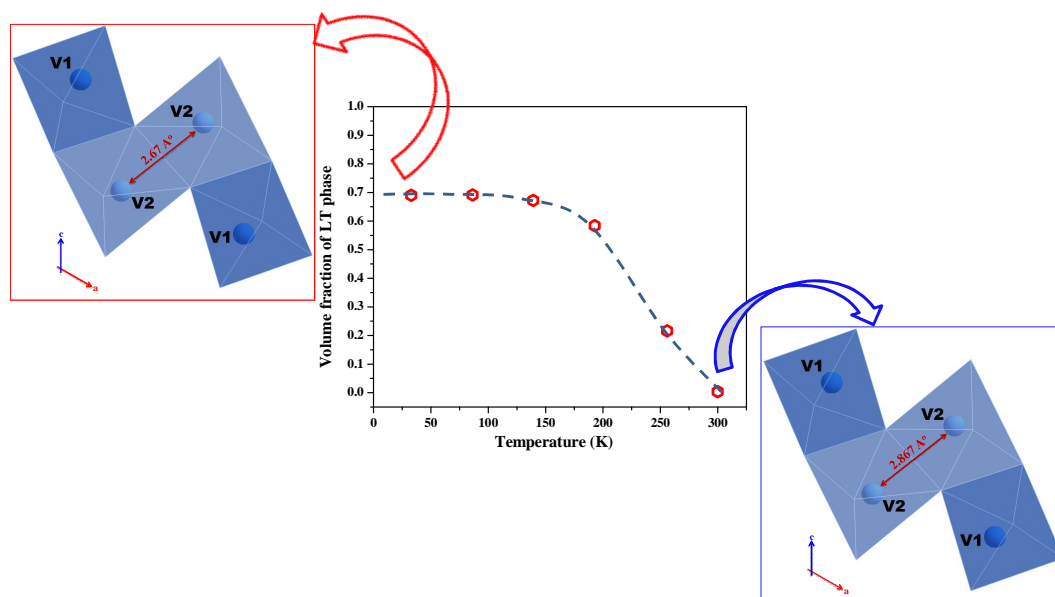
Figure 14. Temperature dependence of the low temperature phase volume fraction [98].

VO_2 (B) is an attractive material for lithium ion battery cathode and exhibits a good reversible capacity but it was however much less studied than V_2O_5 [100]. Recently, Baudrin et al. [101] showed that crystalline VO_2 (B) exhibits a specific capacity as high as 500 mA h g^{-1}. In battery applications, the operating properties not only depend on the structure, but also on the morphology of the electrode components [102]. Some efforts have been devoted to fabricate 1D VO_2 (B) material to improve its electrochemical performance by studying different morphologies like nanorods [103], nanowires [104], nanoribbons [105] and nanobelts [106] etc. However, all of these materials suffer from a fast capacity fade and could hardly display a long-term stable cycling performance. Therefore, it is still a big challenge to design VO_2 (B) with functional properties. In striking contrast to the VO_2 (M1) phase, the main attention of VO_2 (B) was focused on the synthesis and electrochemical characterization; the electrical properties of VO_2 (B) have so far not been reported across the phase transition. **Table 1** summarizes some of the synthesis protocol (precursors, temperature, synthesis process and morphology of final products) till now reported for the preparation of polymorph VO_2 (B).

Year	Author	Precursors	Temperature (°C)	Time (h)	Morphology	Technique	Ref.
1976	Franois Thiobald	V_2O_5	Above 500	--	--	Reduction	**93**
1987	K.West et al.	Ammonium metavanadate	425	--	--	Decomposition under H/Ar	**107**
1991	Y Oka et al.	VO_2,H_2O	200	48	Plate like	Hydrothermal	**108**
1998	J.C Valmalette et al.	Ammonium Hexavanadate	380	--	--	Decomposition in static N_2	**109**
2003	A M Kannan et al.	Aqueous vanadate ions, Potassium borohydride and Sodium dithionite	230	--	Nanostructure	Reduction followed by heating in vacuum	**110**
2004	Junfeng Liu et al.	Ammonium metavanadate and Formic acid	180	48	Nanobelts	Hydrothermal	**111**
2004	Wen Chen et al.	V_2O_5 and Cetyltrimethylammonium bromide	180	48	Nanorods	Hydrothermal	**112**
2004	Xiangying Chen et al.	V_2O_5 and Absolute ethylene glycol	180	12	Nanowire arrays	Hydrothermal	**113**
2005	Sorapong Pavasupree et al.	Laurylamine hydrochloride, Acetylacetone and Vanadium triethoxide	150	168	Nanorods	Hydrothermal	**114**
2006	Emmanuel Baudrin et al.	Vanadium oxide aerogel	Between 280 and 400 °C	4	Nanotexture	Freeze-drying & Vacuum heating	**101**
2006	F Sediri et al.	V_2O_5 and Aniline	180	24	Nanoneedles	Hydrothermal	**115**
2007	Xueliang Li et al.	V_2O_5 and Butanol	150	36	Nanorods	Hydrothermal	**116**
2007	F Sediri et al.	V_2O_5 and Benzylamine	180	48	Nanorods	Hydrothermal	**117**
2007	Guicin Li et al.	V_2O_5, Oxalic Acid and Ethanol	180	24	Nanobelts	Hydrothermal	**118**
2007	K F Zhang et al.	V_2O_5 and Oxalic acid	160	48	Nanobelts	Hydrothermal	**119**
2007	Kinson C. Kam et al.	Ammonium metavanadate and Formic acid	180	48	Nanorods	Hydrothermal	**120**
2008	Lijuan Mao et al.	V_2O_5, Oxalic acid dehydrate and Polyethylene glycol 600	180	24	Nanoribbons	2 step hydrothermal	**121**
2008	H Liu et al.	V_2O_5, Aniline and Glucose	180 & 400	48 & 8	Hollow spheres	Hydrothermal + heating	**122**
2008	Xinghai Liu et al.	V_2O_5 and Absolute alcohol	180	24	Nanoribbons	Hydrothermal	**123**
2009	Serena A Corr et al.	V_2O_5, Formaldehyde and Isopropanol	180	48	Nanorods	Hydrothermal	**124**
2009	Ch.V. Subba Reddy et al.	V_2O_5 xerogel, Poly (vinyl pyrrolidone)	180	168	Nanorods	Hydrothermal	**125**
2009	Shudong Zhang et al.	Vanadyl acetylacetonate, Polyvinylpyrrolidone	200 .	24	Flowerlike	Hydrothermal	**126**
2009	F. Sediri et al.	V_2O_5, $C_6H_5-(CH_2)_n-NH_2$ (n=2 and 4)	180	48	Nanobelts	Hydrothermal	**127**
2009	Guicin Li et al.	V_2O_5, H_2O_2 and Oxalic acid	180	12	Urchin-like	Hydrothermal	**128**

Table 1. Synthesis protocols reported in literature for the preparation of VO_2 (B).

IV.6. References

[1] C.N.R. Rao, and B. Raveau, Transition Metal Oxides; VCH Publishers, New York (1995)

[2] R.J. Powell, and W.E. Spicer, Phys. Rev. B 2, 2182 (1970)

[3] A. Magneli, Acta Chemica Scandinavica 2, 501 (1948)

[4] Z. Yang, C. Ko, and S. Ramanathan, Annu. Rev. Mater. Res. 41, 8.1 (2011)

[5] A. Dobley, K. Ngala, S. Yang, P.Y. Zavalij, M.S. Whittingham, Chem. Mater. 13, 4382 (2001)

[6] G. Li, S. Pang, L. Jiang, Z. Guo, Z. Zhang, J. Phys. Chem. B 110, 9383 (2006)

[7] H. Qiao, X. Zhu, Z. Zheng, L. Liu, L. Zhang, Electrochem. Commun. 8, 21 (2006)

[8] J. Shi, S. Zhou, B. You, L. Wu, Solar Energy Materials & Solar Cells 91, 1856 (2007)

[9] G.T. Kim, J. Muster, V. Krstic, J.G. Park, Y.W. Park, S. Roth, M. Burghard, Appl. Phys. Lett. 76, 1875 (2000)

[10] J. Muster, G.T. Kim, V. Krstic, J.G. Park, Y.W. Park, S. Roth, M. Burghark, Adv. Mater. 12, 420 (2000)

[11] Inorg. Chem. 48, 1168 (2009)

[12] J. Liu, X. Wang, Q. Peng, Y. Li, Adv. Mater. 17, 764 (2005)

[13] G. Gu, M. Schmid, P.W. Chiu, A. Minett, J. Fraysse, G.T. Kim, S. Roth, M. Kozlov, E. Munoz, R.H. Baughman, Nat. Mater. 2, 316 (2003)

[14] L. Biette, F. Carn, M. Maugey, M.F. Achard, J. Maquet, N. Steunou, J. Livage, H. Serier, R. Backov, Adv. Mater. 17, 2970 (2005)

[15] C. Chen and Z. Zhou, Appl. Phys. Lett. 91, 011107 (2007)

[16] T. Driscoll, H.T. Kim, B.G. Chae, M.D. Ventra, and D.N. Basov, Appl. Phys. Lett. 95, 043503 (2009)

[17] T. Driscoll, S. Palit, M.M. Qazilbash, M. Brehm, F. Keilmann, B.G. Chae, S.J. Yun, H.T. Kim, S.Y. Cho, N.M. Jokerst, D.R. Smith, and D.N. Basov, Appl. Phys. Lett. 93, 024101 (2008)

[18] M.J. Lee, Y. Park, D.S. Suh, E.H. Lee, S. Seo, D.C. Kim, R. Jung, B.S. Kang, S.E. Ahn, C.B. Lee, D.H. Seo, Y.K. Cha, I.K. Yoo, J.S. Kim, and B.H. Park, Adv. Mater. 19, 3919 (2007)

[19] G. Stefanovich, A. Pergament, D. Stefanovich, J. Phys.: Condens. Matter 12, 8837 (2000)

[20] H.T. Kim, B.G. Chae, D.H.Youn, S.L. Maeng, G. Kim, K.Y. Kang, Y.S. Lim (2004)

[21] H.T. Kim, B.J. Kim, S. Choi, B.G. Chae, Y.W. Lee, T. Driscoll, M.M. Qazilbash, D.N. Basov, J. Appl. Phys. 107, 023702 (2010)

[22] F.D. Bouchiat, C. ChampeauxC, A. Catherinot, A. Crunteanu, P. Blondy, Appl. Phys. Lett. 91, 223505 (2007)

[23] A.L. Pergament, P.P. Boriskov, A.A. Velichko, N.A. Kuldin, J. Phys. Chem. Solids 71, 874 (2010)

[24] F.D. Bouchiat, C. ChampeauxC, A. Catherinot, A. Crunteanu, P. Blondy, Materials and Devices for Smart Systems III edition (2009)

[25] J. Su, L.P. Wang, Y. Furuya, S.T. McKinstry and J. Leng, Mater. Res. Soc. Symp. Proc., 1129, 275

[26] J. Givernaud, A. Crunteanu, J-C. Orlianges, A. Pothier, C. Champeaux, A. Catherinot , P. Blondy, IEEE Trans. Microwave Theory Tech. doi 10.1109/TMTT.2010.2057172 (2010)

[27] D. Kim, 34th Int. Conf. Infrared, Millimeter, and Terahertz Waves, IRMMW-THz art. no. 5324735 (2009)

[28] A. Cavalleri, C.S. Tóth, C.W. Siders, J.A. Squier, F. Ráksi, P. Forget, J.C. Kieffer, Phys. Rev. Lett. 87, 237401 (2001)

[29] M. Rini, A. Cavalleri, R.W. Schoenlein, R. López, L.C. Feldman, R.F. Haglund Jr, L.A. Boatner, T.E. Haynes, Optics Lett. 30, 558 (2005)

[30] F. J. Morin, Phys. Rev. Lett., 3, 34 (1959)

[31] T. Matsuishi, Jpn. J. Appl. Phys., 6, 1060 (1967)

[32] Y. Oka, T. Yao and N. Yamamoto, J. Solid State Chem., 86, 116 (1990)

[33] F. Theobald, J. Bernards and R. Cabala, J. Solid State Chem., 17, 431 (1976)

[34] C.Z. Wu, Z.P. Hu, W. Wang, M. Zhang, J.L. Yang and Y. Xie, Chem. Commun., 3891 (2008)

[35] Y.Q. Wang, Z.J. Zhang, Y. Zhu, Z. Li, C.R. Vajtai, L.J. Ci and P.M. Ajayan, ACS Nano, 2, 1492 (2008)

[36] D. Ruzmetov, K.T. Zawilski, S.D. Senanayake, V. Narayanamurti, S. Ramanathan, J Phys Condens Mat 20(46), 465204 (2008)

[37] J. Cao, E. Ertekin, V. Srinivasan, W. Fan, S. Huang, H. Zheng, J. W. L. Yim, D. R. Khanal, D.F. Ogletree, J.C. Grossman, J. Wu, Nat. Nanotechnol. 4, 732 (2009)

[38] G. Stefanovich, A. Pergament, and D. Stefanovich, J. Phys.: Condens. Matter 12, 8837 (2000)

[39] L. Dai, Sol. Energy Mater. Sol. Cells, *doi:10.1016/j.solmat.2010.10.008* (2010)

[40] C. Kim, J.S. Shin , H. Ozaki, J. Phys.: Condens. Matter 19, 096007 (2007)

[41] A. Cavalleri, C. Tóth, C. Siders, J. A. Squier, F. Ráksi, P. Forget, and J. C. Kieffer, Phys. Rev. Lett. 87, 237401 (2001)

[42] T. Yamauchi, M. Isobe, Y.Ueda, Solid State Sci. 7, 874 (2005); M.M. Qazilbash, M. Brehm, B.G. Chae, P.C. Ho, G.O. Andreev, B.J. Kim, S.J. Yun, A.V. Balatsky, M.B. Maple, F. Keilmann, Science, 318, 1750 (2007); J. Wu, Q. Gu, B.S.Guiton, N. Leon, L. Ouyang, H. Park, Nano Lett. 2313 (2006)

[43] V. Eyert, Annalen der Physik 11, 650 (2002)

[44] J. B. Goodenough, J. Solid State Chem. 3 , 490 (1971)

[45] Thin Film Metal-Oxides, *Editor : Shriram Ramanathan*

[46] M. Imada, A. Fujimori, and Y. Tokura, Reviews of Modern Physics 70, 1039 (1998); C. Kaubler, H. Ehrke, R. Huber, R. Lopez, A. Halabica, R.F. Haglund, and A. Leitenstorfer, Physical Review Letters 99, 116401 (2007); M.M. Qazilbash, M. Brehm, B.G. Chae, P.C. Ho, G.O. Andreev, B.J. Kim, S.J. Yun, A.V. Balatsky, M.B. Maple, F. Keilmann, H.T. Kim, and D.N. Basov, Science 318, 1750 (2007); P. Baum, D.S. Yang, and A.H. Zewail, Science 318, 788 (2007); J. B. Goodenough, Journal of Solid State Chemistry 3, 490 (1971); A. Zylbersztejn, N. F. Mott, Physical Review B 11, 4383 (1975); D. Paquet , P. L. Hugon, Physical Review B 22, 5284 (1980); R.M. Wentzcovitch, W.W. Schulz, P.B. Allen, Physical Review Letters 73, 3043 (1994); T.M. Rice, H. Launois, and J.P. Pouget, Physical Review Letters 73, 3042(1994); R.M. Wentzcovitch, W.W. Schulz, and P.B. Allen, Physical Review Letters 72, 3389 (1994); S. Biermann, A. Poteryaev, A.I. Lichtenstein, and A. Georges, Physical Review Letters 94, 026404 (2005); A. Cavalleri, T. Dekorsy, H.H.W. Chong, J.C. Kieffer, R. W.Schoenlein, Physical Review B 70, 161102 (2004); H.T. Kim, Y.W. Lee, B.J. Kim, B.G. Chae, S.J. Yun, K.Y. Kang, K.J. Han, K.J. Yee, Y.S. Lim, Physical Review Letters 97, 266401 (2006)

[47] R.M. Wentzcovitch, W.W. Schulz, P.B. Allen, Physical Review Letters 73, 3043 (1994); R.M. Wentzcovitch, W.W. Schulz, P.B. Allen, Physical Review Letters 72, 3389 (1994)

[48] A. Zylbersztejn, N. F. Mott, Physical Review B 11, 4383 (1975); D. Paquet and P.L. Hugon, Physical Review B 22, 5284 (1980); T.M. Rice, H. Launois, J.P. Pouget, Physical Review Letters 73, 3042 (1994)

[49] R.M. Wentzcovitch, W.W. Schulz, P.B. Allen, Physical Review Letters 73, 3043 (1994); R.M. Wentzcovitch, W.W. Schulz, P.B. Allen, Physical Review Letters 72, 3389 (1994)

[50] D. Paquet and P. Leroux-Hugon, Phys. Rev. B 22, 5284 (1980)

[51] S. Biermann, A. Poteryaev, A.I. Lichtenstein, A. Georges, Physical Review Letters 94, 026404 (2005)

[52] A. Cavalleri, T. Dekorsy, H.H.W. Chong, J.C. Kieffer, R.W. Schoenlein, Physical Review B 70, 161102 (2004)

[53] M.W. Haverkort, Z. Hu, A. Tanaka, W. Reichelt, S.V. Streltsov, M.A. Korotin, V.I. Anisimov, H.H. Hsieh, H.J. Lin, C.T. Chen, D.I. Khomskii, L.H. Tjeng, Physical Review Letters 95, 196404 (2005)

[54] T. Yao, X. Zhang, Z. Sun, Phys. Rev. Lett.105, 226405

[55] M.M. Qazilbash, M. Brehm, B.G. Chae, P.C. Ho, G.O. Andreev, B.J. Kim, S.J. Yun, A.V. Balatsky, M.B. Maple, F. Keilmann, H.T. Kim, and D.N. Basov, Science 318, 1750 (2007)

[56] H.T. Kim, Y.W. Lee, B.J. Kim, B.G. Chae, S.J. Yun, K.Y. Kang, K.J. Han, K.J. Yee, Y.S. Lim, Phys. Rev. Lett. 97, 266401 (2006)

[57] H.T. Kim, B.G. Chae, D.H. Youn, S.L. Maeng, G. Kim, K.Y., Physica C 341, 259 (2000)

[58] M. Netsianda, P.E. Ngoepe, , C.R.A Catlow, S.M. Woodley, Chem. Mater. 20, 1764 (2008)

[59] A. Cavalleri, M. Rini, H.H.W.Chong, S. Fourmaux, T.E. Glover, P.A. Heimann, J.C. Kieffer, R.W.B. Schoenlein, Phys. Rev. Lett. 95, 067405/1 (2005); D.J. Hilton, R.P. Prasankumar, S. Fourmaux, A. Cavalleri, D. Brassard, M.A. El Khakani, J.C. Kieffer, A.J. Taylor, R.D. Averitt, Phys. Rev. Lett. 99, 2265401/1 (2007); P. Baum, D.S. Yang, A.H. Zewail, Science 318, 788 (2007); C. Kubler, H. Ehrke, R. Huber, R. Lopez, A. Halabica, R.F. Haglund Jr., A. Leitensorfer, Phys. Rev. Lett. 99, 116401/1 (2007)

[60] Physica status solidi (a), 45, 123 (2006); J. Mater. Res., 12, 416 (1997)

[61] J.B. MacChesney, J. Guggenheim, J. Phys. Chem. Solids, 30, 225 (1969)

[62] J.W. Pierce, J.B. Goodenough, Phys. Rev B 5. 4104 (1972)

[63] A. Prodan, V. Marinkovid, M. Proek, Mat. Res. Bull. 8, 551 (1973)

[64] A. Romanyuk, R.Steiner, L. Marot, P. Oelhafen, Solar Energy Materials & Solar Cells 91 1831 (2007);T. Hörlin, T. Niklewski, M. Nygren, Materials Research Bulletin, 8, 179 (1973); B. Fisher, J. Phys. Chem. Solids 43, 205 (1982); B. Chen, D.Yang, P.A. Charpentier, M. Zeman, Solar Energy Materials & Solar Cells 93, 1550 (2009); Mat. Res. Bull. 6, 119 (1971); S. LuU, L. Hou, F. Gan, J. Mat. Sci. Lett. 15, 856 (1996); S.K. Misra, S.I. Andronenko, R.R. Andronenko, Phys. Rev. B, 57, 8203(1998); M. Maaza, O. Nemraoui, C. Sella, A.C. Beye, Gold Bulletin, 38/3, 100 (2005); H. Liu, S. Lysenko, A. Rua, V. Vikhnin, O. Vasquez, F.E. Fernandez, Journal of Luminescence 119– 120, 388 (2006); H, Futaki, M Aoki, JJAP, 8 1008

(1969); J. Li, N. Yuan, T. Xie, D. Dan, Proc. SPIE, Vol. 6149, 61490B (2006); M.H.Lee, M.G. Kim , H.K. Song, Thin Solid Films 290-291, 30 (1996)

[65] E. Cavanna, J.P. Segaud, and J. Livage, Materials Research Bulletin, 34, 167 (1999); N.R. Mlyuka, G.A. Niklasson, and C.G. Granqvist, Appl. Phys. Lett. 95, 171909 (2009)

[66] F. Béteille, R. Morineau, J. Livage, M. Nagano, Materials Research Bulletin, 32, 1109 (1997); H, Futaki, M Aoki, Japanese Journal of Applied Physics, 8, 1008 (1969)

[67] B. Chen, D.Yang, P.A.Charpentier, M. Zeman, Solar Energy Materials & Solar Cells 93, 1550 (2009)

[68] S. Lu, L. Hou, F. Gan, J. Mat. Sci. Lett. 15, 856-857 (1996)

[69] M. Drillon, Ph D thesis, Bordeaux (1974); W. Bruckner, U. Gerlach, W. Moldenhauer, H.P. Bruckner, B. Thuss, H. Oppermann, E. Wolf, I. Storbeck, J. De Phys. Coll. C4, 63 (1976); M. Marezio, D.B. Mcwhan, P.D. Dernier, J.P. Remeika, Phys. Rev. B 5, 2541 (1972); F. Bbteille, R Morineau, J. Livage, M. Nagano, Matcrialr Besamh Buktin. 32, 1105 (1997)

[70] Rudorf, W.; Marklin, J., Zeitschrift für anorganische und allgemeine Chemie 334, 142 (1964); K.L. Holman, T.M. McQueen, A.J. Williams, T. Klimczuk, P.W. Stephens, H.W. Zandbergen, Q. Xu, F. Ronning, R.J. Cava, Phys. Rev. B 79, 245114 (2009)

[71] M. Soltani, M. Chaker, E. Haddad, R.V. Kruzelecky, J. Margot, Appl. Phys. Lett. 85, 1958 (2004)

[72] J. Shi, S. Zhou, B. You, L. Wu, Sol. Energy Mater. Sol. Cells 91, 1856 (2007); T.J. Hanlon, J.A. Coath, M.A. Richardson, Thin Solid Films 436, 269 (2003)

[73] W. Burkhardt, T. Christmann, W. Niessner, D. Schalch, A. Scharmann, Thin Solid Films 345, 229 (1999); P. Jin, S. Nakao, S. Tanemura, Thin Solid Films 324, 151(1998)

[74] W. Burkhardt, T. Christmann, S. Franke, W. Kriegseis, D. Merster, B.K. Meyer, W. Niessner, D. Schalch, A. Scharmann, Thin Solid Films 402, 226 (2002)

[75] F. Guinneton, L. Sauques, J.C. Valmalette, F. Cros, J.R. Gavarri, Thin Solid Films 446, 287 (2004); S. Xu, H. Ma, S. Dai, Z. Jiang, J. Mater. Sci. 39, 489 (2004); Z.P. Wu, A. Miyashita, S. Yamamoto, H. Abe, I. Nashiyama, K. Narumi, H. Naramoto, J. Appl. Phys. 86, 5311(1999)

[76] I.Takahashi, M. Hibino, T. Kudo, Proc. SPIE, 3788, 26 (1999); J. Li, D. Dan, N. Yuan, T. Xie, Proc. SPIE, 6723, 672310 (2007); J. Li, Z. Daohua, W.Yan, Z. Meng, Z.Weifeng, Y. Ningyi, PhotonicsGlobal@Singapore, IPGC 2008. IEEE, DOI: 10.1109/IPGC.2008.4781361 (2008); T.C.K. Yang, B.P.P. Hunga, Y.C. Chen, M.H. Lai , T.W. Chung, Sensors and Actuators A 140, 194 (2007); W. Burkhar, T. Christmann, S. Franke, W. Kriegseis, D.

Meister, B.K. Meyer, W. Niessner, D. Schalch, A. Scharmann, Thin Solid Films 402 , 226 (2002); Y. Jiazhen, Z. Yue, H. Wanxia, T. Mingjin, Thin Solid Films 516, 8554 (2008); A. Akroune, A. Casalot, J. Solid State Chem. 68, 163 (1987)

[77] S. Xu, H. Ma, S. Dai, Z. Jiang, J. Mater. Sci. 39, 489 (2004)

[78] M. Soltani, M. Chaker, E. Haddad, R.V. Kruzelecky, J. Margot, Appl. Phys. Lett. 85, 1958 (2004)

[79] I. Takahashi, M. Hibino, T. Kudo, Jpn. J. Appl. Phys. Part 1 Regul. Pap. Short Note Rev. Pap. 40 (2001) 1391

[80] B.S. Guiton, Q. Gu, A.L. Prieto, M.S. Gudiksen, H.J. Park, Am. Chem. Soc. 127, 498 (2005) J. Wu, Q. Gu, B.S. Guiton, N.P. Leon, L. Ouyang, H. Park, Nano Lett. 6, 2313 (2006); J.I. Sohn, H.J. Joo, A.E. Porter, C.J. Choi, K. Kim, D.J. Kang, M.E. Welland, Nano Lett. 7, 1570 (2007)

[81] L.Q. Mai, B. Hu, T. Hu, E.D. Gu, J. Phys. Chem. B 110,19083 (2006); B.G. Chae, H.T. Kim, S.J. Yun, B.J. Kim, Y.W. Lee, H. Youn, K.Y. Kang, Electrochem. Solid-State Lett. 9, C12 (2006); E. Baudrin, G. Sudant, D. Larcher, B. Dunn, J.M. Tarascon, Chem. Mater. 18, 4369 (2006)

[82] T.D. Manning, I.P. Parkin, M.E. Pemble, D. Sheet, Vernardou, Chem. Mater. 16, 744, (2004); R. Binions, G. Hyett, C. Piccirillo, , I.P. Parkin, J. Mater. Chem. 17, 4652 (2007)

[83] J. Rozen, R. Lopez, Jr.R.F. Haglund, L.C. Feldman, Appl. Phys. Lett. 88, 081902 (2006)

[84] R. Balu, P.V. Ashrit, Appl. Phys. Lett. 92, 021904 (2008)

[85] R. Lopez, L.A. Boatner, T.E. Haynes, L.C. Feldman, F.Jr. Haglund, J. Appl. Phys. 92, 4031 (2002)

[86] Z. Peng, W. Jiang, H.J. Liu, Phys. Chem. C 111, 1119 (2007)

[87] J. Liu, Q. Li, T. Wang, D. Yu, Y. Li, Angew. Chem., Int. Ed. 43, 5048. 24 (2004); G. Li, K. Chao, H. Peng, K. Chen, Z. Zhang, Inorg. Chem. 6, 578 (2007); X. Chen, X. Wang, Z. Wang, J. Wan, J. Liu, Y. Qian, Nanotechnology 15, 1685 (2004); G. Armstrong, J. Canales, A. R. Armstrong, P.G. Bruce, J. Power Sources 178, 723 (2008); W. Chen, J. Peng, L. Mai, H. Yu, Y. Qi, Chem. Lett. 33, 1366 (2004); C. Tsang, A. Manthiram, J. Electrochem. Soc. 144, 520 (1997); X. Li, X. Chen, C. Han, C. Shi, J. Cryst. Growth 309, 43 (2007)

[88] W. Burkhardt, T. Christmann, B.K. Meyer, W. Niessner, D. Schalch, A. Scharmann, Thin Solid Films 345, 229 (1999)

[89] R. Lopez, T.E. Haynes, L.A. Boatner, L.C. Feldman, R.F.Jr. Haglund, Phys. Rev. B 65, 224113/1 (2002); R. Lopez, L.A. Boatner, T.E. Haynes, L.C. Feldman, R.F.Jr. Haglund, J.

Appl. Phys. 92, 4031 (2002); R. Lopez, T.E. Haynes, L.A. Boatner, L.C. Feldman, R.F.Jr. Haglund, Opt. Lett. 27, 1327 (2002)

[90] L. Whittaker, H. Zhang, S. Banerjee, J. Mater. Chem. 19, 2968 (2009); L. Whittaker, C. Jaye, Z. Fu, D.A. Fischer, S. Banerjee, J. Am. Chem. Soc. 131, 8884 (2009) S.A. Corr, M. Grossman, J.D. Furman, B.C. Melot, A.K. Cheetham, K.R. Heier, R. Seshadri, Chem. Mater. 20, 6396 (2010); J. Liu, Q. Li, T. Wang, D. Yu, Y. Li, Angew. Chem., Int. Ed. 43, 5048–5052 (2004)

[91] L.Whittaker, C.J. Patridge, S. Banerjee, J. Phys. Chem. Lett. 2, 745 (2011)

[92] J. Liu, Q. Li, T. Wang, D. Yu, Y. Li, Angew. Chem., Int. Ed. 43, 5048 (2004); G. Li, K. Chao, H. Peng, K. Chen, Z. Zhang, Inorg. Chem. 46, 5787 (2007); X. Chen, X. Wang, Z. Wang, J. Wan, J. Liu, Y. Qian, Nanotechnology 15, 1685 (2004); C. Tsang, A.J. Manthiram, Electrochem. Soc. 144, 520 (1997); X. Li, X. Chen, X. Chen, C. Han, C. Shi, J. Cryst. Growth 309, 43 (2007); W. Chen, J. Peng, L. Mai, H. Yu, Y. Qi, Chem. Lett. 33, 1366 (2004)

[93] F. Théobald, J. Less-Comon. Met. 53, 55 (1977)

[94] Y. Oka, T. Yao, N. Yamamoto, J. Solid State Chem. 86, 116 (1990); Y. Oka, S. Sato, T. Yao, N. Yamamoto, J. Solid State Chem. 141, 594 (1998)

[95] T. Yao, Y. Oka, N. Yamamoto, J. Solid State Chem. 112, 196 (1994)

[96] Y. Oka, S. Sato, T. Yao, N. Yamamoto, J. Solid State Chem. 141 594, (1998)

[97] S. JI, Y. Zhao, F. Zhang, P. Jin, Journal of the Ceramic Society of Japan 118, 867 (2010)

[98] Y. Oka, T. Yao, N. Yamamoto, Y. Ueda and A. Hayashi, J. Solid State Chem. 105, 271 (1993)

[99] S.A. Corr, J. Mater. Chem., 19, 4362 (2009)

[100] A.M. Cao, J.S. Hu, H.P. Liang and L. J. Wan, Angew. Chem., Int. Ed., 44, 4391 (2005); Y. Wang and G. Cao, Chem. Mater., 18, 2787 (2006); J. Livage, Chem. Mater., 3, 578 (1991); A. L. Tipton, S. Passerini, B. B. Owens and W. H. Smyrl, J. Electrochem. Soc., 143, 3473 (1996)

[101] E. Baudrin, G. Sudant, D. Larcher, B. Dunn and J.M. Tarascon, Chem. Mater., 18, 4369 (2006)

[102] W.U. Huynh, J. J. Dittmer, A. P.Alivisatos, Science, 295, 2425 (2002)

[103] F. Sediri, N. Gharbi, J. Phys. Chem. Solids 68, 1821 (2007); X. Li, X. Chen, X. Chen, C. Han, C. Shi, J. Cryst. Growth 309, 43 (2007)
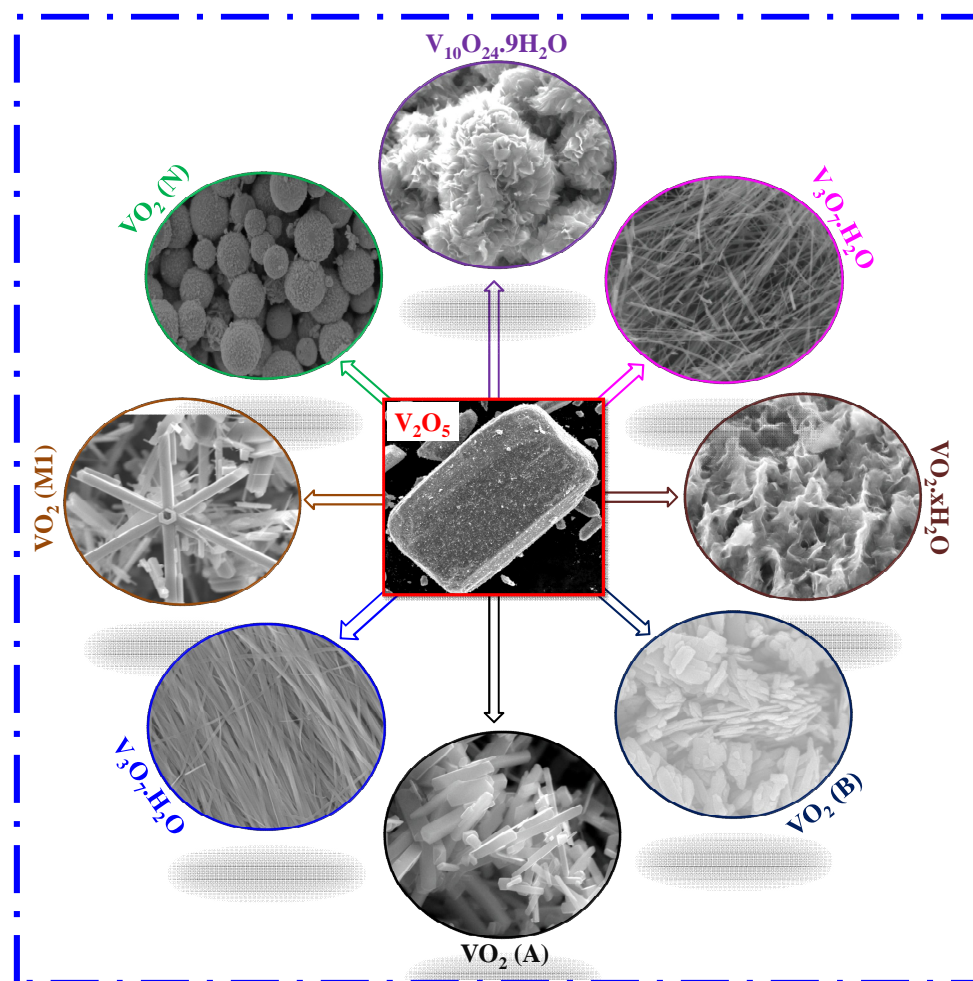
[104] G. Armstrong, J. Canales, A.R. Armstrong and P. Bruce, J. Power Sources, 178, 723 (2008)

[105] L.F. Kong, Z.P. Liu, M.W. Shao, Q. Xie, W.C. Yu, Y.T. Qian, J. Solid State Chem. 177, 690 (2004)

[106] J. Liu, Q. Li, T. Wang, D. Yu and Y. Li, Angew. Chem., Int. Ed. 43, 5048 (2004)

[107] K. West, Journal of Power Sources 20, 165 (1987)

[108] Y. Oka, J. Mater. Chem 1(5), 815 (1991)

[109] J.-C. Valmalette, Materials Science and Engineering B54, 168 (1998)

[110] A. Kannan, Solid State Ionics 159, 265 (2003)

[111] J. Liu, Q. Li, T. Wang, D. Yu, Y. Li, Angew. Chem., Int. Ed. 43, 5048 (2004)

[112] W. Chen, Solid State Comm. 132, 513 (2004)

[113] X. Chen, X. Wang, Z. Wang, J. Wan, J. Liu, Y. Qian, Nanotechnology 15, 1685 (2004)

[114] S. Pavasupree, Journal of Solid State Chem. 178, 2152 (2005)

[115] F. Sediri, Materials Science and Engineering B 129, 251(2006)

[116] X. Li, Journal of Crystal Growth 309, 43 (2007)

[117] F. Sediri, Materials Science and Engineering B 139, 114 (2007)

[118] G. Li, Inorg. Chem. 46, 5787 (2007)

[119] K.-F. Zhang, Mat. Lett. 61, 2644 (2007)

[120] K.C. Kam, Materials Research Bulletin 41, 1015 (2006)

[121] L. Mao, Materials Research Bulletin 43, 1384 (2008)

[122] H. Liu, J. Mat. Chem. 19, 2835 (2009)

[123] X. Liu, Mat. Lett. 62, 1878 (2008)

[124] S.A. Corr, J. Mater. Chem. 19, 4362 (2009)

[125] C.S. Reddy, Current Applied Physics 9, 1195 (2009)

[126] S. Zhang, J. Phys. Chem. C 113, 15058 (2009)

[127] F. Sediri, Mat. Lett. 63, 15 (2009)

[128] G. Li, Inorg. Chem. 48, 1168 (2009)

Chapter V:
Synthesis of vanadium oxides

This section describes the protocols used to prepare the pristine and substituted polymorphs of vanadium dioxide. I used both solid state synthesis and hydrothermal processes. Using solid state process, I prepared pure and Mo-substituted VO₂ (M1) compounds in their bulk form. Using hydrothermal process I explored the mechanisms and sequence behind the evolution of V-O and V-H-O phases using time and ratio dependent studies. Finally using optimized conditions for the preparation of VO₂ (A), VO₂ (B) and VO₂ (M1) polymorphs, I prepared Cr and Mo substituted compounds to analyze their stability, phase transitions and intra-phase conversion mechanisms under hydrothermal and annealed conditions.

Contents

V.1. Introduction

Subtle structural changes can exist close to the boundary of competing phases. The precise control of the stoichiometry is a prerequisite both for determining the intrinsic properties of a specific compound and also for the continuous control of their composition for kinetic studies. The synthesis processes can mostly be divided into two categories: solid state processes (*e.g.* conventional solid state synthesis) and solution processes (*e.g.* hydrothermal). For conventional solid state syntheses solid state precursors containing the required chemical elements are intimately grounded together in stoichiometric ratios and heated at high temperatures for some time. In general, high temperatures and long heating times are used to bring only the most thermodynamically stable phases and there is only little scope for kinetic control and isolation of metastable phases which could have interesting physical and chemical properties. To overcome such shortcomings new routes to the synthesis of inorganic solids, so called solution routes, have been developed. One of these routes is the hydrothermal method.

V.2. Solid state synthesis

Pure and Mo substituted VO_2 (M1) polycrystalline samples were synthesized by solid state reaction. The precursors were V_2O_3, V_2O_5, MoO_3 and Mo powders. Stoichiometric mixtures of these precursors were intimately ground, pressed into pellets and sealed in evacuated silica tubes. The tubes were heated in a tubular furnace at the heating rate of $2^oC/min$. The details about the precursors, reaction temperature and duration are given in the **Table 1** for each composition. The quartz tubes were then cooled down to room temperature at the cooling rate of $5^oC/min$.

	Substituent	Precursors	T (^oC)	Reaction time (Days)
$V_{1-x}Mo_xO_2$	x=0	V_2O_3 and V_2O_5	750	2
	x=0.075, 0.15	V_2O_3, V_2O_5 and MoO_3	1000	6
	0.25≤x≤0.95	V_2O_5, MoO_3 and Mo metal powder	1000	6
	x=1	MoO_3 and Mo metal powder	1000	6
$V_{1-x}W_xO_2$	x=0.005	V_2O_3, V_2O_5 and WO_3	750	2
$V_{1-x}Nb_xO_2$	x=0.005	V_2O_3, V_2O_5 and Nb_2O_5	750	2
$V_{1-x}Cr_xO_2$	x=0.005	V_2O_3, V_2O_5 and Cr_2O_3	750	2

Table 1. Solid state synthesis protocol details for the preparation of pure and Mo/W/Nb/Cr substituted VO_2 (M1).

For 0.5% substitution with W, Nb and Cr a similar synthesis protocol was used but using WO_3, Nb_2O_5 and Cr_2O_3 in place of Mo/MoO_3. Powder X-ray diffraction (P-XRD) patterns of the products were collected using a PANalytical X'Pert PRO MPD diffractometer with graphite monochromatized Cu K_α radiation (λ=1.54178 Å). The phase purity was checked by comparing the experimental P-XRD patterns to standards compiled by the Joint Committee on Powder Diffraction and Standards (JCPDS).
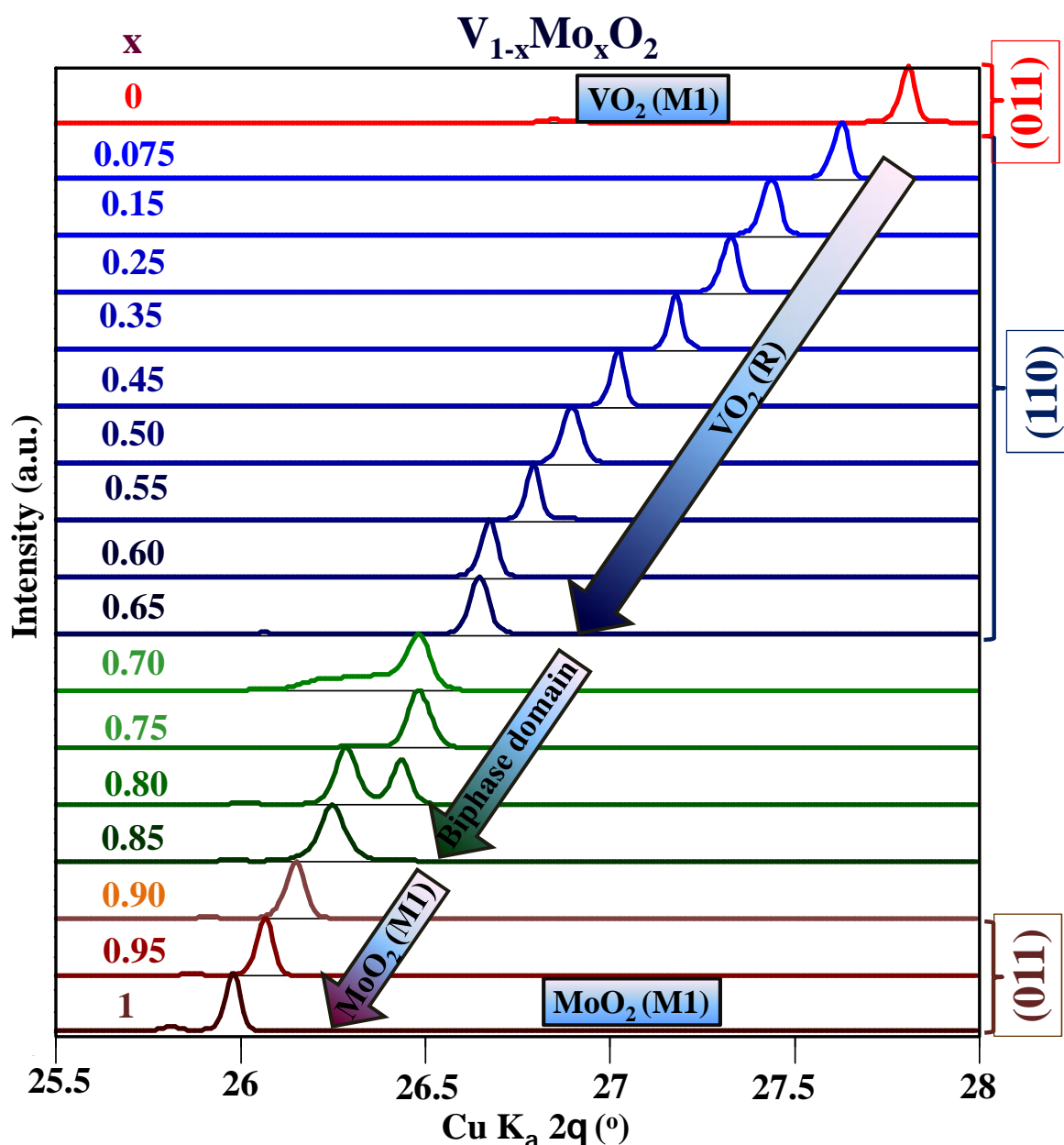
Figure 1. Variation of maximum intensity reflection in P-XRD patterns of $V_{1-x}Mo_xO_2$ system with increasing Mo content. (Here the x value in solid solution was presented left side and corresponding maximum intensity reflection was shown on right side of the figure)

Figure 1 shows the P-XRD patterns of $V_{1-x}Mo_xO_2$ ($0 \leq x \leq 1$). For x=0, all the diffraction peaks correspond to the pure VO_2 (M1) phase at room temperature (JCPDS card no: 01-082-0661). For doping levels $0.075 \leq x \leq 0.65$, the structure is the one of VO_2 (R) (JCPDS card no: 01-076-0678). The region from $0.90 \leq x \leq 1$ shows the reflections corresponding to MoO_2 (M1) (JCPDS card no: 01-078-1069). The system is biphasic between $0.70 \leq x \leq 0.85$. Similar observations were reported by Marinder during his extensive studies on VO_2-MoO_2 systems [1]. In the case of $V_{0.995}M_{0.005}O_2$ with M=W, Nb and Cr, at room temperature all the diffraction peaks match with VO_2 (M1).

Note: The reaction between vanadium and the silica tube can produce V_3Si. Sometimes small amounts of V_3Si are present in the sample and even not observable from X-ray diffraction. These impurities can anyway be detected; thanks to their diamagnetic contribution below 16 K (V_3Si is superconductor below T_C = 16 K) [2].

The nominal chemical composition of the samples was confirmed by Inductively Coupled Plasma Absorption Electron Spectroscopy (ICP-AES) on a Varian 720-ES. Powders were then shaped into pellets and sintered using Spark Plasma Sintering (SPS) to measure their intrinsic transport properties. The heating rate up to the sintering temperature was about 100°C/min in a vacuum level of 10^{-2} mbar. Furthermore, in view of thermoelectric applications, SPS suppresses grain growth, leading to small thermal conductivity. **Table 2** summarizes some of the results obtained using different sintering conditions. They show the necessity for a moderate temperature (1000°C) while the system pressure has to be kept as high as possible.

Atmosphere	T (°C)	Duration (min)	Pressure (M Pa)	Phase	Status of final pellet
Ar	900	5	40	Decomposes	Compacted
Ar	1150	15	40	Decomposes	Compacted
Vacuum	800	0	40	Pure	Powder
Vacuum	900	0	60	pure	Powder
Vacuum	900	2	60	Pure	Fragile
Vacuum	900	5	60	Pure	Fragile
Vacuum	1000	5	60	Pure	Compacted
Vacuum	1000	20	60	Pure	Compacted
Vacuum	**1000**	**20**	**90**	**Pure**	**Compacted**

Table 2. Optimized sintering conditions for $V_{1-x}Mo_xO_2$ phases.

The P-XRD patterns collected on the surface of pellets as well as on crushed powders confirm the phase purity after the SPS treatment.

V.3. Hydrothermal synthesis

Soft chemistry synthesis can provide a simple alternative route with lower synthesis temperature. In particular, hydrothermal synthesis is widely used for the preparation of vanadium oxides, especially the metastable and hydrate phases. Hydrothermal synthesis can be defined as any heterogeneous chemical reaction in the presence of a solvent (whether aqueous or non-aqueous) above room temperature and at pressure greater than 1 atm in a closed system [3]. This synthesis method uses the solubility of inorganic substances in water at elevated temperature and pressures and subsequent crystallization of the dissolved material from the fluid. By applying the desired hydrothermal synthesis temperature, an autogenous pressure will be formed inside the autoclave system. The external pressure is adjusted as soon as the temperature equilibrium is achieved within the autoclave and the reaction process takes place. Hydrothermal technique is not only a low cost solution based technique, but also gives the flexibility of choosing several kinds of phases and the possibility to adjust the morphology by varying the numerous experimental conditions (time, temperature, pH, concentration, filling of the autoclave, pressure, reducing agents, etc).
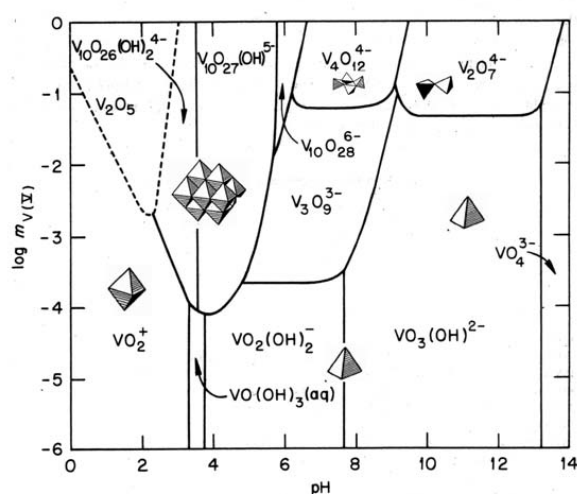
Figure 2. V^{5+} solute species in aqueous solution as a function of pH and concentration [4].

The aqueous chemistry of V^{5+} has been extensively studied and a large number of molecular species have been described [4]. At room temperature under equilibrium conditions, the formation of these molecular species, thanks to hydrolysis and condensation reactions, mainly depends on the vanadium concentration and the pH of the solution (**Figure 2**); a straightforward correlation between the molecular structures of the precursors in the solution and the anions in the solid precipitate exist. It is however no longer valid when the

synthesis is carried out under hydrothermal conditions where the molecular structure of V^{5+} precursors depend in addition on temperature [5].

The first extensive work on hydrate and non-hydrate phases in V-O system using hydrothermal process was reported by Francois Theobald [6]. Then onwards, many compounds were isolated including VO_2 (A) (P4/ncc) [7], VO_2 (B) (C2/m) [8], VO_2 (D) (P2/C) [9], BCC-VO_2 [10], $VO_2 \cdot H_2O$ or VO_2 (C) (P222) [11], $V_2O_4.2H_2O$ [12], $V_{10}O_{24}.9H_2O$ [13], $V_3O_7.H_2O$ [14], Paramontroseite VO_2 [15], Haggite $H_4V_4O_{10}$ [16], Montroseite VOOH [17], etc. However, except with Francois Theobald, very few attempts were made to understand the formation mechanisms of the different phases.

In this work, V_2O_5 (V) (Aldrich) as a vanadium source, oxalic acid dihydrate ($H_2C_2O_4 \cdot 2H_2O$) and citric acid monohydrate ($C_6H_8O_7.H_2O$) (Merck) as Reducing Agents (RA) were used. All chemical reagents were analytical grade and used as received, without any further purification. For each RA the phase diagram was studied using kinetic, time dependent and ratio dependent experiments as follows:

1. Effect of the hydrothermal treatment only on V_2O_5 precursor.
2. Temperature-time kinetic phase diagrams (120-220°C; 0.5-12 h).
3. Time effect at fixed (optimal) temperature.
4. Precursors effect with
   4.1. Variable RA content at fixed V content.
   4.2. Variable V and RA content but keeping a constant V:RA ratio.
5. Substitutions into VO_2 (B), VO_2 (A) and VO_2 (M1) lattice under hydrothermal conditions.

V.3.1. Effect of the hydrothermal treatment on V_2O_5

In order to understand the stability of V_2O_5 under hydrothermal conditions, we performed a simple hydrothermal reaction by dissolving 2.6 mmol of V_2O_5 in 43 mL of deionised water. After magnetic stirring for 15 min the resultant yellow aqueous solution was transferred into the Teflon liner of a stainless steel autoclave. The sealed steel autoclaves were kept at 250°C for 24 h. After the reaction, the autoclave was slowly cooled down to room temperature (RT). The obtained final yellow powders were dried in air at 80°C for 6 h.

Figure 3 shows the P-XRD pattern of the hydrothermal treated V_2O_5 powder. All the peaks correspond to the commercial V_2O_5 without any additional impurity peaks and match with JCPDS data card number 01-089-0612. The refined parameters with space group Pmmn (59) are a = 11.516 Å, b = 3.566 Å, c = 4.372 Å in agreement with available literature.
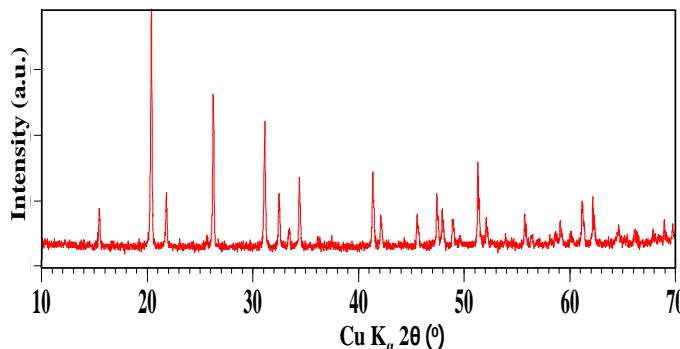
Figure 3. P-XRD pattern of V_2O_5 hydrothermal treated at 250°C/24h.

The morphology of the hydrothermal treated V_2O_5 powder is compared with commercial V_2O_5 precursor in **Figure 4.** The commercial V_2O_5 powder is having 250x300 µm size particles with rectangular morphology. After hydrothermal treatment the morphology changes to microrods what can be explained with an exfoliating–splitting model.
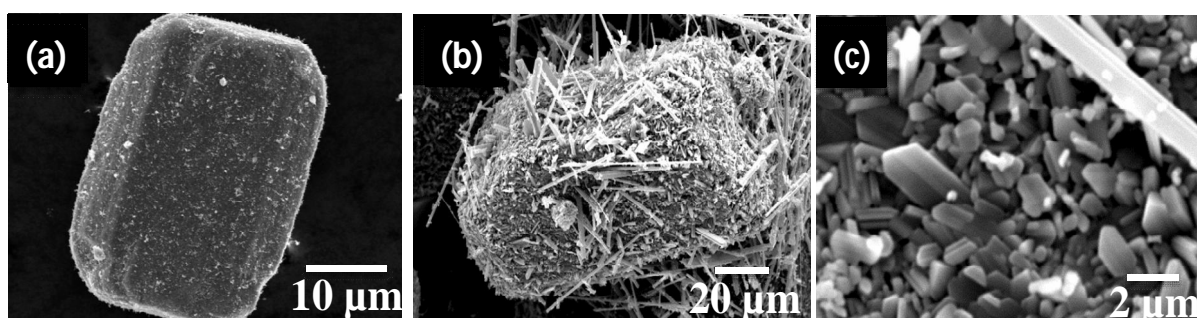
Figure 4. SEM images of commercial V_2O_5 (a) before and (b,c) after hydrothermal treatment at 250°C/24h.

V.3.2. T-t phase diagrams

The concentrations of V_2O_5 and RA were fixed respectively at 0.06 mol/L and 0.09 mol/L (V_2O_5:RA=1:1.5). 2.6 mmol of V_2O_5 were dissolved in 43 mL of deionised water; after magnetic stirring for 15 min the RA was added to the solution and the stirring was prolonged for 15 min resulting either in a yellow (with oxalic acid) or light blue (with citric acid) aqueous solution. The solution was transferred into the Teflon liner of a stainless steel autoclave. The sealed steel autoclaves were kept in oven at selected temperatures between 120 and 220°C for different durations between 0.5 and 12 h. After the reaction process, the autoclaves were slowly

cooled down to RT. The powders were filtered and washed with distilled water and ethanol to remove unreacted chemical species and dried in air at 80°C for 6 h.

V.3.2.1. Results with oxalic acid as reducing agent
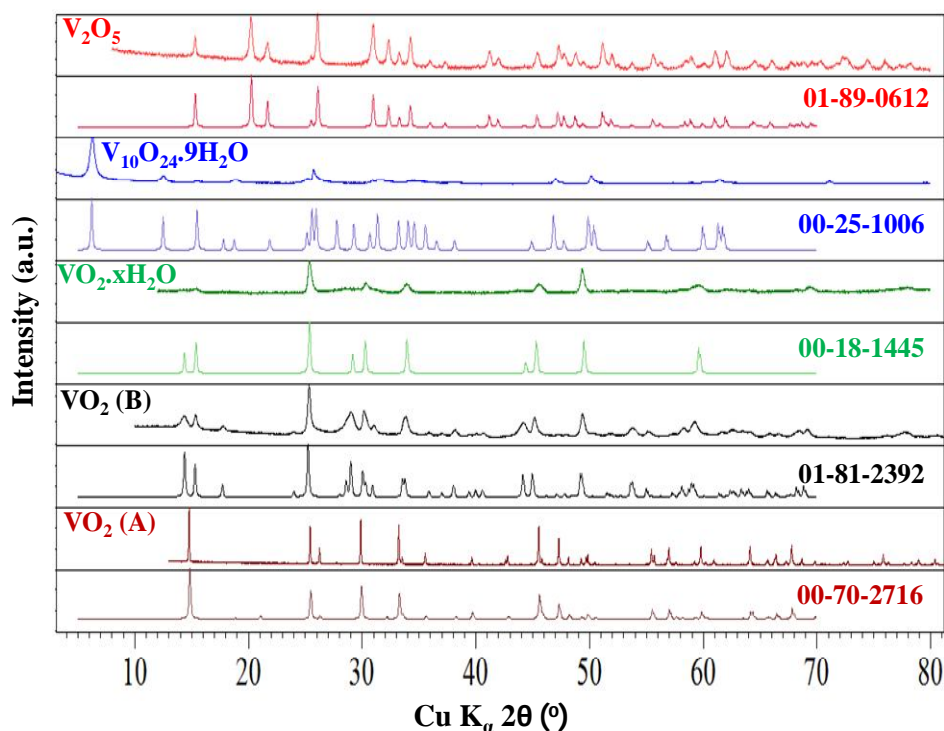
**Figure 5.** P-XRD patterns of the compounds obtained after hydrothermal treatment together with simulated patterns using standard JCPDS data card.

Representative P-XRD patterns of the several products obtained after the hydrothermal treatments (V_2O_5, $V_{10}O_{24}.9H_2O$, $VO_2.xH_2O$, VO_2 (B) and VO_2 (A)) are given in **Figure 5** as well as the simulated patterns using standard JCPDS data card numbers and **Figure 6** shows the resulting T-t phase diagram. Until *ca* 120°C and 5 h reaction duration, only the precursor is present. When the reaction time and/or temperature increase, a mixed valence hydrate $V_{10}O_{24}.9H_2O$ forms: it is known that V_2O_5 structure allows H_2O molecules to be embedded in the intercalation sites without a far-reaching restructuring; in the same time the presence of a reducing agent as well as the increase in reaction duration and/or temperature promotes the reduction of V^{5+} to V^{4+} and accelerates the hydrate formation. Hardening the conditions, a second hydrate $VO_2.xH_2O$ appears whose P-XRD pattern match with JCPDS card number 00-018-1445;

it was first obtained by Deschanvres *et al.* by thermal decomposition of NH_4VO_3 [18]. Its stabilization is here possible from $150^\circ C$ depending on the reaction time and both hydrates $V_{10}O_{24}.9H_2O$ and $VO_2.xH_2O$ seem to coexist only in a small T-t pocket centred at *ca* (190 °C; 6 h). Further increase in duration and/or temperature induces the dehydration to VO_2 (B) and at the extreme limit of the diagram, an island with a mixture of A and B polymorphs appear.
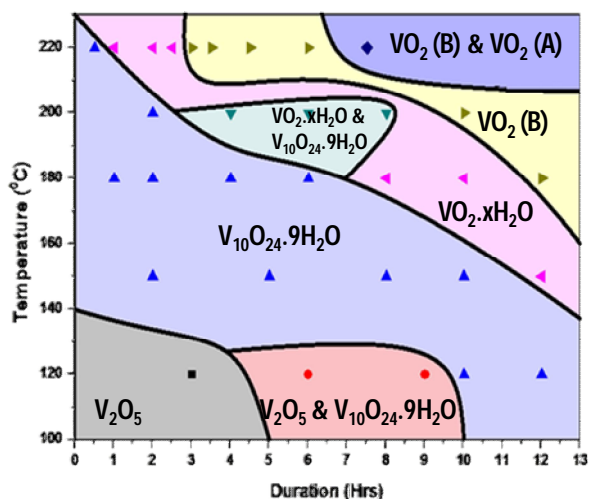
Figure 6. Kinetic phase diagram of V-O system using oxalic acid as a reducing agent (solid lines are guides for the eye)
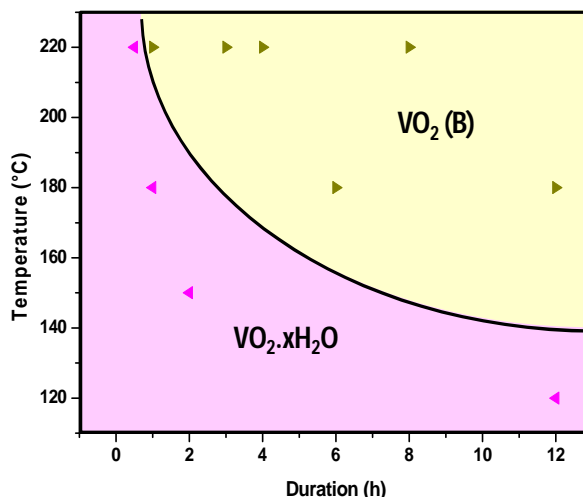
Figure 7. Kinetic phase diagram of V-O system using citric acid as a reducing agent (solid lines are guides for the eye).

Based on this study, we propose the following reactions sequence:

1: $V_2O_5 + H_2O \rightarrow V_{10}O_{24}. 9H_2O$

2: $V_{10}O_{24}. 9H_2O + H_2O \rightarrow VO_2.xH_2O$

3a: $VO_2.xH_2O + H_2O \rightarrow VO_2$ (B) & VO_2 (A)

or 3b: $VO_2.xH_2O + H_2O \rightarrow VO_2$ (B) $\rightarrow VO_2$ (A)
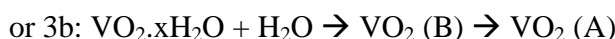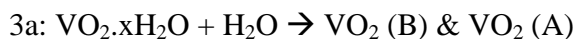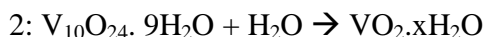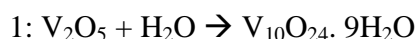
Two alternatives are proposed for the third step because information is missing (one point only!) to decide whether the transformations to B and A polymorphs are competing (3a) or if they are successive (3b).

V.3.2.2. Results with citric acid as reducing agent

The light blue colour of the solution after stirring indicates the partial reduction of V^{5+} to V^{4+} already at room temperature and may be due to the formation of vanadyl oxalate hydrate ($VOC_2O_4.nH_2O$). **Figure 7** shows this T-t phase diagram is much simpler as only two

compounds could be isolated: the hydrate $VO_2.xH_2O$ and VO_2 (B). The diagram highlights the exponential decay for the formation of the hydrate (the necessary time drops fast as the temperature increases) at the benefit of the B polymorph. Just like with oxalic acid, this study evidences that higher temperature and/or longer durations favour the formation of non-hydrate VO_2. However, citric acid hardens the initial conditions which are now more reductive and finally only one intermediate to VO_2 (B) is visible.

V.3.2.3. Understanding the phase evolution

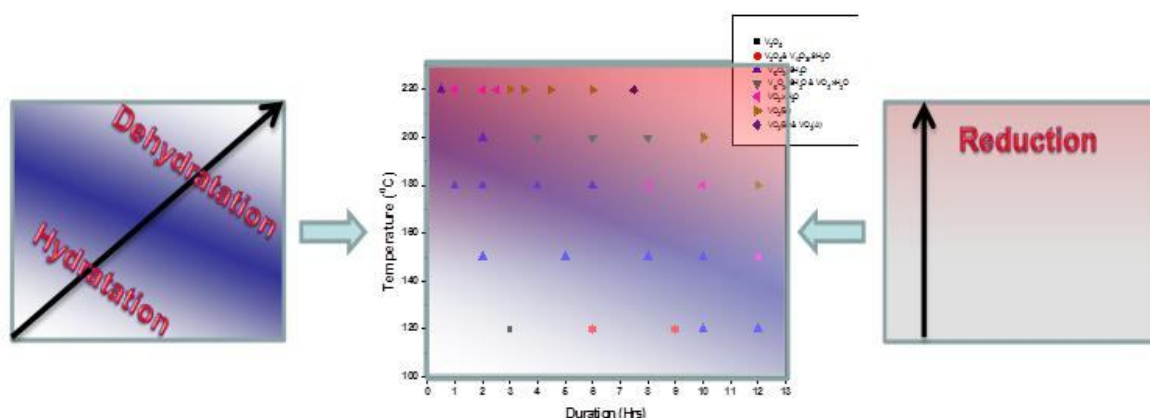All available reports only focus on the specific conditions necessary to isolate a targeted compound in V-O-H system without real care for the possible intermediates and thus the reaction mechanisms, the optimization of the process and the possibility to isolate new compounds.

Figure 8. Proposed formation mechanism for the evolution of phases under hydrothermal conditions, using oxalic and citric acid as a reducing agents.

Following our experiments, we proposed the multi-step sequence given in §V.3.2.1 to explain the formation of the several species. This sequence can easily be understood based on simple mechanisms like (de) hydration and reduction process and can account for the obtained phase diagram as sketched in **Figure 8.** In this picture, the reduction process is mostly governed by the increase in temperature while the hydration/dehydration processes depend both on time and temperature. The superimposition of both mechanisms, even with such low level approximation in the T-t dependence of the several processes, highlights several regions which reasonably match with the observations.

V.3.3. Time dependent studies

In order to better understand the influence of reaction time on the transformation sequence and on the particles morphology, a series of experiments was carried out. The synthesis protocol used is the same than in **§V.3.1** however, the reaction temperature was fixed at 220°C to focus on the dehydrated compounds while the reaction time varied in {0.5, 1, 2, 3, 3.5, 7.5, 15, 23, 30, 60, 120 h}.

V.3.3.1. Results with oxalic acid as reducing agent

Figure 9 shows the P-XRD patterns of the samples obtained after various experimental durations from 0.5 to 120 h.
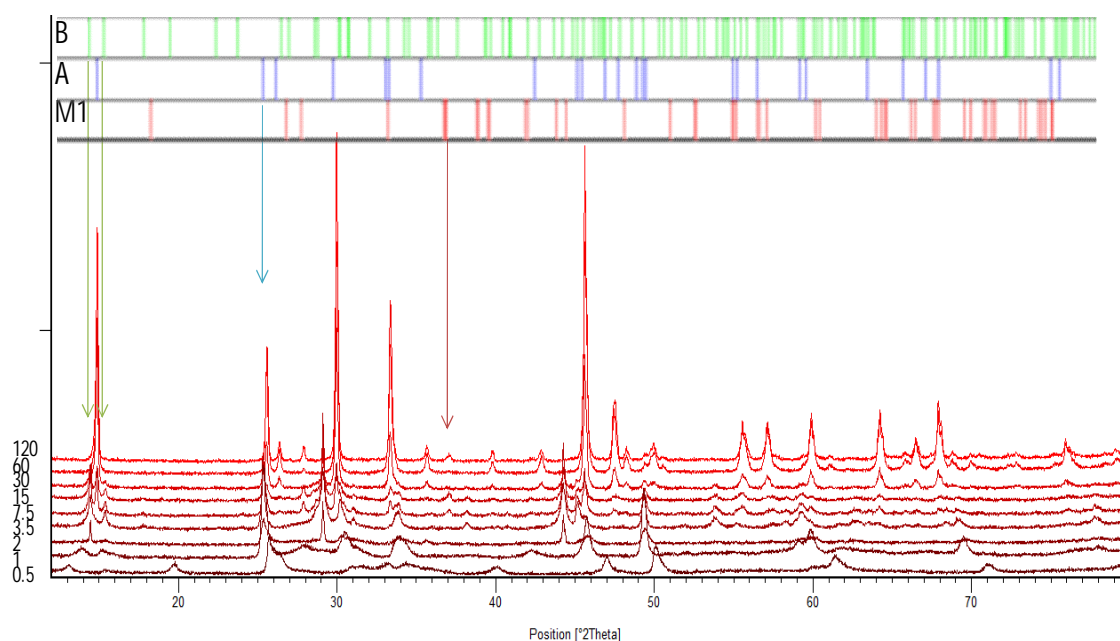
Figure 9. P-XRD patterns of the as-obtained samples using oxalic acid at various experimental durations from 0.5 to 120 h. Top panel gives the Bragg position for A, B and M1 compounds and the arrows point characteristic features for each like the low angle doublet in the case of B polymorph.

The mixed valence hydrate is first obtained after only 30 min reaction. It begins to transform within the first hour to VO_2 (B+hydrate) and the B polymorph is finally obtained pure after only 2 hrs treatment. The crystallinity of this polymorph slowly increases and then it starts to transform into VO_2 (A) with some traces of VO_2 (M1). The complete transformation of B into A and M1 polymorphs is obtained after 60 h. This transformation sequence agrees with our

previous experiments for the early stages up to B polymorph and the available literature concerning a possible {B, A, M1} chain [19,20], however the transformation mechanisms at an atomic scale are not yet fully understood.

The particles morphology after treatment is shown in **Figure 10** for different reaction times. The initial reactant V_2O_5 is a fine powder with a particle size of about 300 μm. After 30 minutes much smaller sand-rose-like $V_{10}O_{24}.9H_2O$ particles are obtained (**Figure 10a**), When VO_2 (B) begins to form the morphology progressively changes with a gradual reduction of the thickness of the substructures forming the sand-roses to peelings (**Figure 10b-c**). As the reaction time increases, when mostly A and M1 polymorphs are present, the particles transform to belt-like (**Figure 10d**). Further increase of reaction time increases the M1 to A ratio and simultaneously the particles morphology evolve to urchin-like (**Figure 10e**) and finally microrods (**Figure 10f**).
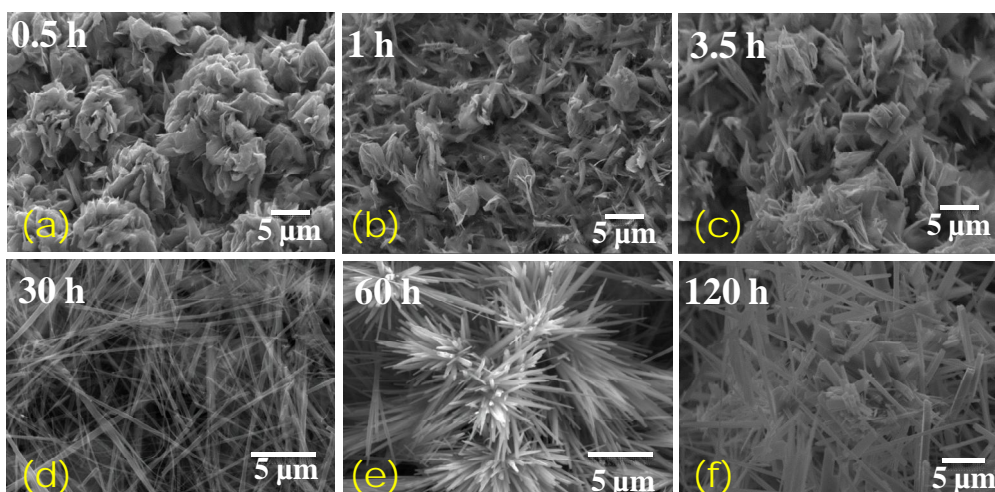
Figure 10. Morphology of the particles after hydrothermal treatment of V_2O_5 and oxalic acid at 220°C during (a) 0.5 h; (b) 1 h; (c) 3.5 h; (d) 30 h; (e) 60 h; (f) 120 h.

Combining the time-dependent morphology and phase evolution studies, it is clear that the formation of multiple morphologies from sand-rose-like to microrods can be rationally expressed as a surface modification of the precursor with further exfoliation and finally an attachment growth mechanism.

V.3.3.2. Results with citric acid as reducing agent

Figure 11 shows the P-XRD patterns obtained using citric acid as a reducing agent. The first formed compound after 30 min is $VO_2.xH_2O$; thanks to the more reducing nature of citric acid as compared to oxalic acid.
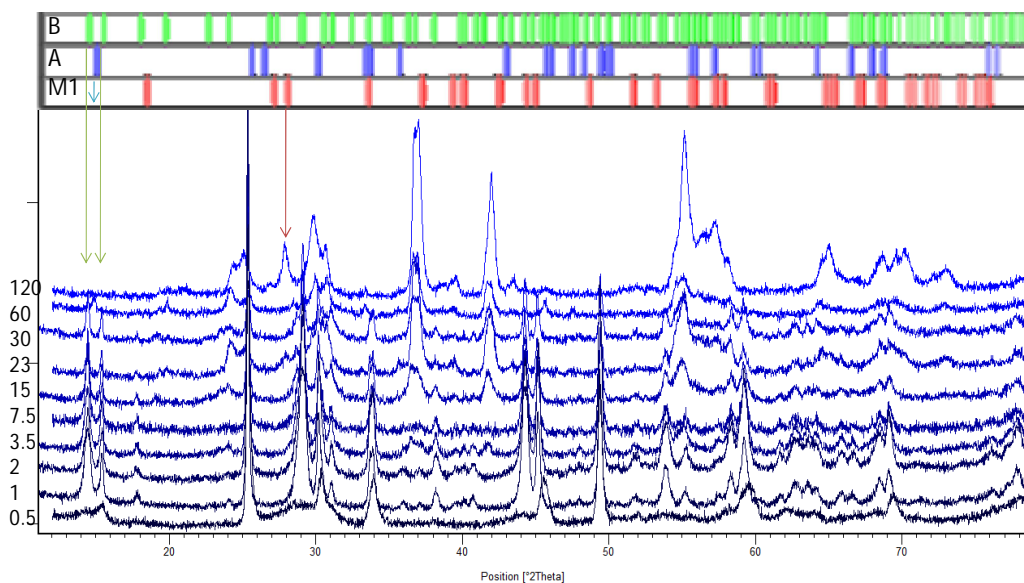

Figure 11. P-XRD patterns of the as-obtained samples using citric acid at various experimental durations from 0.5 to 120 h. Top panel gives the Bragg position for A, B and M1 compounds and the arrows point characteristic features for each, like the low angle doublet in the case of B polymorph.

VO_2 (B) forms after only 1 h reaction; this is both the fastest and lowest temperature condition ever reported for the synthesis of VO_2 (B). The phase is stable at least until 7.5 h after when it transforms progressively to A polymorph; this transformation is completed at 60 h. Increasing further the reaction time leads to the transformation of VO_2 (A) to VO_2 (M1) and VO_2 (N).

Figure 12 shows the SEM images of the different products and highlights the strong influence on morphology of the use of citric acid. The first compound $VO_2.xH_2O$ has flower-like particles most probably arising from an exfoliation process (**Figure 12a**). When the reaction time increases VO_2 (B) particles change to flake-like (**Figure 12b**), sphere that may result from the aggregation of the flake-like particles from Ostwald ripening process (**Figure 12c**), and finally compact sand-roses (**Figure 12d**). VO_2 (A) particles are like small sticks that aggregates into

bigger spheroid particles (**Figure 12e**). Finally at 120 h well known star like particles of VO_2 (M1) appear.
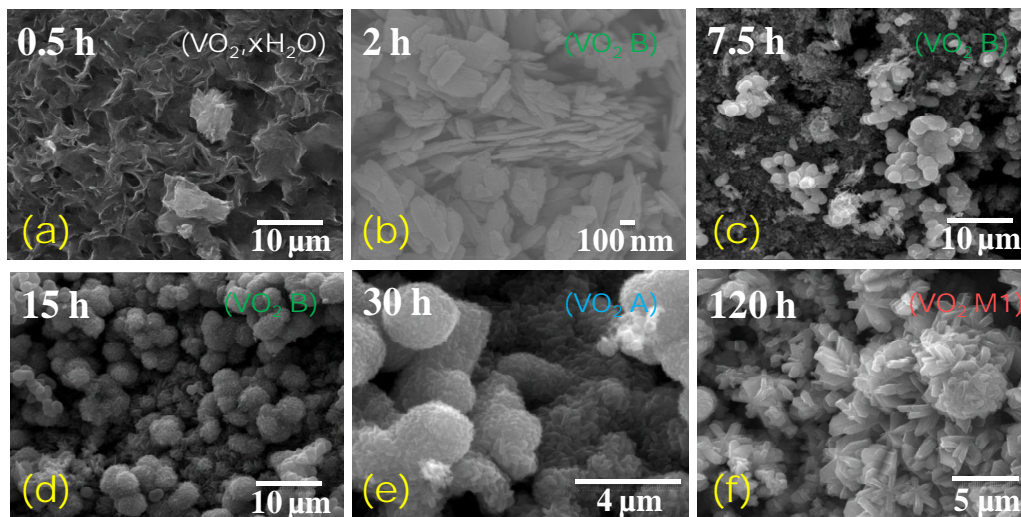
Figure 12. Morphology of the particles after hydrothermal treatment of V_2O_5 and citric acid at 220°C during (a) 0.5 h; (b) 2 h; (c) 7.5 h; (d) 15 h; (e) 30 h; (f) 120 h.

V.3.3.3. Summary

The observations resulting from the use of either RA are summarized in **Figure 13**. It clearly highlights that the use of citric acid contracts "time" with the early appearance of VO_2 hydrate, the fast growth of pure VO_2 (B), the possibility to isolate the pure A polymorph and most probably the pure M1 polymorph in the time window 60-120 h. In addition traces of the new N polymorph are also visible with the longest reaction time; no attempt with longer time was anyway carried out to isolate it. These results match with the sequence {1, 2, 3b} proposed in §V.3.2 and suggest two further steps with the transformation of A to M1 and next the transformation of M1 to N. Our results also highlight the possibility to control the particles shape (flowers, urchins, stars...) and dimensionality (flakes, peelings, rods, spheres...) playing both with the reaction time and the nature of the RA. Finally, we emphasize again that the combine use of {citric acid, 220 °C, 2 h, V_2O_5:RA=1:1.5 with [V_2O_5]=0.06mol/L} is the softest condition ever reported to synthesize VO_2 (B) polymorph.
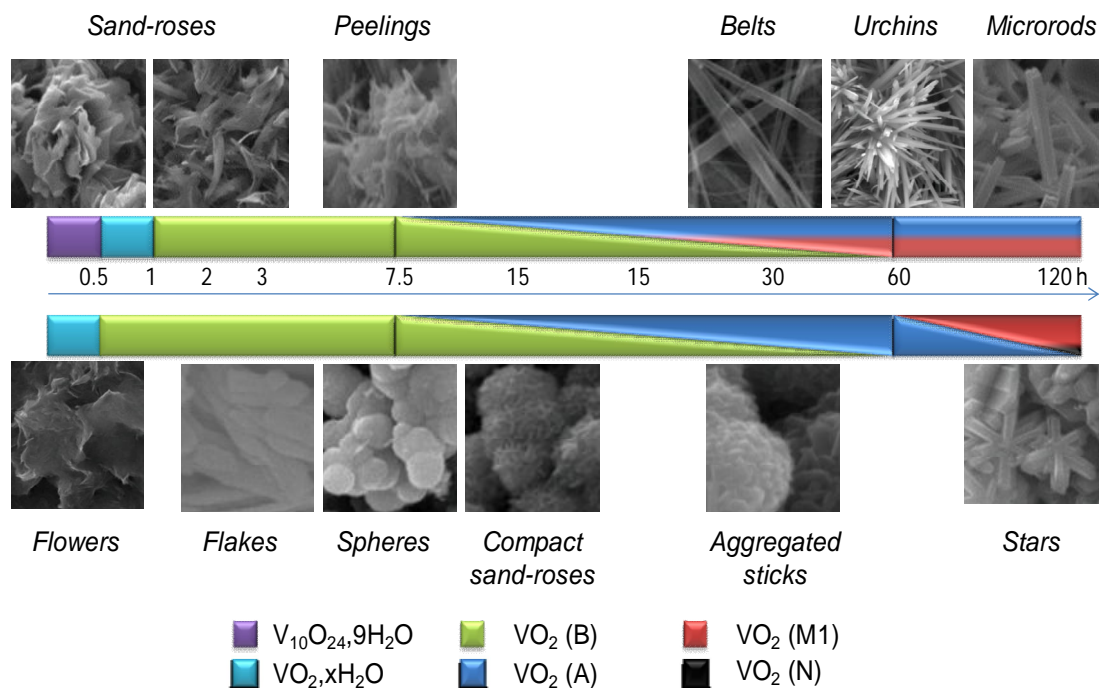
Figure 13. Summary of the time dependent studies with top the results with oxalic acid and bottom the results with citric acid.

V.3.4. Study of the precursors effect

The only available related reports are (i) the one of Ji et al. [21] who observed that with ratios higher than 1:3 only valence lower than 4+ for vanadium can be stabilized and (ii) the one of Changzheng Wu et al. [22] who studied the effect of HNO_3 addition using a $V(OH)_2NH_2$ precursor and observed the transformation sequence VOOH $\rightarrow$ VO_2 (N) $\rightarrow$ VO_2 (M1) $\rightarrow$ $V_3O_7.H_2O$. In a similar manner, we present for both RAs the analysis of the vanadium to RA ratio effect and the total precursors' concentration effect at fixed ratio.

V.3.4.1. Study of the effect of the vanadium to reducing agent ratio

The synthesis details are as in §V.3.1 except that the proportion of the precursors is allowed to vary as summarized in **Table 3**. The temperature was fixed at 250°C for 24 h (in the top-right T-t domain, the increase in temperature compensates for the time shortening as far as only the isolation of a specific compound matters).

V$_2$O$_5$	2.6										
Oxalic acid			2.6	3.9		6.5	7.8	9.1	11.7	19.5	23.4
Ratio			**1**:1	**1**:1.5		**1**:2.5	**1**:3	**1**:3.5	**1**:4.5	**1**:7.5	**1**:9
Citric acid	0.26	1.3	2.6	3.9	5.2						
Ratio	**1**:0.1	**1**:0.5	**1**:1	**1**:1.5	**1**:2						

Table 3. Precursors content in mmol for 0.43 mL of deionised water.

V.3.4.1.1. Results with oxalic acid as reducing agent

The P-XRD patterns for all the samples are shown in **Figure 14**. For a 1:1 ratio the majority phase is VO$_2$ (A) with minor amount of V$_6$O$_{13}$; this can easily be understood from the insufficient amount of reducing agent to reduce all the V^{5+} ions into V^{4+}.
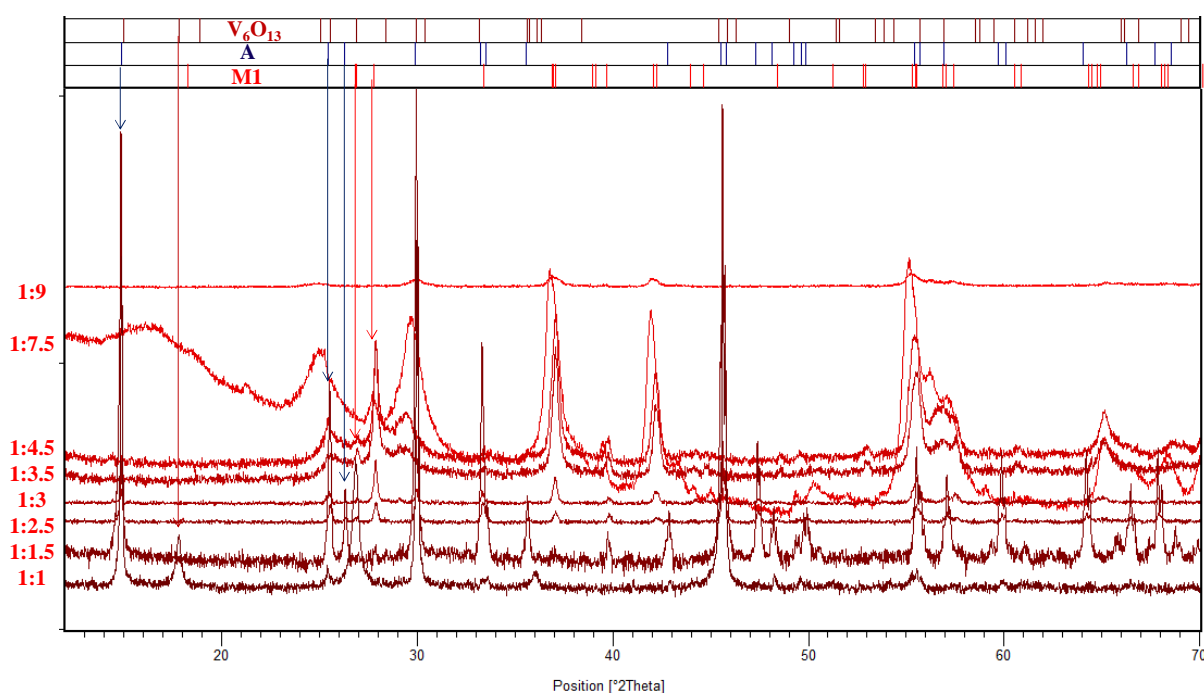

Figure 14. P-XRD patterns of the samples obtained at 250°C/24 h from increasing the V$_2$O$_5$ to oxalic acid ratio from 1:1 to 1:9.

When the ratio increases to 1:1.5 pure VO$_2$ (A) is obtained. With further increase up to 1:3, VO$_2$ (A) transforms into VO$_2$ (M1) (traces of VO$_2$ (B) also appeared for the 1:3 ratio only).

With higher ratios, the A polymorph is not anymore visible and only M1 and N polymorphs are observed with an increasing N/M1 ratio with the RA amount; finally, for the 1:9 ratio, only VO_2 N remains. These results agree with the last steps of the sequence proposed in §V.3.2: VO_2 (A) → VO_2 (M1) → VO_2 (N).

Figure 15 illustrates the change in the morphology on going from A to M1 and N polymorphs with respectively microrods, stars and spherical particles. These morphologies are similar to the ones already reported [23] and several mechanisms has been proposed to explain their formation such as the Kirkendall effect [24,25], corrosion-based inside-out evacuation [26,27], oriented attachment and Ostwald ripening process [28,29,30]. The TEM images at bottom of **Figure 15** shows for instance the existence of interconnected nanorods in a single microrod; this reveals an oriented attachment type formation mechanism as already proposed for the formation of VO_2 (A) ultra-long nanobelts [31]. The formation of VO_2 (M1) star like particles is more likely related to a dissolution-nucleation-recrystallization process.
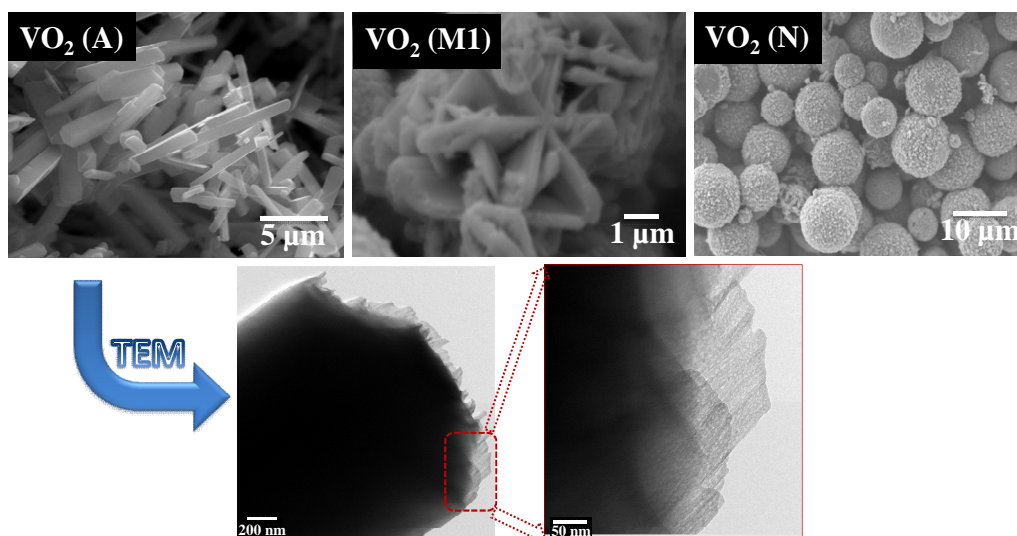
Figure 15. Top: SEM images of the samples synthesised at 250°C/24 h with V_2O_5 to oxalic acid ratios of (a) 1:1.5 {VO_2 (A)} (b) 1:3.5 {VO_2 (M1)} (c) 1:9 {VO_2 (N)}. Bottom: TEM image of (left) extremity of a single VO_2 (A) micro-rod and (right) zoomed region on tips of VO_2 (A).

We tried to optimize the conditions for the preparation of pure VO_2 (M1) with the 1:3.5 ratio increasing solely the reaction time from 24 h to 72 h. **Figure 16** shows the resulting P-XRD patterns. Unexpectedly, rather than forming VO_2 (M1), VO_2 (A) was stabilized. This result suggests that the RA strongly boosts the transformation sequence but leave the system in a

highly non-equilibrated state and that the additional time only serves the return to equilibrium. Such proposition could also help to understand the presence of the VO_2 (B) traces above mentioned with some beginning of relaxation.
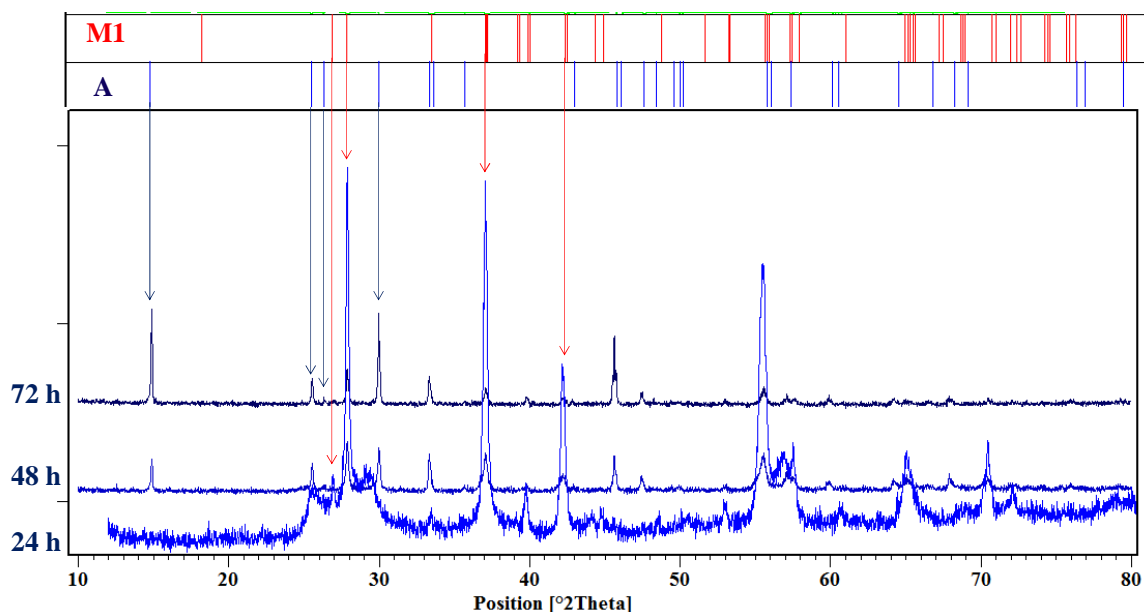
Figure 16. P-XRD patterns of the samples obtained at 250 °C with V_2O_5 : oxalic acid = 1:3.5 after various reaction time from 24 to 72 h.

V.3.4.1.2. Results with citric acid as reducing agent

The results when using citric acid are quite similar to the previous ones as shown in **Figure 7**. With the lowest/RA ratio, the first compound obtained is $V_3O_7.H_2O$ with nanowire shape (inset in **Figure 17**). Further increase in the ratio leads to the successive appearance of VO_2 (A), VO_2 (M1) and VO_2 (N) what perfectly matches with previous results and the already proposed transformation sequence.
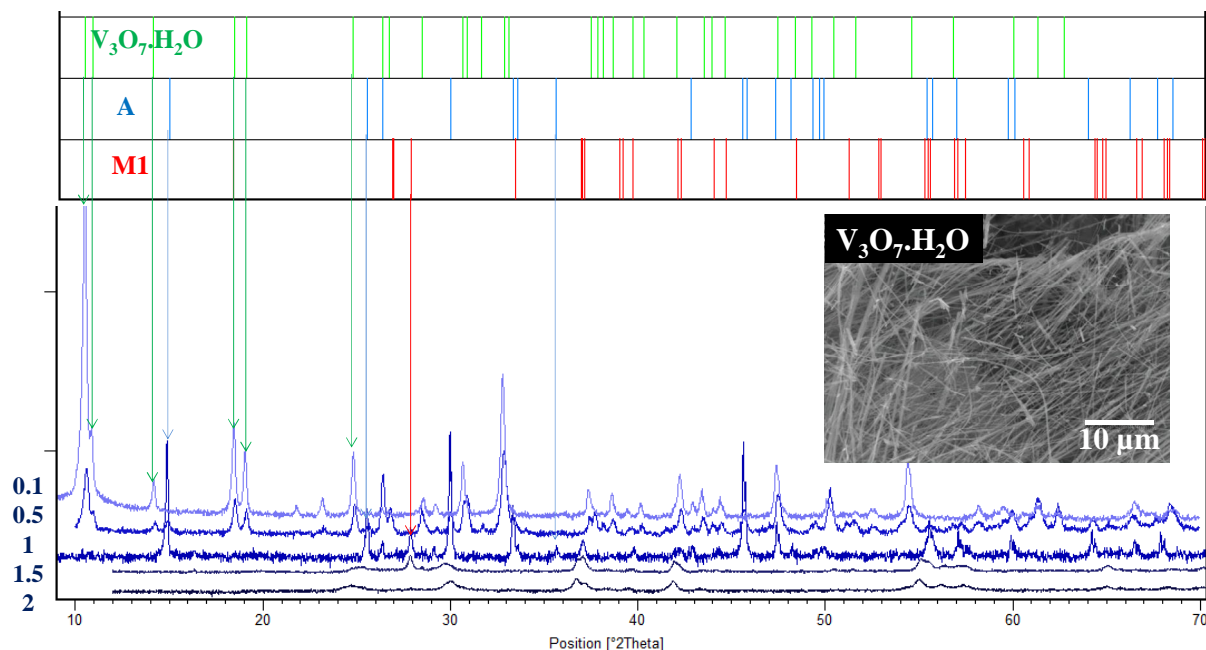
Figure 17. P-XRD patterns of the samples obtained at 250°C/24h from increasing the V_2O_5 to citric acid ratio from 1:0.1 to 1:2. Inset: SEM picture of $V_3O_7.H_2O$ for a 1:0.1 V_2O_5 to citric acid ratio.

V.3.4.2. Concentration dependent studies

The synthesis details are as in §V.3.2 except that the total concentration of the precursors is allowed to vary while keeping their ratio constant as summarized in **Table 4**.

Ratio	1:1.5	4:6	6:9	8:12	10:15	12:18	14:21
V_2O_5	2.6	10.4	15.6	20.8	26	31.2	36.4
RA	3.9	15.6	23.4	31.2	39	46.8	54.6

Table 4. Precursors content in mmol for 0.43 mL of deionised water.

The P-XRD patterns for all the samples are shown in **Figure 18** when RA is the oxalic acid. Only for the lowest precursors concentration a single VO_2 (A) phase is obtained otherwise mixtures of A and M1 up to 6:9 proportion and A, M1 and B otherwise are obtained. When citric acid is used, only M1/N mixtures were observed (**Figure 19**). This highlights that high concentrations offer lower control on the reaction and are unlikely to produce single phases.
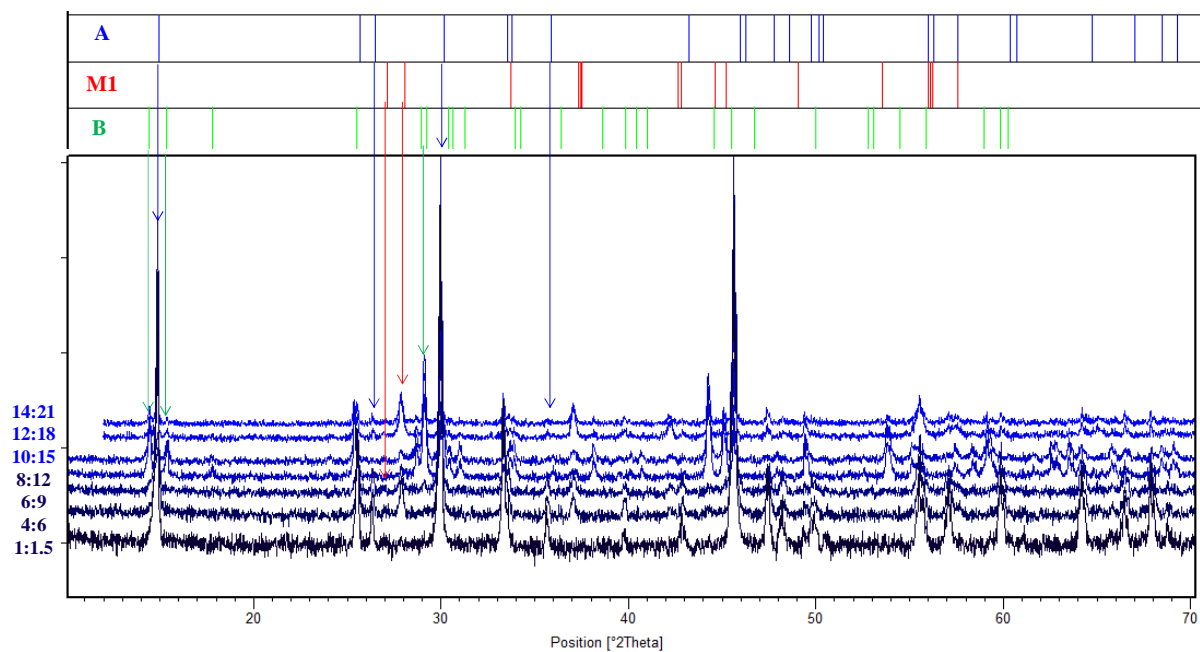
Figure 18. P-XRD patterns of the samples obtained at 250°C/24h with variable content inV_2O_5 and oxalic acid from 1:1.5 to 14: 21.
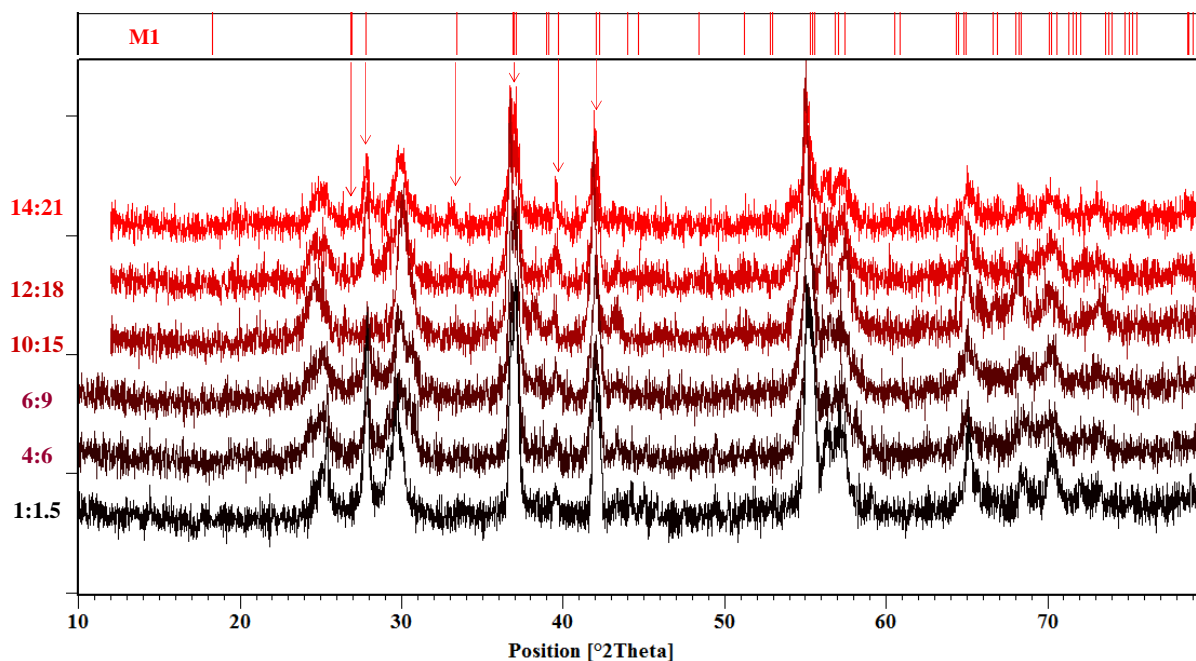

Figure 19. P-XRD patterns of the samples obtained at 250°C/24h with variable content inV_2O_5 and citric acid from 1:1.5 to 14: 21.

V.3.5. Summary of synthesis conditions

The following **Table 5** summarizes our optimized conditions to obtain a number of (almost) pure hydrate and non-hydrate vanadium oxides with possibly different particle shapes.

Quantity of water = 43 ml			Filling percentage of autoclave = 70 %			
Phase	V_2O_5 (mmol)	Oxalic acid (mmol)	Citric acid (mmol)	T (^{o}C)	t (h)	Morphology
$V_{10}O_{24}.9H_2O$	2.6	3.9		220	0.5	Flower like
$VO_2.xH_2O$	2.6		3.9	220	0.5	Urchin like
VO_2 (B)	2.6	3.9		220	3.5	---
	2.6		3.9	220	1-7.5	Platelets
VO_2 (A)	2.6	3.9	---	220	60	Micro needles
	2.6	3.9	---	250	24	Microrods
VO_2 (M1) (minor VO2 (N))	2.6	9.1	---	250	24	Star like
VO_2 (N)	2.6	23.4	---	250	24	Micro spheres
	2.6	---	5.2	250	24	---
$V_3O_7.H_2O$	2.6	---	0.26	250	24	Nanowires
V_2O_5 (partial)	2.6	---	---	250	24	Microrods
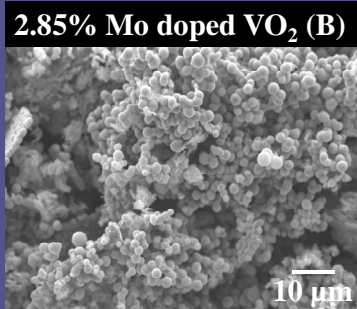
Table 5. Summary of optimized preparation conditions for several V-H-O phases.

V.3.6. Mo and Cr Substituted VO_2 (B), VO_2 (A) and VO_2 (M1)
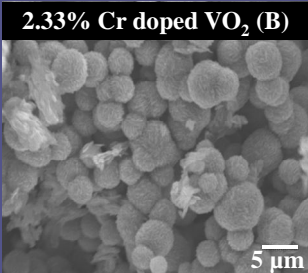
The substitution at V site is often one of the efficient ways to modify the phase transition behaviors and to stabilize the selective VO_2 polymorphs. To understand the influence of doping on the phase stability and morphology, we studied the effect of Mo and Cr substitution into VO_2 (B), VO_2 (A) and VO_2 (M1) under optimized hydrothermal preparation conditions.

The synthesis protocol used is the same than in §V.3.2 however, the reaction temperature was fixed at 220°C/ 3 h; 250°C/ 24 h and 250°C/ 24 h for substitution of VO_2 (B); VO_2 (A) and VO_2 (M1) respectively. To prepare Mo and Cr doped polymorphs, under continuous magnetic stirring we added sources of Mo (MoO_3) and Cr (CrO_3 or Cr ($NO_3)_3$) with different Mo/V and Cr/V molar ratios, respectively. To study the phase conversion mechanism from doped VO_2 (B) to VO_2 (M1) samples, we annealed the products under a flow of argon flow at 1000°C for 2 h. The compositions of prepared Mo and Cr substituted samples are verified by ICP analysis.

At% of Mo in the solution	At% of Mo from ICP	Phase at RT (P-XRD)	After annealing at 1000ºC/2 h (P-XRD)	Morphology
0	0	VO$_2$ (B)	VO$_2$ (M1)	**2.85% Mo doped VO$_2$ (B)**
1	0.4	VO$_2$ (B)	VO$_2$ (M1)	
3	1.6	VO$_2$ (B)	VO$_2$ (M1)	
5	2.8	VO$_2$ (B)	VO$_2$ (M1)	
6.6	3.8	VO$_2$ (B)	VO$_2$ (M1)	
8	5.2	VO$_2$ (B)	VO$_2$ (M1)	
10	5.7	VO2 (B)	VO2 (M1)	10 µm
15	7.9	VO$_2$ (B)	VO$_2$ (M1)	

Table 6. Details about the composition, crystal structure and morphology of Mo substituted VO$_2$ (B).

At% of Cr in the solution	At% of Cr from ICP	RT phase (P-XRD)	Morphology
0	0	VO$_2$ (B)	**2.33% Cr doped VO$_2$ (B)**
1	0.5	VO$_2$ (B)	
2	0.9	VO$_2$ (B)	
4	1.5	VO$_2$ (B)	
6	2.3	VO$_2$ (B)	
8	2.4	VO$_2$ (B)	
10	2.9	VO$_2$ (B)	5 µm

Table 7. Details about the composition, crystal structure and morphology of Cr substituted VO$_2$ (B).

Atomic % of Mo in the solution	Atomic % of Mo from ICP	Phase at RT (P-XRD)
0	0	VO$_2$ (A)
1	0.4	VO$_2$ (A) + VO$_2$ (M1)
3	0.5	VO$_2$ (B) + VO$_2$ (M1)
5	1.7	VO$_2$ (B) + VO$_2$ (M1)
6.6	2.7	VO$_2$ (B) + VO$_2$ (M1)
8	3.6	VO$_2$ (B) + VO$_2$ (M1)
10	3.5	VO$_2$ (B) + VO$_2$ (M1)

Table 8. Details about the composition, crystal structure and morphology of Mo substituted VO$_2$ (A).

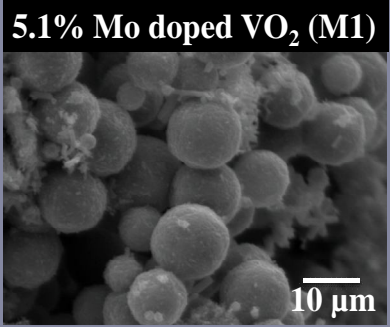| At% of Mo in the solution	At% of Mo from ICP	Phase at RT (P-XRD)	Morphology
0	0	VO_2 (M1)	
3	2.3	VO_2 (R)	
6	3.4	VO_2 (R)	
10	5.2	VO_2 (R)	
14	8.8	VO_2 (R)	
20	9.3	VO_2 (R)	
30	13	$V_{2-x}Mo_xO_5 + V_{1-x}Mo_xO_2$ (R) (24 h) $V_{1-x}Mo_xO_2$ (R) (48 h)	
50	------	$V_{2-x}Mo_xO_5 + V_{1-x}Mo_xO_2$ (R) (24 h)	

5.1% Mo doped VO$_2$ (M1)

10 µm

Table 9. Details about the composition, crystal structure and morphology of Mo substituted VO_2 (M1).

Atomic % of Cr in the solution	Atomic % of Cr from ICP	Phase at RT (P-XRD)	Phase after annealing at 1000°C for 2 h (P-XRD)
0	0	VO_2 (M1)	VO_2 (M1)
5	3.1	VO_2 (B)	VO_2 (M2)
10	4.5	VO_2 (B)	VO_2 (M2)
15	7.4	VO_2 (B)	VO_2 (M4)
20	9.5	VO_2 (B)	---

Table 10. Details about the composition and crystal structure of Cr substituted VO_2 (M1), before and after annealing under argon atmosphere.

From P-XRD patterns of as-prepared Mo substituted VO_2 (B) samples until 7.9 % of Mo content {**Table 6**} and Cr substituted VO_2 (B) until 2.9 % of Cr {**Table 7**}, the crystal structure of VO_2 (B) phase is stable at room temperature. After annealing, all the Mo substituted VO_2 (B) compositions are yield VO_2 (M1) phase and well matched with JCPDS card number: 01-082-0661. Mo and Cr doping had strong influence on the morphology of the VO_2 (B) products. The morphology was changed from platelet like shaped particles in pure VO_2 (B) to spherical like particles in the case of Mo and Cr doped VO_2 (B).

On the other hand VO_2 (A) is unstable against small concentration of Mo substitution, as low as 0.36 atomic % of Mo. From P-XRD studies we noticed the appearance of bi-phases between either A and M1 or A and B phases {**Table 8**}. For Mo substituted VO_2 (M1), the

stabilization of VO_2 (R) (JCPDS No. 01-076-0678) phase to room temperature between 2.3-13 % of Mo concentration shows the large suppression of phase transition temperature. Interestingly when the nominal concentration of Mo is higher than 30% was introduced in the solution, we noticed the formation of Mo doped V_2O_5 (PDF: 00-050-0535) and Mo doped VO_2 phases at 250^oC for 24 h reaction duration. These kinds of observations are indicating that, at higher doping concentrations, Mo doping into V_2O_5 lattice is more favourable. By increasing the duration of the reaction from 24 h to 48 h, reduction process progresses, intern we obtained pure VO_2 (R) for 30% Mo nominal composition {**Table 9**}. The morphology of Mo doped sample composed of uniform VO_2 (R) micro-spheres.

The substitution of VO_2 (M1) lattice with Cr under hydrothermal conditions is gives rise to important and very interesting structural modifications. Between 5-20 % of nominal compositions, we noticed VO_2 (B) phase using both CrO_3 and Cr $(NO_3)_3$ as Cr sources. In order to study and evaluate the possible phases those will be formed after thermal annealing, we annealed the prepared compositions of Cr doped VO_2 (B) (obtained by Cr doped VO_2 (M1)) under argon atmosphere for 2 h. As we have shown in the **Table 10**, for 3, 4.5 and 7.39 % of Cr substituted VO_2 (B) samples, we obtained VO_2 (M2) (C2/m), VO_2 (M2) (C2/m) and VO_2 (M4) (P2/m) respectively. These kinds of transformed phases are exactly in agreements with structural phase diagram for $V_{1-x}Cr_xO_2$ proposed by J.B. Goodenough et al. [32]. The morphology of the as synthesized 3% Cr doped VO_2 (B) products and after annealing (VO_2 (M2)) was presented in **Figure 20**.
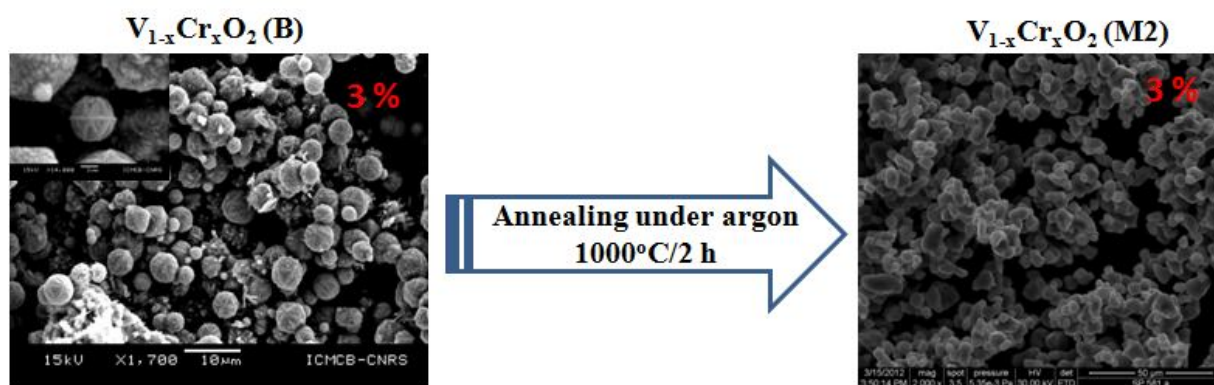
Figure 20. SEM morphology studies of 3% Cr doped VO_2 (B) prepared by hydrothermal process andVO_2 (M2) samples obtained by thermal annealing.

V.4. Conclusions

From oxalic and citric acid kinetic phase diagrams, the formation of different phases can actually be described with a three step process from partial reduction-hydration to complete reduction-hydration and finally dehydration: $V_2O_5 + H_2O \rightarrow V_{10}O_{24}. 9H_2O$; $V_{10}O_{24}. 9H_2O + H_2O \rightarrow VO_2.xH_2O$; $VO_2.xH_2O + H_2O \rightarrow VO_2$ (B) & VO_2 (A). Using time depdendent studies (both oxalic and citric acid cases), the evolution of phases noted as $V_{10}O_{24}. 9H_2O \rightarrow VO_2.xH_2O \rightarrow VO_2$ (B) $\rightarrow VO_2$ (A) $\rightarrow VO_2$ (M1) $\rightarrow VO_2$ (N). Oriented attachment formation mechanism was noticed for the formation of VO2 (A) microrods.

We studied the influence of Mo and Cr doping on the phase stability, phase transition properties and morphological evolution of VO_2 (B), VO_2 (A) and VO_2 (M1) under hydrothermal conditions. In the case of VO_2 (B), we found that this polymorph is stable against Mo as well as Cr doping under prepared compositions and conditions. Mo content higher than 0.36 % led to the destabilization of VO_2 (A) phase and transformed into VO_2 (M1) and VO_2 (B) phases. Mo substitution into VO_2 (M1) lattice stabilizes VO_2 (R) and on the other hand, Cr substitution in to VO_2 (M1) lattice stabilized VO_2 (B) under hydrothermal conditions.

V.5. Prospectives

These kinds of exploration studies can be extended to high temperature and high pressures (by simply changing the filling percentage of auto clave) to develop new kinds of hydrate, non-hydrate phases and even Magneli or Wadsley phases of vanadium oxides.
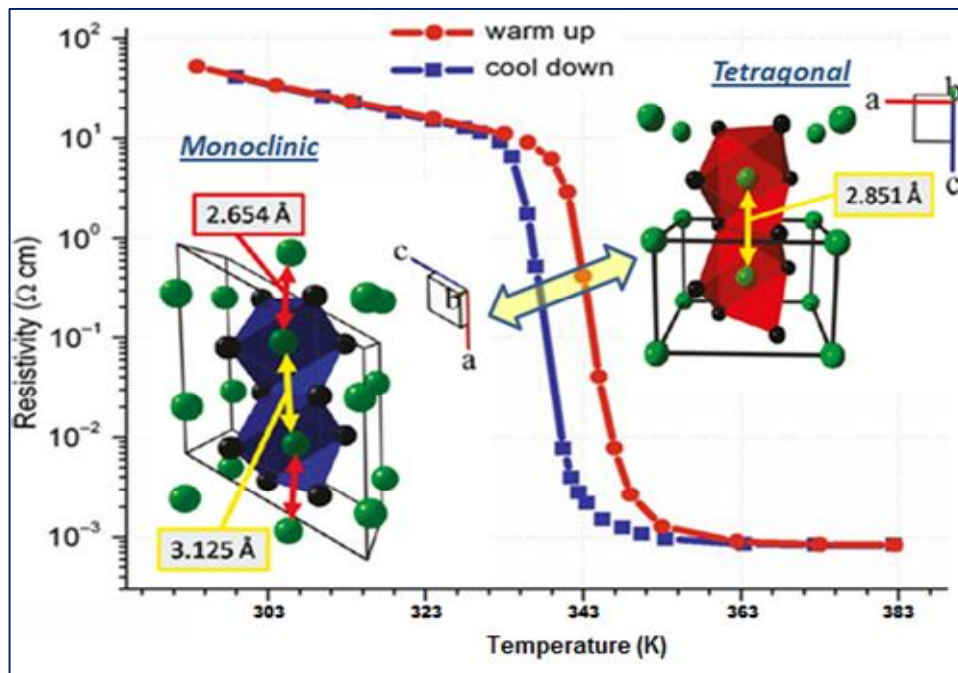
V.6. References

[1] B.O. Marinder, Mat. Res. Bull. 10, 909 (1975)

[2] J.B. Goodenough, F. Rivadulla, E. Winkler and J-S. Zhou, Europhys.Lett. 61, 527 (2003)

[3] K. Byrappa, I. Yoshimura, and M. Yoshimura. Handbook of Hydrothermal Technology. William Andrew Publishing, New York (2001)

[4] J. Livage, Materials 3, 4175 (2010)

[5] L. Bouhedja, N. Steunou, J. Maquet, J. Livage, J.Sol.Stat.Chem. 162, 315 (2001)

[6] F. Theobald, J Less-Common Met. 53, 55 (1977)

[7] Y. Oka, S. Sato, T. Yao, N. Yamamoto, J. Solid State Chem. 598, 594 (1998)

[8] F. Theobald, R. Cabala, J. Bernard, J. Solid State Chem. 438, 431 (1976)

[9] L. Liu, F. Cao, T. Yao, Y. Xu, M. Zhou, B. Qu, B. Pan, C. Wu, S. Wei, Y. Xie, New J. Chem. 36, 619 (2012)

[10] Y. Wang, Z. Zhang, Y. Zhu, Z. Li, R. Vajtai, L. Ci, P.M. Ajayan, ACS nano 2, 1492 (2008)

[11] Z. Gui, R. Fan, X.H. Chen, Y.C. Wu, J. Solid State Chem. 157, 250 (2001)

[12] Y. Gao, L. Bai, W. Li, H. Luo, P. Jin, J. Ceram. Soc. Jpn. 116, 395 (2008)

[13] W.G. Menezes, D.M. Reis, T. M. Benedetti, M.M. Oliveira, J.F. Soares, R.M. Torresi, A.J.G. Zarbin, J. Colloid Interface Sci. 337, 586 (2009)

[14] G.C. Li, S.P. Pang, Z.B. Wang, H.R. Peng, Z.K. Zhang, Eur. J. Inorg. Chem. 2005, 2060 (2005)

[15] C. Wu, Z. Hu, Z. Wang, M. Zhang, J. Yang, Chem. Commun. 3891 (2008)

[16] C. Wu, J. Dai, X. Zhang, J. Yang, Y. Xie, J. Am. Chem. Soc. 131, 7218 (2009)

[17] C. Wu, F. Feng, J. Feng, J. Dai, J. Yang, Y. Xie, J. Phys. Chem. C DOI: 10.1021/jp109967j (2010)

[18] Deschanvres, C. R. Seances Acad. Sci. (Paris), 261, 31 (1965)

[19] Y. Oka, T. Yao and N. Yamamoto, J. Mater. Chem., 1, 815 (1991)

[20] S. Zhang, B. Shang, J. Yang, W. Yan, S. Wei, Y. Xie, Phys Chem Chem Phys. 13(35), 15873 (2011)

[21] S. Ji, F. Zhang, P. Jin , Res Chem Intermed., 37(2), 493 (2012)

[22] C. Wu, X. Zhang, J. Dai, J. Yang, Z. Wu, S. Wei and Y. Xie, J. Mater. Chem. 21, 4509 (2011)

[23] S. Ji, F. Zhang, P. Jin, Journal of Physics and Chemistry of Solids 73, 762 (2012)

[24] Y. Yin, R.M. Rioux, C.K. Erdonmez, S. Hughes, G.A. Somorjai, A.P. Alivisatos, Science, 304, 711 (2004)

[25] J. Liu, F. Liu, K. Gao, J. Wu and D. Xue, J. Mater. Chem., 19, 6073 (2009)

[26] L.P. Zhu, H.M. Xiao, W.D. Zhang, G. Yang, S. Y. Fu, Cryst. Growth Des., 8, 957 (2008)

[27] Y. Xiong, B. Wiley, J. Chen, Z.Y. Li, Y. Yin, Y. Xia, Angew. Chem., Int. Ed., 44, 7913 (2005)

[28] X.W. Lou, Y. Wang, C. Yuan, J.Y. Lee, L.A. Archer, Adv.Mater., 18, 2325 (2006)

[29] H.G. Yang and H.C. Zeng, J. Phys. Chem. B, 108, 3492 (2004)

[30] R.L. Penn, J.F. Banfield, Science 281 (5379), 969 (1998)

[31] M. Li, F. Kong, L. Li, Y. Zhang, L. Chen, W. Yan, G. Li, Dalton Trans., 40, 10961 (2011)

[32] J. B. Goodenough, H.Y.P. Hong, Phys. Rev. B 8, 1323 (1973)

Chapter VI:
Mo substituted VO$_2$ (M1)-
Phase transition, metal-insulator transition studies and thermoelectric properties

The aim of this chapter is to present results related to correlations between structural phase transitions and metal insulator transitions in $V_{1-x}Mo_xO_2$ (M1). Here, I give details about the structural phase diagram for phases achieved by solid state route. I studied the changes in the valence degree of V and Mo using photoelectron spectroscopy. The structural phase transitions are investigated by in-situ X-ray diffraction studies and compared with the magnetic transitions, in order to understand the relation between structural and metal insulator transitions. Furthermore, I present the thermoelectric properties of the $V_{1-x}Mo_xO_2$ system, evaluated on spark plasma sintered pellets.

Contents

VI.1. Introduction

Bulk VO_2 (M1) is known to undergo a reversible insulator to correlated-metal transition (MIT) at temperatures close to 340 K [1], followed by a drastic changes in electrical and optical properties. The driving mechanism responsible for the metal-insulator transition has long been argued whether being of Mott, Peierls or Mott-assisted Peierls nature. Based on crystal structural studies, the distinction between the two types of transitions is often hindered by structural inhomogeneity near the MIT. Here the structural inhomogeneity arises from the coexistence of both the low temperature insulating monoclinic phase and high temperature metallic tetragonal phase near the MIT [2]. For room temperature applications, MIT can be triggered by either reducing the particles size, electron substitution at V sites or fluorine substitution to oxygen anions, application of an electric field or optical excitation. Among these possibilities, substituting with higher valence elements such as W, Mo, and Nb is extensively studied.

In the case of W and Nb substituted VO_2, it was incontrovertibly established that the preferred valence of Nb and W are 5+ and 6+ respectively [3]. However, the existing reports about oxidation degree of Mo substitutional ions in VO_2 are contradictory in nature: Manning et al. suggests a Mo valence of 4+ and Xu et al. have reported molybdenum valence as 6+ in their thin film samples [4]. A recent work by Holman et al. with up to 50 % of Mo content shows that Mo substitution will introduce major changes in the structural and electronic phase diagram of $V_{1-x}Mo_xO_2$. They noticed changes in the insulating as well as metallic phases; with increasing Mo content, the singlet insulator state transforms into a Curie-Weiss insulator, and intermediate mass metallic state converts into a Curie-Weiss metal for 50% Mo content. Even they claimed that the metallic phase has an average tetragonal symmetry but that short-range pairing of adjacent metal ions is still present [5]. Here, we attempted to address the effect of structural inhomogeneity on the metal-insulator transition and the impact of the correlated metallic phase generated by the Mo substitution on the thermoelectric properties.

VI.2. Experimental details

Powder X-ray powder diffraction (P-XRD) patterns of the final products were recorded using a PANalytical X'Pert PRO MPD diffractometer with graphite monochromatized Cu K_α radiation (λ=1.54178 Å) and phase purity of obtained products were identified by comparing the

experimental XPRD patterns to standards compiled by the Joint Committee on Powder Diffraction and Standards (JCPDS). The above mentioned P-XRD diffractometer was further used with an Anton-Paar high temperature and low temperature chamber under vacuum (9.2×10^{-5} bar) to study the phase transition between two different polytypes (M1 and R) of vanadium dioxide.

The morphology of the products and surface of the SPS pellets were examined by a field emission scanning electron microscope (FESEM, JEOL JSM - 6300F, 15 kV). The powder sample were deposited on double coated copper conductive tapes and subsequently sputter coated with a thin layer of gold on the surface to prevent the charging effects. The valence states of V and Mo were studied by means of X-ray photoemission spectroscopy (XPS) with a VG Escalab 220i XL X-Ray Photoelectron Spectrometer using an aluminium monochromatic source ($h\upsilon = 1486.6$ eV) with energy resolution 0.3 eV under ultrahigh vacuum conditions.

The $V_{1-x}Mo_xO_2$ (M1) powders were densified using Spark Plasma Sintering technique (SINTER® LAB Series; SPS-511S) (relative density $\geq$ 90%). Transport properties were measured on SPS sintered pellets. Electrical dc resistivity measurements were performed with the four-probe method in the 4-300 K range, while thermoelectric power measurements were collected with the homemade equipment previously described [6]. The measurements of magnetic properties and thermal conductivity/specific heat were carried out using Quantum Design Magnetic Property Measurement System (MPMS®) and Physical Property Measurement System (PPMS®), respectively.

VI.3. Structural studies: P-XRD

Crystallographic structures of Mo-substituted VO2 samples were examined by P-XRD, and the powder diffraction patterns were analyzed by the profile matching using FULLFROF-SUITE-2000 software [7]. **Table 1** summarizes the structural phase diagram of $V_{1-x}Mo_xO_2$ system at room temperature. Four distinct composition regions can be identified with Mo substitution: pure VO2 (M1) crystallizes in monoclinic crystal structure with space group P2₁/c. Between 7.5 to 65 % of Mo substitution, we obtained VO2 (R) phase which crystallizes in a tetragonal crystal structure with space group P4₂/mnm. Between 70 to 90% of Mo substitution, we noticed the mixture of phases which can be assigned with VO2 (R) phase with space group

P4$_2$/mnm and MoO$_2$ type monoclinic phase with space group P2$_1$/c. For higher Mo contents, i.e. between 90 and 100 %, we obtained MoO$_2$ phase with space group P2$_1$/c.

Compound	VO$_2$	V$_{1-x}$Mo$_x$O$_2$ (0.075≤x<0.65)	V$_{1-x}$Mo$_x$O$_2$ (0.70≤x<0.90)	V$_{1-x}$Mo$_x$O$_2$ (0.90≤x<1)
Crystal **structure** (300 K)	Monoclinic P2$_1$/c	Tetragonal P4$_2$/m n m	Tetragonal/ Monoclinic	Monoclinic P2$_1$/c (MoO$_2$)

Table 1. Structural phase diagram of VO$_2$-MoO$_2$ solid solution (V$_{1-x}$Mo$_x$O2; 0≤x≤1) at room temperature.

Figure 1a shows the P-XRD patterns of the pure monoclinic VO$_2$ (M1). To display the representative P-XRD patterns of the tetragonal phase VO$_2$ (R), we present the P-XRD pattern for 35 % Mo substituted VO$_2$ sample in **Figure 1b**.
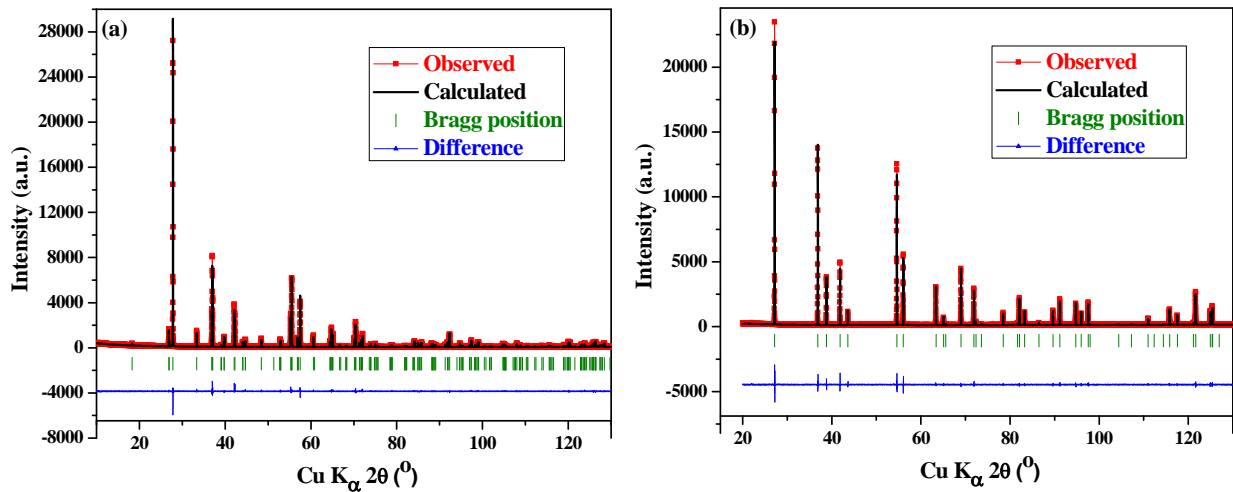
Figure 1. X-ray powder diffraction pattern of (a) un-doped VO$_2$ (M1) and (b) 35% Mo substituted VO$_2$ (V$_{0.65}$Mo$_{0.35}$O$_2$) prepared by solid state reaction process. The observed and calculated X-ray diffraction intensities are represented by red squares and black solid line, respectively. Green ticks indicate the positions of Bragg reflections. The blue solid line at the bottom shows the difference between observed and calculated intensities.

At room temperature, all P-XRD peaks for pure VO$_2$ (M1) can be indexed to monoclinic VO$_2$ (M1) phase, with lattice constants a=5.752 Å, b=4.526 Å, c=5.382 Å, β=122.6^o and space group P2$_1$/c. These details exactly match JCPDS standard with reference code 01-082-0661. Under Mo substitution, we notice a stabilization of a tetragonal phase at room temperature with space group P4$_2$/mnm (136). This shows the structural phase transition from monoclinic to

tetragonal along with Mo substitution. The overall variation of lattice parameters for $V_{1-x}Mo_xO_2$ (R) with $0.075 \leq Mo \leq 0.50$, at room temperature, is shown in **Figure 2**.
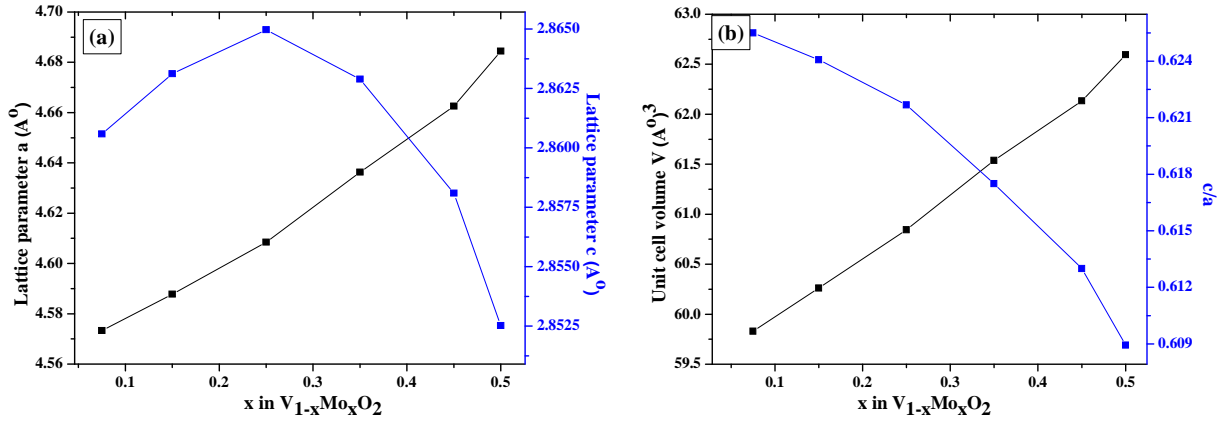
Figure 2. Evolution of (a) lattice parameters a and c and (b) unit cell volume and c/a ratios vs. Mo content in $V_{1-x}Mo_xO_2$.

In pure VO_2 (M1), the intensity of X-ray diffraction peak (011) suggests a preferred orientation that is progressively changed into (110), in case of rutile phase, with Mo substitution. Furthermore, in $V_{1-x}Mo_xO_2$, the position of the diffraction peak (110) changes regularly with x and no evidence is found for two phase domains at single composition, showing that phase separation does not occur and that the solid solution is formed until $V_{0.5}Mo_{0.5}O_2$ system. With Mo substitution, a and c lattice parameters show different variations; lattice parameter a increases monotonically. On the other hand, lattice parameter c, which defines the unit cell along the chain direction, increases linearly until 25% Mo content, and then drops almost linearly with increasing Mo content. The variation of lattice parameters does not follow Vegard's law in the whole Mo substitution range. From the crystal structure perspective, at RT, pristine VO_2 (MI) can be described as a distorted rutile structure built up of edge-sharing VO_6 octahedra with short and long V-V distances along the c axis (V-V = 2.65 Å and 3.12 Å). The Mo substitution stabilized rutile phase is built up of edge-sharing VO_6 octahedra with equidistant V atoms along the tetragonal c axis. Therefore, the Mo substitution has a major influence on the V-V pairing along the c-axis. In order to understand the effect of Mo substitution on combination of both a and c parameters and lattice volume, we have plotted in **Figure 2b** the variation of the c/a ratio and unit cell volume with Mo concentration. We notice that the unit volume increases linearly with the Mo content, similar to the variation of lattice parameter a. The c/a ratio decreases

continuously with increasing Mo concentration in the rutile phase. The absence of pronounced maximum in c/a rules out the possibility of an ordering between cations in $V_{1-x}Mo_xO_2$ until x=0.5. In order to get better insight into the possible ordering between V and substituted cations such as W, Nb and Mo, we compared the variation of c/a for $V_{1-x}W_xO_2$, $V_{1-x}Nb_xO_2$ and $V_{1-x}Mo_xO_2$ systems, as shown in **Figure 3**.
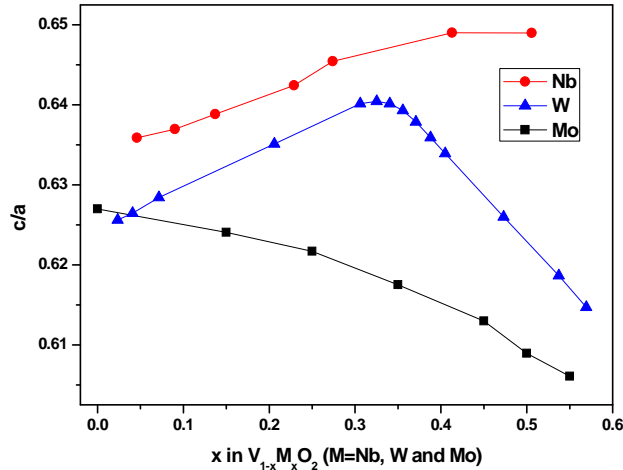
Figure 3. Variation of c/a ratios in $V_{1-x}M_xO_2$ (M=Nb, W and Mo).

For $V_{1-x}W_xO_2$, a clear maximum in c/a value is observed near x = 0.33. In this case, the maximum was attributed to the ordering of V^{3+} and W^{6+} cations, corresponding to the transfer of two d-shell electrons from W to neighbour V ions, to form V^{3+}-W^{6+} and V^{3+}-V^{4+} pairs according to $V^{4+}_{1-3x}V^{3+}_{2x}W^{6+}_xO_2$ [8]. In contrast, the $V_{1-x}Nb_xO_2$ system exhibits a slight maximum near x=0.5, even though no ordering between V^{3+} and Nb^{5+} ions were observed in P-XRD patterns. However, a modification of the electronic configuration with cationic distribution was noticed: for 0<x<0.5, the electronic configurations were assigned as $V_{1-2x}^{4+}V^{3+}_xNb^{5+}_xO_2$ for 0<x<0.5, and $V^{3+}_{1-x}Nb^{5+}_{1-x}Nb^{4+}_{2x-1}O_2$ for 0.5<x<1 [9]. In the present case, with Mo content the smooth decrement of c/a ratio is noticed. This variation is quite different compared to the effect of W and Nb substitution, despite their close ionic radii ($r_V^{4+}_{[VI]}$=0.58 Å; $r_{Nb}^{5+}_{[VI]}$=0.64 Å; $r_W^{6+}_{[VI]}$=0.6 Å; $r_{Mo}^{6+}_{[VI]}$=0.59 Å). Here the non-linear variation of lattice parameter along the chain direction could be related to a modification of the electronic configurations, within the cationic distribution in the solid solution. This shows the importance of dopant ion electronic structure on the alteration of structural phase transition behavior.

Morphology of the as-synthesized VO_2 (M1) polycrystalline powder samples prepared by solid state process is shown in **Figure 4a**. **Figure 4b** shows the morphology of the powder

samples obtained from grounding the SPS pellet. **Figure 4c** and **Figure 4d** shows the surface morphology of the pellet, obtained directly by the SPS treatment and after annealing this SPS pellet under vacuum for several hours. The average particle size of the bulk VO_2 powders prepared by solid state process and spark plasma sintering was found to be similar, around 20 µm. As shown in **Figure 4**c, the micro size grains of the sintered pellet are well attached to each other, and the surface porosity gradually decreases along with the annealing process (**Figure 4d**). The relative densities of pellets are more than 90%.
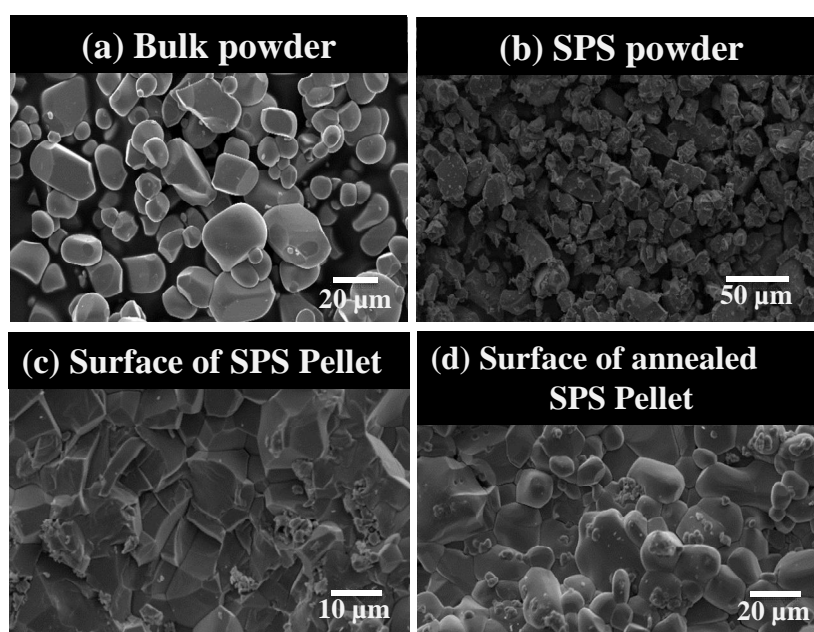
Figure 4. Morphologies of VO_2 powders prepared by (a) solid state process and (b) spark plasma synthesis. Surface of pellets after (c) spark plasma sintering and (d) annealing of the SPS pellet under Ar atmosphere.

VI.4. Spectroscopic studies: XPS

The XPS measurements were performed on SPS treated pellets of pure and Mo-substituted VO_2 samples. Samples were cleaved in ultra-high vacuum, so that the pellet surfaces were free from contamination of carbon. For energy calibration, the position of the Fermi energy E_F was determined using a clean gold foil and atmospheric carbon as reference. The high-resolution core-level XPS V 2p spectra and O 1s spectra were measured on pure VO_2, $V_{0.925}Mo_{0.075}O_2$ and $V_{0.85}Mo_{0.15}O_2$ and are depicted in **Figure 5**. In order to show the spectrums clearly, we subtracted the background contribution from photoelectrons inelastic scattering for

both V $2p_{3/2}$ and O 1s energy regions; a Shirley function was used. The V 2p line acquired on pure and Mo-substituted VO_2 samples consists of a doublet with binding energies of 515.7 and 523.2 eV for the V $2p_{3/2}$ and V$2p_{1/2}$ components, respectively.

The binding energy of the core levels depends on the ion oxidation state. In the present case, the profile fitting of the V$2p_{3/2}$ signal gives a binding energy corresponding to vanadium in the 4+ oxidation state. The binding energies of V 2p levels do not shift noticeably with an increase in Mo substitution rate, suggesting that almost all V ions remain at oxidation degree 4+, at least until 15 % of Mo substitution. In order to further confirm the oxidation degree of vanadium, we compared the difference between oxygen O 1s and vanadium $2p_{3/2}$ binding energies. This approach is recommended for the determination of the oxidation degree of vanadium oxides, because of the widely spread values in oxygen 1s as well as vanadium 3d binding energies available in literature. In the present case the difference is nearly 14.1 eV, which is further matching with the +4 oxidation state of vanadium [10]. On the other hand, the full width at half maximum (FWHM) of the V$2p_{3/2}$ line slightly increases with increasing Mo content and is more pronounced for 15% Mo. The width of a XPS core line depends upon several factors of intrinsic and instrumental nature: the lifetime of the core hole created during photoemission, X-ray line width, the finite resolution of the analyzer, etc. [11]. Here, the line width due to X-ray line width and resolution of the analyzer can be discarded as we have acquired all the spectra with the same source and energy resolution. It is well known that the FWHM of the XPS core line may increase due to either structural or chemical changes on the surface, i.e. reduction of elements on the surface of samples. The surface reduction is probably not the case here, as there is no noticeable difference in the V 2p level binding energy. Thus, the line broadening may be due here to structural changes and/or changes in distribution of ions due to the relatively high content of Mo in the samples. The increase in width of V 2p core levels can also be related to the decrease of the core-hole lifetime in Mo- substituted VO_2 compared to pure VO_2.

We also noticed a small change in the binding energy of the O 2p level, from 529.8 eV for pure VO_2 into 530.04 eV for Mo-substituted samples. This variation in the binding energy may due to presence of different kinds Mo oxidation ions [12]. In addition, the XPS spectrum for O 1s (**Figure 5b**) also indicates an asymmetric nature of the peak in the higher energy side. This peak tail cannot be attributed to surface oxidation, as V_2O_5 and VO_2 show the similar O 2p

binding energies. The tails here can be associated to surface pollution or some satellite feature in the V 2p spectrum.

In conclusion, from our XPS studies around V core levels, we did not observe any change in the oxidation degree of vanadium, which is present as 4+ for all studied compositions. The role of changes in chemical distribution of ions becomes significant for high Mo contents in our samples.
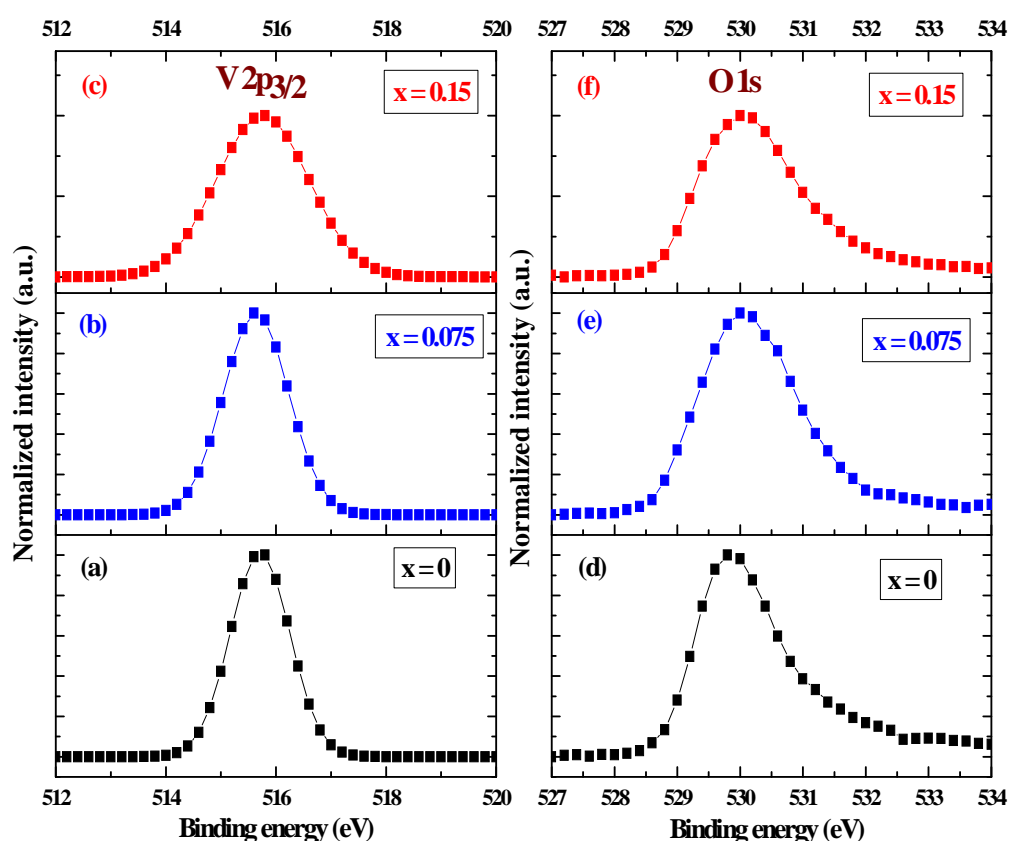
Figure 5. High resolution core-level V 2p and O 1s XPS spectra of the pure and Mo substituted vanadium dioxides $V_{1-x}Mo_xO_2$. Left panel: V $2p_{3/2}$ level in the case of (a) VO_2 (x=0), (b) $V_{0.925}Mo_{0.075}O_2$ and (c) $V_{0.85}Mo_{0.15}O_2$.Right panel: O 1s levels.
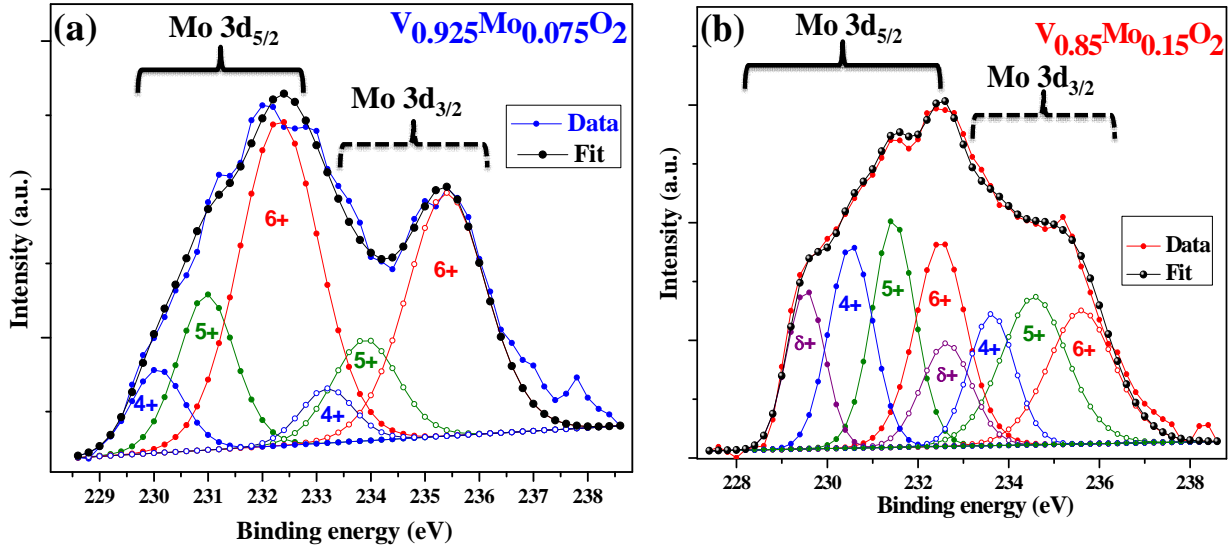
Figure 6. Typical core-level XPS spectrum in Mo 3d energy region, for (a)$V_{0.925}Mo_{0.075}O_2$; (b)$V_{0.85}Mo_{0.15}O_2$.

Figure 6 displays the XPS spectra of $V_{0.925}Mo_{0.075}O_2$ and $V_{0.85}Mo_{0.15}O_2$ samples around Mo 3d core levels. The de-convolution of the spectra are dominated by spin-orbit doublets Mo ($3d_{5/2}$ and Mo $3d_{3/2}$) with peaks at binding energies 232.5, 231.46, 230.52, and 235.6, 234.59, 233.62 eV, respectively. These peaks are associated with Mo in the formal oxidation states 6+, 5+, and 4+. For $V_{0.85}Mo_{0.15}O_2$, we even noticed binding energies less than Mo^{4+} values (229.55 and 232.62 eV); we assigned these as $Mo^{\delta+}$ (similar to Mo^{3+}). Our values of binding energy are close to the reported values [13]. From **Figure 6b** one can observe that, with increasing Mo substitution, there is a large change in the ratio between Mo^{6+}, Mo^{5+} and Mo^{4+}. This observation is in agreement with a fixed valence state V^{4+} for $V_{0.925}Mo_{0.075}O_2$ and $V_{0.85}Mo_{0.15}O_2$ samples and partial reduction of the Mo^{6+} to lower oxidation degrees of Mo ions; a mixed valence for Mo occurs in the prepared compositions.
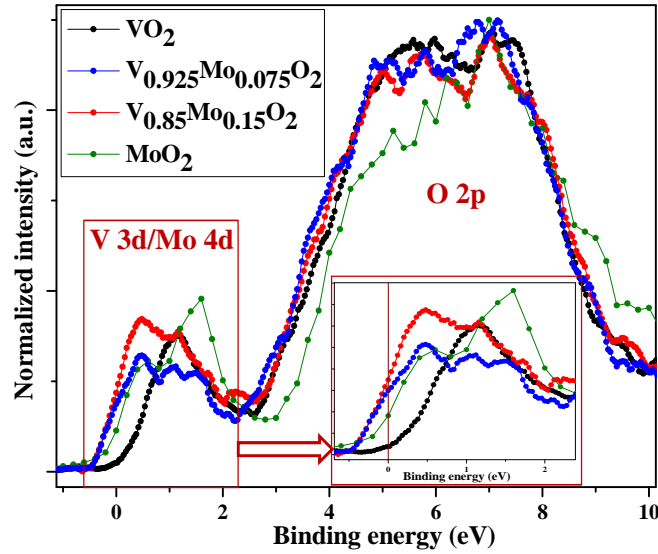
Figure 7. Normalized valence band region XPS spectra of VO_2, $V_{0.925}Mo_{0.075}O_2$, $V_{0.85}Mo_{0.15}O_2$ and MoO_2 taken at room temperature. The inset highlights the region near Fermi level, in order to compare the spectral weight for the mentioned samples.

Valence band XPS of VO_2, $V_{0.925}Mo_{0.075}O_2$ and $V_{0.85}Mo_{0.15}O_2$ are shown in **Figure 7**. These spectra were compared with the valence band spectrum of MoO_2 to gain insight in the valence state of Mo in Mo-substituted VO_2 compounds. For the four compositions shown here, the valence band region can be separated into two main regions; from 0-2 eV which can be assigned V 3d or Mo 4d levels; between 2-10 eV from the O 2p contribution. The only major changes in the valence band spectra, among all investigated compounds, occur in the region of Fermi level. These changes are related to V 3d and Mo 4d bands. No detectable changes associated with the Mo content were found for the O 2p bands. The negligible spectral weight at Fermi level in case of pure VO_2 is consistent with the semiconducting nature of pristine VO_2 at room temperature. The peak around 1 eV is purely due to V 3d states. For MoO_2, the metallic character corresponds to the finite density of states at the Fermi edge. Two intense and distinct bands at 0.55 and 1.53 eV, have been assigned to the two different Mo^{4+} sites in the MoO_2 lattice [14]. Along with Mo substitution in $V_{1-x}Mo_xO_2$, the spectral weight at Fermi level increases and corresponds to the metallic nature of samples at room temperature, in agreement with the decrease of MIT below room temperature for $V_{0.925}Mo_{0.075}O_2$ and $V_{0.85}Mo_{0.15}O_2$ compositions. Even from $V_{0.925}Mo_{0.075}O_2$ to $V_{0.85}Mo_{0.15}O_2$ samples, the intensity of the peak at 0.5 eV grows in intensity.

The increase in intensity with the Mo substitution reflects the increasing occupancy of the d states. This observation is consistent with an increase of the contribution of Mo^{5+} or Mo^{4+} with the increase of Mo concentration, as observed from the core level XPS spectra of Mo 3d levels. On the basis of the XPS measurements, we can observe strongly hybridized Mo 4d, V 3d and O 2p states. Very recently, a noticeable transfer of the V 3d spectral weight from the incoherent part to the coherent part was reported in case of W-substituted VO_2 compounds [15]. The valence band spectrum below 2 eV didn't show any contributions from V_2O_5 (V^{5+}) and MoO_3 (Mo^{6+}) as they are in the d^0 configuration. By combining these XPS results with the observations made in literature for lower concentrations of Mo- substituted VO_2, we can conclude that Mo is in 6+ oxidation state for lower contents and turns into a mixed valence states along increasing Mo content in $V_{1-x}Mo_xO_2$ [16].

VI.5. Phase transition studies

Structural and electronic inhomogeneities in correlated transition metal oxides have been the subject of a long standing and ongoing debate. In the present case, the samples were dispersed freely on a platinum strip and in situ P-XRD patterns were collected during heating cycle from room temperature to over 373 K. Here, the samples are free from any kind of stress, which would be responsible for stabilization of intermediate phases. All temperature-controlled P-XRD patterns shown for pure or substituted VO_2 are taken in the heating cycle; the sample temperature was monitored carefully with sufficient stabilization time at each measurement. We further investigated the structural inhomogeneity, across the phase transition, by substituting the VO_2 lattice with small concentration of W, Nb and Cr as impurity ions. We have chosen a very low concentration of substitution ions, since it has been shown that higher concentrations deteriorate the "quality" of the MIT. Here, the structural inhomogeneity was studied by using in-situ P-XRD and compared with the evolution of magnetic properties across the phase transition.
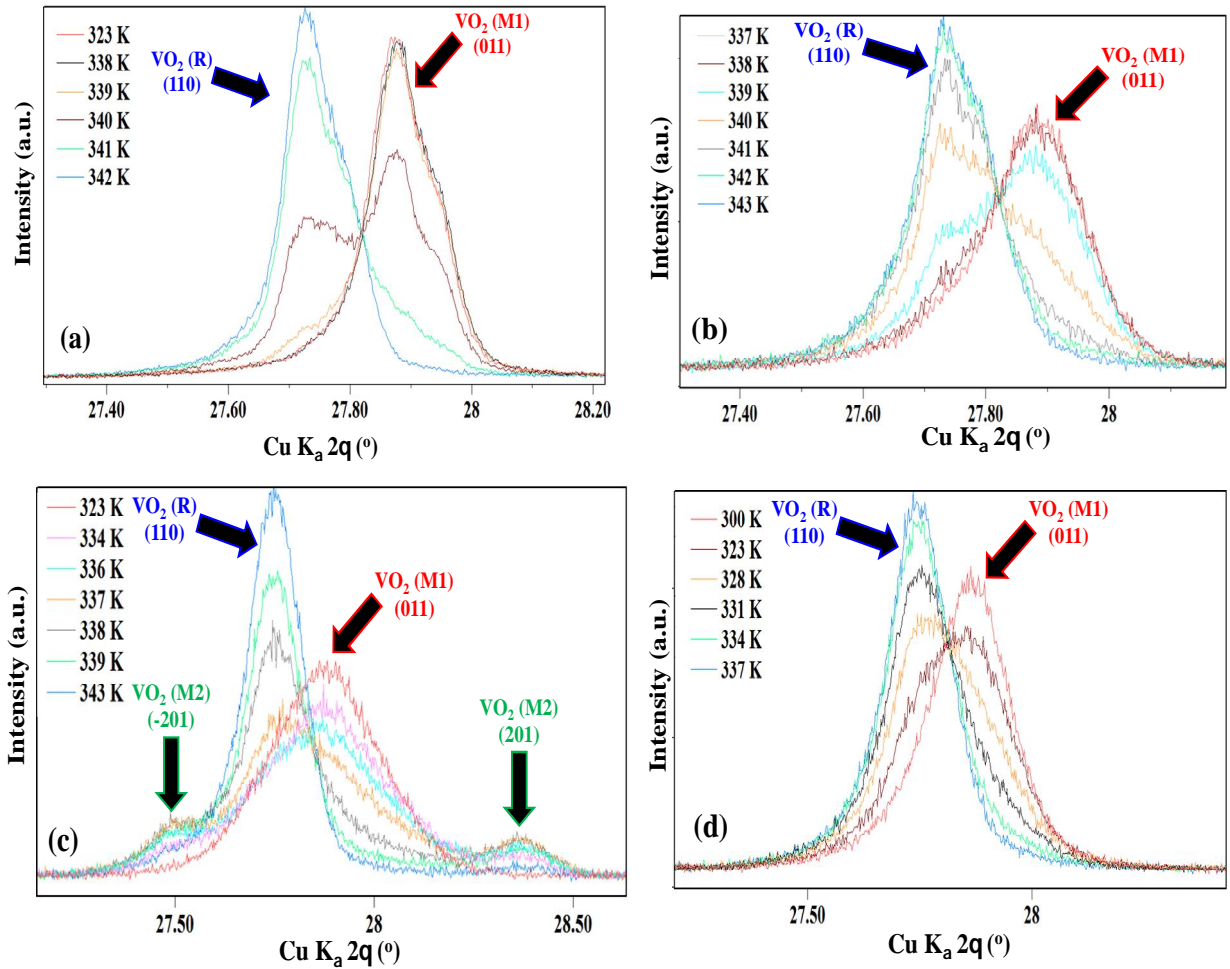
Figure 8. Changes in the (011) VO$_2$ (M1) reflection during in situ P-XRD vs. temperature: structural phase transition from VO$_2$ (M1) to VO$_2$ (R) in the case of (a) pure VO$_2$;(b) 0.5 % Nb- substituted VO$_2$ (M1); (c) in the case of 0.5 % Cr- substituted VO$_2$ (M1), through VO$_2$ (M2); (d) 0.5 % W- substituted VO$_2$ (M1).

Figure 8a shows the modification of the (011) reflection for VO$_2$ (M1) during the heating process. From room temperature to 338 K, no noticeable changes in the peak intensity or position were found. At 340 K, the intensity of the diffraction peak of M1 (011) reflection decreases drastically and splits into two different peaks that correspond to a mixing of M1 (011) reflection and R (110) reflection; this indicates the co-existence of M1 and R phases at the typical transition temperature for VO$_2$ (M1). When the temperature is further increased to 341 K, we observed a non-vanishing intensity of VO$_2$ (M1) (011) reflection, which indicates the extension of co-existence of M1 and R phases. This indicates the co-existence of the two phases extends over nearly 3 K. Above 342 K, we notice a rapid shift in peak position to lower

diffraction angles, which shows the complete structural transition into VO_2 (R). This co-existence behavior was found reproducible by taking repetitive measurements. Furthermore, the absence of the VO_2 (M2) phase revealed the free standing or stress/strain free nature of the samples under consideration.

Figure 8b shows the change in intensity of the (011) reflection of 0.5% Nb-substituted VO_2 across the transition. The phase transformation started from monoclinic VO_2 (M1) to tetragonal VO_2 (R) at 338 K. The phase co-existence of M1 and R phases was extended over a large temperature range of 5 K, compared to pure VO_2. **Figure 8c** shows the structural transition process in case of 0.5 % Cr- substituted VO_2 sample. In the case we observed an evolution of the transition from monoclinic M1 to tetragonal R phases through the additional monoclinic M2 phase. The intermediate M2 phase has a partial dimerization of the V–V chains compared to the M1 phase. However, this M2 phase is usually associated with the lattice stress, and mostly found within the nanostructures with strong surface-induced stress. Otherwise, Al- or Cr- substituted bulk VO_2 samples could stabilize the M2 phase [17]. **Figure 8d** represents the changes in the (011) reflection for 0.5 % W- substituted VO_2 (M1) monoclinic phase vs. temperature. Here, the transformation from VO_2 (M1) to VO_2 (R) started below 323 K, which indicates a decrease of structural phase transformation temperature from 340 K. The phase co-existence of VO_2 (M1) and VO_2 (R) exists until 337 K, which shows a large increase (more than 15 K) compared to pristine M1.

From these results we can conclude that the substitution of VO_2 lattice with W, Nb and Cr affect both the structural phase transition temperature and the phase coexistence region.

The magnetic properties of W-, Nb- and Cr-substituted VO_2 samples were measured and compared with pure VO_2, shown in **Figure 9**. The effect of substitution is even more pronouncedly reflected in magnetic properties. At very low temperatures, we noticed a small increase in magnetic susceptibility (χ) in pure VO_2 and that systematically increased for W-, Nb- and Cr-substituted VO_2 samples. In the case of pure VO_2 this increase was attributed to the crystallographic defects and confirmed by the EPR measurements [18].
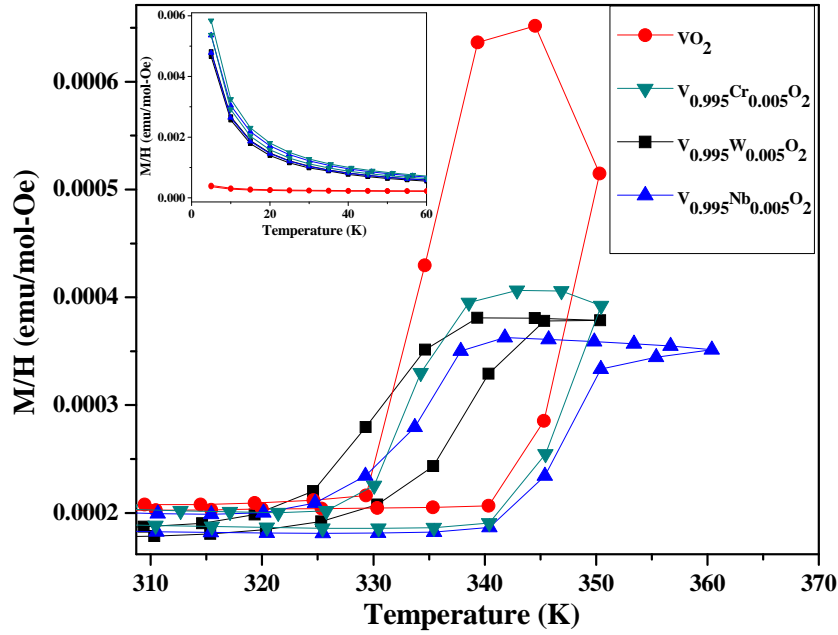
Figure 9. Variation of magnetic susceptibility with temperature around the structural phase transition in pure and 0.5 % W-, Nb- and Cr-substituted VO$_2$ (M1). The inset shows the variation of magnetic susceptibility at very temperature for the above specified compositions.

The increase in the χ across the transition was greatly reduced by substitutions and the slight changes in transition temperature are clearly visible from the horizontal shift of the hysteresis loops. This kind of hysteresis is usually ascribed to the martensitic nature of the structural phase transition. In this nature of transitions, the changes in the electrical and magnetic properties at the MIT in polycrystalline samples are generally not sharp and give rise to hysteresis loops. A substantial supercooling and superheating is required for atoms to move simultaneously to reach a phase of lower free energy [19]. In order to precisely determine the temperature at which the MIT starts and to compare with the structural phase transition temperature, we calculated the derivative of the M/H vs. temperature curves. Even though the major increase in the χ, due to a relatively high density of charge carriers in the metallic R phase, occurs nearer to the *structural* phase transitions (at 339, 338, 337 and 323 K for pure VO$_2$ (M1), Nb-, Cr- and W- substituted VO$_2$ (M1) samples, respectively (**Figure 8**)), but we obtained increase in χ (from the changes in sign of the dχ/dT) at 270, 330, 330 and 305 K for pure VO$_2$, Nb-, Cr- and W- substituted VO$_2$ samples, respectively. We also observed an anomaly in the derivative of the magnetic susceptibility curve of Cr-substituted VO$_2$ (M1) sample at 260 K, which was ascribed to a transition from VO$_2$ (M1) to VO$_2$ (M2) [20]. These observations indicate

the differences in initialization of the MIT and structural phase transition temperatures in the case of pure and lightly substituted VO_2 (M1) phase.

In order to study the structural coexistence in case of higher substituting levels, we extended the in-situ structural phase transition studies to 7.5% Mo- substituted VO_2 (M1). **Figure 10a** shows the P-XRD pattern acquired during cooling cycle, for the structural phase transition from tetragonal R phase to monoclinic M1 phase below the MIT transition. **Figure 10b** shows the variation of resistivity with temperature along the cooling cycle, indicating an MIT around 245 K. We noticed that the transformation from R into M1 phases starts at 250 K and nearly completes at 200 K. The coexistence of the two phases is noticed around the metal to insulator transition temperature. We analyzed the P-XRD pattern obtained at 10 K by profile fitting (using FullProf suite) considering VO_2 (M1) with JCPDS card number 01-082-0661. The obtained lattice parameters at 10 K (a=5.7346 Å, b=4.545 Å, c=5.3905 Å and β=122.41^o) obey a_{M1}~a_R; b_{M1}~a_R; c_{M1}~3*(b_R-c_R) with lattice parameters calculated at room temperature (a=4.5733 Å, c=2.8605 Å). The phase co-existence between M1 and R phases across the MIT is also present for 7.5% Mo- substituted VO_2 (M1) and confirms the transition from equally spaced metal ions (R phase) at room temperature into alternating long-short metal-metal bonds (M1 phase) below the MIT temperature.
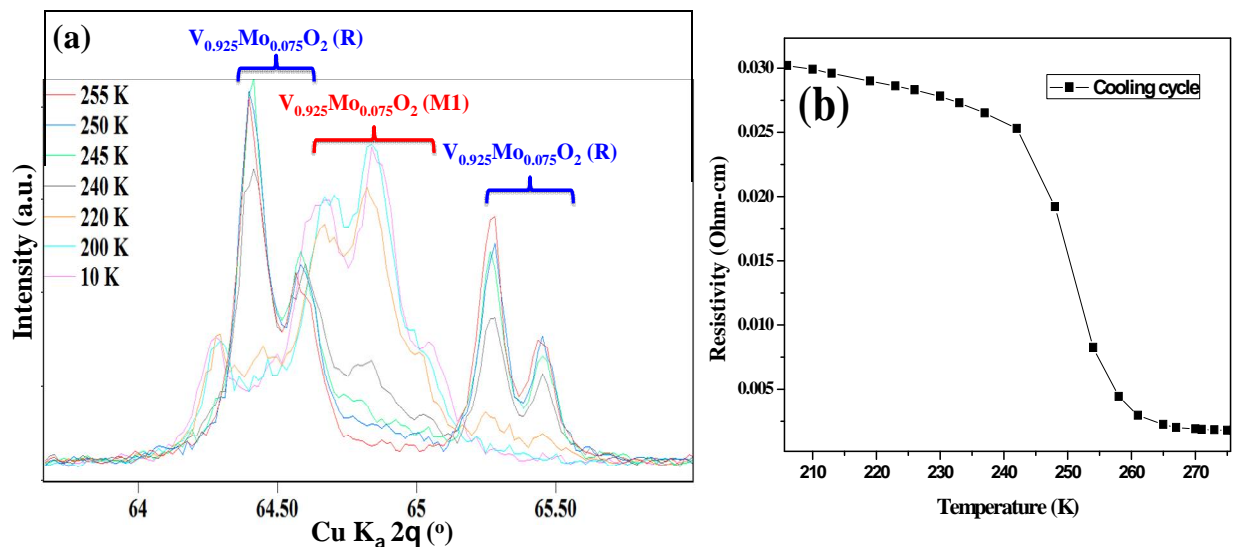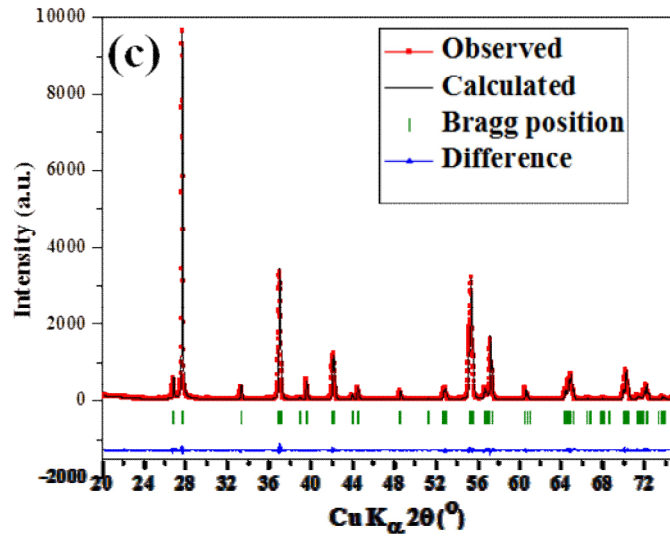
Figure 10. (a) Structural phase transformation from tetragonal R to monoclinic M1 phase of $V_{0.925}Mo_{0.075}O_2$ from low temperature in-situ P-XRD patterns. (b) Variation of resistivity with temperature along the cooling cycle (c) X-ray profile matching using FullProf suite for $V_{0.925}Mo_{0.075}O_2$ (M1), obtained at 10 K.

VI.6. Thermoelectric and Physical properties

VI.6.1 Electrical resistivity and Seebeck coefficient

Figure 11a shows the temperature dependence of the electrical conductivity for pure VO_2 below room temperature. As expected below 300 K, a typical semi-conducting behaviour is found and no hysteretic behaviour is noticed. The semi logarithm plot of electrical conductivity versus temperature is shown in **Figure 11b.** The linear variation is mainly associated with a thermally activated mechanism of Arrhenius type. The activation energy for the charge mobilization was extracted using the Arrhenius equation: $\sigma=\sigma_0\exp(-E_a/KT)$ where E_a is the activation energy, K the Boltzmann's constant, T the absolute temperature and σ_0 is a pre-exponential factor. We identified two different regimes: between 80-100 K and 104-300 K with activation energies of 37 and 53 meV, respectively.
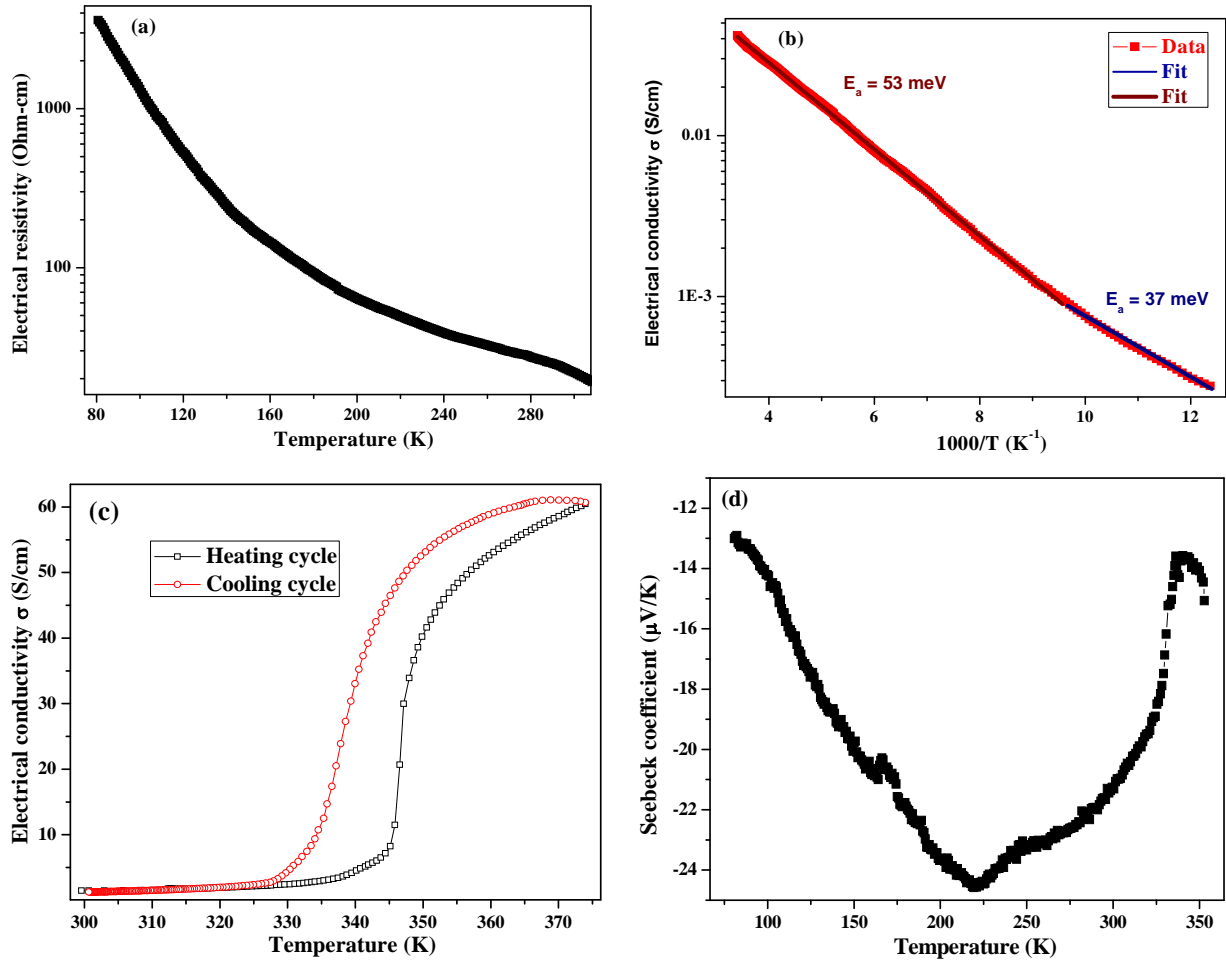
Figure 11. (a) Temperature dependence of the electrical conductivity of VO$_2$ (M1) below room temperature; (b) semi-log plot of electrical conductivity vs. inverse temperature, fitted using Arrhenius law; (c) temperature dependence of the electrical conductivity of VO$_2$ (M1) around the insulator to metal transition; (d) variation of the Seebeck coefficient (thermopower) with temperature.

The electrical transport studies were carried out around 340 K (**Figure 11c).** A large increase in conductivity across the MIT temperature, from nearly 1 S/cm at RT to 60 S/cm at 370 K, is observed. This can be attributed to the delocalization of charge carriers and noticed a hysteresis between cooling and heating cycles around 340 K. From dσ/dT curve, we obtained the precise insulator to metal (heating cycle) and metal to insulator (cooling cycle) transition temperatures as 347 and 339 K, respectively. From structural phase transition studies, we obtained the pure tetragonal phase at 342 K (**Figure 8a**). In the case of insulator to metal transition, even though we observed a continuous increase in conductivity, the actual

conductivity jump occurs at 345 K **(Figure 11c).** These observations further support the occurrence of a structural inhomogeneity/coexistence across the structural and metal insulator transitions and the martensitic nature of both transitions [21].

The variation of Seebeck coefficient with temperature for pure VO_2 is shown in **Figure 11d.** The Seebeck coefficient increases linearly between 80 and 220 K, and reaches a maximum value of -24 µV/K at 220 K. Afterwards it decreases down to -14 µV/K at 340 K. The negative sign of the Seebeck coefficient indicates that electrons are the dominant charge carriers.
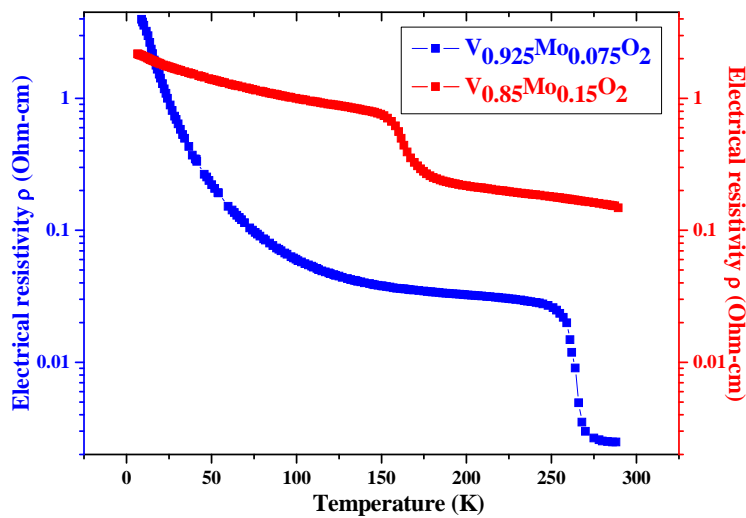
Figure 12. Temperature dependence of the electrical conductivity for $V_{1-x}Mo_xO_2$ (x=0.075, 0.15).

The temperature dependence of the electrical resistivity in various Mo- substituted VO_2 ($V_{1-x}Mo_xO_2$) samples is shown in **Figure 12**. At first sight we observe that the MIT temperature was reduced with increasing Mo content. The reduction rate of the transition temperature is of the order at 10 K/at%. Furthermore, breaking the homopolar V^{4+}-V^{4+} bonds destabilizes the semiconducting phase of VO_2, thus lowering the MIT temperature. The resistivity decreases across the MIT, due to the addition of charge carriers and the rate is diminishes from 7.5 % to 15 % of Mo content. At room temperature, the electrical resistivity increases with increasing Mo concentration. This is mainly due to the increase in resistivity in both metallic and semiconducting regions of 15% Mo- substituted VO_2. In addition to this, the transition becomes broader compared to pure and 7.5% Mo- substituted VO_2, indicating a progressive MIT.
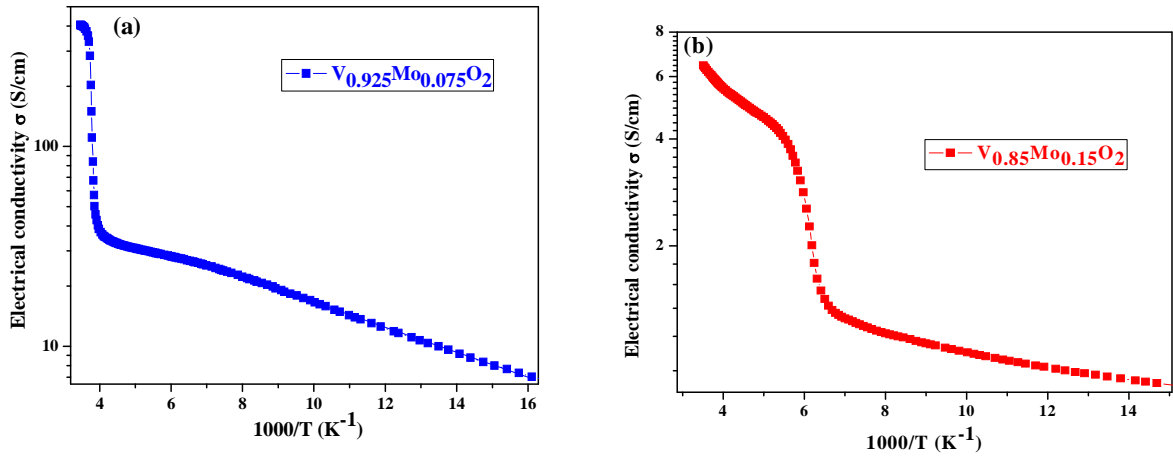
Figure 13. Arrhenius plots for (a) $V_{0.925}Mo_{0.075}O_2$ (b) $V_{0.85}Mo_{0.15}O_2$ samples.

Figure 13 shows the electrical conductivity Arrhenius plots of $V_{1-x}Mo_xO_2$ (x=0.075 and 0.15). For 7.5 % Mo substituted VO_2, the activation energy was continuously decreased with increasing the temperature, but on the other hand we noticed the opposite trend for 15 % Mo substituted VO_2. Values of Seebeck coefficient for $V_{1-x}Mo_xO_2$ with x=0.075 and 0.15 are plotted in **Figure 14** as a function of temperature. The Seebeck coefficients for both specimens are negative in sign, indicating n-type conduction behaviour. The decrease of insulator to metal transition temperature is showed in the Seebeck coefficient measurements and matches with the MIT temperatures.
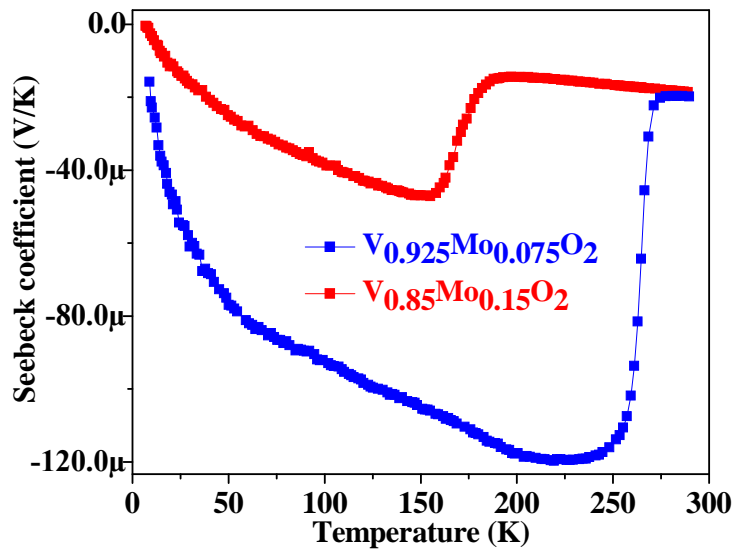
Figure 14. Temperature dependence of Seebeck coefficient for $V_{1-x}Mo_xO_2$ (x=0.075, 0.15).

For both compositions, around the transition, the large enhancement in the Seebeck coefficient is noticed compared to pure VO_2 (**Figure 11d**), reflects the changes introduced by Mo substitution. These changes could be due to the modification of the electronic structure (carrier density) and entropy of the system due to the mixed cationic valence as seen by X-ray photoelectron spectroscopy.

In the case of $V_{1-x}Nb_xO_2$, it was claimed that until 15% Nb content, the metal to non-metal transition was suppressed and, for higher Nb content the high temperature phase becomes insulating instead of metallic. In addition, the modification of dominant charge carriers from electrons to holes around 35 % Nb substitution was noticed [22]. Very recently, Shibuya et al. reported the re-entrant behaviour to insulating phase with tetragonal crystal structure above 10 % substitution rate in W- substituted VO_2. This behaviour was assigned to the phase separation between metallic and insulating phases. According to these observations, a percolation of a metallic matrix and tiny insulating puddles may coexist in 10% W substituted VO_2 films and further increase of W content causes the re-entrance to the insulating phase (by increase of MIT temperature) [23]. Similar nano-scale percolation-type metal-insulator transition behaviour was reported for pure VO_2 (M1) by Qazilbash et al. using infrared microscopy [24]. In order to understand the effect of higher Mo contents on the metal-insulator transition behaviour and check the possible re-entrance to insulating type behaviour as reported for Nb and W substitutions and type of charge carriers, we performed electrical resistivity and Seebeck measurements for 35 and 50 % Mo-substituted VO_2 samples.
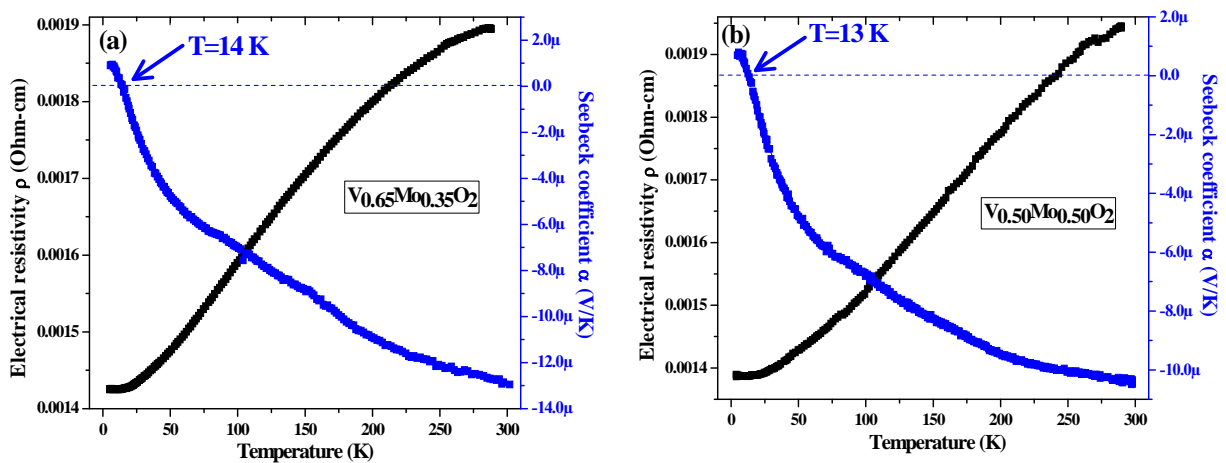
Figure 15. Temperature dependence of electrical resistivity and Seebeck coefficient for (a) $V_{0.65}Mo_{0.35}O_2$ and (b) $V_{0.50}Mo_{0.50}O_2$.

Figure 15 displays the variation of electrical resistivity and Seebeck coefficient with temperature for 35 and 50 % Mo-substituted VO_2. The substitution with such high Mo contents has minor effects on the electrical resistivity, thereby on Seebeck voltages. In both cases, a typical metallic behaviour is observed. The sign of the Seebeck coefficient is negative over the temperature range 14-300 K for both samples, indicating that the major conductivity carriers are electrons. The type of charge carriers did not change with increasing Mo content, up to 50% and room temperature, as in the case of Nb-substituted VO_2. However, we have noticed changes in the charge carriers type at very low temperatures, near 14 K and 13 K for 35 and 50% of Mo substitution rates, respectively. It is of particular interest to note that the Seebeck coefficient for high Mo content substituted VO_2 is lower than that of pure VO_2 at room temperature. The observed temperature dependence of both the electrical resistivity and the Seebeck coefficient can be explained by a conventional picture based on band theory and electron–phonon scattering.

VI.6.2. Thermoelectric power factor

The temperature dependence of the power factor, $\sigma\alpha^2$, calculated from the electrical conductivity and Seebeck coefficient data of pure and Mo-substituted VO_2, is presented in **Figure 16**.
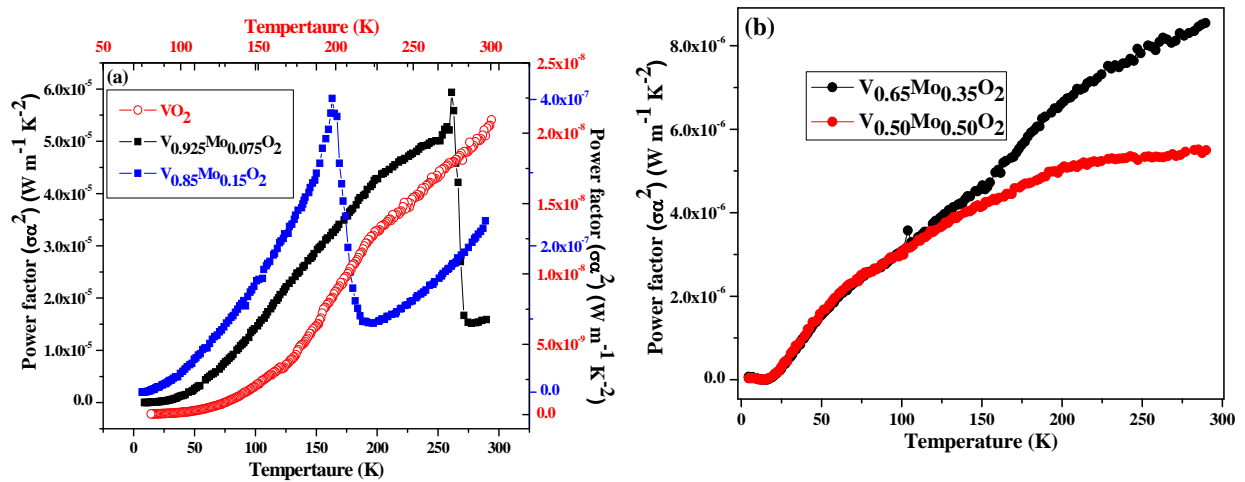
Figure 16. Low temperature dependence of thermoelectric power factors of (a) $V_{1-x}Mo_xO_2$ (x=0; 0.075; 0.15); (b) $V_{1-x}Mo_xO_2$ (x=0.35; 0.50)

For low Mo contents, for which the MIT transition occurs below room temperature, the power factors increase monotonically up to the metal-insulator transition and then drop to lower

values. The power factor values for 7.5 % Mo-substituted VO_2 are particularly high compared to any other composition in the series under study. The 7.5 % Mo-substituted VO_2 sample exhibited a highest value of power factor of 6×10^{-5} W/m.K^2 at 260 K, which is two order of magnitude larger than the maximum value for pure VO_2 (5.8×10^{-7} W/m.K^2 at 290 K). Even above the insulator to metal transition, the value is 1.5×10^{-5} W/m.K^2, which is close to the power factor value of polycrystalline $Na_{0.7}CoO_2$ ($1.8x10^{-5}$ W/m-K^2 at 277 K). For higher Mo contents, the decrease in power factor values results from the lower Seebeck coefficients. Thus, low Mo substitution rates appear efficient for enhancing the thermoelectric properties of VO_2.

VI.6.3. Thermal conductivity and figure of merit

Figure 17a shows the temperature dependence of the thermal conductivities for pure, 7.5 and 15 % Mo-substituted VO_2 samples. The thermal conductivity of a material can be expressed as $\kappa = \kappa_l + \kappa_e$ where κ_l and κ_e are the lattice and electronic thermal conductivities, respectively. The electronic thermal conductivity can be roughly estimated by the Wiedemann-Franz law as $\kappa_e = L\sigma T$, where L is the Lorenz number 2.45×10^{-8} W.Ω/K^2.
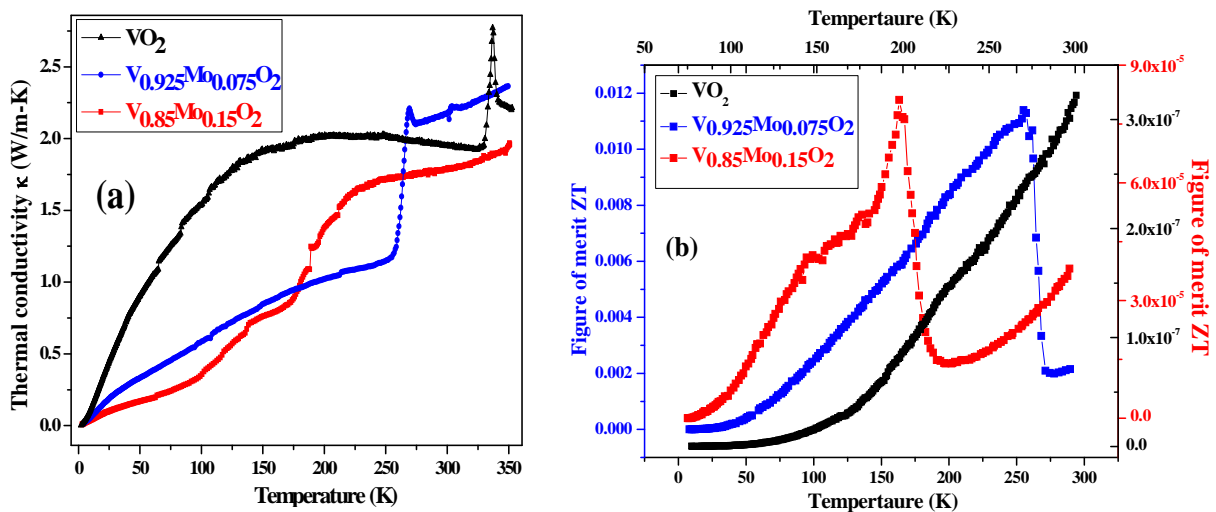
Figure 17. Temperature dependence of (a) the thermal conductivity; (b) the thermoelectric figure of merit (ZT) of $V_{1-x}Mo_xO_2$ (x=0; 0.075; 0.15)

It is known that, in the case of semiconductors, the contribution of electronic thermal conductivity to total thermal conductivity is dominant over the lattice contribution. With

increasing temperatures the thermal conductivities increases which shows that the major part of the thermal conductivities is composed of electronic contributions. In the case of VO_2, the change in thermal conductivity across the MIT is mostly due to the change in the electronic contribution, with a constant lattice thermal conductivity [25].

It is found that the thermal conductivities of Mo-substituted VO_2 are lower than that of pure VO_2 over the measured temperature range. The partial substitution of Mo for V leads to an increase in the distortions, due to size effects. Moreover, these observations are consistent with the fact that heavy atoms and a complex unit cell will reduce the lattice thermal conductivity, by increasing the scattering cross-section for phonons. The thermal conductivity increases across the MIT temperature by as much as 43% for VO_2 (from 1.94 to 2.78 W-m/K); 89 % for 7.5 % Mo (from 1.16 to 2.2 W-m/K) and 97 % for 15 % Mo (from 0.81 to 1.6 W-m/K) substitution rates. This increase in conductivity is in good agreement with the expected variation of the electronic contribution, due to the increase in the charge carrier density.

It is important to mention that we have noticed a small discrepancy between the MIT temperature measured by electrical conductivity and thermal conductivity measurements. The peak of thermal conductivity is found at 337 K in the case of pure VO_2 (**Figure 17a**). We believe that this difference is not due to experimental errors, but rather due to the intrinsic nature of the two properties versus the change in volume fraction of the metallic phase in the insulating phase, during heating cycle. In the case of electrical conductivity, the volume fraction of the metallic phase must cross a percolation threshold with temperature, in order to achieve the rise in conductivity. On the other hand, the thermal conductivity difference between the two phases (metallic and insulating) is not very large, therefore the transition will appear earlier (i.e. at a slightly lower temperature) in the thermal conductivity curve. The percolation threshold required for the metallic domain formation was extensively studied by Qazilbash et al., and similar discrepancies between metal-insulator transition temperatures from thermal and electrical conductivities were reported by Oh et al. [26]**.**

Figure 17b shows the temperature dependence of the dimensionless figure of merit, ZT, calculated from the thermal conductivity (κ), Seebeck coefficient (α), and electrical resistivity (ρ) in the case of pure and Mo- substituted VO_2 samples, according to $ZT = \alpha^2 T/\kappa\rho$. The maximum

value for ZT = 0.011 is obtained for the $V_{0.925}Mo_{0.075}O_2$ sample at 256 K. The maximum value of thermoelectric power factor 6×10^{-5} W/m-K^2 is obtained for the same composition at 260 K. The ZT value in the present case is not so high compared to traditional non-oxide based thermoelectric materials; however, this value is one of the highest observed so far in this temperature range for oxide based thermoelectric materials.

To develop thermoelectric materials for high-temperature applications, considerable attention has been focused on oxides. Some of the existing oxide based thermoelectric materials are suffering from high thermal conductivity along with poor electronic conductivity and Seebeck coefficient. Mo substitution in VO_2 appears to improve both factors, opening up a new possibility: to apply this strongly correlated metal oxide as a thermoelectric material.

VI.7. Magnetic properties

Figure 18 shows the variation of the magnetic susceptibility versus temperature for various pure and Mo-substituted VO_2 compounds.
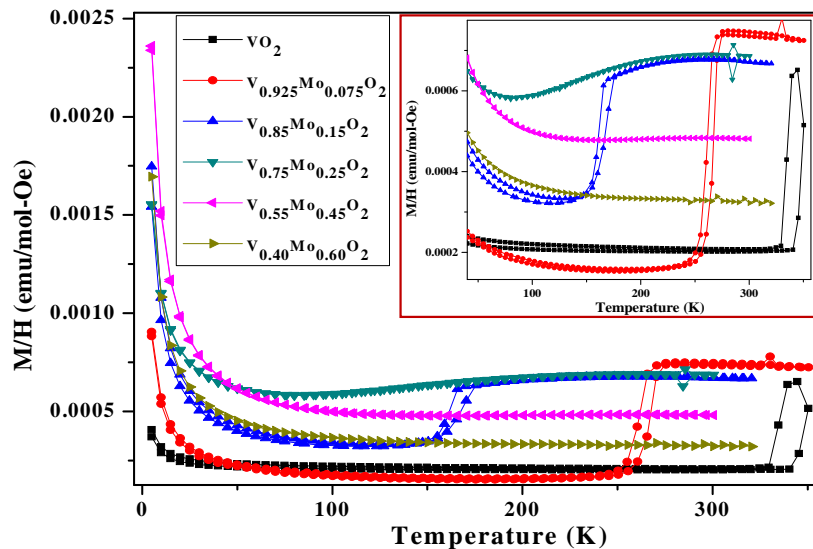
Figure 18. Temperature dependent magnetic susceptibilities for $V_{1-x}Mo_xO_2$ (0≤x≤0.6). Inset : variation of magnetic susceptibility with Mo content near room temperature.

In the case of pure VO_2, we notice a temperature-independent magnetic susceptibility at low temperatures. To explain such kind of temperature-independent magnetic susceptibility, the formation of covalent V - V pairs with single d electron per vanadium ion was introduced by

Goodenough [27]. This assumption was further confirmed by the magnetic properties of Cr- and Fe- substituted VO_2, in which the substitution impurities break the V-V pairs and release a localized magnetic moment [28]. At very low temperature, we observe a small increase in the magnetic susceptibility, which may be due to a small number of vanadium defects in the pure VO_2 system; these defects release free spins and give rise to an increase in the magnetic susceptibility. Such defects have also been observed by electron spin resonance measurements in the case of pure VO_2, and the observed magnetic moment was attributed to the broken V-V ion pair due to defects [29]. The susceptibility increases sharply with temperature on heating through the insulator to metal transition. This is due to transfer of charge carriers into conduction band due to the breakup of dimers along the structural phase transition. Above the MIT, the magnetic susceptibility decreases for temperatures above 340 K. In this region, all the dimers are separated and one d conduction electron is available per vanadium atom. This type of variation is in-between Pauli and Curie-Weiss behaviors, and is probably related to significant electron correlations in the metallic phase.

For 7.5% Mo substitution rate, major changes occur in the magnetic characteristics: compared to pure VO_2, the magnetic susceptibility is weaker in the low temperature region and larger above the MIT. The large step in susceptibility at MIT and the tail at very low temperature is enhanced compared to pure VO_2. The enhancement in low temperature tails indicates the increase of charge carrier density with Mo substitution. Along with this, the MIT temperature was decreased whereas and the sharpness of the MIT was maintained. When the Mo concentration was increased to 15%, the magnetic susceptibility increased in the insulating region and decreased in the metallic region, compared to the 7.5% Mo composition. For 25% of Mo substitution rate, the MIT temperature further decreased to 82 K and the transition is no longer sharp, but broadens over a large temperature range; the high temperature susceptibility value is similar to the value for the 15% Mo-substituted sample. For higher concentrations (45 and 60 % Mo), the MIT was completely suppressed, whereas the susceptibility values continuously decreased with increasing Mo concentration. The magnetic susceptibility at 5K increased up to 45 % Mo substitution rate, and decreased for the 60 % Mo composition.
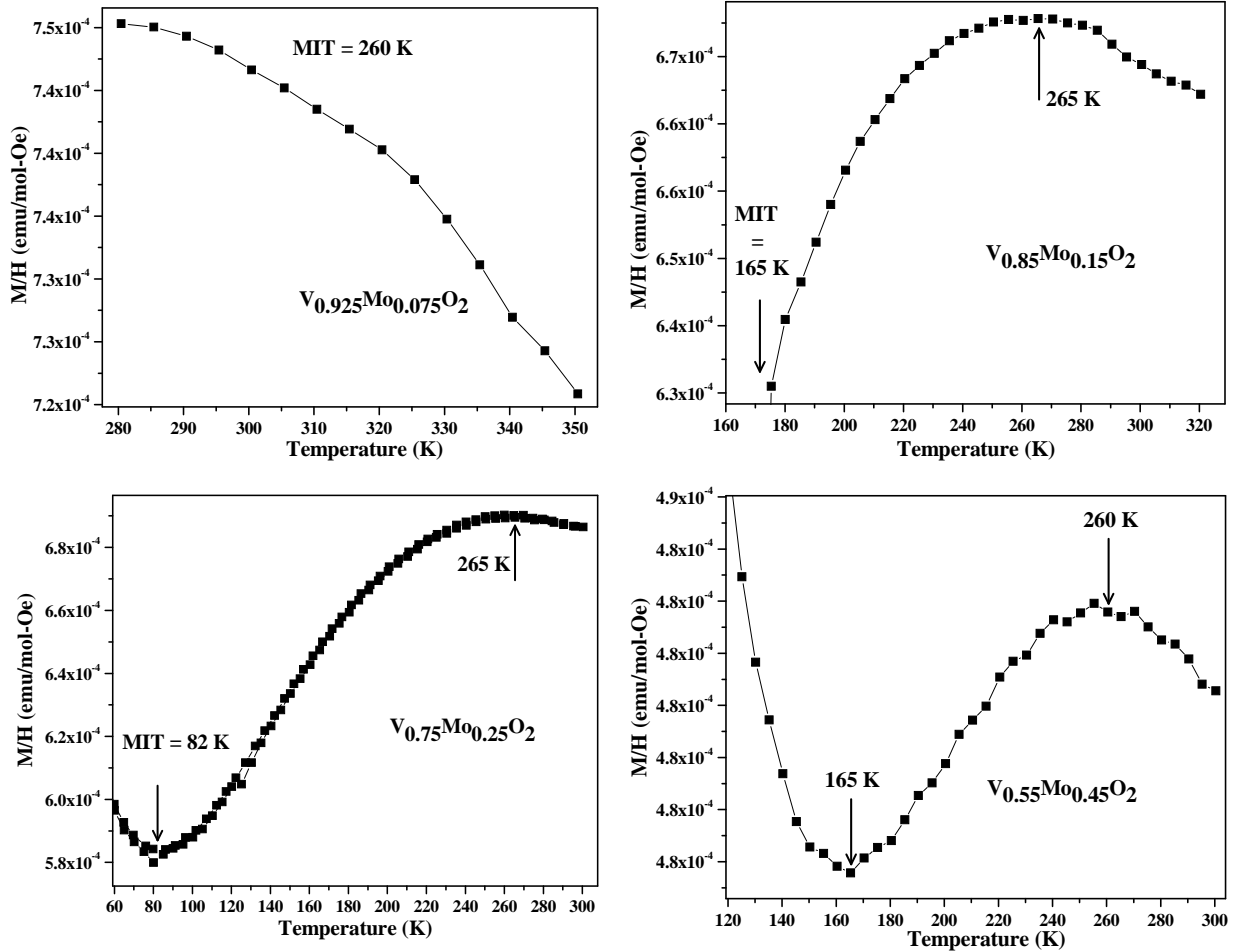
Figure 19. Variation of magnetic susceptibility above the MIT temperature for 7.5, 15, 25 % Mo-substituted VO$_2$ (M1) and 45 % Mo- substituted VO$_2$ in the metallic region.

Figure 19 shows the variation of magnetic susceptibility above the MIT temperature for 7.5, 15, 25 % and 45 % Mo concentrations. For 7.5%, the decrease in the magnetic susceptibility above MIT is similar to the case of pure VO$_2$, and related to strongly correlated metallic behavior. For the 15 and 25% cases, MIT temperatures were 165 and 82 K, respectively. In these two cases, magnetic susceptibility variation with temperature is quite different from the 7.5 % Mo case. Here the magnetic susceptibility increases above the MIT, until 265 K, and then decreases. In the case of pair breaking mechanisms, we expect a decrease in the magnetic susceptibility values above the MIT temperature.

These observations suggest that the insulating and metallic phases coexist in 15 % Mo-substituted VO$_2$ well above the MIT temperature. Thus, the MIT extends over a finite

temperature range, from 165 to 265 K. In this case, the continuous increase of susceptibility above the MIT might be due to inhomogeneous pair breaking distribution. In a similar way, in the case of 25 % Mo- substituted VO_2, the MIT was extends over a finite temperature range between 82 and 265 K. On the other hand, for the 45% Mo-content sample, which exhibits a full metallic behavior, the susceptibility decreases continuously with temperature from 5 K to 165 K, then goes through a slight increase until 260 K and thereafter decreases slowly with increasing temperature.
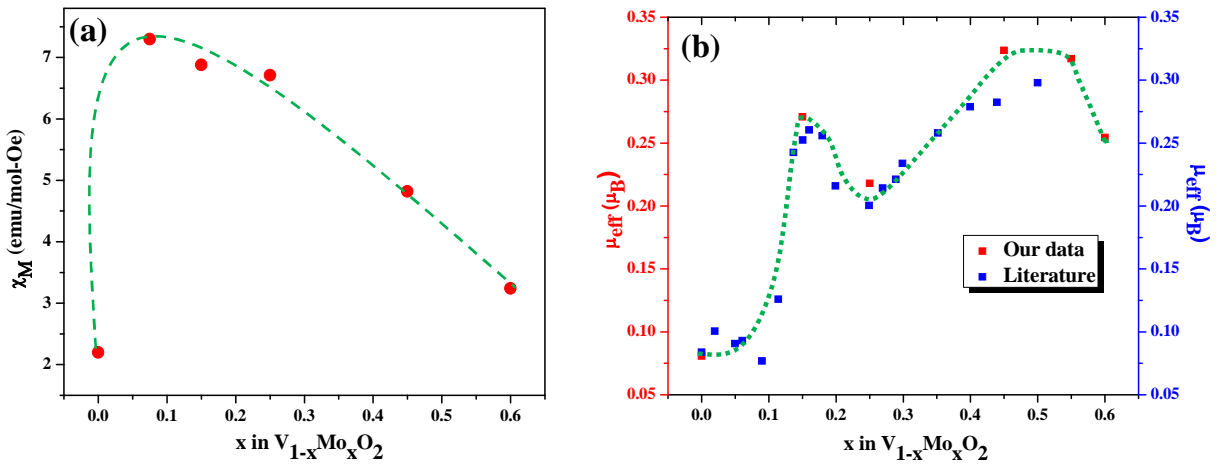
Figure 20. Variation of the magnetic susceptibility at 300 K by changing the Mo content in $V_{1-x}Mo_xO_2$ (b) Variation of effective magnetic moment, calculated by fitting the low temperature region of magnetic susceptibility versus temperature curves using the Curie Weiss law. We compared our results with data published in reference [5].

Figure 20a shows the variation of magnetic susceptibility at 300 K with increasing Mo concentration. Except pure VO_2, all samples are of metallic nature for conductivity at room temperature. Even though a sharp increase in magnetic susceptibility was expected because of the structural phase transition (breakup of dimers and increase in the free spins density), the linear decrease of magnetic susceptibility in the metallic region with Mo concentration is unusual. These variations indicate that the Mo concentration has a significant effect even in the metallic region, in the solid solution.

From the Curie-Weiss fits of the magnetic susceptibility at low temperatures, the effective moments in the Mo-substituted VO_2 compounds was obtained and plotted in **Figure 20b.** The variation of effective magnetic moment shows a non-linear behavior with Mo

concentration up to 60 % of substitution rate. Linear variations are observed in the case of Nb, Ga and W substituted VO_2, in which the variation of magnetic moment was assigned to the broken V-V singlet pairs [30]. If simple breakages of V-V pairs are assumed along with the Mo substitution, then the magnetic moment should vary linearly with Mo concentration and should reach the value of 1.73 μ_B, which is the spin only moment value for free V^{4+}. Therefore, in the $V_{1-x}Mo_xO_2$ system, the observed magnetic moments cannot be explained solely by the breakage of V-V dimers, and the decrease in transition temperature is not only related to broken pairs. The metal ions in the rutile phase of $V_{1-x}Mo_xO_2$ (0.075<x<0.50) are displaced significantly from the ideal rutile sites 2a (0,0,0) to 4e (0, 0, Z) along the chain directions [5]. The displacement of metal ions from ideal positions is indicating the existence of a Peierls-type distortion (metal-metal ion pairs) in the rutile phase. These observations got further support from the electron diffraction studies on nanometer scale at room temperature, which showed the presence of monoclinic VO_2 (M1)-like signatures.

So in the rutile phase there still exists metal-metal pairs which strongly affect the expected linear increase of magnetic moment with increasing Mo content.

VI.7.1. Variation of transition temperature
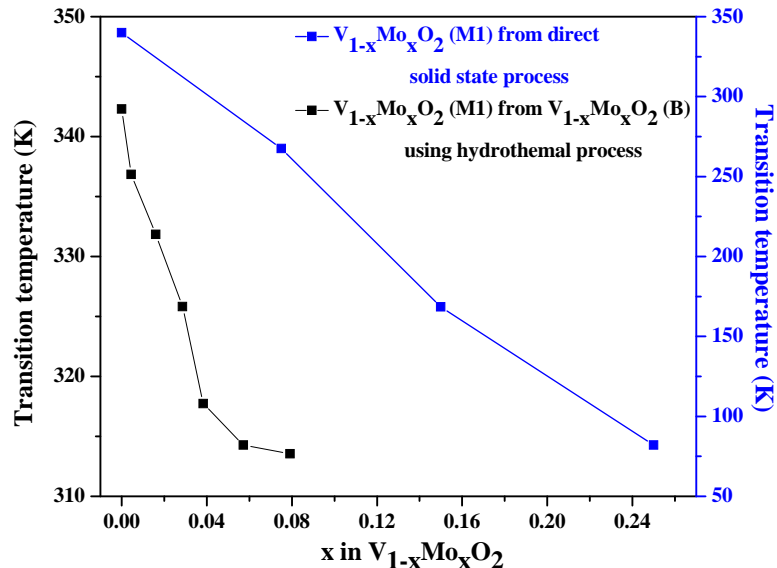
Figure 21. Variation of the MIT temperature with Mo content for $V_{1-x}Mo_xO_2$ (M1). Blue: samples prepared by direct solid state method. Black: samples prepared by argon annealing of $V_{1-x}Mo_xO_2$ (B).

Figure 21 shows the variation of the MIT temperature with Mo content in the case of $V_{1-x}Mo_xO_2$. In this figure we show the results for two different set of samples prepared i) by direct solid state reaction and ii) by direct annealing process from Mo substituted VO_2 (B) prepared by hydrothermal process. We found a linear decrease of MIT temperature in the case of direct solid state reaction synthesized samples. On the other hand, in the case of Mo-substituted VO_2 (M1) samples obtained by annealing of Mo-substituted VO_2 (B) samples with microsphere like morphology, the MIT temperatures were determined by DSC measurements. In this case we noticed a non-linear variation of MIT temperatures with Mo content. A steep decrease of the phase transition temperature is observed for Mo substitution up to 4 %, and further addition of substitutional dopant only modestly influences the MIT temperature. The distinctive composition dependence can be explained by finite size effects. Due to the small particle size of the samples prepared by hydrothermal processes, after certain concentration substitutional Mo ions may accommodated at subsurface and surface sites thereby have less influence on alteration of the transition temperature [31].

VI.8. Specific heat measurements

Figure 22a reproduces the low temperature specific heat measurements for 7.5% Mo-substituted VO_2 between 2 and 270 K. Beyond the continuous increase of specific heat with increasing temperature, a drastic increase (peak) is observed around the MIT temperature.
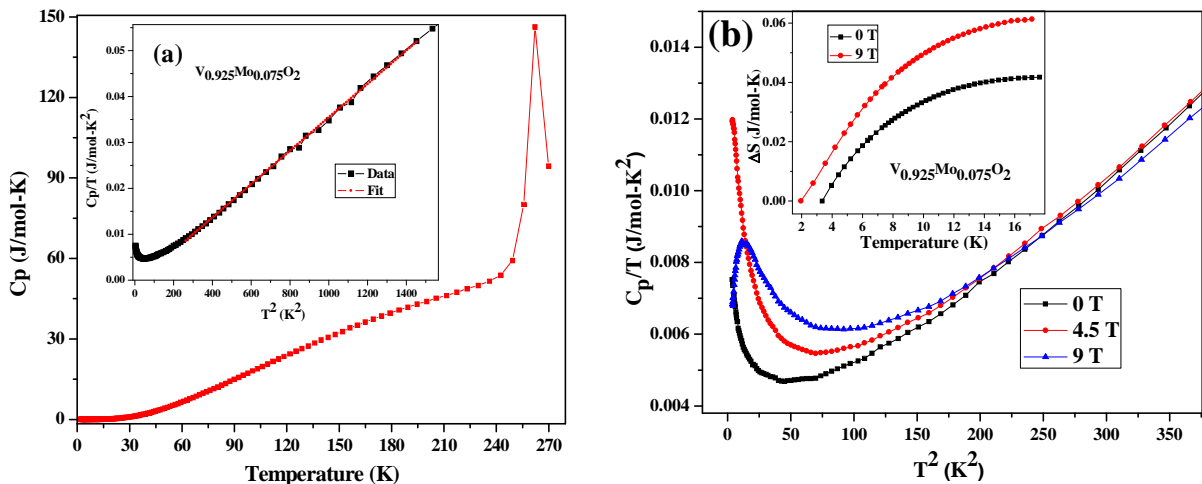
Figure 22. (a) Low-temperature specific heat for $V_{0.925}Mo_{0.075}O_2$. Inset: fits to the linear portions of C_p/T vs. T^2; (b) C_p/T vs. T^2 as function of magnetic field for $V_{0.925}Mo_{0.075}O_2$ (inset: Variation of entropy at low temperature for $V_{0.925}Mo_{0.075}O_2$, under magnetic field of 0 and 9 T).

This large change in the specific heat corresponds to the change in entropy, which has mainly lattice and electronic contributions. Here, the lattice contribution arises from crystalline distortions across the structural phase transition, and the electronic contribution arises from the conduction electrons, i.e. from the discontinuity in the charge carrier density across the MIT.

In order to get some insight into the electronic states and the electronic contribution to the specific heat (γ), we fitted the low temperature data with the Debye formula $C_p=\gamma T+\beta T^3$. The inset of the **Figure 22a** shows plot between C_p/T versus T^2; we notice a small upturn in C_p/T at very low temperatures. This behaviour shows that an additional contribution should be considered, in addition to the electronic (linear term) and lattice (cubic term) contributions to the total specific heat. We assumed that this third contribution raised from the defects. By ignoring in a first approximation the upturn in C_p/T, we fitted the data. From the β value, we obtained Debye temperatures as 474 and 458 K and an electronic contribution as 0.93 and 5.45 mJ/mol.K^2 for 7.5% and 50 % Mo respectively. The increase in electronic contribution to the specific heat from 7.5 to 50 % substitution rate indicates the increase in charge carrier density with Mo substitution. The increase in Mo content also yields a reduction of the Debye temperature.

To further study the electronic states and origin of the upturn in the Cp/T^2 curves at low temperature, we have measured the specific heat as a function of magnetic fields up to 9 T for 7.5% Mo- substituted VO$_2$ (**Figure 22b**). With increasing applied magnetic field, the onset of the upturn in the specific heat is shifted to higher temperatures. For 9 T, the upturn is followed by a decrease in C_p/T value. The magnetic field dependence of the low temperature specific heat is supported by defects-generated magnetic moment fluctuations at low temperatures. This kind of behaviour can be assigned to Schottky anomalies that arise from magnetic fluctuations of a spin ½ in a two-level, non-degenerate system. Here the magnetic field slightly increased the Debye temperature from 474 without any magnetic field to 476 for 4.5 T and 490 K for 9 T. From the magnetic measurements we already noticed that the magnetic moment at low temperatures increased with increasing Mo content, which is due to defect-generated magnetic moments from the broken spin ½ pairs (**Figure 20**). To calculate the variation in entropy (ΔS) associated to the Schottky anomaly, we used the standard expression

$$\Delta S = \int_{Ti}^{Tf} \frac{C}{T} dT$$

Where T_i and T_f are two temperatures which are chosen around the low temperature anomaly, and C is the specific heat obtained after subtracting the electronic and lattice contributions from the experimental data. The entropy variation, associated to the Schottky anomaly is shown in inset of **Figure 22b** and appears to increase as a function of the magnetic field. So, the observed low temperature Schottky anomalies in the specific heat for 7.5 and 50 % substituted VO_2 is due to defect-stabilized spin states.

VI.9. Conclusions

The experimental results in the case of $V_{1-x}Mo_xO_2$ system was summarized in **Figure 23**.
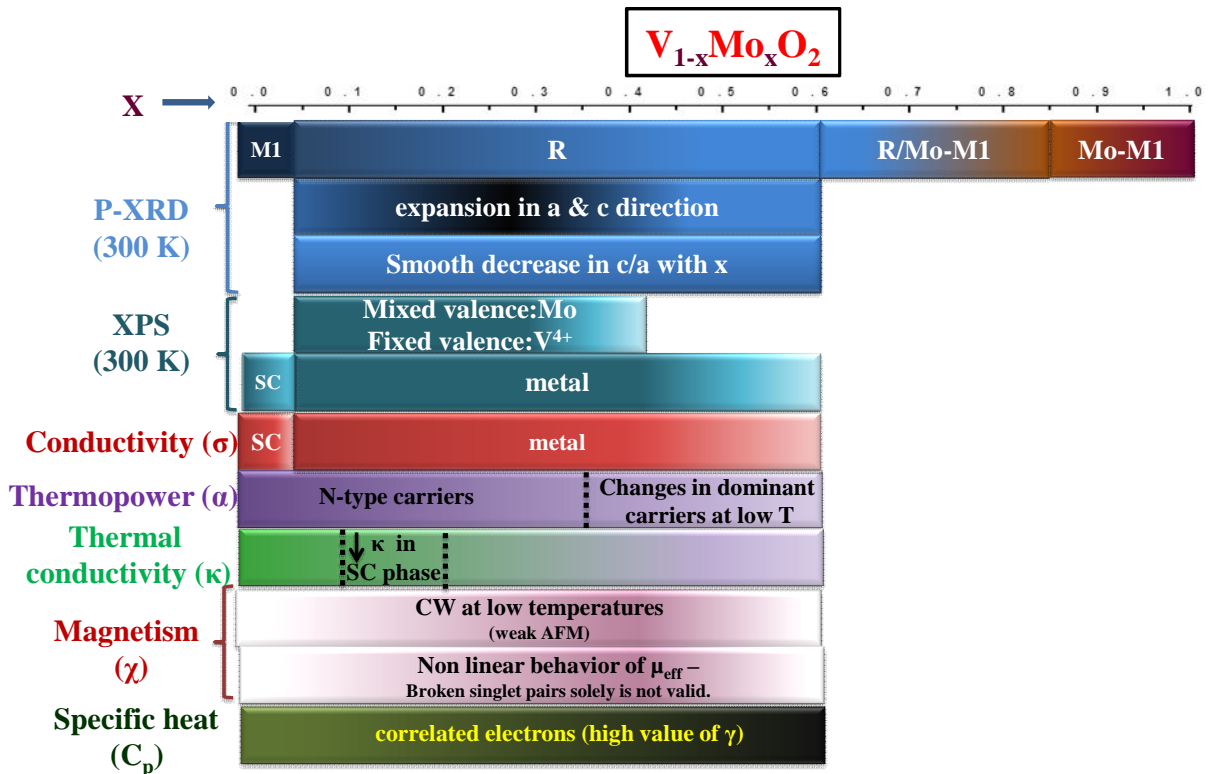
Figure 23. Summary of structural and electronic properties in $V_{1-x}Mo_xO_2$.

The complete structural phase diagram of $V_{1-x}Mo_xO_2$ revealed that VO_2-MoO_2 system is not forming complete solid solution. The Mo substitution has a major influence on the V-V pairing along the c-axis, and the absence of pronounced maximum in c/a values rules out the possibility of an ordering between V and Mo cations. From spectroscopic studies, mixed valence nature of Mo cations is observed and the reduction of Mo to more and more lower oxidation

degrees was observed along with increasing Mo content. Phase coexistence across the metal insulator transition was noticed from the in-situ X-ray powder diffraction studies. From transport measurements, a linear decrease of the metal insulator transition temperature with increasing Mo content. With increasing in both electrical conductivity and Seebeck coefficient, 7.5% Mo substitution in VO_2 led to an enhancement of thermoelectric power factor *by two orders of magnitude* compared to pure VO_2. A decrease in thermal conductivity was observed with increasing Mo concentration, possibly due to enhancement in the phonon scattering. The reasonable figure of merit, ZT = 0.011, was obtained at 256 K for the $V_{0.925}Mo_{0.075}O_2$ sample. Low temperature Curie-Weiss fits to the magnetic susceptibility data revealed an unexpected variation of effective magnetic moments as a function of Mo content. As the magnetic moment never reached spin ½ values, the observed magnetic moments in $V_{1-x}Mo_xO_2$ cannot be attributed solely to broken singlet V-V ion pairs. This observation raises the "clues" about presence of V-V ion pairs in the metallic tetragonal phase.

VI.10. Prospectives

In situ electron diffraction structural studies would be interesting to probe the possible presence of cation pairs in metallic phase, to support anomalies in the magnetic properties. And also spectroscopic studies around the MIT transitions at high substitution rates could provide useful information about the possible changes in valence states of cations.

VI.11. References

[1] F.J. Morin, Phys. Rev. Lett. 3, 34 (1959)

[2] H.S. Choi, J.S. Ahn, J.H. Jung, T.W. Noh, D.H. Kim, Phys. Rev. B 54, 4621 (1996); Y.J. Chang, J.S. Yang, Y.S. Kim, D.H. Kim, T.W. Noh, D.W. Kim, E. Oh, B. Kahng, J.S. Chung, Phys. Rev. B 76, 075118 (2007)

[3] C. Tang, P. Georgopoulos, M.E. Fine, J.B. Cohen, M. Nygren, G.S. Knapp, A. Aldred, Phys. Rev. B 31, 1000 (1985); L. Whittaker, T.L. Wu, C.J. Patridge, S. Ganapathy, S. Banerjee, J. Mater. Chem. 21, 5580 (2011); H. Takami, T. Kanki, S. Ueda, K. Kobayashi, Y. Tanaka, Appl. Phys. Express 3, 063201 (2010); J.M. Booth, P.S. Casey, Phys. Rev. Lett. 086402 (2009)

[4] T.D. Manning, I.P. Parkin, C. Blackman, U. Qureshi, J. Mater. Chem. 15, 4560 (2005); S. Xu, H. Ma, S. Dai, Z. Jiang, J. Mater. Sci. 39, 489 (2004)

[5] K.L. Holman, T.M. McQueen, A.J. Williams, T. Klimczuk, P.W. Stephens, H.W. Zandbergen, Q. Xu, F. Ronning, R.J. Cava, Phys. Rev. B 79, 245114 (2009)

[6] P. Dordor, E. Marquestaut, G. Villeneuve, Rev. Phys. Appl. 15, 1607 (1980)

[7] J. Rodríguez-carvajal, Physica B 192, 55 (1993)

[8] C. Tang, P. Georgopoulos, M. F. Fine, J. B. Cohen, M. Nygren, G. S. Knapp, and A. Aldred, Phys. Rev. B 31, 1000 (1985)

[9] W. Rudorf, J. Marklin, Z. anorg: allg. Chem. 334, 142 (1964)

[10] J. Mendialdua, R. Casanova, Y. Barbaux, J. Electron Spectrosc. Relat.Phenom. 71, 249 (1995); E. Hryha, E. Rutqvistb, L. Nyborg, Surf. Interface Anal. DOI 10.1002/sia.3844 (2011); G. Silversmit, D. Depla, H. Poelman, G.B. Marin, R.D. Gryse, J. Electron Spectrosc. Relat.Phenom. 135, 167(2004)

[11] D. Briggs and M. P. Seah, Practical Surface Analysis by Auger and X-ray Photoelectron Spectroscopy, John Wiley & Sons (1983)

[12] D.O. Scanlon, G.W. Watson, D.J. Payne, G.R. Atkinson, R.G. Egdell, D.S.L. Law, J. Phys. Chem. C 114, 4636 (2010)

[13] J.G. Choi, L.T. Thompson, Applied Surface Science 93,143 (1996)

[14] O.M. Flores, L. Scudiero, S. Haa, Surf. Sci. 603, 2327 (2009); R.T. Sobieraj, K. Hermann, M. Witko, A. Blume, G. Mestl, R. Schlogl, Surf. Sci. 489, 107 (2001)

[15] H. Takami, T. Kanki, S. Ueda, K. Kobayashi, H. Tanaka, Phys. Rev. B 85, 205111 (2012)

[16] X.S. Qing, M.H. Ping, D.S. Xun, J.Z. Hong, Chinese Phys. Lett. *doi:10.1088/0256-307X/20/1/344*

[17] H. Guo, Nano Lett. 11, 3207 (2011) ; L. Whittaker, C.J. Patridge , S. Banerjee , J. Phys. Chem. Lett. 2, 745 (2011); C. Marini, Phys. Rev. B 77, 235111 (2008) ; J.P. Pouget, Phys. Rev. B 10, 1801 (1974)

[18] J. Pietrzak, J. Kudynska, and Z. Kruczynski, Phys. Status Solidi A 67, K175 (1981)

[19] V.A. Klimov, I.O. Timofeeva, S.D. Khanin, E.B. Shadrin, A.V. Ilinski, F. Silva-Andrade, Tech. Phys. 47, 1134 (2002); J. Narayan and V. M. Bhosle, J. Appl. Phys. 100, 103524 (2006)

[20] G. Villeneuve, A. Bordet, A. Casalot, P. Hagenmuller, Mater. Res. Bull. 6, 119 (1971); M. Marezio, D.B. Mc Whan, J.P. Remeika, P.D. Dernier, Phys. Rev. B 5, 2541 (1972)

[21] M.M. Qazilbash, A. Tripathi, A.A. Schafgans, B.J. Kim, H.T. Kim, C. Zhonghou, M.V. Holt, J.M. Maser, F. Keilmann, O.G. Shpyrko, D.N. Basov, Phys. Rev. B 83, 165108 (2011)

[22] G. Villeneuve, A. Bordet, A. Casalot, J.P. Pouget, H. Launois and P. Lederer, J. Phys. Chem. Solids. 33, 1953 (1972)

[23] K. Shibuya, M. Kawasaki, Y. Tokura, Applied Phys. Let. 96, 022102 (2010)

[24] M.M. Qazilbash, M. Brehm, B.G. Chae, P.C. Ho, G.O. Andreev, B.J. Kim, S.J. Yun, A.V. Balatsky, M.B. Maple, F. Keilmann, H.T. Kim, D. N. Basov, Science 318, 1750 (2007); M.M. Qazilbash, M. Brehm, G.O. Andreev, A. Frenzel, P.C. Ho, B.G. Chae, B.J. Kim, S.J. Yun, H.T Kim, A.V. Balatsky, O.G. Shpyrko, M.B. Maple, F. Keilmann, D. N. Basov, Phys. Rev. B 79, 075107 (2009)

[25] V.N. Andreev, F.A. Chudnovskii, A.V. Petrov, and E.I. Terukov, Phys. Status Solidi A 48, K153 (1978); C.N. Berglund, H.J. Guggenheim, Phys. Rev. 185, 1022(1969); D.W. Oh, C. Ko, S. Ramanathan, D.G. Cahill, Applied Phys. Lett. 96, 151906 (2010)

[26] M.M. Qazilbash, M. Brehm, G.O. Andreev, A. Frenzel, P.C. Ho, B.C. Chae, B.J. Kim, S.J. Yun, H.T. Kim, A.V. Balatsky, O.G. Shpyrko, M.B. Maple, F. Keilmann, D. N. Basov, Phys. Rev. B 79, 075107 (2009); D.W. Oh, C. Ko, S. Ramanathan,D. G. Cahill, Applied Phys. Lett. 96, 151906 (2010)

[27] J.B. Goodenough, Phys. Rev. 117, 1442 (1960)

[28] J. Kousuge, J. Phys, Soc. Japan 22, 551 (1967); G. Villeneuve, A. Casalot, P. Hagenmuller, Mat. Res. Bull., 6, 119 (197 I)

[29] J. Pietrzak, J. Kudynska, and Z. Kruczynski, Phys. Status Solidi A 67, K175 (1981)

[30] W. Bruckner, H.P. Bruckner, U. Gerlach, B. Thuss, G. Foersterling, Phys. Status Solidi A 38, K13 (1976); T. Horlin, T. Niklewski, and M. Nygren, Mater. Res. Bull. 7, 1515 (1972); W. Rüdorff and J. Märklin, Z. Anorg. Allg. Chem. 334, 142 (1964); G. Villeneuve, A. Bordet, A. Casalot, J. P. Pouget, H. Launois, and P. Lederer, J. Phys. Chem. Solids 33, 1953 (1972); J. P. Pouget, P. Lederer, D.S. Schreiber, H. Launois, D. Wohlleben, A. Casalot, and G. Villeneuve, J. Phys. Chem. Solids 33,1961 (1972)

[31] S.C. Erwin, L. Zu, M.I. Haftel, A.L. Efros, T.A. Kennedy and D.J. Norris, Nature 436, 91 (2005); D.S. Kim, J. H. Yang, S. Balaji, H.J. Cho, M.K. Kim, D.U. Kang, Y. Djaoued, Y.U. Kwon Cryst. Eng. Comm, 11, 1621 (2009); L. Whittaker, T.L. Wu, C.J. Patridge, G. Sambandamurthy, S. Banerjee, Journal of Materials Chemistry, *DOI: 10.1039/c0jm03833d*

Chapter VII:
Structural, phase transition studies and electronic properties of VO$_2$ (A)

The aim of this chapter is to clarify the discrepancies about space group assignment and phase transition behavior in the case of VO$_2$ (A) and to reinvestigate its crystal structure using well crystallized microrods. I also study the phase transition mechanisms between LTP-A to HTP-A phase and HTP-A to VO$_2$ (M1), and the effect of phase transformations on their morphology. Furthermore, I attempted to get insights into the formation mechanism of crystals and finally I will present the physical properties of VO$_2$ (A) measured on spark plasma sintered VO$_2$ (A) pellets.
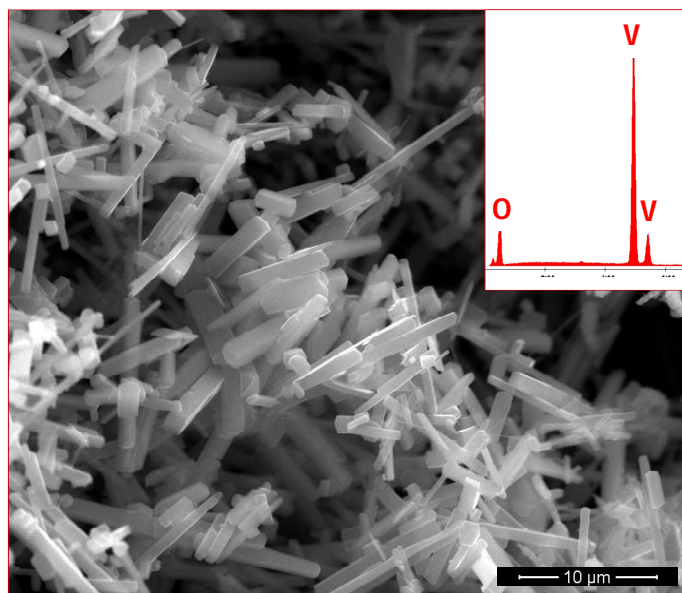
Contents

VII.1. Introduction

VO$_2$ (A) undergoes a progressive first-order structural transition from primitive tetragonal (LTP-A) to body-centered tetragonal (HTP-A) at 435 K, related to slight deviation of V^{4+}–V^{4+} bond length [1]. The lack of good crystalline VO$_2$ (A) samples are often leads to ambiguous assignment of space groups for this phase. For example, Y Zhang et al. [2] and Ming Li et al. [3] prepared ultralong nanobelts of VO$_2$ (A) using hydrothermal process, in which they assigned the observed reflections with different space groups i.e. P4/ncc (JCPDS card No. 70-2716) and P4$_2$/ncm (JCPDS card No. 80-0690) respectively. On the other hand, although a number of morphologies have been reported, the investigation of the relation between different morphologies is still crucial for realizing morphology-controlled synthesis and for the investigation of effect of size/morphology dependence on phase transitions. In terms of physical properties, the reported studies are still at synthesis stage and complete understanding of the electronic properties are still lacking.

VII.2. Synthesis

Here we are going to briefly schematically describe the synthesis procedure implemented for the preparation of different kinds of morphologies of VO$_2$ (A) and VO$_2$ (M1), which is explicitly described in *chapter V*. As the synthesis conditions play an important role in the obtained phases, we summarized the complete details about the synthesis procedure and obtained morphologies of the final products in **Figure 1**. The results showed here indicate that, in hydrothermal processes, different structures and morphologies can be obtained by simply varying the reaction temperature and the duration without adding any other reactants.
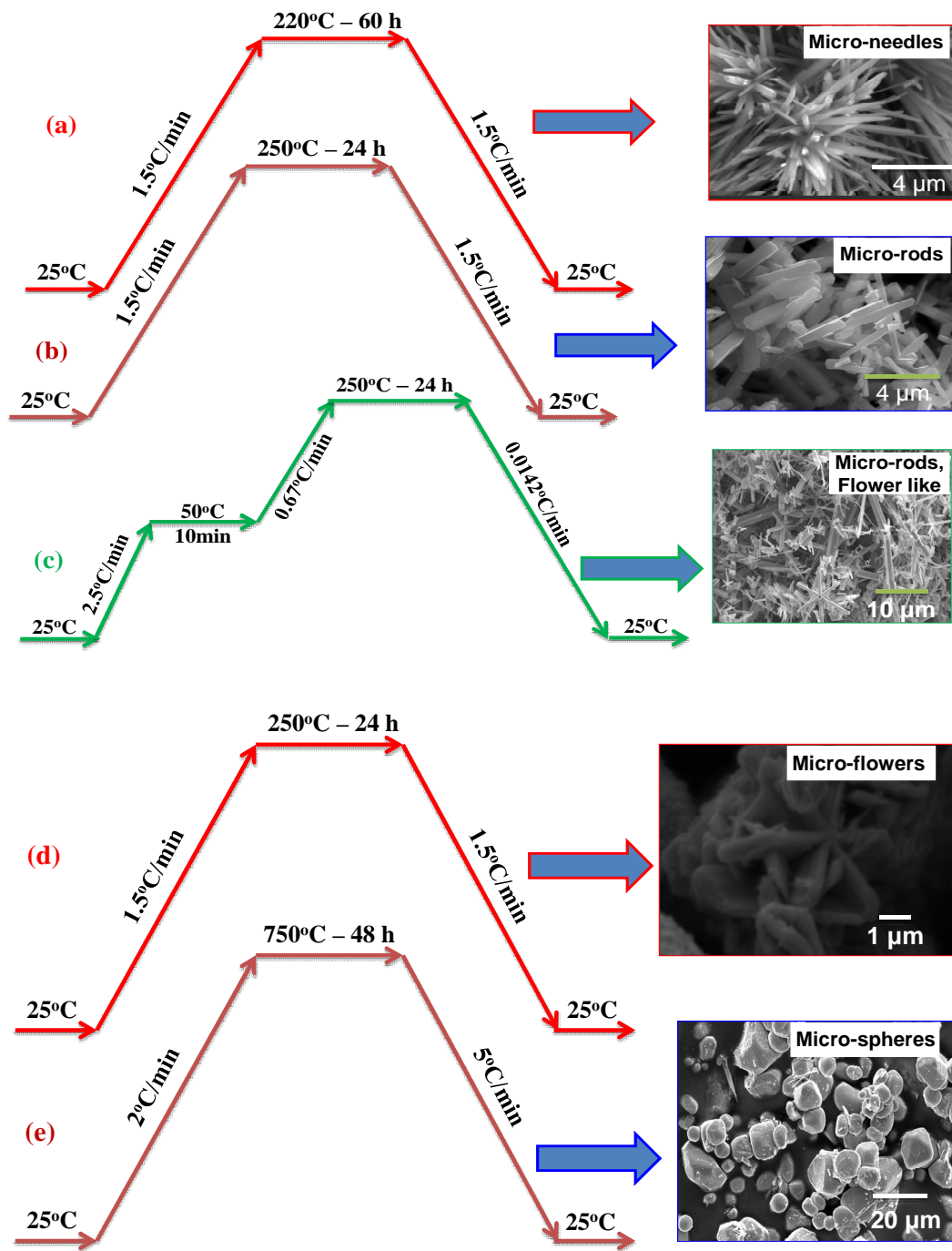
Figure 1. Schematic representation of experimental conditions used for the preparation of VO$_2$ (A) and VO$_2$ (M1) (a) hydrothermal VO$_2$ (A) micro-needles; (b) hydrothermal VO$_2$ (A) micro rods; (c) slow cooling hydrothermal VO$_2$ (A) and VO$_2$ (M1); (d) hydrothermal VO$_2$ (M1) micro flowers; (e) solid state VO$_2$ (M1) micro spheres.

VII.3. Experimental details

P-XRD patterns of the final products were recorded using a PANalytical X'Pert PRO MPD diffractometer with graphite monochromatized Cu K$_\alpha$ radiation (λ=1.54178 Å) and the phase purity of obtained products were checked by comparing the experimental P-XRD patterns to standards compiled by the Joint Committee on Powder Diffraction and Standards (JCPDS). The morphology of the products was examined by a field emission scanning electron microscope (FESEM, JEOL JSM - 6300F, 15 kV). The products were deposited on double coated copper conductive tapes and subsequently sputter coated with a thin layer of gold on the surface to prevent the charging effects. Energy Dispersive X-ray spectroscopy (EDX) coupled to field emission scanning electron microscope was used to determine the chemical elements present in the prepared products.

The above mentioned P-XRD diffractometer was further used with an Anton-par high temperature and low temperature chamber under vacuum (9.2×10^{-5} bar) to study the phase transition between two different polytypes of vanadium dioxide. In order to study the phase transition behaviours, we carried out Differential scanning calorimetry (Perkin Elmer DSC 8500) measurements under argon atmosphere over a temperature range from 300 to 500 K along heating/cooling cycles. The chemical composition and room temperature electronic structure of VO$_2$ (A) micro rods were studied by means of X-ray photoemission spectroscopy (XPS) with a VG Escalab 220i XL X-Ray Photoelectron Spectrometer using Aluminium monochromatic source (hυ = 1486.6 eV) under ultrahigh vacuum conditions. Electrical direct current resistivity measurements were performed with four probe method with a homemade setup. Low temperature magnetization measurements were performed using a Quantum Design MPMS magnetometer. High temperature magnetization measurements (HTMag) were performed using a MANICS susceptometer. Specific heat measurements were carried out using Physical Property Measurement System (PPMS®).

The Spark Plasma Sintering (SPS) (SINTER® LAB Series; SPS-511S) technique enabled us to overcome the densifying difficulty in conventional sintering of VO$_2$ (A), which is caused by the low transformation temperature of this metastable phase. The VO$_2$ (A) powders were densified by SPS at 250 °C for 5 min in a vacuum level of 10^{-2} mbar with an applied pressure of 90 MPa. The heating rate up to the sintering temperature was about 100 °C/min. The density of

obtained pellets is around 71 %. **Figure 2** shows the surface morphology of the VO_2 (A) pellet prepared by SPS process.
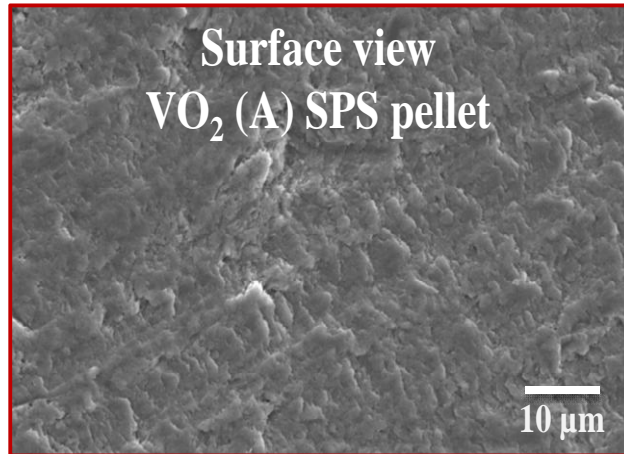
Figure 2. Surface morphology of a VO_2 (A) pellet obtained by spark plasma sintering process.

VII.4. Structural studies: P-XRD

P-XRD studies were carried out to establish the phase purity and identify the presence of any kind of impurities in the VO_2 (A) powders. We examined P-XRD patterns collected at room temperature by Rietveld analysis using FullProf program [4].

Figure 3 shows the P-XRD pattern of the LTP phase of VO_2 (A) with micro rod morphology prepared at 250°C for 24 h, and crystallographic details (lattice parameters and atomic positions) are presented in **Table 1.**
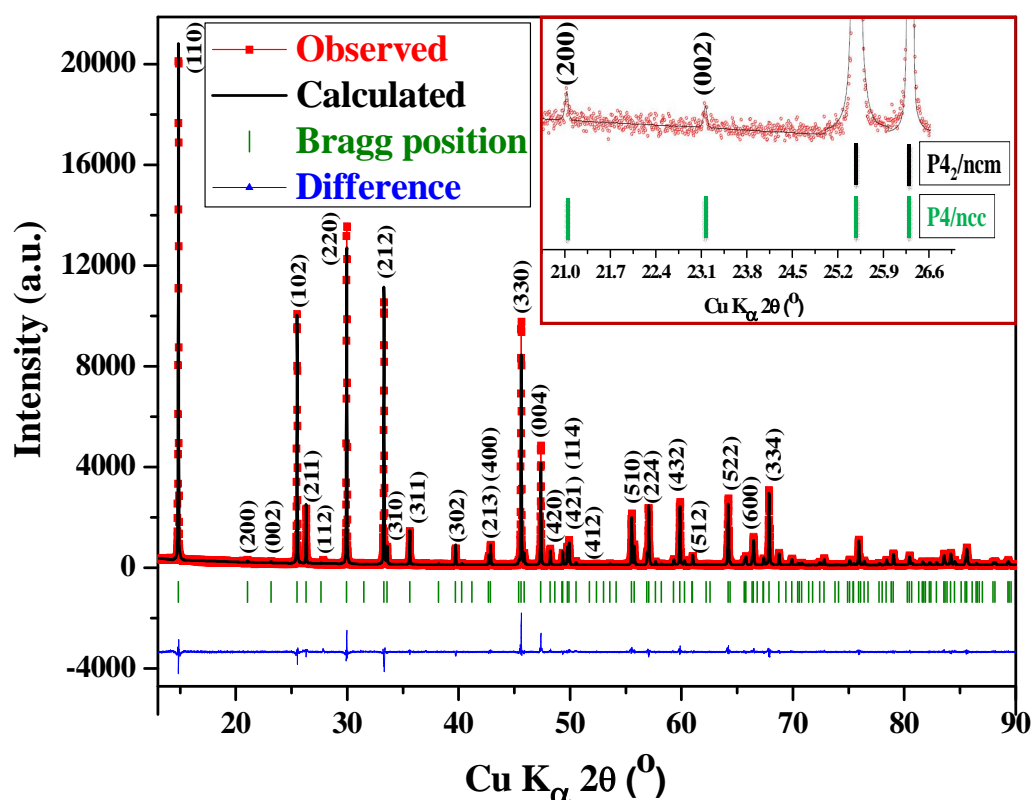
Figure 3. Observed and calculated X-ray powder diffraction pattern of VO_2 (A) phase taken at room temperature (LTP-A). Here the inset compares the reflections between $2\theta=21\text{-}26.6°$, assigned by two different space groups ($P4_2/ncm$ and $P4/ncc$), in which $P4/ncc$ is taking care of even low intensity reflections (200) and (002).

LTP-VO₂ (A) Space group: P4/ncc (130)					
Lattice parameters	a = 8.43478 (4) Å; c = 7.67220 (4) Å; Z = 16				
Profile parameters	Function: Pseudo-Voigt *Halfwidth parameters* U = 0.010 (3) V = -0.0022 (3) W = 0.004 (3)				
Atomic positions	Atom label	x	y	z	Occupancy
	V	0.44835 (7)	0.72427 (6)	0.12959 (13)	1
	O1	0.40550 (2)	0.7481 (2)	0.3765 (7)	1
	O2	0.4102 (2)	0.4098 (2)	0.3727 (8)	1
	R-factors	Rₚ: 6.66 %	R_wp: 8.58 %	R_exp: 6.62 % χ²: 1.68	

Table 1. Lattice parameters details and atomic position from the Rietveld refinement of VO_2 (A) at room temperature (LTP-A)

At room temperature, all detectable peaks in the P-XRD pattern of the synthetic VO_2 (A) (LTP-A) can be readily indexed to a pure tetragonal unit cell with space group P4/ncc, lattice

constants a=8.435 Å, c=7.624 Å. The experimentally determined cell parameters were compared to those reported in JCPDS data card 70-2716. These lattice parameters are also in agreement with values reported in the literature by Oka et al. using single crystals [5]. In the inset of **Figure 3,** we compared the reflections between $2\theta=21\text{-}26.6^o$, assigned by two different space groups P4$_2$/ncm and P4/ncc. Here the space group P4/ncc is taking care of even low intensity reflections (200) and (002), whereas P4$_2$/ncm is not accounting these reflections. In the case of some of the previous reports, un-identification of these low intensity reflections due to less crystallized VO$_2$ (A) samples, often leads to propose P4$_2$/ncm as a spacegroup. So in our case, well crystallized VO$_2$ (A) micro structures helped us to observe the low intensity reflections in the P-XRD pattern and to assign P4/ncc as the appropriate space group for VO$_2$ (A) at room temperature. The high crystalline nature of the obtained VO$_2$ (A) micro structures are further supported by the sharp diffraction peaks of P-XRD patterns. In this case, the relative intensities of reflections along (110) planes are strong compared to other directions, which show the preferential orientation nature of samples along (110) direction. This can be understood on the basis of morphology-preferential growth relationships defined by the Bravais–Friedel–Donnay–Harker (BFDH) law [6]. The equilibrium form of crystal growth mechanism would be in such a way that the total surface energy for a given volume will be minimum and thus the crystal growth would be bounded by faces located at distances proportional to their surface energies. Under equilibrium conditions, greater interplanar distance (d_{hkl}) planes are expected to have lowest surface energies, thereby larger probability of growth in that direction. In case of VO$_2$ (A), the (110) plane is situated at greater $d_{110} = 6$ Å compared with any other plane. This argument is in agreement with the crystal structure of VO$_2$ (A) in which, the V-O distance along the (110) direction is shorter than the distance along the other directions [7]. These conditions favors the preferential growth of VO$_2$ (A) samples along the (110) plane due to high growth rate along the (110) axis.

VII.5. Stability studies: TGA

Before manipulating any kind of properties, we performed TGA measurements under argon atmosphere until 573 K to study the phase stability of the VO$_2$ (A) polymorph at high temperatures. The corresponding TGA analysis provides the stability information for the as-prepared VO$_2$ (A) samples, as shown in **Figure 4.** A small weight loss of around 0.3% was found below 100°C and may be due to the release of adsorbed water molecules on the surface of the

micro rods. In order to check the phase stability, we acquired the P-XRD pattern after TGA analysis *(not shown here)*. All P-XRD reflections can be indexed to the tetragonal structure using FullProf profile matching and are in agreement with **LTP-A** (**Figure 3**).This confirmed the stability of the phase until $300^{\circ}C$ under Ar.
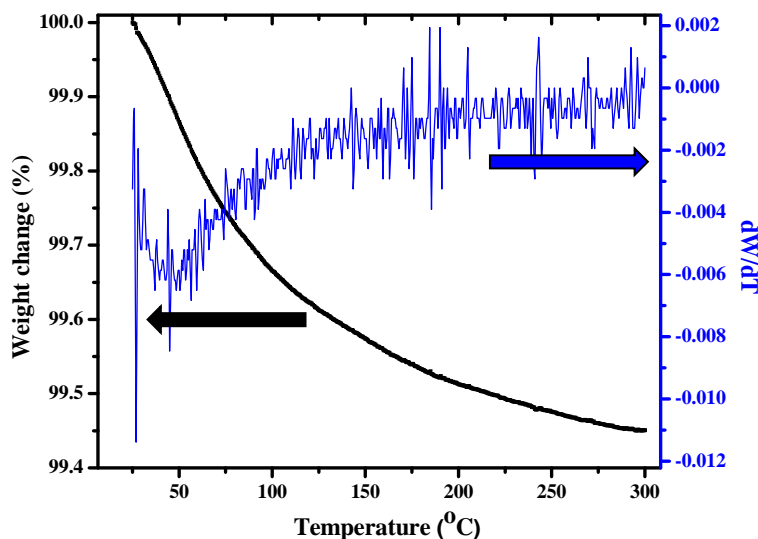
Figure 4. TGA analyses of the as-synthesized VO_2 (A) micro-rods.

VII.6. Spectroscopic studies

XPS experiments were carried out to access some details of the electronic structure. **Figure 5** shows the XPS the survey spectrum, valence band region and core level spectra for V and O elements in VO_2 (A). No other peaks of impurity elements other than atmospheric carbon were observed in the survey spectrum (**Figure 5a**). The binding energy obtained in our XPS analysis was calibrated with respect to reference C 1s line to 284.4 eV. Along with survey spectra, we acquired the high resolution spectra in the selected energy level regions of C 1s, $V2p_{3/2}$, $V2p_{1/2}$, O 1s, V 2s. For a better understanding of VO_2 (A) electronic structure, we acquired high resolution XPS measurements have been performed around the valence band region. The valence band region (**Figure 5b**) consists of V 3d and O 2p bands in the energy ranges between 0-2 and 3-9 eV, respectively and zero spectral weight at Fermi level is consistent with room temperature insulating behavior. We found that the binding energies of the V 2p3/2, V 2p1/2 and O 1s peaks are centered at 516.4, 523.9 and 530.05 eV (**Figure 5c**), which are characteristic of the V^{4+} oxidation state and in a good agreement with most of the reported

values. As proposed by Mendialdua et al. [8], in order to confirm the composition of obtained microrods as VO_2, we compared the difference in binding energies between oxygen and vanadium core levels, which is 13.65 eV in agreement with +4 oxidation degree of V.
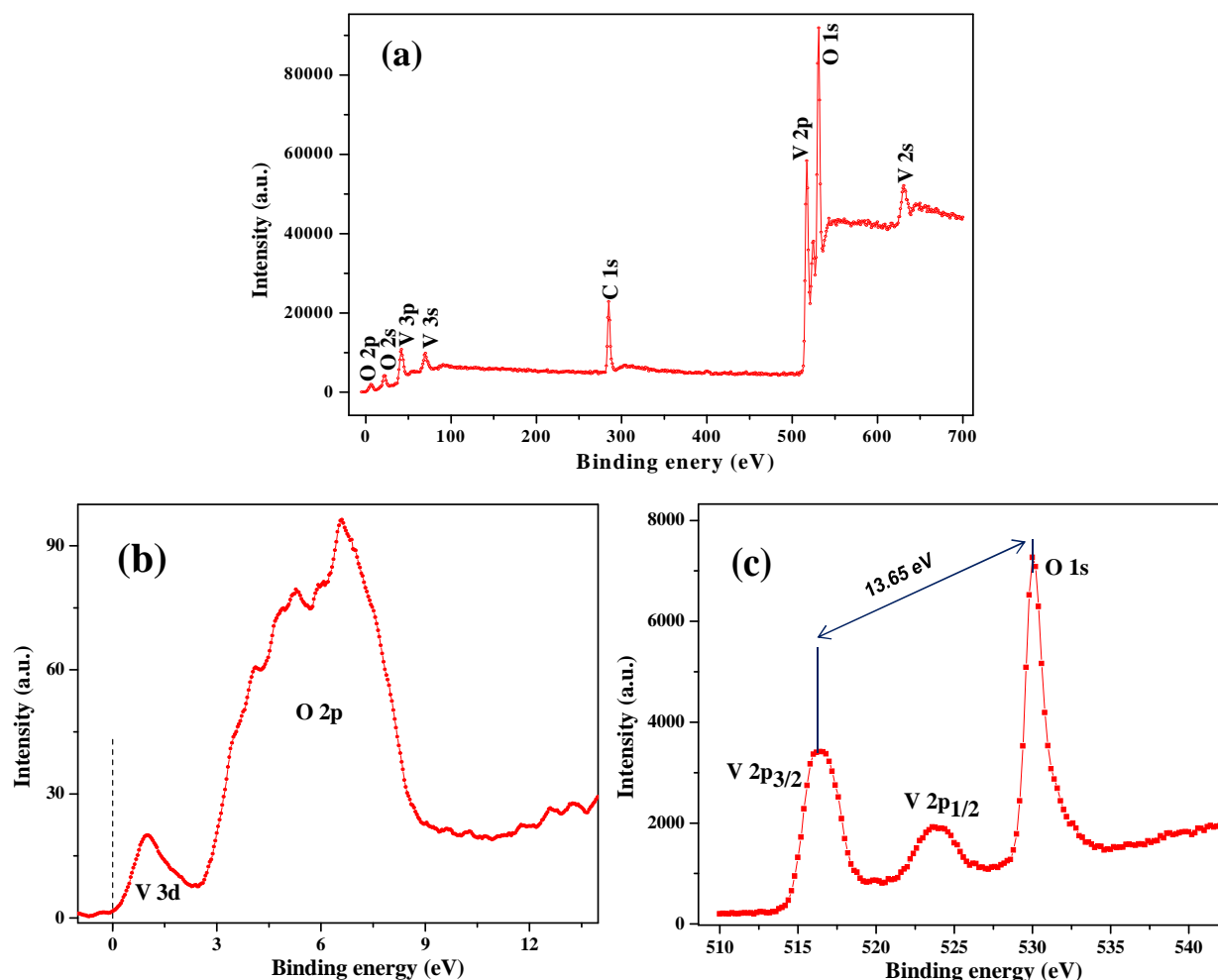
Figure 5. (a) Surface XPS survey spectrum of VO_2 (A); (b) XPS spectra of V 3d and O 2p at low binding energy region; (c) Core level XPS spectra of the V 2p and O 1s region.

From core level and valence band studies by XPS, we can conclude that the sample in our study is indeed a pure phase with composition VO_2 and is semiconducting / insulating in nature at room temperature.

VII.7. Phase transition studies

VII.7.1. High temperature studies: LTP-A to HTP-A

For the first time, in the case of VO_2 (A), Oka et al. observed a phase transition at 435 K only upon heating using DTA measurements; they did not observe it on cooling cycle [1]. On the contrary, some recent studies report the signature of the phase transition of VO_2 (A) during heating as well as cooling cycles. In order to clarify this issue related to the absence of transition during cooling cycles, and to study the phase transition, we performed the DSC measurements around the phase transition temperature on VO_2 (A) micro rods, and shown in **Figure 6.**
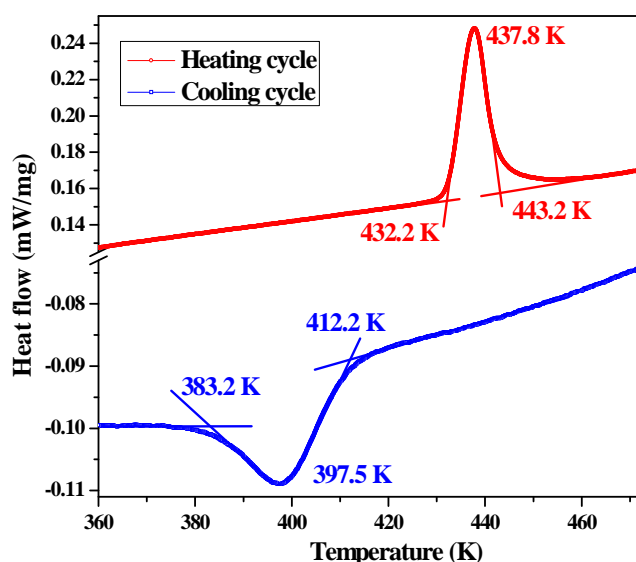
Figure 6. DSC curves of VO_2 (A) powders during heating and cooling cycles.

We have observed a *giant* hysteresis (40 K) between heating and cooling cycles. This hysteresis between cooling and heating cycles indicates the first-order nature of the phase transition. The giant 40 K hysteresis, reported here, is the largest among the reported hysteresis (32 K) in VO_2 (A) micro or nano structures [3]. A similar hysteresis behavior was observed by Feldman et al. and Luisa Whittaker et al. for VO_2 (M1) nanostructures, which were grown by preparation methods such as ion implantation and hydrothermal processes [9]. In addition to this, we also noticed the non-symmetric transition peak during heating cycle and broader transition peak during cooling cycle ca. 29 K (compared to heating cycle ca. 11 K). The most striking features of these observed hysteresis loops can be associated with martensitic type structural transformations, to which the VO_2 (M1) phase transition belongs. This kind of structural

transformations take place at two fixed temperatures if only a single interface between the two transformable phases is involved, like in case of single crystals. In the case of polycrystalline samples, this transition can be extended over a range of temperatures due to the existence of several interfaces. In order to understand the relation between the observed transition in DSC measurements and reported structural phase transition (from LTP-A to HTP-A), we studied the structural phase transition process using in-situ P-XRD measurements. Usually, the first-order phase transitions involve a change in the entropy of the system. In the case of VO_2, this change in entropy is due to small lattice distortions. So thermal studies can be used to study the first order phase transition, through which we can provide the necessary energy for the phase transition.
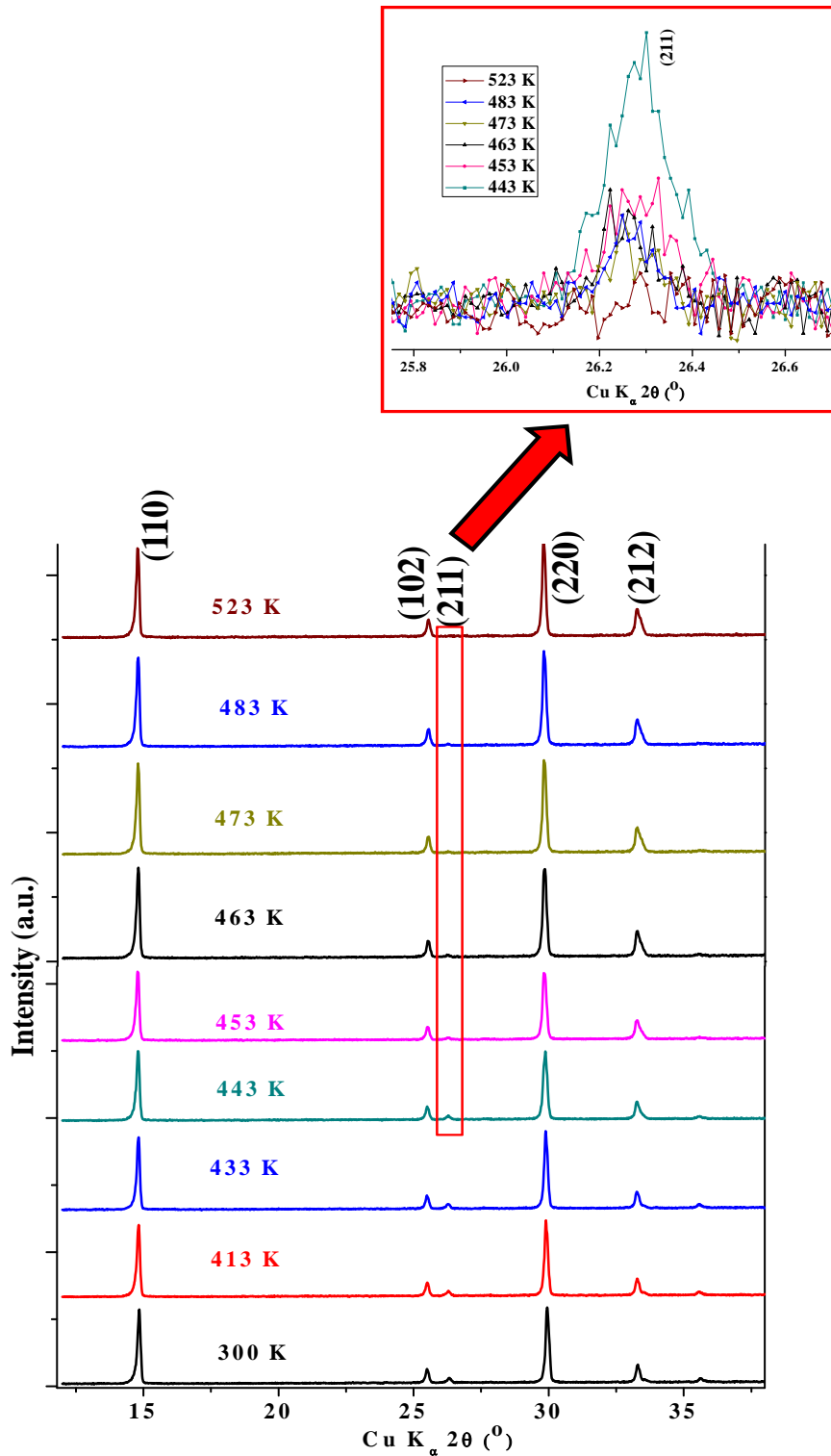
Figure 7. In-situ high temperature X-ray diffraction patterns of VO_2 (A) during heating cycle (inset highlights the disappearance of the (211) reflection during the structural phase transition).
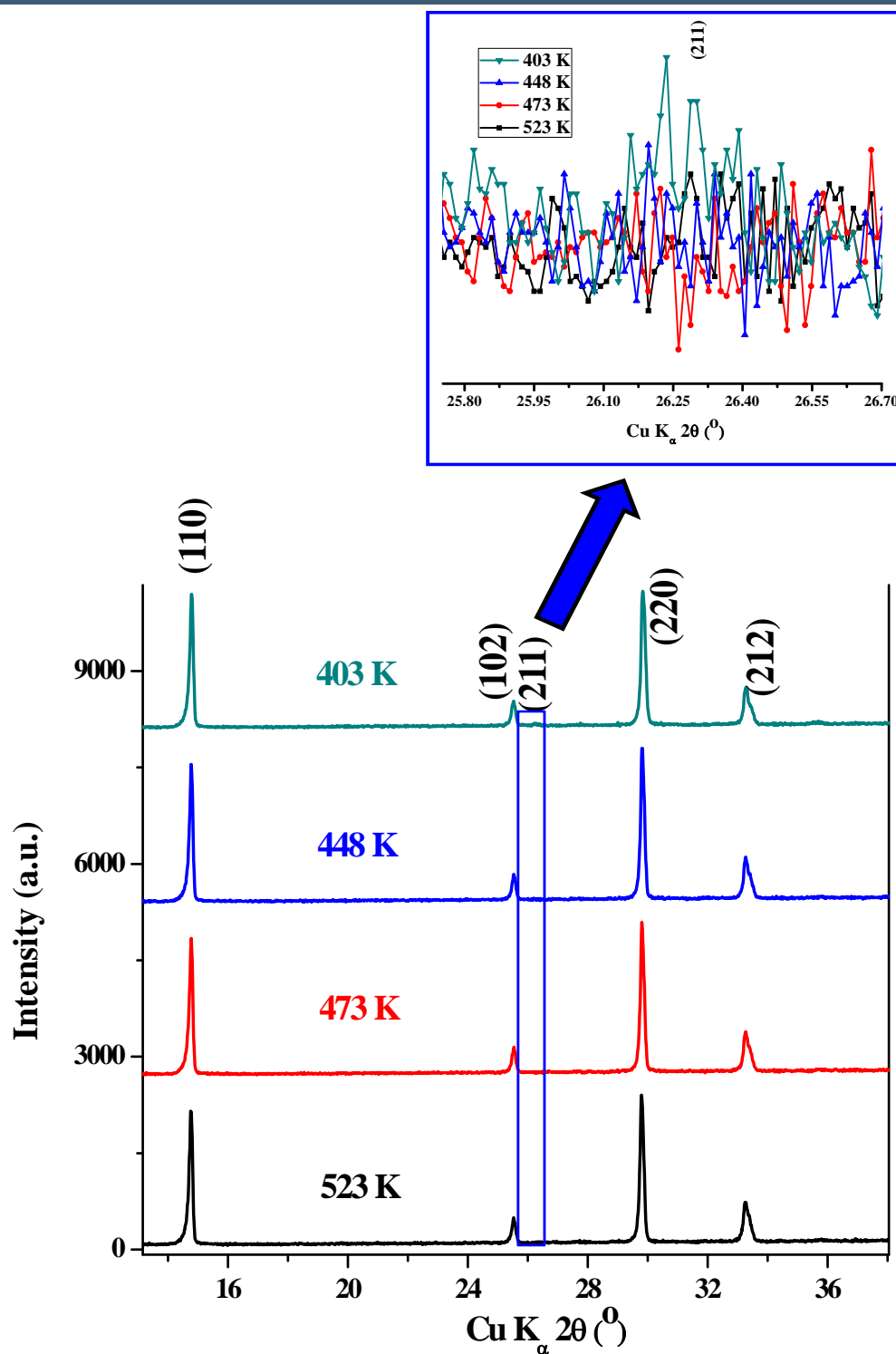
Figure 8. In-situ high temperature X-ray diffraction patterns of VO_2 (A) during cooling cycle (inset highlights the appearance of the (211) reflection during the structural phase transition).

The P-XRD patterns during heating (from 300-523 K) and cooling cycles (523-403 K) are shown in **Figure 7** and **Figure 8** respectively**.** During the heating cycle, the profile of P-XRD

peaks changed drastically and there is a continuous disappearance of reflections such as (211) and (311). Whereas on contrary to observations made by Oka et al., we didn't find any flattening on the top of the (600) peaks, which was attributed to the irregularity along a axis [1]. Interestingly, we noticed that a complete structural phase transition occurs at much higher temperatures, around 483 K or above (zoomed region in **Figure 7**), compared with the transition temperature observed using DSC which is around 437 K. This observation rules out the possibility of simultaneous occurrence of structural and insulator to metal phase transitions, with presence of LTP phase in HTP phase region. The structural phase transition in LTP-A may be initiated at particular nucleation sites from which HTP-A phase domains evolves and extend much above the transition temperature. In this transition temperature region, both LTP-A and HTP-A phase domains may coexist. This kind of transformations often leads to spatial inhomogeneity and strongly influences the properties of the materials [10]. During the cooling cycle, the structural transition from HTP-A to LTP-A is starting at 403 K (zoomed region in **Figure 8**), which is in agreement with giant hysteresis observed using DSC measurements and supported with the reversible structural phase transition mechanism. At the structural phase transition on heating cycle, the cell parameter 'a' was increased while the cell parameter 'c' becomes the half [1].
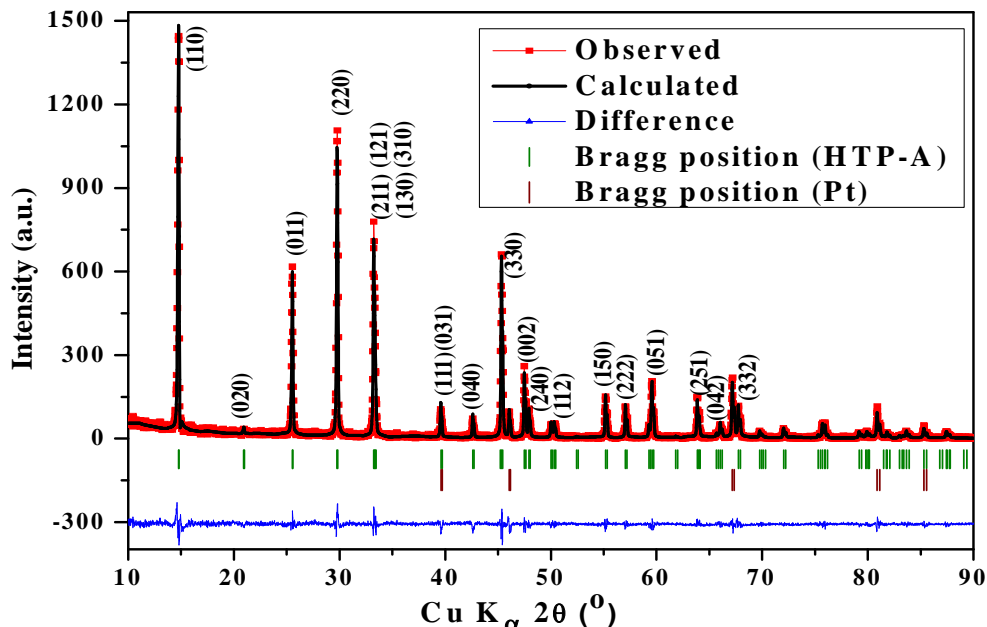
Figure 9. Observed and calculated X-ray powder diffraction pattern of VO$_2$ (A) phase recorded at 400°C (HTP-A).

HTP-VO$_2$ (A)				
Space group: **I 4/m (87)**				
Lattice parameters	a = 8.4819 (3) Å ; c = 3.8257 (2) Å ; Z = 8			
Profile parameters	Function: Pseudo-Voigt *Halfwidth parameters* U = 0.055 (2) V = -0. 038 (2) W = 0.0204 (9)			
Atomic positions				
Atom label	x	y	z	Occupancy
V	0.3000 (5)	0.0242 (6)	0	1
O1	0.5018 (2)	0.1588 (1)	0	1
O2	0.1622 (4)	0.157 (2)	0	1
Pt (sample holder)				
Space group: **F m -3 m (225)**				
Lattice parameters	a = b = c = 3.93823 (3) Å			
Profile parameters	Function: Pseudo-Voigt *Halfwidth parameters* U = 0.046 (1) V = -0. 037 (1) W = 0.0199 (7)			
***R*-factors**	R$_p$: 15.7 % R$_{wp}$: 23.9 % R$_{exp}$: 20.52 % χ^2: 1.36			

Table 2. Lattice parameters and atomic positions from the Rietveld refinement of VO$_2$ (A) at 400°C (HTP-A), and profile parameters for Pt (sample holder).

Figure 9 shows a typical P-XRD pattern of VO$_2$ (A) sample at 400°C (HTP-A) and the structural details are summarized in **Table 2**. Here the platinum peaks in the P-XRD pattern comes from the sample holder. All the XRD peaks can be indexed to the space group I4/m with lattice constants a=8.4819 Å, c= 3.8257 Å. The 'a' lattice parameter increased from LTP-A to HTP-A phase but, the 'c' lattice parameter decreased. This can be related to the de-pairing of V^{4+}-V^{4+} ions along the 'c' axis above the transition. In the LTP-A phase, pairing of V^{4+} ions leads to alternating distances between two V^{4+} ions along the c axis (2.766 and 3.106 Å); in the HTP phase, depairing of V^{4+} leads to equal distances between neighbor V^{4+} ions (3.082 Å).

VII.7.2. Low temperature studies: P-XRD

The low temperature behaviour of VO$_2$ (A) has not been reported yet. We studied the crystal structure of VO$_2$ (A) by recording P-XRD patterns down to 10 K, shown in **Figure 10**. All of them can be indexed with the same space group (P4/ncc) than at RT using Rietveld

analysis. We noticed the gradual modifications in the P-XRD patterns by decreasing the temperature, indicating a decrease in the distance between (421) and (114) reflections. The variation of lattice parameters at 10 K (a=8.42103 (6) Å; c=7.67324 (6) Å) and at 100 K (a=8.42374 (9) Å; c=7.6737 (1) Å) reveals the contraction of 'a' axis and the expansion along 'c' axis. This leads to increase in the c/a ratio with decreasing temperature. These changes could be due to some structural rearrangement at low temperature and this phenomenon is reversible. This shows some similarities with the phase transition observed in VO_2 (B) phase, in which the phase transition from room temperature (un-paired state) to low temperature (paired state), occurs at 240 K [11].
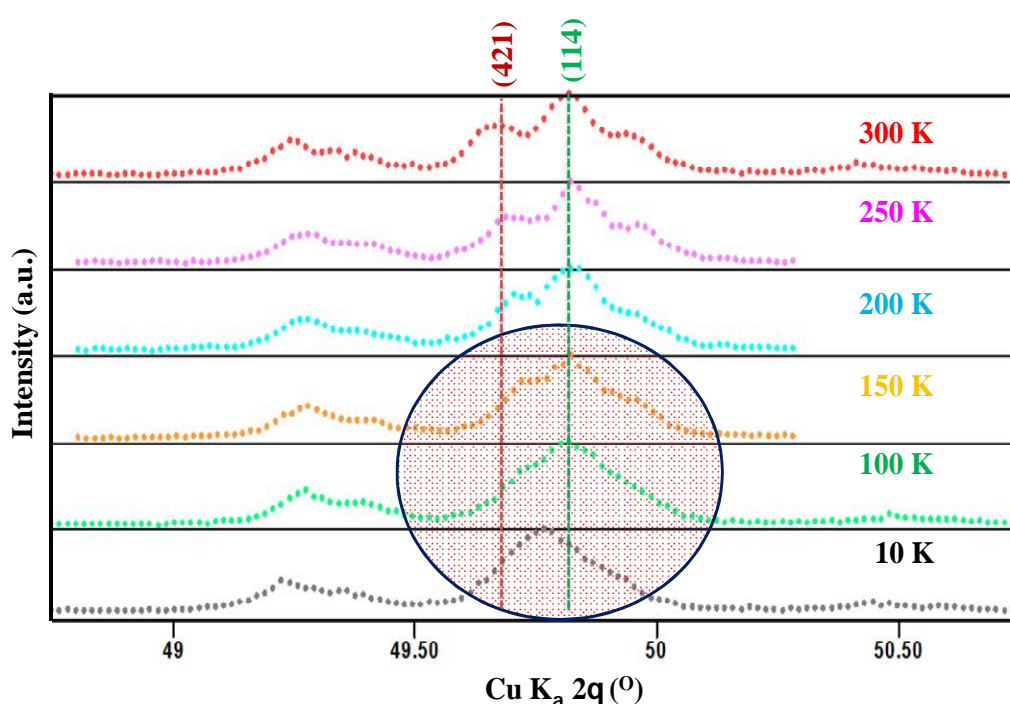
Figure 10. Low temperature X-ray diffraction patterns of VO_2 (A) micro-rods (blue circle highlights the changes in P-XRD patterns).
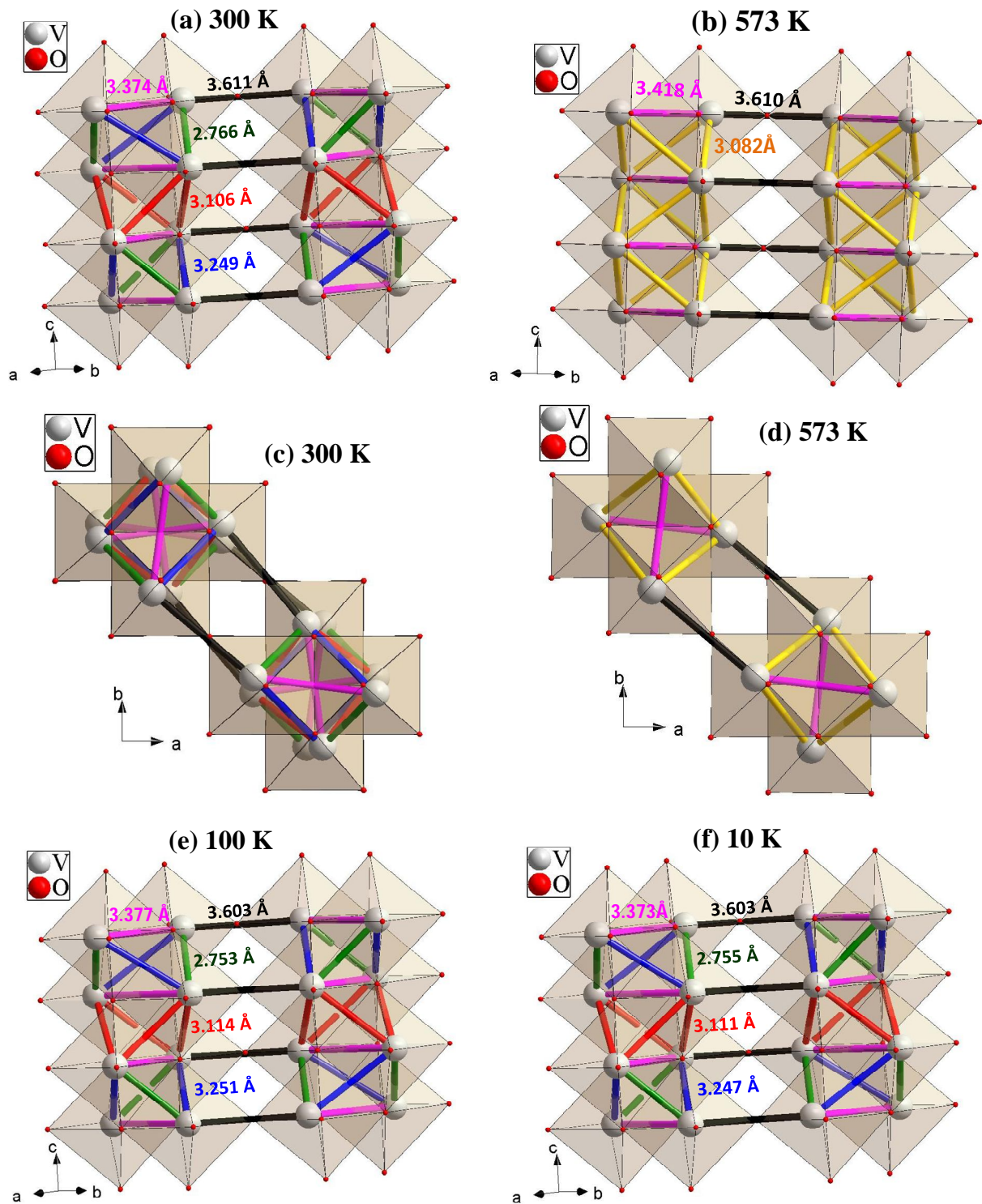
Figure 11. Structure of (a) LTP-VO$_2$ (A) and (b) HTP-VO$_2$ (A) with V-V distances; projection along c axis (c) LTP-A and (d) HTP-A;   Structure of VO$_2$ (A) with V-V distances at (e) 100 K and (f) 10 K.

Figure 11 represents the resulting structure of VO_2 (A) at different temperatures. In specific, **Figure 11c** and **d** shows the crosses of four edge shared octahedra along c direction link in-plane by corners. It highlights the difference in the V-V bonds depending their distances, in which V site has a crude C4v symmetry. At all temperatures presented here, the structures consists of distorted VO_6 octahedra, in which distortion caused by the displacement of V atoms from centre position towards O (2) site.

Upto 300 K (LTP-A), V-V sites are separated by mainly 5 different distances and these distances are reduced to three at 570 K (HTP-A).

Here the structure can also be viewed as an edge shared V tetrahedra running along 'c' direction and two different sequences of this type are separated by distance 3.611 Å at 300 K (black line). This bond length is less affected through the structural transition. The bond length between two edge shared V octahdra in the ab plane, is 3.374 Å at 300 K (pick line). Along c axis the long blue bonds, medium red bonds and short green bonds bridge V sites and leads to zig-zag chain fashion. From LTP-A to HTP-A phase, the rotation of V sites in ab plane leads to single yellow V bridges i.e. an alternate distances of medium red bond (3.114 Å) and short green bond (2.753 Å) converts to uniform yellow bond (3.082 Å) in HTP-A phase. **Figure 11e** and **f** indicates the corresponding changes in the different bonds lengths at low temperatures. From this we can infer that short green bond becomes shorter and medium red bond becomes bit longer compared with LTP-A.

VII.7.3. High temperature studies: HTP-A to VO_2 (M1)

In order to study the phase transition process from HTP-A to VO_2 (M1), we extended in-situ P-XRD studies from 523 to 1023 K, and corresponding patterns are shown in **Figure 12a**. We observed that the HTP phase of VO_2 (A) is stable until 673 K and the phase transformation from HTP-A to VO_2 (R) occurs in between 773 - 873 K. In this temperature range, we noticed a phase coexistence of HTP-A and VO_2 (R) phases. The complete phase transformation process from HTP-A to VO_2 (R) was realized at 973 K.
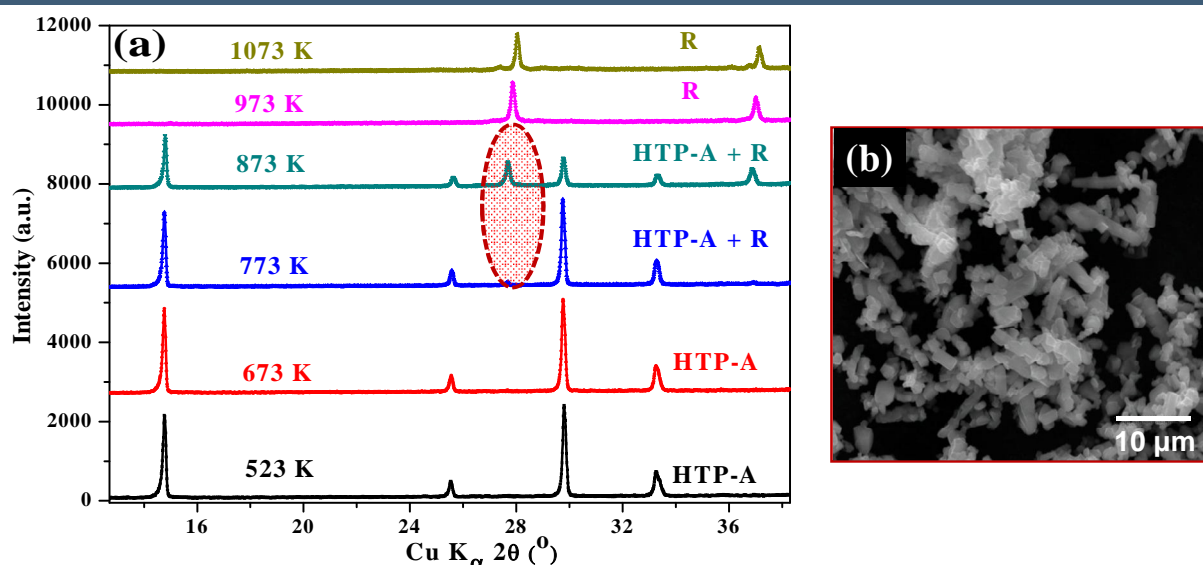
Figure 12. (a) X-ray diffraction study of phase transformation process from HTP-A to VO_2 (R) (circle highlights the phase transformation process) (b) Morphology of VO_2 (M1) sample obtained after high temperature in-situ XRD study.

At the end of in-situ P-XRD study, we acquired the P-XRD pattern at room temperature, which shows the VO_2 (M1) phase, indicates the irreversible phase transformation between HTP-A and VO_2 (M1). This irreversible phase transformation can be explained by the drastic differences in crystal structures of the two phases. The structure of VO_2 (M1) contains a 3D pattern of VO_6 octahedra, whose 4 fold axes are aligned along two perpendicular directions, whereas in HTP-A, VO_6 octahedra are aligned along one direction only. **Figure 12b** shows the morphology of obtained VO_2 (M1) microstructures after in-situ high temperature P-XRD studies. The obtained morphologies are quite different from as synthesized VO_2 (A) microrods and a breaking of microstructures is noticed when transformation to VO_2 (M1) occurs.

To confirm the phase transformation, we annealed VO_2 (A) microrods for 1 h at 623, 823, 923 and 1023 K under argon atmosphere using a tubular furnace (2^oC/min and 5^oC/min heating and cooling rates respectively). The corresponding P-XRD patterns are described in **Figure 13a.**
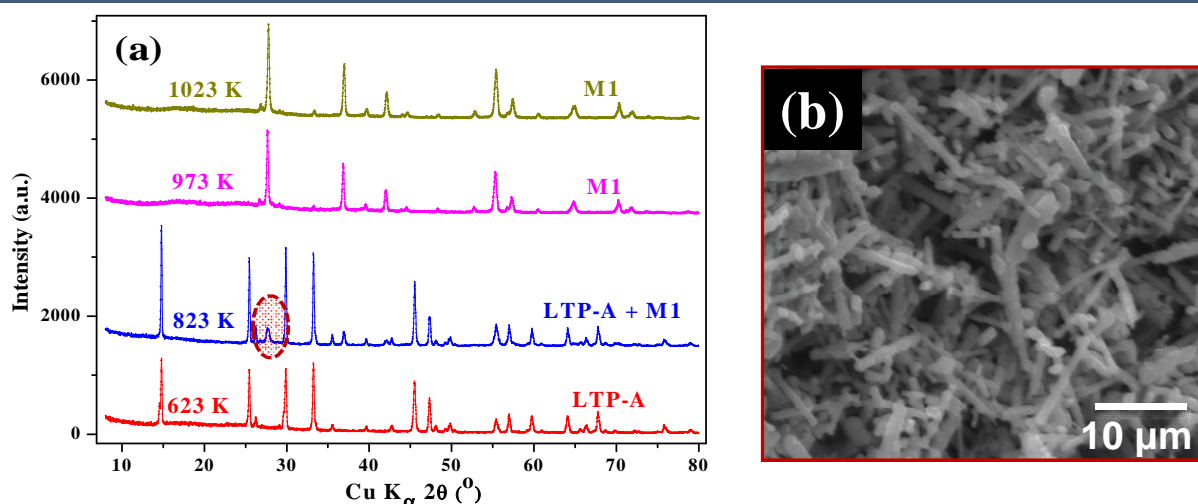
Figure 13. (a) X-ray diffraction patterns of annealed VO_2 (A) samples under different temperatures (b) Morphology of VO_2 (M1) phase, obtained after annealing VO_2 (A) at 1023 K for 1 h.

The phase transformation from HTP-A to VO_2 (M1) phase, which was studied by in-situ P-XRD study, was further supported by the observed phase transformation process (by P-XRD patterns) in the annealed case, by showing the complete transformation from HTP-A into VO_2 (M1) between 823 - 923 K. The **Figure 13b** shows the morphology of obtained VO_2 (M1) microstructures after in-situ high temperature P-XRD studies and Ar annealing at 1023 K for 1 h. The obtained morphologies are quite similar to as synthesized VO_2 (A) microrods, with minor breaking of microstructures noticed when transformation into VO_2 (M1) occurs. This can be explained in view of the different arrangement of VO_6 octahedra in both phases and difference in unit cell volume (from LTP-A with 34.1183 $(\text{Å})^3$ to HTP-A with 34.3969 $(\text{Å})^3$ and VO_2 (M1) with 29.5083 $(\text{Å})^3$ per formula unit). As we can notice here, there is a nearly 0.8% increase in the cell volume from LTP-A to HTP-A, whereas this difference was significantly increased to 14% from HTP-A to VO_2 (M1). In the case of VO_2 (M1), morphologies obtained after in-situ P-XRD studies, show a pronounced breaking of microrods (**Figure 12b**). This may be due to larger duration of heating process (ca. 2 h) during in-situ P-XRD study compared to Ar annealing process (1 h). This observation is consistent with the morphology changes observed during the in-situ electron microscopy phase transformation study from VO_2 (B) to VO_2 (M1) [12]. Upon continuous heating, VO_2 (B) platelets abruptly break up into nanocrystallites and recrystallize into VO_2 (M1).

VII.8. Crystal growth and insights into formation mechanism:

Increase of crystallite size of single phase VO_2 samples under hydrothermal conditions are often challenging because of the formation of a variety of stable vanadium oxide crystalline phases in narrow range of preparation conditions. We attempted to increase the crystal size and understand the formation mechanism, by slowly cooling the autoclave from reaction temperature to room temperature. After slowly cooling of autoclave for 264 h, we studied the crystal structure using P-XRD pattern and morphology of the sample (**Figure 14**).
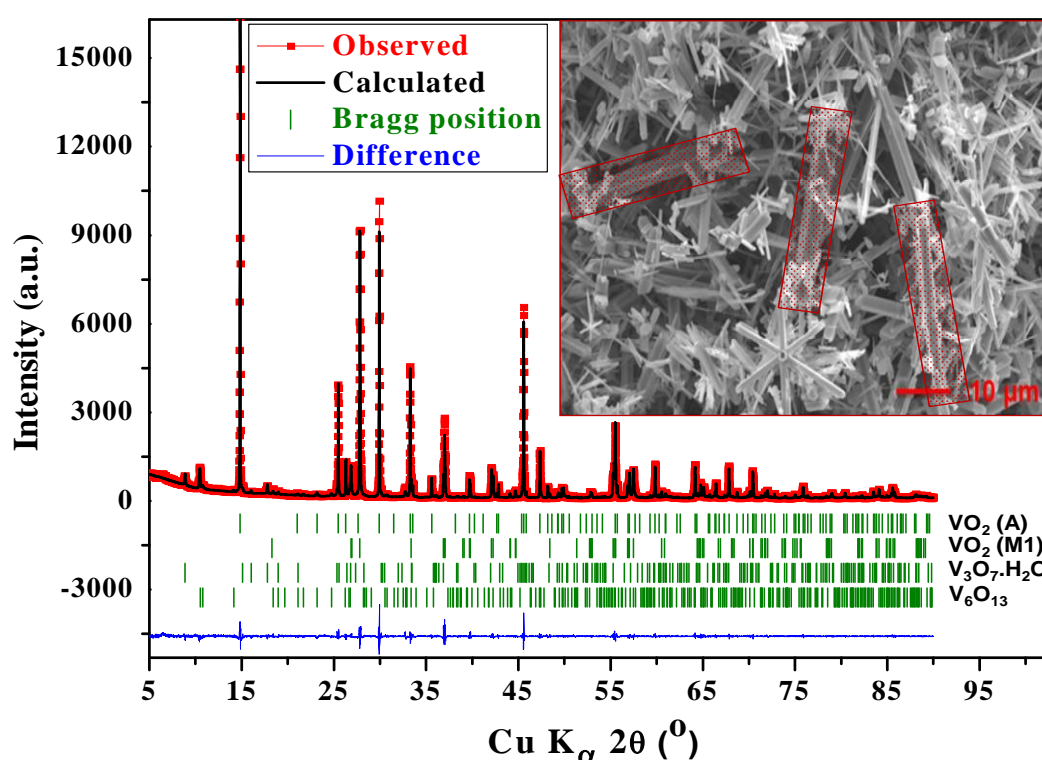
Figure 14. X-ray diffraction pattern of final product obtained after slow cooling of autoclave for 264 h (inset: Morphology of final products and red squares shows the increase in the micro rod sizes).

A careful analysis of P-XRD pattern after slow cooling of autoclave reveals the presence of multiple crystalline phases along with VO_2 (A). By analysing these phases by FullProf suite profile matching, we have identified these phases as VO_2 (M1) (JCPDS card no: 01-082-0661), $V_3O_7.H_2O$ (JCPDS card no: 01-085-2401) and V_6O_{13} (JCPDS card no: 01-075-1140). This observation is in agreement with morphological studies, in which we noticed the presence of different morphologies along with 3-fold increase in size of the VO_2 (A) microrods. Under similar hydrothermal preparation conditions, it was reported in the literature that, VO_2 (M1)

phase appeared mainly as snowflake or flower-like, VO_2 (A) phase as fibers or micro rods-like and $V_3O_7.H_2O$ phase as nanowires. In our case, we do see the several morphologies, i.e. flower-like, microrod and nanowires, which may correspond to VO_2 (M1), VO_2 (A) and $V_3O_7.H_2O$ as noticed in P-XRD pattern. Till now, the crystallographic transformation process from VO_2 (A) to VO_2 (M1) was not clearly known. Our observations indicate the existence of step wise transformation mechanisms from VO_2 (A) to VO_2 (M1) through V_6O_{13}, under hydrothermal conditions. These observations receive the support from the recent reports involved in the transformation process of VO_2 (A) or VO_2 (B) to VO_2 (M1) under reduced atmospheres, in which the existence of V_6O_{13} during the transformation was noticed [13,14]. Similar transformation processes can be very well explained for several vanadium oxides, using cooperative movement of octahedra or crystallographic shear mechanisms. For example, under soft reducing conditions, V_2O_5 can only yield V_6O_{13} and VO_2 (B) phases, not VO_2 (A). On the other hand, the transformation from VO_2 (B) to VO_2 (A) can be possible through a crystallographic shear mechanism, which was proposed by Galy et al., and the transition from V_6O_{13} to VO_2 (M1) can be described by the cooperative movement of V-O octahedra [15,16].

In the case of VO_2 (M1) flower-like morphology formation, mainly two kinds of mechanisms are proposed; starting from VO_2 nano crystals, similar growth along the six low energy facets of {20-1} planes in layer by layer manner, results in flower like morphology [17]. On the other hand, breaking of VO_2 (A) microrods into VO_2 (M1) embryo followed by recrystallization results in VO_2 (M1) flower-like morphology [18]. In a qualitative way, our observations support the formation of VO_2 (M1) flower like crystals from nanocrystals, formed by nucleation process. The qualitative understanding of the overall formation process behind the flower-like morphology is summarized in **Figure 15.**
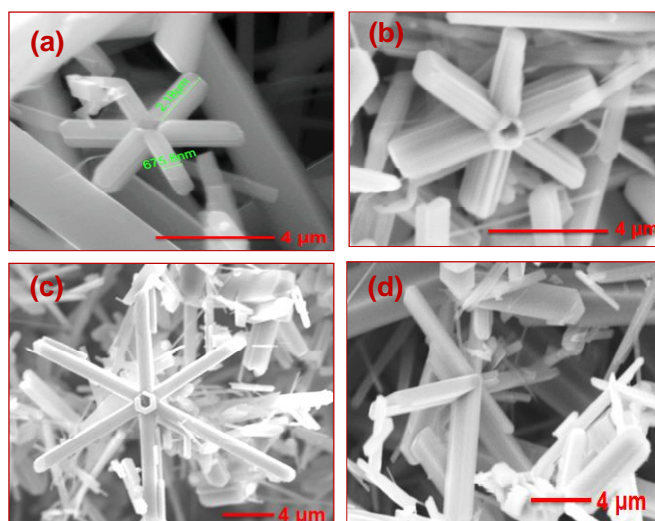
Figure 15. Different morphologies of final product obtained after slow cooling of autoclave for 264 h. These morphologies are arranged in the order of possible formation steps for the flower-like morphologies of VO$_2$ (M1).

Figure 15a and **Figure 15b** show the layer by layer formation of flower-like morphologies. The petals of these flowers are growing in longitudinal way, resulting in an increase in crystal size, as shown in **Figure 15c** and **Figure 15d**. From this observation, we can speculate that the layer by layer formation process may be the main mechanism behind the formation of VO$_2$ (M1) flower-like crystals. An in-situ formation mechanism study is needed to further confirm these observations.

VII.9. Effect of morphology on hysteresis: VO$_2$ (M1)

The formation of single phase VO$_2$ (M1) with controlled morphology has always been one of the main tasks towards appropriate applications. The insulator to metal transition temperature (340 K) of VO$_2$ (M1) has important implications but requires to be slightly reduced to room temperature. This is usually done by elemental doping in VO$_2$. However, such kind of doping will often decrease also the magnitude of changes in electric and optical properties across the transition [19]. For example, Lopez et al. [20] have observed that the optical contrast between the semiconducting VO$_2$ (M1) and metallic VO$_2$ (R) nanoparticles is dramatically enhanced in the visible region, exhibiting size-dependent multipole optical resonance and transition temperatures. Another possibility that was recently explored for the tuning of transition temperature to room temperature is the reduction of particle size [21]. On the other hand, morphology dependent electrical properties are reported in the case of VO$_2$ nanostructures,

whereas morphology dependent phase transition behavior has not been specifically studied till now [22]. In order to study the effect of morphology on phase transition behavior of VO_2 (M1), we have selected spherical shape particles, microrod and flower-like morphologies of VO_2 (M1) microstructures prepared using solid state, argon annealing and hydrothermal processes respectively. The morphologies of spherical flower-like and micro-rod like morphologies of VO_2 (M1) are shown in **Figure 1e**, **Figure 1d**, **Figure 13b**. **Figure 16** shows the DSC studies related to these three types of VO_2 (M1) morphologies. We observed the increase in hysteresis between heating and cooling cycles from spherical (5°C) to micro-rod (7.5^{o}C) and to flower-like (15°C) morphologies.
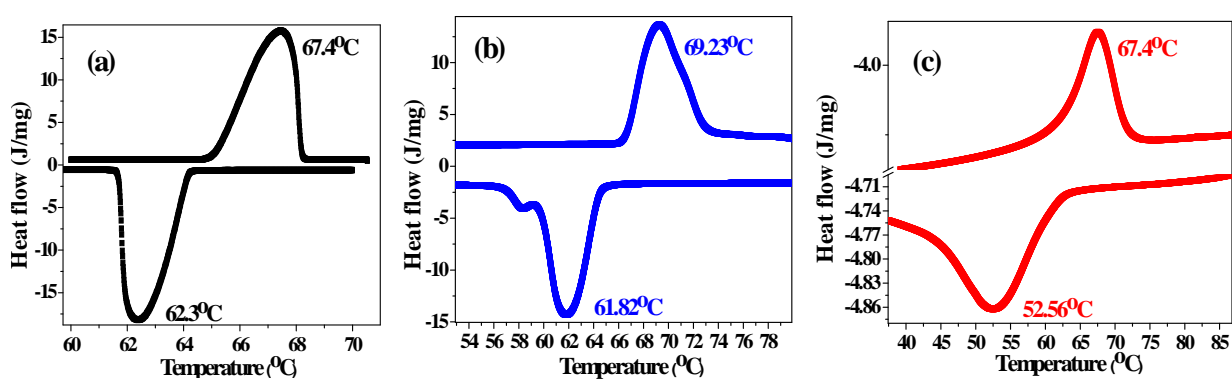
Figure 16. DSC curves of VO_2 (M1) samples obtained by (a) solid state reaction process with micro-sphere morphology (b) annealing process from VO_2 (A) with microrod morphology and (c) hydrothermal process with flower-like morphology.

The observed hysteresis in the phase transition between cooling and heating cycles in all three cases further supports the first-order nature of structural phase transition in VO_2 (M1). In case of spherical particles prepared by solid state process, the phase transition temperature matches exactly the reported values in case of bulk samples. For the micro-rod morphology, we observed a small increase and a decrease in transition temperature during heating and cooling cycles, respectively, thus the overall increase in hysteresis magnitude is due to both cycles. Similar observations are reported by Lopez et al. in case of nanoscale VO_2 (M1) [23]. In addition, we noticed a shoulder in DSC curve during cooling as well as heating cycles, which can be explained on the basis of non-uniform particle size (shown in **Figure. 16b**). In the case of flower-like morphology, we observed a small increase and a large depression in transition temperature during heating and cooling cycles, respectively, thus the overall increase in hysteresis magnitude is mainly due to the suppression of the phase transition temperature during the cooling cycle. We also notice that the flower-like morphology sample, which exhibits the

largest depression in transition temperature and hysteresis, shows the largest broadening of the {011} reflection (0.1674°) compared with spherical (0.0466°) and micro-rod (0.1306°) VO_2 (M1) morphologies. Similar observations were made by Whittaker et al. in the case of VO_2 (M1) samples prepared by hydrothermal treatment of bulk VO_2(M1) with 1,3-butanediol and methanol [24]. These observations are consistent with finite size effects on the observed depression in transition temperatures; however, the larger effect of finite size during cooling cycle is still an open question.

VII.10. Physical properties

VII.10.1. Resistivity measurements

The variation of low temperature resistivity with respect to temperature was shown in **Figure 17a.** The temperature dependence and magnitude of the resistivity correspond to a semiconducting behaviour, in agreement with the negligible spectral weight at the Fermi level in XPS measurements. The thermally activated resistivity obeys an Arrhenius law as illustrated by the linear relationship between the logarithm of conductivity (σ) and reciprocal temperature (inset: **Figure 17a**). On the basis of the Arrhenius equation, we extracted the activation energy (E_a) at low temperatures, as 0.147 eV.

The variation of high temperature resistivity with respect to temperature is shown in **Figure 17b.** A discontinuity in the resistivity is noticed around 437.8 K and 410 K during heating and cooling cycles, respectively. The activation energies below and above the transition temperature were calculated, from the Arrhenius law: we found i) 0.209 and 0.274 eV, respectively, for the heating cycle, and ii) 0.192 and 0.203 eV, respectively, for the cooling cycle. The difference in the activation energies below and above the transition temperature is very small both for heating and cooling cycles. The changes in the crystal structure and conductivity of VO_2 (A) seem to be very faint and distributed over a range of temperature. These observations may rule out the possibility of semiconducting to metallic transition at (or near) the structural phase transition as in VO_2 (M1), rather supports the semiconductor to semiconductor transition. Even structural aspect, supports this proposition, as the distance between V-V in HTP-A phase (3.082 Å) is much higher than metallic VO_2 (R) (2.85 Å) and Goodenough critical distance for metallic phase (2.94 Å).
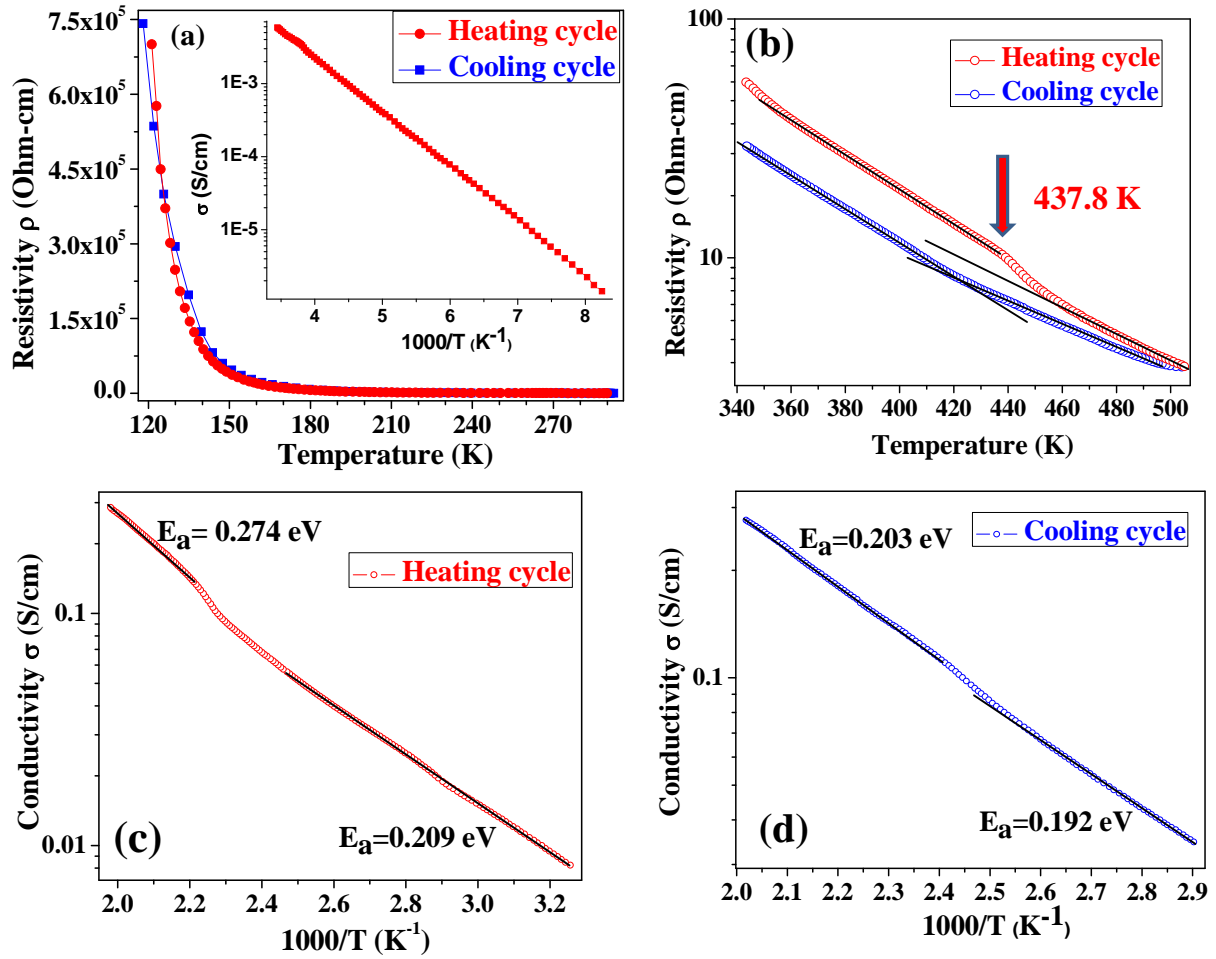
Figure 17. (a) Low temperature dependence of resistivity for VO$_2$ (A) during heating and cooling cycles. The inset shows the semi log plot of conductivity versus reciprocal temperature during the heating cycle. Semi-logarithmic plots of (b) Resistivity versus temperature during heating and cooling cycles; Conductivity versus reciprocal temperature during heating cycle (c) and cooling cycles (d) for VO$_2$ (A).

In the literature, Oka et al. measured the resistivity of as-pressed pellets of VO$_2$ (A) powder [25]. They observed a rather high resistivity (5x10^3 Ω-cm at 350 K), probably due to the non-sintered character of the pellets, and activation energies of 0.8 eV for the low-temperature phase (below 440 K) and 0.65 eV for the high-temperature phase (above 440 K) in the heating process. In another recent report, Ming Li et al. obtained an activation energy of 0.28 eV for the low-temperature VO$_2$ (A) phase (below 440 K) using resistance measurements on individual nanobelts [3]. The large discrepancy in the reported activation energy values must be caused by the different nature of the samples: an individual nanobelt vs. pressed powders. In our case,

rather low resistivity values were obtained, i.e. 45 Ω-cm at 350 K; and the activation energy value for the low-temperature phase (0.274 eV) is very close to the case of single nanobelts; this shows the intrinsic character of the properties of our VO_2 (A) sample. Thermopower measurements are consistent with n-type charge carriers in VO_2 (A), with a value of room temperature Seebeck coefficient of -158 µV/K.

VII.10.2. Magnetic properties

Figure 18 shows the magnetization curves, M (T), recorded in both field- and zero field-cooling (FC, ZFC) modes under an applied field of 1000 Oe. In case of ZFC (FC also!) below 350 K, three distinct regions are observed as temperature is increased. In the 3–17 K interval, there exists a linear variation of M/H with temperature (The linear variation is between log (M/H) and log T). In the 19–166 K interval, M/H smoothly decreases with temperature and above 166 K, M/H increases with temperature. In contrast, (M/H has also a large T dependence (log-log scale)) the $1/\chi$-χ_0 curves for VO_2 (A) had strong temperature dependence, as it is illustrated in inset of **Figure 18a**.
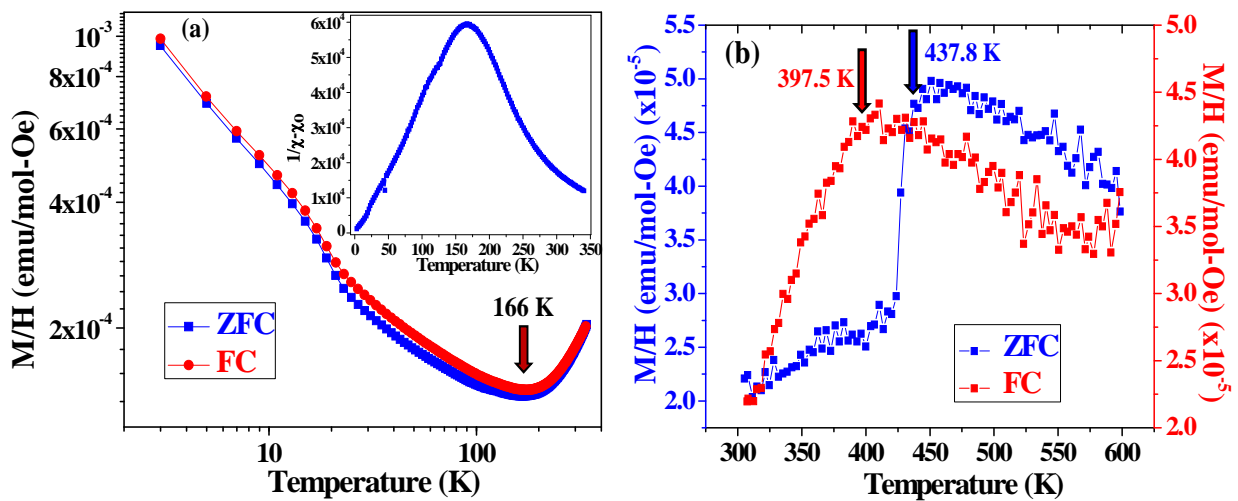
Figure 18. Low temperature (a) and high temperature (b) molar magnetic susceptibility measurements of VO_2 (A), under magnetic field of 1000 Oe. The Low T zero field and field-cooled curve shows an increase in susceptibility at approximately 166 K.

A Curie–Weiss-like behaviour is found from 25 to 150 K, demonstrating a paramagnetic state. By fitting the experimental data by means of the Curie–Weiss-law, we obtained a Curie constant of 2.46e-3 and Weiss temperature θ = -6.5 K. If we assume that the magnetic signal

originates from spins S = 1/2 as it is suggested by the presence of V^{4+} ions (c=0.369), our analysis implies about 0.66% V^{4+}-ions with free spins available below 150 K. This negligible number of free spins confirms the pairing of V^{4+} ions in LTP-A phase.

The variation of molar magnetic susceptibility around the structural transition temperature is shown in **Figure 18b**. We notice signatures of phase transitions during heating as well as cooling cycles. In particular, the transition is faint during the cooling cycle in M/H curves; this could be reason for the unobservable nature of the transition by Oka et al. [1]. The increase in magnetic susceptibility across the phase transition is believed to be due to depairing of V^{4+}-V^{4+} ions. The decrease in M/H during the cooling cycle may be related to the partial oxidation of VO_2 (A) into V_2O_5 because of poor vacuum conditions during the high temperature measurements using MANICS magnetometer. By fitting the experimental data in the 467-588 K range by a Curie–Weiss law, we have obtained a Curie constant of 0.285 and Weiss temperature θ = -120 K. The obtained curie constant is somewhat lower than expected for V^{4+} free spins (c=0.369); this discrepancy may be due to the partial presence of V^{5+} ions because of oxidation. These values confirm the de-pairing of V^{4+} ions in HTP-A phase. Due to the much higher density of free spins than in the low T case, significant antiferromagnetic interactions arise, as revealed by the θ value -120 K.

According to low as well as high temperature magnetic measurements, the increase in magnetic susceptibility may be related to the de-pairing of V^{4+}-V^{4+} ions, which releases free spins from individual V^{4+} ion. So the breaking of V^{4+} ion pairs is starting at 166 K and continues until 437 K. From the high temperature in-situ structural transformation studies, the structural transition from LTP-A phase to HTP-A phase is not a sharp transition and spreads over a large range of temperature. Even from low temperature structural studies, we noticed a decrease in distance between (421) and (114) reflections. These changes are also spread over a large temperature range. This kind of structural behaviour can be simply due to a movement of VO_6 octahedra with temperature, thereby changing the distance between different vanadium atoms. ESR experiments for VO_2 (A) were carried out at X-band frequency (at 9.5 GHz) by using a continuous flow of liquid nitrogen cryostat and resulting spectra upto 190 K is shown in **Figure 19.** The ESR spectra of VO_2 (A) showed the 8 hyperfine resonance lines, is similar to VO_2 (M1). These hyperfine lines are indicating that the 3d electrons of the V^{4+} ion are strongly localized. The integrated intensity of ESR lines follows continuous decrease of intensity with increasing

temperature. As it is known, the ESR intensity is proportional to the paramagnetic defects concentration and to susceptibility in the paramagnetic phase. The observed ESR spectra below 100 K, is supports the presence of small amount of quasi free V^{4+} ions and V^{4+}-V^{4+} ion pairs.
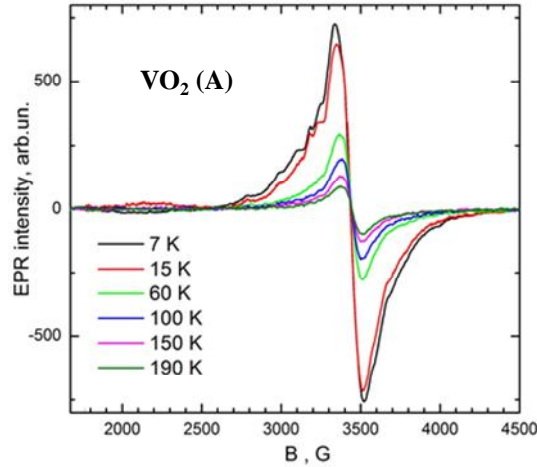
Figure 19. Electron resonance spectra of VO_2 (A) between 7-190 K.

VII.10.3. Specific heat measurements

The low-temperature specific heat as a function of T^2, for VO_2 (A), is shown in **Figure 20.** With the exception of temperatures below 5 K, the specific heat behaves as $Cp=\gamma T+\beta T^3$. Fits to the linear portions of Cp /T vs. T^2 for temperatures below 12 K allowed us to estimate the electronic (γ) and lattice (β) contributions to the specific heat. The β values yield Debye temperature in the range of 347 K and γ is approximately 7.53 mJ/mol-K^2.
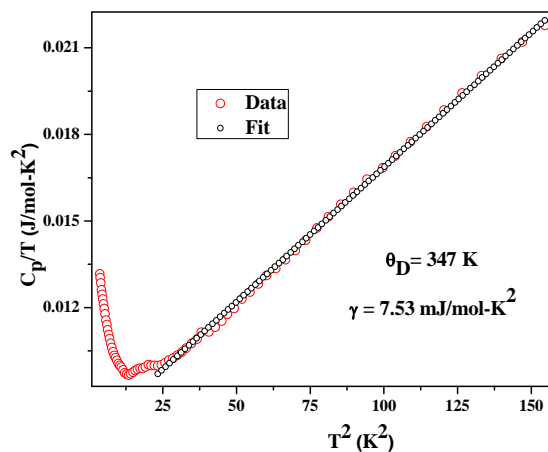
Figure 20. C_p/T plotted as function of T^2 for VO_2 (A).

VII.11. Discussion and conclusions

Our observations and conclusions related to structural phase transition and crystal growth mechanism of VO_2 (A) using different experimental techniques are summarized in **Figure 21**. After successful synthesis of VO_2 (A) and VO_2 (M1) polymorphs using single step, template free hydrothermal synthesis, we verified P4/ncc as an appropriate space group for VO_2 (A) at RT. Reversible phase transition from LTP-A to HTP-A with giant hysteresis and strong dependence of this hysteresis on size, morphology was noticed. The irreversible phase transition from HTP-A to VO_2 (M1) is studied followed by drastic changes in morphologies.
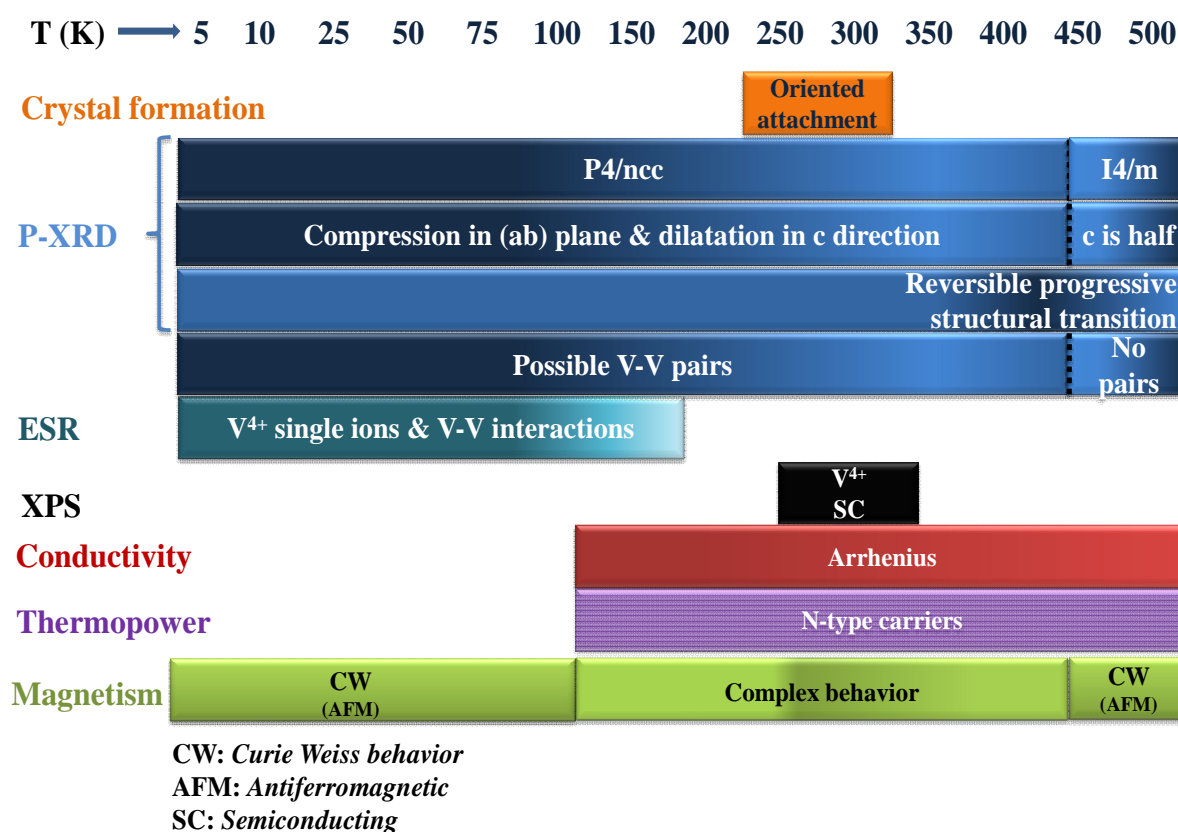
Figure 21. Summary of experiments results for VO_2 (A).

High-temperature P-XRD studies around structural phase transition temperatures indicates the "progressive" kind of structural transition. This structure transition extends over semiconductor-semiconductor transition temperature. From the magnetic measurements, we noticed that the complete pairing of V^{4+} ions below 150 K and de-pairing of V^{4+} ions above 470 K.

The intermediate temperature domain shows more complex behaviour. Thermopower measurements established the n-type charge carriers in VO_2 (A) and kept its nature of carriers across the structural phase transition temperature. The phase conversion process from VO_2 (A) to VO_2 (M1) under hydrothermal conditions is seems to involve several stable intermediate steps. Layer by layer formation mechanism behind the flower like VO_2 (M1) crystals is noticed.

VII.12. Prospectives

Our results suggest that detailed studies of the structural and magnetic characterizations through local probes, such as microscopic techniques on the nanometer length scale with spatial and temporal resolution, would be very interesting to determine the exact character of structural and electronic homogeneities noticed in VO_2 (A). Low and high temperature high resolution synchrotron radiation studies may be useful to get more insight into the nature of structural phase transition and pairing-depairing mechanisms in the case of VO_2 (A) around magnetic properties anomalies.

VII.13. References

[1] Y. Oka, T. Ohtani, N. Yamamoto, T. Takada, Nippon Seramikkusu Kyokai Gakujutsu Ronbunshi, 97 (10) 1134-37 (1989)

[2] S. Zhang, B. Shang, J. Yang, W. Yan, S. Wei and Y. Xie, *DOI: 10.1039/c1cp20838a* (2011)

[3] M. Li, F. Kong, L. Li, Y. Zhang, L. Chen, W. Yan, G. Li, Dalton Trans., 40, 10961 (2011)

[4] J. Rodríguez-carvajal, Physica B 192, 55 (1993)

[5] Y.Oka, S. Sato, T. Yao and N. Yamamoto, J. Solid State Chem. 141, 594 (1998)

[6] J.D.H. Donnay, D. Harker, Am. Mineral. 22 446 (1937); P. Hartman, W.G. Perdok, Acta Crystallogr. 8, 49 (1955)

[7] L. Dai, Y. Gao, C. Cao, Z. Chen, H. Luo, M. Kanehira, J. Jin, and Y. Liu, RSC Advances, *DOI: 10.1039/c0xx00000x*

[8] J. Mendialdua, R. Casanova, Y. Barbaux, J. Electron Spectrosc. Relat. Phenom. 71, 249 (1995)

[9] L. Whittaker, C. Jaye, Z. Fu, D.A. Fischer, and S. Banerjee, J. Am. Chem. Soc. 131, 8884 (2009); R. Lopez, L.A. Boatner, T.E. Haynes, L.C. Feldman, R.F. Haglund Jr, J. Appl. Phys. 92, 4031 (2002)

[10] M.M. Qazilbash, A. Tripathi, A.A. Schafgans, B.J. Kim, H.T. Kim, Z. Cai, M. V. Holt, J.M. Maser, F. Keilmann, O.G. Shpyrko, and D.N. Basov, Phys. Rev. B 83, 165108 (2011)

[11] Y. Oka, T. Yao, N. Yamamoto, Y. Ueda and A. Hayashi, J. Solid State Chem. 105, 271 (1993)

[12] Ch. Leroux, G. Nihoulm, G.V. Tendeloo, Phys. Rev. B 57, 5111 (1998)

[13] H. Yin, J. Ni , W. Jiang , Z. Zhang, K.Yu, Physica E 43, 1720 (2011)

[14] Y. Zhang, M. Fan, F. Niu, W. Wu, C. Huang, X. Liu, H. Li, X. Liu, Current Applied Physics 12, 875 (2012)

[15] J. Galy, J. Solid State Chem. 148, 224 (1999)

[16] S.Horiuchi, M.Saeki, Y. Matsui, F. Nagata, Acta Cryst. A31, 660 (1975)

[17] C. Cao, Y. Gao, and H. Luo, J. Phys. Chem. C 112, 18810 (2008)

[18] S. Ji, F. Zhang, P. Jin, J. Solid State Chem. 184, 2285 (2011)

[19] E. Cavanna, J.P. Segaud, J. Livage, Mater. Res. Bull. 2, 167 (1999); T.D. Manning, I.P. Parkin, C. Blackman, U. Qureshi, J.Mater.Chem.15, 4560 (2005)

[20] R. Lopez, L.C. Feldman, R.F. Haglund, Phys. Rev. Lett. 93, 403 (2004)

[21] R. Dmitry, J. Appl. Phys. 102 (113715), 1 (2007); S.H. Chen, H. Ma, J. Dai, X.J. Yi, Appl. Phys. Lett. 90, 1 (2007); L. Whittaker, C. Jaye, Z.G. Fu, D.A. Fischer, S. Banerjee, J. Am. Chem. Soc.131, 8884 (2009)

[22] H. Yin, K. Yua, Z. Zhang, Z. Zhu, Applied Surface Science 257, 8840 (2011)

[23] R. Lopez, L.A. Boatner, T.E. Haynes, L.C. Feldman, R.F Haglund Jr. J. Appl. Phys. 92, 4031 (2002)

[24] L. Whittaker, C. Jaye, Z. Fu, D.A. Fischer, and S. Banerjee, J. Am. Chem. Soc. 131, 8884 (2009)

[25] Y. Oka, T. Ohtani, N. Yamamoto, T. Takada, Nippon Seramikkusu Kyokai Gakujutsu Ronbunshi, 97, 1134 (1989)

Chapter VIII: Structural and electronic properties of VO$_2$ (B)

VO$_2$ (B) is one of the well-known polymorphs of vanadium dioxide and is a promising cathode material for aqueous lithium ion batteries. I have synthesized VO$_2$ (B) using a convenient hydrothermal synthesis and novel precursor's combination of V$_2$O$_5$ and citric acid (chapter V) and compacted pellets using Spark Plasma Sintering (SPS). In this chapter, I will present the structural and physical properties (electrical and magnetic properties) of VO$_2$ (B).
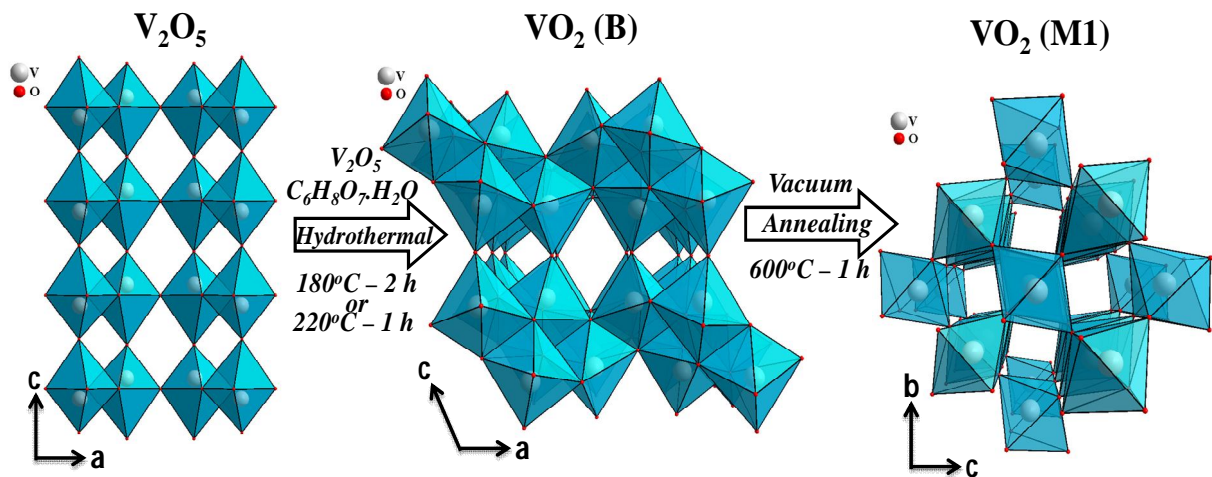
Contents

VIII.1. Introduction

VO_2 (B) is known for three decades but most of the studies focus on its electrochemical characterizations while its electronic properties remain poorly understood. To date, electrical transport studies of VO_2 (B) have been limited to the work of Liu et al., [1] who reported the semiconducting behaviour up to room temperature of VO_2 (B) nanobelts and of Corr et al. who performed resistivity measurements on a pressed pellet of VO_2 (B) and on a drop of VO_2 (B) suspension dried on a wafer [2]. In light of those observations, we will, in this chapter first detail the structure of this polymorph and then we will focus on its physical properties.

VIII.2. Experimental details

VO_2 (B) samples were prepared using V_2O_5 and citric acid in hydrothermal process at 220^oC for 2 h (*Chapter V*).

Pellets were prepared by Spark plasma sintering (SPS). The powder was put into a carbon die and heated to a 250^oC with a heating rate of 100 K/min and a pressure of 90 MPa. After dwelling 5 min, the pressure was released and the sample was cooled to room temperature. The morphology of the cross-sectional view of the SPS pellet is shown in **Figure 1**. The final compacity of the pellet is 76%.
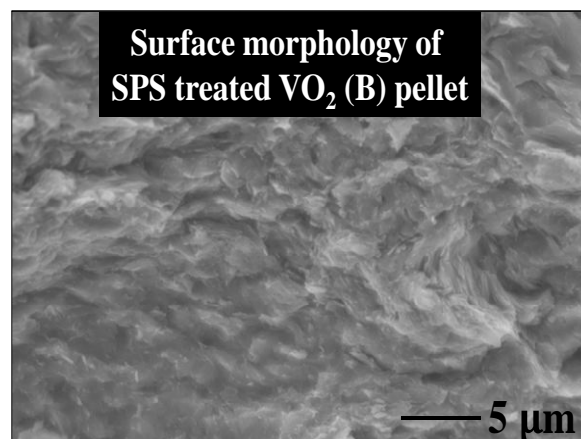
Figure 1. Surface morphology of VO_2 (B) pellet treated by Spark Plasma Sintering (SPS).

P-XRD patterns for Rietveld refinement were recorded with a 0.01313° step size and 700 s/step using a PANalytical X'Pert PRO MPD diffractometer with Cu K_α radiation (40 KeV; 30 mA), a divergent slit of 1 degree and a receiving slit size of 0.1 mm. For temperature studies, an Anton-par chamber under vacuum ($9.2x10^{-5}$ bar) was used; the powder was dispersed in ethanol and deposited on a platinum strip; the diffractometer was calibrated using the peak shift of the platinum strip; the HT-P-XRD patterns were acquired using 0.003° step and 66 s/step.

The morphology of the compounds was observed using a high resolution scanning electron microscopy (HRSEM- JSM 6700F) under 5 KeV; the powder was glued on a carbon tape and sputter coated with a thin layer of gold to prevent from charging effects.

Fourier Transform InfraRed spectrometer (FTIR-8400S, SHIMADZU) was used to confirm the formation and purity of the desired compound; spectra collection were acquired on mixtures of $VO_2(B)$ and KBr in the range 400-2800 cm^{-1} and averaged over 100 scans.

The room temperature electronic structure was studied by means of x-ray photoemission spectroscopy (XPS) and ultraviolet photoelectron spectroscopy (UPS) with a VG Escalab 220i XL X-Ray Photoelectron Spectrometer using an Aluminium monochromatic source (hυ = 1486.6 eV) and He (I) ultraviolet light (21.22 eV) as excitation sources under ultrahigh vacuum.

Electrical direct current resistivity measurements were performed with four probe method with a homemade setup.

Low temperature magnetization measurements were performed using a Quantum Design MPMS magnetometer.

VIII.3. Structural properties

Prior to investigate the structure details, the gross quality of the powders was checked with routine P-XRD experiments as well as infrared spectroscopy studies to discard from any hydration of the compound. The routine pattern match with the JCPDS data card 01-081-2392 assigned to VO_2-B. The FTIR results are shown in **Figure 2**. The main vibrational bands are at 551, 669, 936, 1012, 1624, 2339 and 2360 cm^{-1}. From the comparison with the spectra of KBr only, only bands at 551, 936 and 1012 cm^{-1} can be considered as intrinsic to vanadium oxide what matches well with earlier reports: the initial broad vibrational band at 551 cm^{-1} is assigned to the V-O-V octahedral bending modes; [3] the band at 936 cm^{-1} is attributed to the coupled vibration of V=O and V-O-V; [4] the band at 1012 cm^{-1} is attributed to the stretching of short V-O bonds. The high and low frequency bands arise from CO_2, which is present in the atmosphere: the asymmetrical stretch of CO_2 can give a strong band in the IR at 2350 cm^{-1} and the bands appearing around this region i.e. 2339, 2360 cm^{-1} is reasonably assigned to the asymmetrical stretch of CO_2 molecules; in the same way, the vibrational band appearing in at 666 cm^{-1} can be assigned to degenerate bending vibration of CO_2. The band at 1624 cm^{-1} is assigned to different

vibration models of an O–H group of adsorbed water molecules on the surface of the VO_2 (B) powders [3]. These observations confirm that VO_2 (B) is water-free.
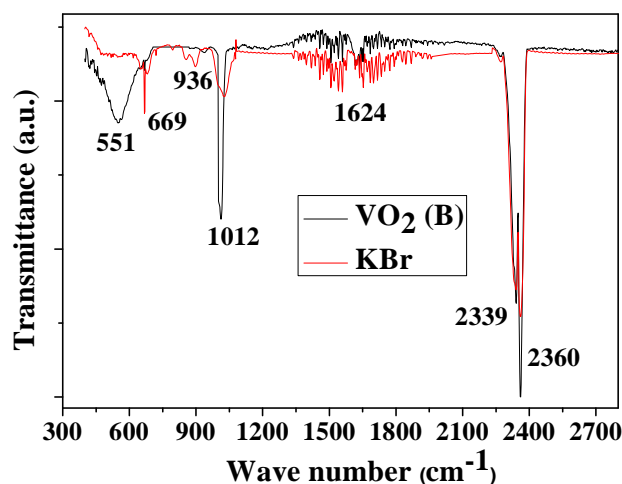
Figure 2. FTIR spectra of VO_2 (B), compared with KBr.

The Rietveld refinement made using FullProf program [5] for the high temperature phase (HTP) is shown in **Figure 3** and the refined parameters are given in **Table 1.**

HTP-VO$_2$ (B)				
Space group: C 2/m (12)				
Lattice parameters	a = 12.0426 (4) Å b = 3.6897 (1) Å c = 6.4304 (2) Å β = 106.949 (2)			
Profile parameters	Function: Thompson-Cox-Hastings pseudo-Voigt Axial divergence asymmetry Half-width parameters: $U = 0.9388$ $V = -0.3771$ $W = 0.0375$			
Atomic positions				
Atom label	x	y	z	Occupancy
V1	0.3037	0	0.7223	1
V2	0.4025	0	0.3046	1
O1	0.3686	0	0.9980	1
O2	0.2331	0	0.3295	1
O3	0.4470	0	0.6465	1
O4	0.1300	0	0.6964	1
R-factors	R_p: 6.81 %	R_{wp}: 9.00 %	R_{exp}: 3.98 %	χ^2: 5.11

Table 1. Refined room temperature parameters for VO_2 (B) compound. The occupancy was fixed.
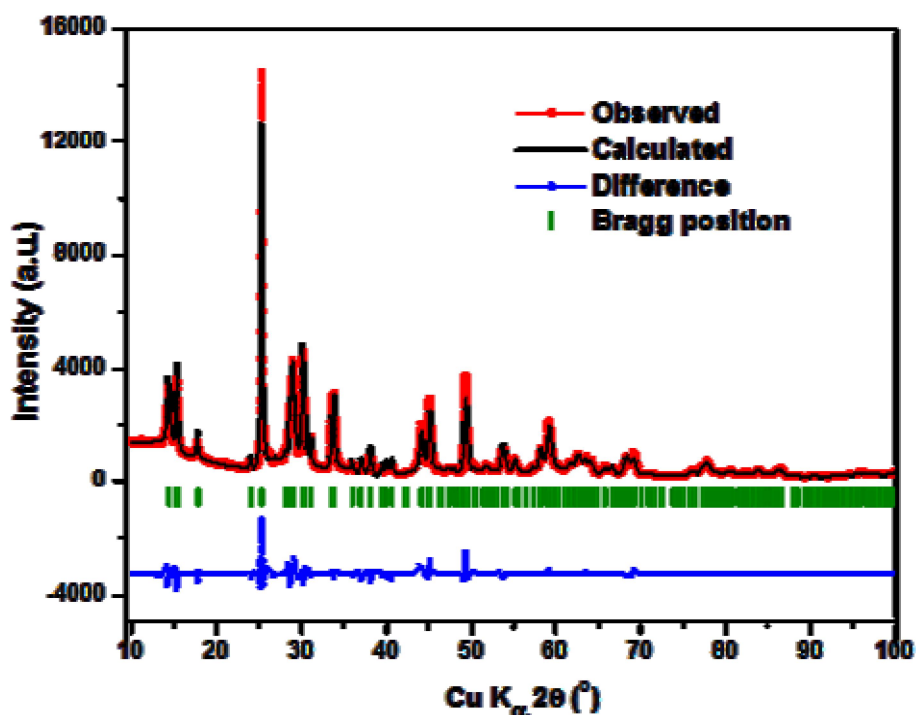
Figure 3. P-XRD pattern of VO$_2$ (B) synthesized at 220°C/2 h.

All diffraction peaks are indexed in C2/m space group and no trace of secondary phases or impurities were detected. The broadening of (00l) peaks as compared to other reflections was already explained by the disorientation in (00l) layers of flake-like particles [6]. In addition, using the Scherrer expression, we calculated an average coherence length (D) of *ca* 65 nm. Both the flake-like morphology and this size are consistent with the SEM observations of *chapter V*.

Figure 4 sketches the resulting structure. It highlights the difference in the V-V bonds depending if they bridge V1 and/or V2 sites (**Figure 4a-d**) as well as the highly distorted VO$_6$ octahedral environment (**Figure 4e**). V1 site has a crude C4v symmetry with an additional rhombic perturbation and a pseudo 4-axis approximately directed along [106]. V2 site has an even more crude C4v symmetry due to an additional strong C2v perturbation followed by a rhombic one and a pseudo 4-axis approximately perpendicularly directed along [60$\bar{1}$]. Both sites are strongly off-centred.

Figure 4. Structure of HTP-VO$_2$ (B). a): perspective view; b): projection in (101) with V-V distances; c): projection in (110); d) perspective view with highlighting of V-V bonding scheme (oxygen ions not shown); e): perspective view with V-O distances.

In **Figure 4**, **a-d,** the short blue bonds bridge V1 and V2 sites in zig-zag chains along the b-axis and approximately in (ab) plane while the red long bonds bridge V1 only sites in an almost perpendicular zig-zag chain (crudely in (bc) plane); orange medium bonds bridge V1 and V2 sites along ca [001] and green short bonds bridge V2 sites along ca [101] forming in this way zig-zag quadrimers along the a-axis with a sequence of medium-short-medium bonds. This structure can simply be understood as bent ladders (or leaflet) made of short blue poles and medium orange steps between V1 and V2 sites further tied with long red bridges between V1 sites; the individual ladders are then bridged together with short green bonds between V2 sites (**Figure 4d**). In this HTP-VO$_2$ (B), the shortest green bond (2.896Å) is a bit longer than the V-V bond in HTP-VO$_2$ (R) (2.85Å).

Figure 5 shows the P-XRD patterns recorded down to 6 K. All of them can be indexed with the same space group (C2/m) than at RT and no specific feature is visible.
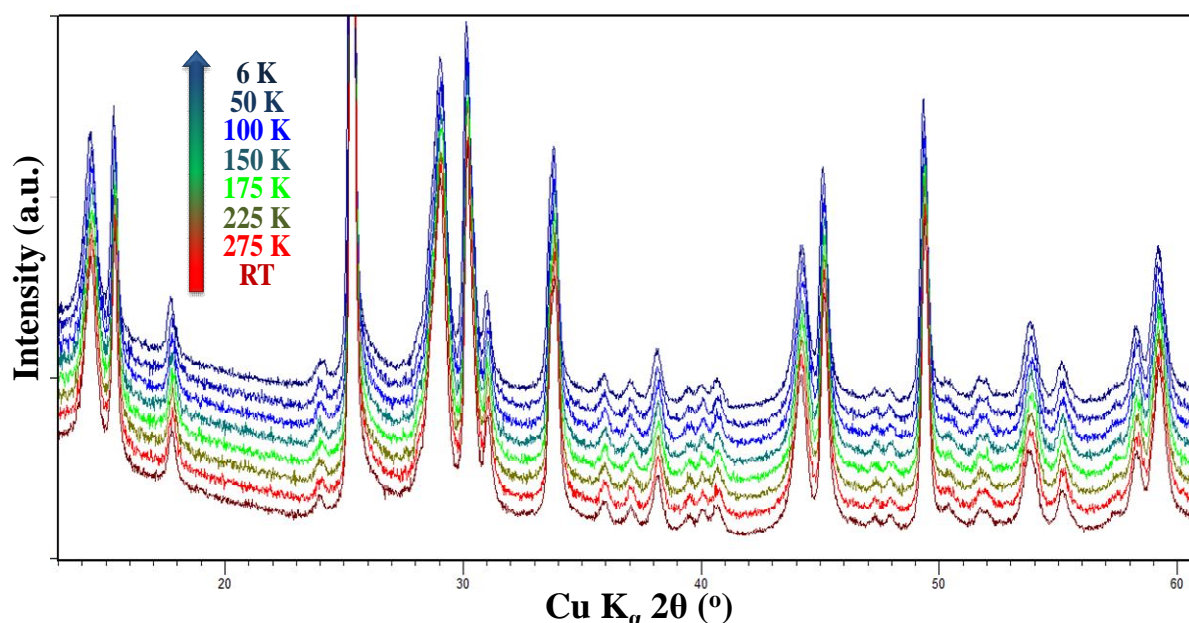
Figure 5. Low temperature evolution of VO$_2$ (B) P-XRD patterns.

The results of the refinements given in **Figure 6** highlight some discreet evolution of the cell parameters. In particular, they evidence the slight compression of the (ab) plane along with the dilatation of the c-axis as the temperature increases; the monoclinic angle also decreases with temperature. Interestingly, an abrupt change occurs at *ca* 250 K with a rise of 'c' parameter, a

drop in β and as a result, a rise of the unit cell volume. This temperature is close to the one reported by Oka et al. [7] for the mean transition temperature in VO_2 (B). The cell parameters changes are however too small to strongly impact on the bonds lengths and no straight pairing like in the case of M1 polymorph appears. Actually, within our experimental limits, the bonds lengths hardly vary (<3.7%) and even at *ca* 250 K, the V2-V2 distance ($\approx$2.827Å) is very close to the RT one suggesting a soft redistribution of the distances.
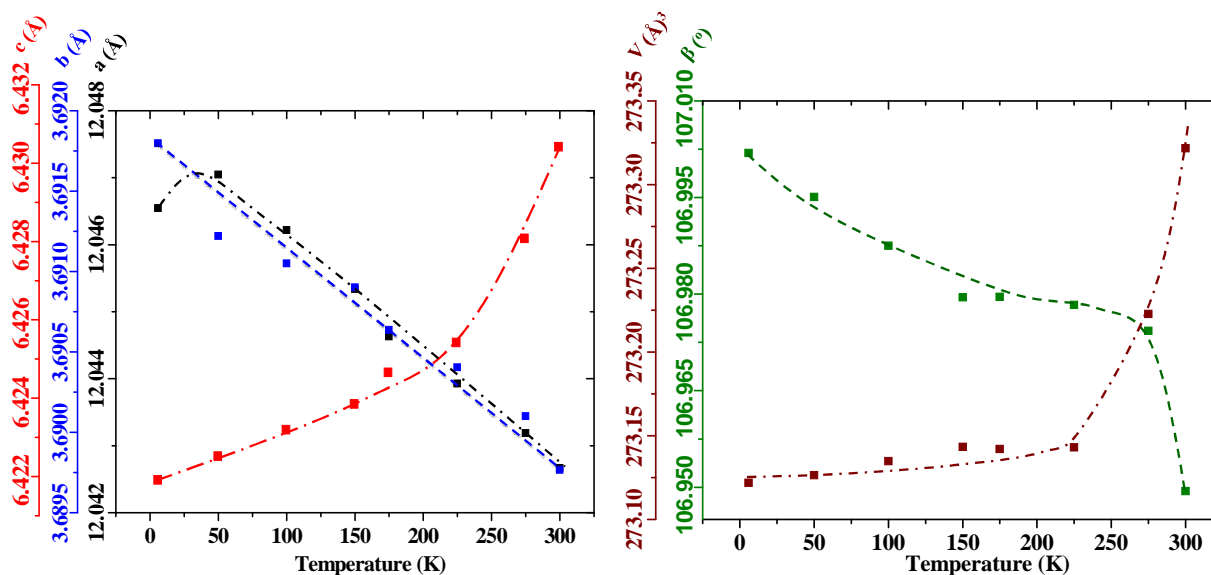
Figure 6. Low temperature evolution of VO_2 (B) cell parameters. *Lines are guides for the eyes*.

The stability of VO_2 (B) and its phase transformation into VO_2 (M1) was checked from high temperature P-XRD up to 600°C under vacuum to prevent from oxidation to V_2O_5 [8]. The results in **Figure 7** evidence that VO_2 (B) is stable up to 400°C and that the transformation starts between 400°C and 500°C where both polymorphs still coexist. The transformation is complete at 600°C. Further P-XRD recording after vacuum annealing at high temperature actually show that the transformation to M1 is already complete at 550°C in agreement with previous reports [9].
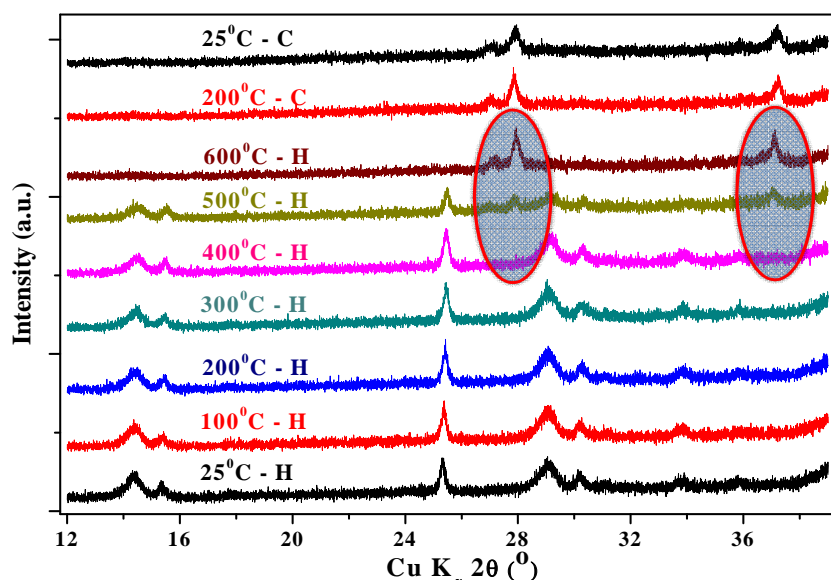
Figure 7: High temperature P-XRD patterns of VO_2 (B) evidencing its transformation to VO_2 (M1) (H: heating cycle; C: cooling cycle; the shadowed regions highlight the transformation to VO_2 (M1)

The P-XRD patterns recorded during cooling show the only presence of VO_2 (M1) what confirms the irreversible character of the phase transformation.

VIII.4. Spectroscopic studies

Spectroscopy experiments were carried out to access some details of the electronic structure.

VIII.4.1. XPS studies

XPS measurements were carried out on the surface of powders, SPS pellet and in-situ cleaved SPS pellet. **Figure 8a** shows the region corresponding to C 1s signal. In the case of the powders and pellet, an intensive peak at 284.3 eV is present due to C-C bond from atmospheric pollution. Along with this, two less intensive but higher binding energy components are visible at 285.8 and around 288 eV in agreement with the fact that the C–O(H) and C=O bonds in the C1s signal should be found at 1.5 and 3.0 eV higher binding energy than the C–C bond [10]. After *in-situ* cleaving of the pellet, no carbon peaks are any more visible evidencing a carbon free surface after the removal of the surface layer. The wide *survey* spectrum recorded after in-situ cleaving of the SPS pellet surface (**Figure 8b**) confirms the presence of only O 2p, O 2s, V 3p, V 3s, V 2p, O 1s and V 2s peaks.

The surface contamination has nearly no effect on the position of the core level V 2p binding energy, whereas there is minor shift to higher binding energy in the case of O 1s. The V 2p spectrum (**Figure 8c**) is spin–orbit split into $2p_{3/2}$ and $2p_{1/2}$ with a 7.368 eV gap. This doublet is followed by the O 1s emission at 530.24 eV (**Figure 8d**); in the case of the cleaved pellet, the intensity of the high energy tail decreases signing the decrease of surface pollution. The asymmetric nature of O 1s is attributed to the presence of V 2p spectrum [11].
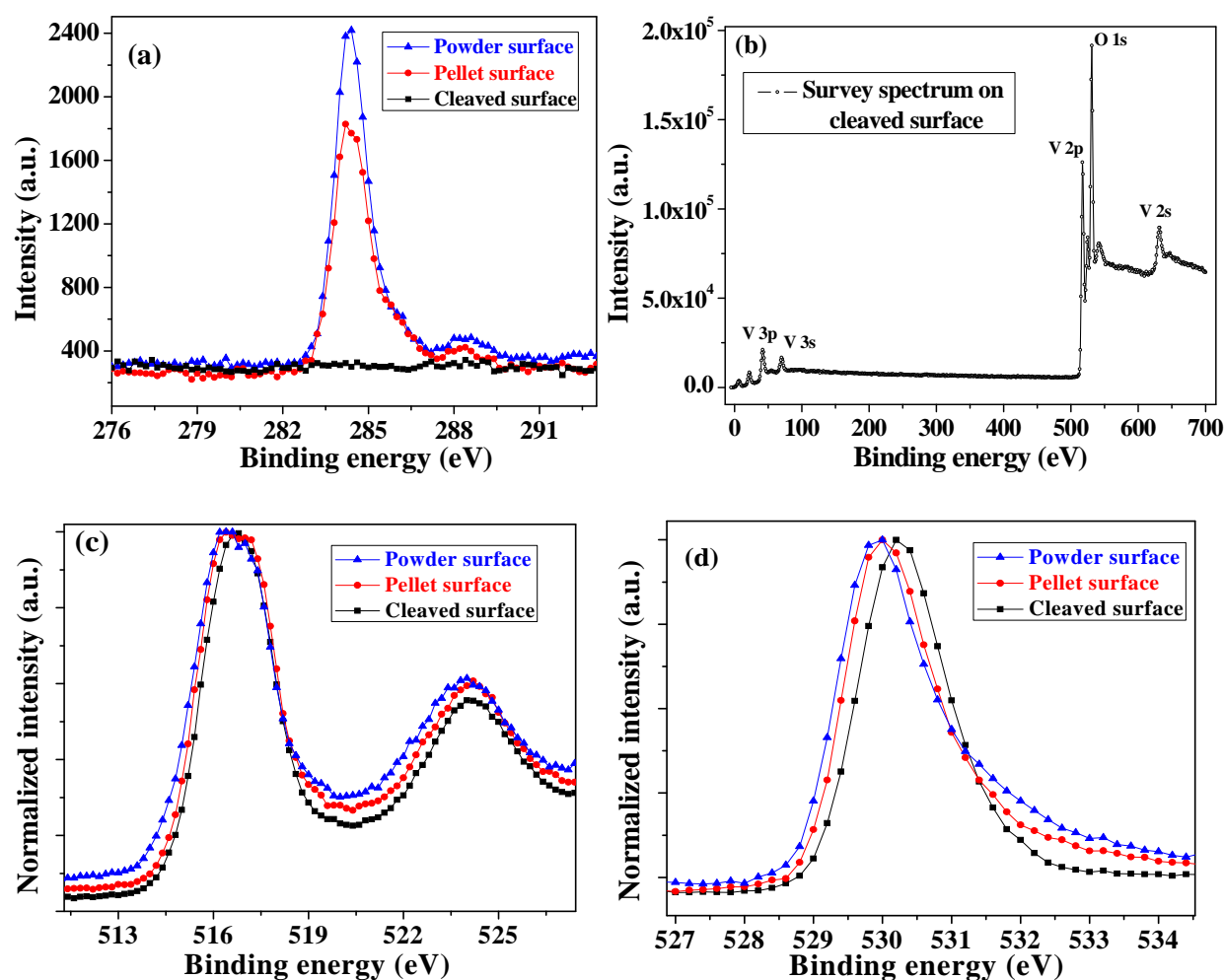
Figure 8. XPS spectra of VO_2 (B) in C 1s region on powder, pellet and cleaved pellet surfaces. (a) XPS survey spectrum of VO_2 (B) on in-situ cleaved pellet surface and normalized core level V 3d (b) and O 1s spectra (c) of VO_2 (B) on powder surface, pellet surface and is-situ cleaved pellet surfaces.

The oxidation degree of vanadium ions was determined by comparing the binding energy of O 1s and V $2p_{3/2}$. This kind of method was recommended for the determination of the oxidation degree of vanadium oxides because of the wide spread in O 1s as well as V 3d binding

energies available in literature. In the present case the difference is nearly 13.46 eV, which is matching with the +4 oxidation state for vanadium [12].

The valence band region spectra are shown in **Figure 9** evidencing that this region is more sensitive to surface pollution. In all cases, 2 main domains appear: (i) one spreads over 0 - 2.5 eV and can be assigned to O 2p shell; (ii) a second one spreads over 2.5 - 9 eV and can be assigned to V 3d shell. The room temperature spectrum of the cleaved surface shows no Fermi edge what is consistent with the semiconducting behavior of VO_2 (B) at this temperature; on the other hand, in the case of powders, a clear V 3d tail at the Fermi level is visible.
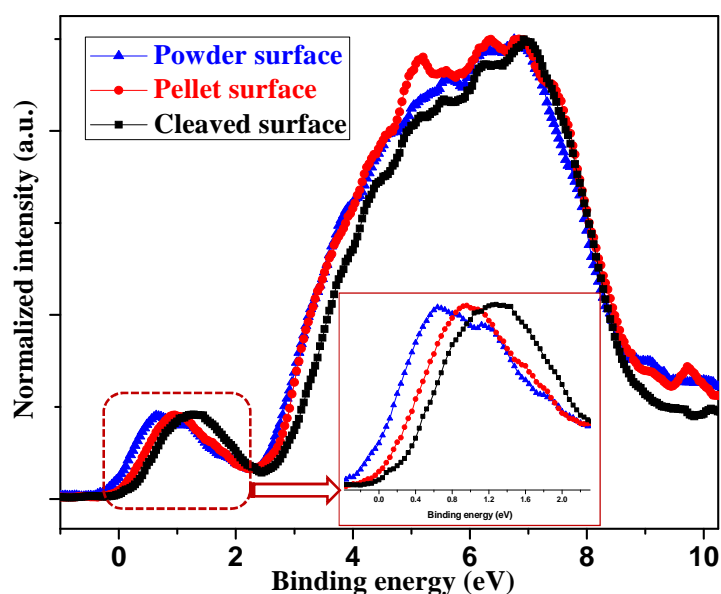
Figure 9. Normalized XPS spectra of O 2p and V 3d valence bands on difference surfaces (Inset shows expanded view around Fermi edge).

VIII.4.2. UPS Studies

Figure 10a shows a typical UPS spectrum of the VO_2 (B) cleaved pellet surface. The width of the kinetic energy spectrum is determined from the difference between the sample inelastic cutoff and the Fermi edge as illustrated in **Figure 10b** and **Figure 10c** respectively. The main purpose of this study is to measure the work function of VO_2 (B) by UPS analysis. The work function, Φ, can be defined as the amount of energy required to extract an electron at the Fermi level from a material surface to vacuum; such information is relevant to design electronic devices such as metal-oxide junctions and field-effect devices [13].
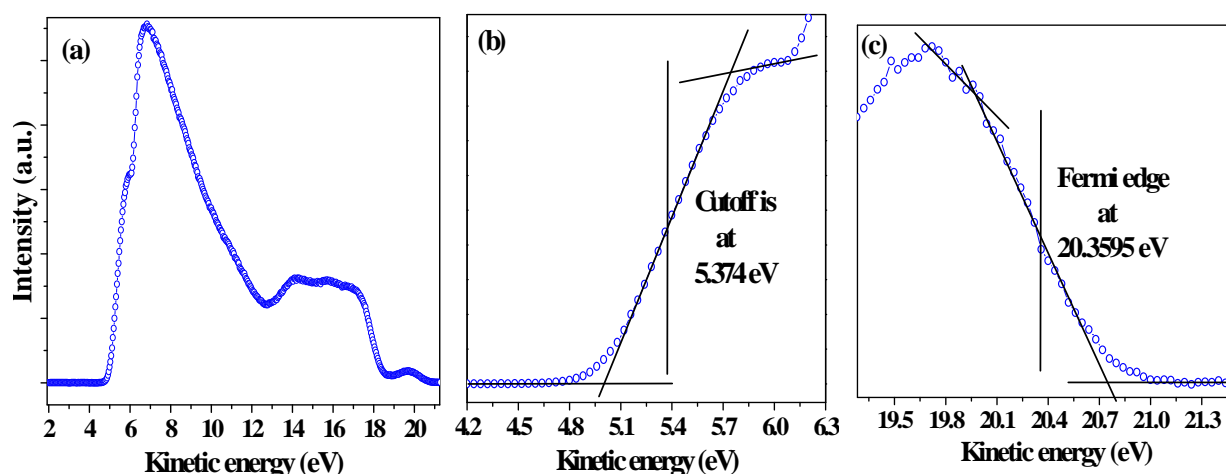
Figure 10. (a) UPS spectrum of VO_2 (B) using He I ($h\upsilon$=21.22 eV) excitation source. (b) Shows a part of inelastic cutoff region. (c) Shows a spectrum of Fermi edge region.

Here we measured the work function in ultrahigh vacuum (UHV) using an inelastic secondary electron cutoff. The absorbed photons transfer their energy to the electrons bound to the surface so that they overcome the surface potential barrier. The kinetic energy (E) of these photoelectrons is thus the difference between the photon energy ($h\upsilon$=21.22 eV) and the work function (Φ) of the sample [14]: $E = h\upsilon - \Phi$. The measured work function of VO_2 (B) is 6.23 eV what is much larger as compared other VO_2 polymorphs: for nanorods bcc-VO_2, $\Phi \sim$4.81 eV [15]; for nanobundles VO_2 (M1) $\Phi \sim$4.10 eV while for VO_2 (R), $\Phi \sim$3.65 eV [16]. The higher value of work function could be due to the increase in the optical band gap, when compared to bcc-VO_2 (E_g=2.7 eV) and VO_2 (M1) (E_g=0.7 eV) [17].

VIII.5. Electronic properties

Figure 11 shows the transport properties measured on the SPS pellet. It should be clear that the transport results reported here can be tarnished with the low compacity of the pellet. However, we believe that the observed global trend account for some intrinsic features of the compound.
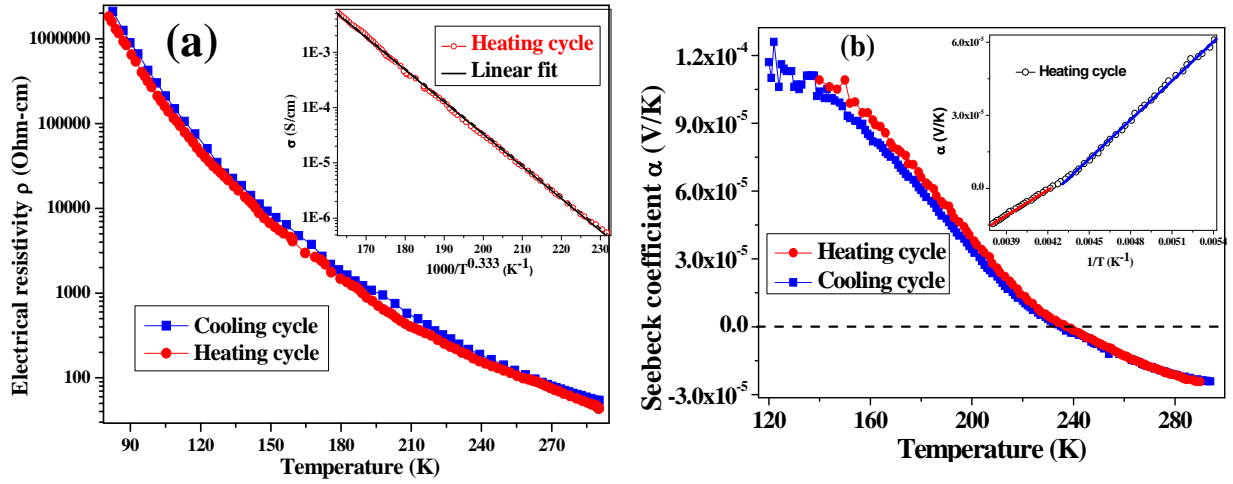
Figure 11. T dependence of the transport properties of VO$_2$ (B). (Left) electrical resistivity in the range 80–290 K (inset: log σ *vs* $1000/T^{\frac{1}{3}}$ in the range 80-230 K only); (Right) Temperature dependence of the Seebeck coefficient (inset: 1/T *vs* α).

The electrical resistivity decreases with increasing temperature evidencing a semiconducting behavior; at 290 K ρ=45 Ohm-cm *ca* 5 times lower than already reported by Corr et al. [18] (on compacted powders). The thermopower decreases with temperature and its magnitude is in agreement with the semiconducting behavior; bellow 120 K it was not possible to measure it because of the too high resistance of the sample. The sign of the Seebeck coefficient changes at 240 K indicating a possible change in the carriers' type and/or in the transport mechanism. In the temperature range 80-230 K, the resistivity obeys Mott's law ρ (T) = ρ$_0$ exp(T$_0$/T)$^{1/3}$ indicating in a strong localization picture a variable range hopping mechanism in two dimensions (2D-VRH) [19]. $T_0 = \frac{4\pi.R^3}{3k_B} \cdot \frac{W}{\zeta^3}$, where ζ is the localization length, R is the hopping distance and W is the hoping energy; ρ$_0$ depends on the phonon spectrum and scales as ν$_{Ph}$$^{-1}$. Such 2D mechanism is consistent with the details of the structure. The refined values are T$_0$=2.42 10^6 K and ρ$_0$=6.63 10^{-8} Ω.cm. Such high value for T$_0$ suggests (ignoring any microscopic effect due to the low pellet compacity) a small localization length or a high hopping distance and/or a high hoping energy. At higher temperature, for T>240 K, the resistivity obeys an Arrhenius law with ρ$_0$=0.09 Ω.cm and an activation energy E$_\sigma$≈152 meV while the Seebeck coefficient scales as 1/T with a carrier activation energy E$_\alpha$≈31 meV; this suggests that the mobility of the carriers is activated in this compound (E$_\sigma$=E$_\alpha$+E$_\mu$) [20]. In the small temperature

region 185-240 K, the Seebeck coefficient also scale as 1/T but the carrier activation energy increases and $E'_\alpha \approx 52$ meV; this suggests that in this region, the creation of carriers is impeded. The Seebeck coefficient can be easily affected by various parameters and its increase is generally due to i) a decrease in carrier concentration, ii) the formation of resonant states near the Fermi level, iii) the scattering by lattice defects, and/or localized magnetic moments. Referring to the present knowledge of M1-R transition, a possible explanation in the case of VO_2 (B) would be the formation of spin singlets below 240 K that would result in a decrease of the carrier concentration.
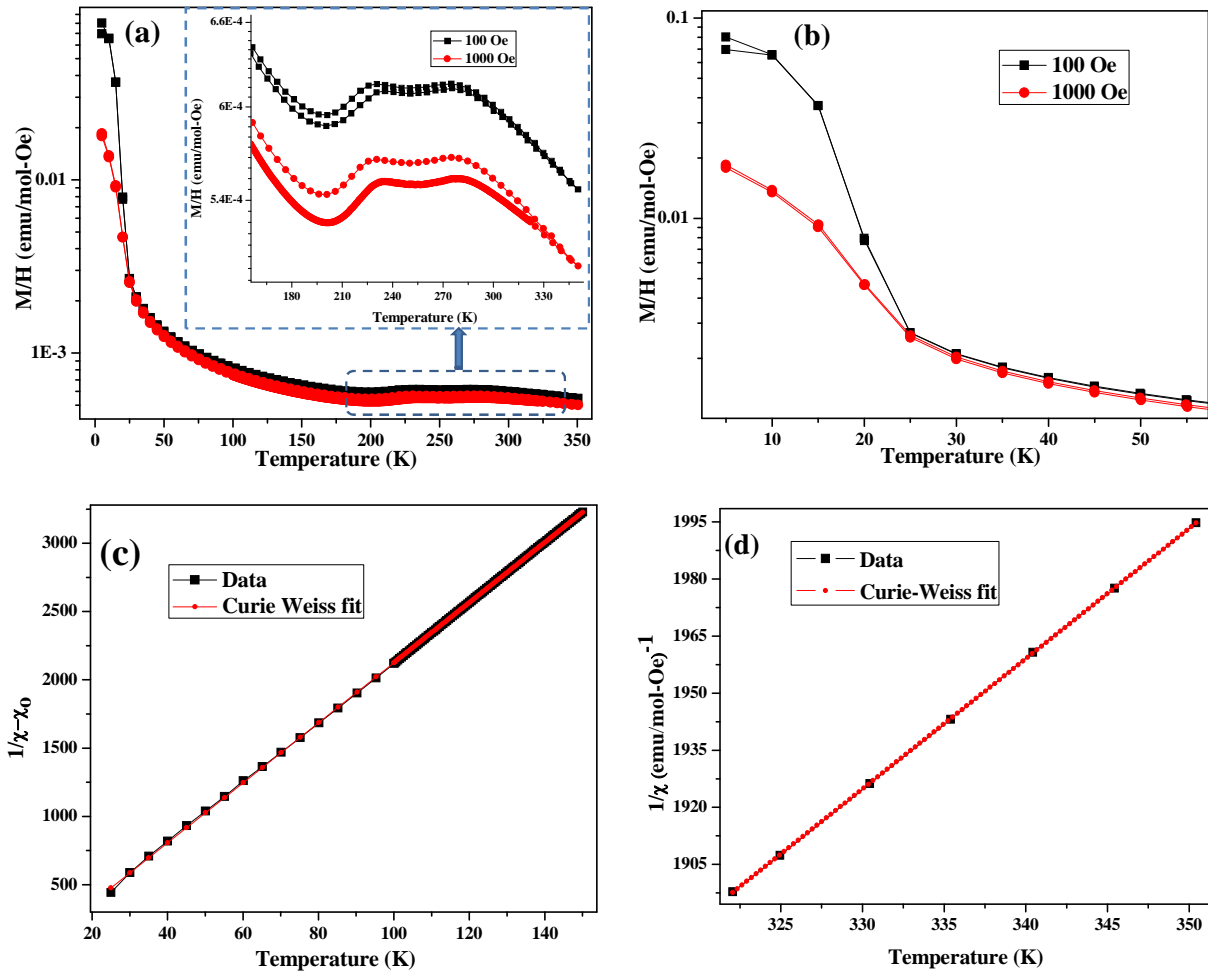

Figure 12. a) ZFC and FC curves of VO_2 (B) measured at 100 and 1000 Oe. b) Zoom in the magnetic susceptibility measured below 60 K at 100 and 1000 Oe. c) Inverse magnetic susceptibility (black squares) and the Curie–Weiss fit from 25-150 K (red circles). d) Inverse magnetic susceptibility (black squares) and the Curie–Weiss fit from 320-350 K (red circles).

Junfeng Liu et al. reported that VO_2 (B) has a weak paramagnetic behavior, without any anomaly in the magnetic properties [21]. **Figure 12a** shows the magnetic susceptibility data in the ZFC and FC regimes evidencing however an anomalous temperature dependence as already reported by Zakharova et al [22]. They attributed this behavior to the simultaneous presence of paramagnetic vanadium ions of the high temperature phase and the formation of non-magnetic V-V pairs of the low temperature phase. Below 25 K (**Figure 12b**), the magnetic susceptibility saturates what could be assigned to the ordering of some remaining free spins.

Both low (25-150 K) and high (320-350 K) temperature regions of the magnetic susceptibility were modelled with a Curie–Weiss law and if necessary a temperature independent term (χ_0). The fits $\chi(T) = \chi_0 + C/(T + \theta)$ are shown in **Figure 12c** and **Figure 12d** respectively. At low temperature the fitted parameters are $\chi_0 = 2.7632*10^{-4}$ emu/mole, C=0.0454 and $\theta = -3.37$ K suggesting the presence of *ca* 12% free spins from $3d^1$ V^{4+} ions ($C_{th} = 3/8$) and very small AFM interactions. At high temperature C=0.292 what represents nearly 80% of V^{4+} free spins and $\theta = -233$ K denoting AFM interactions. These results agree with the observations of Corr et al. that the low and high temperature phase can coexist over a large temperature domain far beyond the mean transition temperature [18].

The intermediate temperature domain between *ca* 190 K and 300 K is more complex to analyse. In this region, two humps are visible in the magnetic susceptibility data centred nearly at 235 and 280 K. A small hysteresis between FC and ZFC regimes is also present. Oka et al. reported similar magnetic behaviour with only one broad hump centred 300 K [21] and he ascribed it to structural changes. **Figure 13** shows some high temperature EPR spectra in the region of the transition. In the case of this B polymorph, the intensity of the spectra was quite weak and the signal-to-noise ratio was very low. However, several conclusions could be drawn from these experiments: i) by comparison of the signals with the ones recorded for A and M1/R polymorphs, spectrum can be assigned to resonances from single V^{4+} ions and to resonances resulting from the interactions within V-V pairs; ii) as the signal is very small, it suggests that the V-V interaction are very weak; iii) at least in the narrow temperature interval 220-280 K, the evolution of the signal is soft, in good agreement with magnetization measurements, while beyond these limits the change in the magnitude of the signal looks more important with a drop (but not vanishing) of the central signal and the appearance of a new resonance in low magnetic

field (B ~ 2000 G) near RT; this might reflect the beginning of a phase modification (*e.g.* beginning of structural transition), however, because of experimental limit (max. T = 300 K with our instrumental setup) the exact transition temperature as well as the details of the high temperature phase could not be accessed.
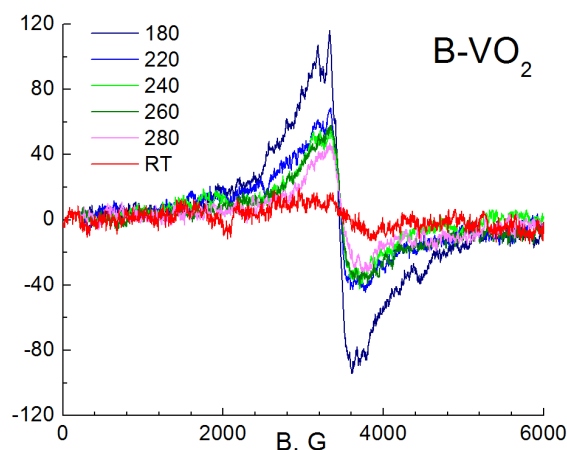
Figure 13. Electron paramagnetic resonance spectra of VO_2 (B) in the range 180 K-RT.

VIII.6. Discussion and conclusions

Figure 14 summarizes our observations on VO_2 (B) using different experimental techniques. It is worth noting that all these experiments converge to a transition temperature at *ca* 240 K but in the same time they show that the transition is very wide. Though the transition might have its origin in similar mechanisms than the other polymorphs the properties evolve much smoother. Actually the details of the structure are quite different and they prevent from an abrupt change like for M1/R transition. In particular, unlike the case of M1 or even A polymorphs in which an obvious Peierls pairing can occur in the linear or the zig-zags chains, the structure of B polymorph is more constrained and is unlikely to offer the possibility of long range pairing though all the basic ingredients are present (d^1 state, "short" distances, AFM interactions). **Figure 4d** shows that the shortest V2-V2 bond are separated by two (short and medium) pairs and that only a strong structural rearrangement would lead to a Peierls state.
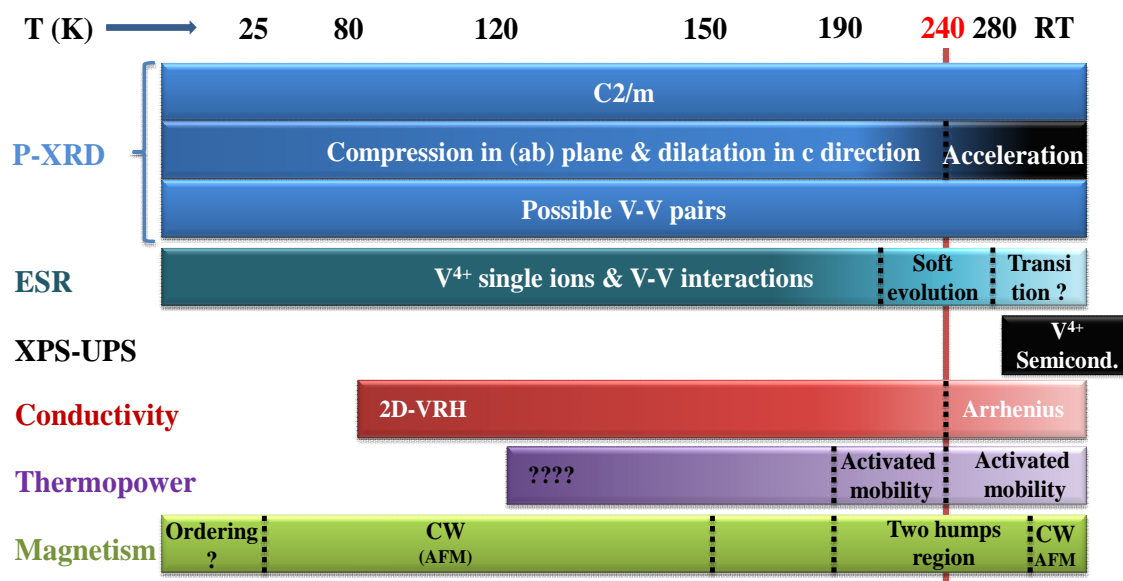
Figure 14. Schematic view of the evolution of the studied properties *vs* temperature.

In this context, we actually can propose a two-step scenario in which, like in the case of the other polymorphs, a first transition occurs at high temperature ($\approx$ RT) with the pairing of V2 ions followed just below by a standard AFM transition implying either V1 ions in the long (red) zig-zag chains (or V1-V2 couples in the short (blue) zig-zag chains). Within such scenario, the two humps in the magnetic properties could be understood as marking each transition while the low temperature regime could sign V1-V2 interactions (or V1 interactions). At each transition, more and more carriers are trapped in agreement with the observation and the increase in E_α as T decreases.

VIII.7. Prospectives

In light of the present results, the interest of this compound sounds obvious both because it can help to give some insight in the behaviour of other polymorph by comparison of the evolution of their structure and properties but also because it's intrinsic behaviour which appears quite complex. Ideally, studies on single crystals could help understanding better the mechanisms we just "touched" in this chapter. It is important that a deep work on the structure will be done using synchrotron radiation to clarify the evolution of the details of the structure with temperature and even small angle neutron diffraction to study the magnetic properties. V oxides are likely to orbitally order and such high precision experiments would provide precious information in this sense.

VIII.8. References

[1] J. Liu, Q. Li, T. Wang, D. Yu and Y. Li, Angew. Chem., Int. Ed. 43, 5048 (2004)

[2] S.A. Corr, M. Grossman, Y. Shi, K.R. Heier, G.D. Stucky and R. eshadri, J. Mater. Chem. 19, 4362 (2009)

[3] C.V Subba Reddy, E.H. Walker, S.A.Wicker, Q.L. Williams, R.R. Kalluru, Curr. Appl Phys. 9, 1195 (2009)

[4] F. Sediri, N. Gharbi, Mater. Sci. Eng., B 139, 114 (2007)

[5] J. Rodríguez-carvajal, Physica B 192, 55 (1993)

[6] J. Valmalette, Gavarri, J. Mater. Sci. Eng. B 54, 168 (1998)

[7] Y. Oka, T. Yao, N. Yamamoto, Y. Ueda, A. Hayashi, J. Solid State Chem. 105, 271(1993)

[8] S. Pavasupree, Y. Suzuki, A. Kitiyanan, J. Solid State Chem. 178, 2152 (2005)

[9] Ch. Leroux, G. Nihoulm, G. Van Tendeloo, Phys. Rev. B 57, 5111 (1998); C.V. Subba Reddy, E.H. Walker, S. A. Wicker, Q. L. Williams, R.R. Kalluru, Curr. Appl. Phys. 9, 1195 (2009)

[10] D.T. Clark, H.R. Thomas, J. Polym. Sci. Polym. Chem. Ed. 14, 1671(1976); E. Desimoni, G.I. Casella, A. Morone, A.M. Salvi, Surf. Interface Anal. 15, 627(1990)

[11] R. Zimmermann, R. Claessen, F. Reinert, P. Steiner and S. Hufner, J. Phys.: Condens. Matter 10, 5697 (1998)

[12] J. Mendialdua, R. Casanova, Y. Barbaux, J. Electron Spectrosc. Relat.Phenom. 71, 249 (1995); E. Hryha, E. Rutqvistb and L. Nyborg, Surf. Interface Anal. *DOI 10.1002/sia.3844*, (2011)

[13] D.A. Neaman, Semiconductor Physics and Devices, 3rd ed.; McGraw-Hill Publishing Ltd: New York (2007)

[14] C.N. Berglund and W.E. Spiecer, Phys. Rev., 136, A1030 (1964)

[15] Y. Wang, Z. Zhang, Physica E 41, 548 (2009)

[16] H. Yin, M. Luo, K. Yu, Y. Gao, R. Huang, Z. Zhang, M. Zeng, C. Cao, Z. Zhu, ACS Appl. Mater. Interfaces 3, 2057 (2011)

[17] Y. Wang, Z. Zhang, Y. Zhu, Z. Li, R. Vajtai, L. Ci, and P.M. Ajayan, ACS Nano 2, 1492 (2008); C.N Berglund and H.J. Guggenheim, Phys. Rev. B 185, 1022 (1969)

[18] S.A. Corr, M. Grossman, Y. Shi, K.R. Heier, G.D. Stucky and R. Seshadri, J. Mater. Chem., 19, 4362 (2009)

[19] N.F. Mott, E.A. Davis, Electronic Process in Non-Crystalline Materials, Oxford, 1979

[20] P. Cox, Transition metal oxides: an introduction to their electronic structure and properties; Clarendon Press: Oxford, 1995.

[21] J. Liu, Q. Li, T. Wang, D. Yu and Y. Li, Angew. Chem., Int. Ed. 43, 5048 (2004)

[22] G.S. Zakharova , I. Hellmann, V.L. Volkov, Ch. Taschner, A. Bachmatiuk, A. Leonhardt, R. Klingeler, B. Buchner, Materials Research Bulletin 45, 1118 (2010)

In this thesis, two dimensional (2D) layered cobalt double oxides and quasi one dimensional (1D) vanadium oxides were studied with the aim of synthesizing new compounds and understanding their electronic properties in relation with their crystal structures.

IX.1. General conclusions

The following table summarizes the several issues that existed in the literature for the systems under consideration in this study, contributions from this work and directions for future work.

System	Issues	Contributions and conclusions	Prospective
P2-$Na_{0.7}Co_{1-x}M_xO_2$ D2-$AgCo_{1-x}M_xO_2$ (M=Mg and Mn)	To improve thermoelectric properties.	Charge localization, Strong disorder.	Shaping of the materials.
VO_2 (M1)	Mott or Peierls or Mott-Peierls? Simultaneous SPT and MIT?	Spin, orbital and lattice degrees of freedom are strongly coupled. Inter-chain interactions are envisioned at 270 K.	The investigations are necessary around T_t, not only at T_t.
$V_{1-x}Mo_xO_2$	Role of substituent? Oxidation state of Mo.	Along with ionic radii, electronic structure is a key factor. Mo is in high valent state that changes with increasing concentration. Electronic correlations enhance the thermoelectric properties.	The complete phase diagram. In-situ TEM studies. Strongly correlated systems for thermoelectrics.
VO_2 (A)	Proposed to have a MIT at SPT? Nature of the transition is not known.	Orbital energy gap separates SPT and ET, the magnitude of the changes across ET. Longer distances in HT phase limit MIT.	More systematic kinetic phase diagrams. In-situ structural studies. Single crystals. Structure-Property anisotropy.
VO_2 (B)	Proposed to have a MIT at SPT?	There is no SPT and MIT Unfavorable orbital arrangement prevents the long range orbital ordering. Changes in the magnetic interactions and dominant charge carriers centered at 240 K.	

SPT: Structural phase transition; MIT: Metal-insulator transition; ET: Electronic transition; T_t: Transition temperature

- In the case of layered cobalt oxide systems, electronic properties studies highlight the high sensitivity of the electronic properties to changes in the structure, even weak; the expansion in the lattice parameters with substitutions generally increases the charge localization and introduces strong disorder in the system leading to a drastic reduction of the conductivity. As far as the thermoelectric performances are concerned, and for low substitution rates, this effect is counterbalanced with an increase of the Seebeck coefficient that can punctually result in a higher power factor. Even though our results give some insight in the behavior of substituted delafossites, the main drawback of this study stands in the difficulty to shape the materials and then to access the intrinsic properties of the compounds.

- Novel materials with interesting properties are always on a high demand and it is crucial to achieve "pure" samples. Solid state and hydrothermal methods are the most versatile techniques employed to prepare several stable and metastable polymorphs of vanadium dioxides. Using single step hydrothermal synthesis and constructing systematic kinetic phase diagrams, we were able to propose optimized paths to stabilize the several VO_2 polymorphs and some other phases. Preliminary hydrothermal experiments on substitution of several stable polymorphs result in different transformation sequences among the polymorphs as compared to solid state processes, indicating the possible existence of intermediate phases. Oriented growth attachment and layer by layer formation mechanisms were established to be responsible for the microrod and flower like crystals, in case of VO_2 (A) and VO_2 (M1) materials synthesized under hydrothermal conditions.

- Our studies on M1-VO_2 confirm the possibility of a Mott transition which can be enhanced by the presence of a Peierls state, originating from the orbital ordering. In this case the spin, orbital and lattice degrees of freedom are strongly coupled and Mott, orbital ordering and Peierls states develop simultaneously, leading to the abrupt changes across the transition. The interest of strongly correlated systems for the enhancement of the thermoelectric efficiencies is confirmed by the work on $V_{1-x}Mo_xO_2$ (M1/R) which evidences a clear efficiency maximum as the correlations peak at *ca* 7.5% substitution in the Curie-Weiss metallic regime. This maximum was shown to be related to the complex balance of the cation valences depending on the substitution rate thereby highlighting the possible role of charge transfers on the strength of correlations and the resulting electronic properties. The unexpected variation of the effective

magnetic moments as a function of the Mo content brings clues about the presence of V-V ion pairs in the metallic tetragonal phase.

- High pressure Spark Plasma Sintering was used to consolidate VO_2 (A) materials and access to the intrinsic electronic properties of this polymorph. VO_2 (A) is characterized by a progressive and reversible structural phase transition accompanied by a semiconductor-semiconductor transition between 150 K and 470 K. Magnetic measurements confirmed the complete pairing of V^{4+} ions below 150 K while the de-pairing is complete above 470 K. In this case, direct-indirect interactions between the neighboring V atoms lead to an orbital ordering at 530 K. The separation between orbital ordering and Mott/Peierls states, which develop at 437 K, leads to smaller changes across the electronic transition.

- VO_2 (B) polymorph has a quite different structure than A and M1 polymorphs, though some obvious similarities exist. Unlike A and M1, no long range ordering and no deep change in the structures occur on changing the temperature, and the cell parameters evolve mostly within the same space group. This result in a soft semiconductor-semiconductor transition centred at *ca* 240 K, but the width of the transition is very large as compared to M1. Though the transition might basically have its origin in similar mechanisms than the other polymorphs, we actually proposed, based on the details of the structure, a more developed scenario implying two transitions to account for our observations, with a short range pairing at high temperature followed by a long range AFM ordering at lower temperatures.

IX.2. Prospectives

- For delafossite layered cobalt oxides, an obvious perspective is to remove some ambiguities on the properties and on the effect of substitutions with the shaping of delafossite-type materials; either polycrystalline materials using for instance the advantages of Spark Plasma Sintering techniques, or single crystals using the versatility of hydrothermal methods.

- In the case of vanadium oxides, from the synthesis perspective, the kinetic and ratio dependent studies presented in this work can be extended to high temperature and high pressures (by simply changing the filling percentage of auto clave) to develop new kinds of hydrate, non-hydrate phases and even Magneli or Wadsley phases of vanadium oxides. The inter/intra phase transformation processes among the several VO_2 polymorphs and studies related to the stability

of the phases vs. substitutions under hydrothermal conditions will be useful to synthesize novel possible intermediate polymorphs.

- In the case of Mo-VO_2, in-situ electron diffraction structural studies would be interesting to probe the possible presence of cation pairs in metallic phase, to support anomalies in the magnetic properties. Also, synchrotron spectroscopy studies around the MIT transitions at high substitution rates could provide useful information about the possible changes in valence states of cations. The complete thermoelectric phase diagram of $V_{1-x}Mo_xO_2$ could be constructed to obtain the optimum composition region for enhanced thermoelectric properties. In light of the present thermoelectric properties, several "simple" strongly correlated transitional metal oxides can be explored for the thermoelectric applications.

- For VO_2 (A) and VO_2 (B), the proposed single crystal growth procedures could be further extended to prepare the larger single crystals to study the structure-property anisotropy in these quasi 1D and 2D systems. Since our results suggest the progressive nature of structural and electronic transitions, detailed studies of the structural and magnetic characterizations through local probes, such as microscopic techniques on the nanometer length scale with spatial and temporal resolution, would be very interesting to determine the exact character of structural and electronic homogeneities in VO_2 (A) and VO_2 (B). On the other hand, complementary studies like in-situ temperature dependent structural and Raman spectroscopic experiments would be interesting to deeper investigate the behaviour of these polymorphs.

Résumé:

Les oxydes doubles lamellaires de cobalt et les oxydes de vanadium ont récemment suscité un vif intérêt suite à la découverte de leurs propriétés thermoélectriques prometteuses. Nos efforts visent à synthétiser de nouveaux composés dérivés de ces systèmes en utilisant la synthèse à l'état solide, l'échange d'ions et/ou les techniques hydrothermales. Afin de moduler et d'optimiser leurs caractéristiques thermoélectriques, nous avons ajusté la composition des oxydes de cobalt grâce à des substitutions appropriées. Au sein du dioxyde de vanadium quasi-1D, nous avons considéré trois différentes structures polymorphes : M1, A et B. Nous avons exploré les différents systèmes en construisant l'ensemble des diagrammes de phases. Nous avons également étudié l'effet de la substitution du vanadium par le molybdène et le chrome sur la stabilité de ces structures polymorphes et caractérisé leurs propriétés électroniques en relation avec les mécanismes de transition de phase.

Mots clés :

- Oxydes de cobalt lamellaires
- L'état solide et la synthèse hydrothermale
- Polymorphes de VO_2
- Transitions métal-isolant
- Les diagrammes de phases cinétiques
- Propriétés thermoélectriques

Title: Experimental investigation of structure - property relationships and dimensionality aspects in some cobalt and vanadium oxides.

Abstract :

Lamellar cobalt double oxides and vanadium oxides have recently attracted tremendous interest after the discovery of their interesting thermoelectric properties. Our efforts aimed at synthesizing novel related compounds using standard solid state, ion exchange and/or hydrothermal techniques. In order to modulate and optimize their thermoelectric characteristics, we have tuned the composition of cobalt double oxides by appropriate substitutions. In quasi 1D vanadium oxides, the interplay between spin, charge and orbital degrees of freedom often leads to remarkable properties. Here we dealt with three different polymorphs of vanadium dioxide, namely M1, A and B. We explored the several novel systems by constructing systematic phase diagrams. We also studied the effect of Mo and Cr:V substitution on the stability of these polymorphs and characterized their electronic properties in relation with the structural phase transition mechanisms. Finally, we explored their potentiality for thermoelectric applications.

Keywords :

- Layered cobalt oxides
- Solid state and hydrothermal synthesis
- Polymorphs of VO_2
- Metal-insulator transitions
- Kinetic phase diagrams
- Thermoelectric properties